UNIVERSITÀ
DEGLI STUDI
DI PADOVA

UNIVERSITÀ DEGLI STUDI DI PADOVA

Dipartimento di Ingegneria Civile, Edile e Ambientale

SCUOLA DI DOTTORATO DI RICERCA IN SCIENZE
DELL'INGEGNERIA CIVILE ED AMBIENTALE
CICLO XXVIII

FINITE ELEMENT REGULARIZATION FOR POST LOCALIZED BIFURCATION IN VARIABLY SATURATED MEDIA

Direttore della Scuola: Ch.mo Prof. Stefano Lanzoni

Supervisori: Ch.mo Prof. Lorenzo Sanavia
Ch.mo Prof. Bernhard Schrefler

Dottoranda: Maria Lazari

JANUARY, 2016

to Achilleas

‘Της παιδείας οι μεν ρίζες είναι πικρές, οι δε καρποί γλυκοί’

Αριστοτέλης

Acknowledgements

The present dissertation was carried out during my research as a doctoral candidate at the University of Padova in the frame of the MuMoLaDe (Multiscale Modelling of Landslides and Debris Flow) project. This thesis has been performed for the first two years in the University of Padova and for the last year at BAUGRUND DRESDEN Ingenieurgesellschaft mbH, geotechnical design and construction company. I owe my gratitude to all those who helped in making this thesis possible.

First and foremost, I would like to express my deepest gratitude to my supervisor prof. Lorenzo Sanavia for giving me the opportunity to do my doctoral study under his guidance on a research project that really interested me. His invaluable advice, support and encouragement have made this work possible. I feel incredibly privileged to have him as my supervisor.

I am immensely thankful to prof. Bernhard Schrefler, co-supervisor of this thesis. His broad knowledge and prominent publications in the field of multiphase porous materials were very important foundations of this thesis.

I would like to convey my gratitude to prof. Peter-Andreas von Wolffersdorff and to Dr. Thomas Meier for the nice cooperation we had this year. I will never forget the warm welcome given to me in Dresden by them and their colleagues.

An important part of this work, the constitutive modelling for unsaturated soils, was done in cooperation with prof. Claudio di Prisco from Politecnico di Milano and prof. Federico Pisanò from Delft University of Technology. I am very grateful to both of them for guiding me from the beginning of this goal, for the constant assistance and the precious advice for improving my numerical results. I am personally indebted to Federico for all the time he devoted to my research, for immediate answering my innumerable questions and for supervising this part of my thesis in the most effective way. My gratitude is also extended to prof. Giuseppe Buscarnera for his assistance with finalizing the implementation of the elastoplastic model for unsaturated soils in the Comes-geo code and for the very fruitful discussion we had during the EMI conference. Special thank goes to his PhD student, Constance Mihalache for providing the data I needed for the model's validation and for being so kind as to perform some extra tests with the material point driver for comparison. My sincere thanks to prof. Claudio Tamagnini for his feedback on this part of my work during the interview as an external reviewer of my thesis.

I would like to thank prof. Jacques Desrues and Dr. Yvonne Lins for providing experimental data and information for the Hostun sand.

I would like to acknowledge the financial support provided by the 7th Framework Programme of the European Union (ITN MuMoLaDe project 289911). The work on this project enabled me not only to write on my PhD thesis but also to be introduced to the scientific community and come into contact with internationally recognized scientists.

Next, I would like to thank all my colleagues at the University of Padova for creating a pleasant and friendly working atmosphere. My appreciations and sincere thanks also go to my colleagues and friends at Baugrund Dresden, who made my stay here a most pleasant one. Special thanks to my MuMoLaDe colleagues for the nice memories we share the last three years, the encouragement and support we received from each other every time we met.

Heartfelt thanks to my friends and family in Greece for their endless support and love. Although we were far these years they never let me feel this distance.

Finally, to my husband Achilleas, to whom this thesis is dedicated. I could never find the words to describe my gratitude for always being here…

Dresden, January 20th 2016

Abstract

Computational investigation of the stability of natural slopes within a coupled hydro-mechanical approach becomes more and more attractive due to an increasing number of slope movements caused by heavy rainfall events. Seasonal cycles of summer drying and winter-spring wetting affect the stability and serviceability of natural and man-made slopes, threatening lives and property worldwide. Heavy rainfall will increase the soil moisture content and lead to a reduction in suction and a consequent weakening of the soil. As a result, the slope may fail either in a diffused or in a localized pattern.

The localization process is a classical mode of mechanical instability and is described as the concentration of shear strains in narrow bands within the soil strata. As it is well-known, the width of those bands cannot be properly computed using the standard continuum mechanical approach with unstable materials (in the sense of Drucker). In the framework of the standard finite element method the computation of shear band phenomena reveals a strong mesh dependency of the numerical solution and the objectivity of the computational results is blown. Each mesh refinement results in an overall different outcome and the width of the localization band has the size of the element of the adopted mesh. In the literature two main categories of methodologies can be found for regularizing this problem. One is to simulate the formation and propagation of such discontinuities via suitable enrichment functions and is the concept of the so-called extended finite elements. The other solution is to exploit enhanced continuum theories. These theories contain an internal length scale which is an additional material parameter related to the shear band width and removes the spurious mesh sensitivity of the numerical simulation results.

The present work is focused on the second category. In this context, viscoplasticity and non-local theories are adopted to effectively study strain localization mechanism, assuming the soil as a multiphase porous medium. This means that the localization analysis is considered as a fully coupled hydro-mechanical problem with the material consisting of an elasto-viscoplastic skeleton and open pores filled with incompressible liquid water and compressible gas. Both regularization techniques are physically sound. Rate dependency is experimentally motivated as the mechanical response of granular materials seems to be rapid, but not instantaneous and a viscoplastic constitutive model is able to reproduce creep and relaxation processes. The physical interpretation of the non-local theory stems from the fact that no real material is an ideal continuous medium and the evolution of the microstructure at one point influences the surrounding points when irreversible strains take place.

Two types of viscoplastic models are applied; the Perzyna and the Duvaut-Lions. The former is extended with respect to the non-local integral approach. In the first part of this work, the generalized effective stress is limited by the Drucker-Prager yield criterion. The models are implemented and numerically validated in the finite element code Comes-geo and further verified by simulating an experimental plane-strain biaxial test and a benchmark slope failure problem. This work is in essence

aimed at answering key questions, such as: what are the most significant influential factors in the development of strain localization for each regularization technique and what is the role of suction and drainage conditions; is the viscosity of the soil affected by the presence of water and how does this fact influence the regularizing capabilities of the method; how do the internal lengths introduced by viscosity and non-locality interact with each other and under which circumstances is the one method preferable to the other?

The second half of this work comprises the extension to viscoplasticity of the existing advanced elastoplastic constitutive model for unsaturated sands developed by Buscarnera and Nova. This model allows for hydraulic bonding and debonding effects and therefore the main mechanisms of unsaturated materials are captured. The elastoplastic version of the model is first implemented in the finite element code Comes-geo and validated with results from the literature. The model is then extended to viscoplasticity and is also implemented and validated in the code. The proposed viscoplastic formulation, as further novelty, is enhanced with the dependence of the constitutive parameters on the relative density. To validate the elastoplastic model in the finite element code Comes-geo a series of tests are simulated: triaxial shear tests at different suction and net confining pressure, oedometric tests with drying and wetting paths and triaxial and plane-strain compression tests in drained and undrained conditions. The viscoplastic model is also validated through oedometric tests, creep tests and triaxial compression tests on different sand densities. The onset of shear strain localization is then studied and the finite element results are compared with the results of a theoretical stability analysis. The verification of the viscoplastic model is finalized with the simulation of a triaxial compression test.

The main motivation for the present work stems from these premises and this thesis presents an efficient tool to simulate strain localization with regularization techniques, which do not need to increase the number of the state variables of the numerical model, taking into account fully coupled hydro-mechanical analysis and using advanced constitutive model for unsaturated sands.

This dissertation has been performed for the first two years in the University of Padova (Italy) and for the last year at Baugrund Dresden (Germany), geotechnical design and construction company within the Marie Curie Initial Training Network project MuMoLaDe (Multiscale Modelling of Landslide and Debris flow, 7th Framework Programme of the European Union, project n. 289911, http://www.mumolade.com/). This practice is in the scope of linking academia and industry and the transfer of knowledge. In this framework, the advanced elastoplastic and elasto-viscoplastic models for unsaturated soils are implemented and validated in PLAXIS commercial finite element analysis software. The validation included single element tests of drained and undrained triaxial loading and triaxial tests at different suction levels. The implementation is verified and the effectiveness of the model is displayed by numerical simulations of a partially saturated slope failure of the laboratory scale.

Sommario

Lo studio numerico della stabilità dei pendii con un approccio idro-meccanico accoppiato è sempre più importante e necessario nella pratica ingegneristica a causa del continuo aumento dei fenomeni franosi, che determinano perdite di vite umane e danni all'ambiente naturale e costruito. In genere, tali fenomeni sono provocati da eventi metereologici violenti, che determinano la riduzione delle forze capillari intergranulari e della resistenza del materiale costituente i pendii. Inoltre, anche cicli stagionali di essicazione estiva e imbibizione invernale e primaverile favoriscono l'instabilità di pendii naturali e artificiali.

Il collasso dei pendii avviene con un meccanismo diffuso oppure localizzato; in quest'ultimo caso avviene mediante la formazione di zone di ampiezza limitata dette bande di taglio in cui si concentrano le deformazioni del materiale. Quando si simula numericamente il collasso causato dalla formazione di bande di taglio e si utilizza la meccanica classica del continuo di Cauchy con un modello costitutivo per materiale instabile nel senso di Drucker, è noto che la larghezza delle bande di taglio non può essere calcolata né definita nel modello. In particolare, lo studio numerico di fenomeni di localizzazione delle deformazioni con il metodo degli elementi finiti evidenzia una forte dipendenza della soluzione numerica e della larghezza delle bande di taglio dalla mesh utilizzata, con perdita della soluzione all'infittimento della mesh. Infatti, accade che la larghezza delle bande di taglio risulta fissata dalla dimensione dell'elemento finito utilizzato, tendendo a zero al tendere a zero della dimensione dell'elemento finito. Di conseguenza, per poter simulare in modo obiettivo fenomeni di localizzazione delle deformazioni, è necessario modificare (o regolarizzare) il continuo di Cauchy.

In letteratura si trovano due classi principali di regolarizzazione a cui ricorrere per risolvere questo problema. Il primo propone di simulare la formazione e la propagazione delle bande di taglio utilizzando campi discontinui di spostamento, dando origine al metodo degli elementi finiti estesi (extended finite element method). Il secondo propone di arricchire il modello continuo a livello cinematico oppure a livello costitutivo (enhanced continuum theories), in modo da fornire al modello una lunghezza di scala interna da cui dipende la larghezza della banda di taglio, eliminando in questo modo il problema della mesh dipendenza citata in precedenza.

Questa tesi di dottorato è svolta scegliendo di arricchire il continuo di Cauchy a livello costitutivo e individua nella viscoplasticità locale e non-locale l'approccio utile allo studio della localizzazione delle deformazioni nei suoli. Inoltre, per tenere conto delle interazioni fra la parte solida e quella fluida, i suoli sono analizzati come mezzi porosi multifase. Di conseguenza, l'analisi della localizzazione delle deformazioni nei suoli è compiuta considerando il materiale dei pendii come un mezzo poroso costituito da uno scheletro solido elasto-viscoplastico e pori contenenti acqua liquida e aria umida. La scelta delle due tecniche di regolarizzazione sopra citate è stata dettata dal loro significato fisico, in quanto la risposta meccanica dei materiali granulari non è istantanea a causa dei processi viscosi o di rilassamento. Inoltre, l'introduzione della teoria non-locale deriva dalla considerazione che nessun materiale reale è un continuo nel senso matematico, a causa dell'evoluzione della microstruttura in un punto materiale che influenza i punti del suo intorno quando si sviluppano deformazioni irreversibili.

In questa tesi sono utilizzati due approcci viscoplastici: quello di Perzyna e quello di Duvaut-Lions. Il primo è stato esteso con l'approccio non-locale. Nella prima parte di questo lavoro di tesi i modelli viscoplastici sono sviluppati utilizzando il criterio di snervamento di Drucker-Prager, implementati nel codice agli elementi finiti Comes-geo, validati e verificati numericamente simulando test sperimentali di compressione biassiale in stato piano di deformazione e un test numerico di collasso di un pendio. Questa parte del lavoro ha lo scopo di rispondere alle seguenti domande-chiave sulla localizzazione delle deformazioni nei mezzi porosi viscoplastici: quali sono i fattori più importanti che influenzano lo sviluppo della bande di taglio e qual è il ruolo delle pressioni capillari e delle condizioni di drenaggio; se la viscosità dei suoli è influenzata dalla presenza dell'acqua e se influenza le proprietà di regolarizzazione del metodo locale o non-locale; come interagiscono la lunghezza di scala interna indotta dalla viscosità e quella introdotta dalla non-località; quando un metodo è preferibile ad un altro.

La seconda parte di questo lavoro di tesi ha per oggetto lo sviluppo di un nuovo e avanzato modello viscoplastico a partire dal modello costitutivo elasto-plastico per le sabbie parzialmente sature proposto da Buscarnera e Nova. Questo modello permette di simulare i principali meccanismi del comportamento micromeccanico di materiali parzialmente saturi, ovvero la coesione idraulica (hydraulic bounding) e gli effetti di decoesione (debonding) nelle sabbie. Questa parte del lavoro è stata svolta in due fasi; nella prima fase si è discretizzato e implementato il modello elasto-plastico nel codice agli elementi finiti Comes-Geo, successivamente validato utilizzando risultati di letteratura. In particolare sono state simulate: test di taglio a vari valori di pressione capillare (suzione) e pressione di confinamento, test di compressione edometrica con percorsi di desaturazione e saturazione e test di compressione drenata e non drenata in condizione di stato piano di deformazione. Nella seconda fase, questo modello è stato esteso alla viscoplasticità, in modo da tener conto del comportamento viscoso delle sabbie, implementato nel codice Comes-Geo e validato simulando prove di laboratorio di letteratura. La formulazione viscoplastica proposta è stata poi arricchita formulando la dipendenza dei parametri costitutivi dalla densità relativa. Il modello viscoplastico di base e quello arricchito sono stati validati simulando prove di compressione edometrica, prove di viscosità e prove di compressione triassiale a vari valori di densità. Inoltre, con il modello arricchito, è stata simulata una prova di localizzazione su sabbie dense e sciolte e i risultati numerici ottenuti sono stati confrontati con i risultati dell'analisi di stabilità.

Con questa tesi si è sviluppato uno strumento numerico efficiente per la simulazione della localizzazione delle deformazioni con metodi regolarizzati che non necessitano di aumentare il numero di variabili di stato e che utilizza modelli costitutivi avanzati considerando il comportamento idro-meccanico accoppiato delle sabbie parzialmente sature.

Questo lavoro è stato svolto presso l'Università degli Studi di Padova (Italia) durante i primi due anni di dottorato e presso l'unità di ricerca e sviluppo della società di progettazione e costruzione Baugrund Dresden (Germania) durante il terzo anno di dottorato; l'attività è stata svolta all'interno del progetto Marie Curie Initial Training Network MuMoLaDe (Multiscale Modelling of Landslide and Debris flow), 7th Framework Programme of the European Union, progetto n. 289911, http://www.mumolade.com/. I modelli costitutivi avanzati elasto-plastico e viscoplastici sono stati inoltre implementati e validati anche nel codice commerciale agli elementi finiti Plaxis durante la collaborazione con Baugrund Dresden.

Contents

Chapter 1

Introduction and Overview

Chapter 1: Introduction and Overview

1.1 Motivation and State of the Art

Localization of deformation into shear bands is one of the most interesting bifurcation problems in solid mechanics as it is considered to be the precursor of failure. As is well known, the occurrence of those bands within the soil strata can eventually lead to the activation of dramatic slope failures, Figure 1.1.

Figure 1.1: Strain Localization: experimental evidence [12] and real massive landslide obstructing highway in Taiwan.

In the early 1900s, Mohr gave his perspective by pointing to the following general property of localized deformation:

"...The deformations observed in a homogeneous body after the elasticity limit [is reached] are not confined in the smallest domains of the body. They consist more or less in that, parts of the body of finite dimension displace with respect to each other on two sets of slip bands..."

In order to properly characterize the mechanisms of strain localization, investigation is needed both numerically and experimentally. Experimental studies of strain localization in varieties of geomaterials have been performed extensively for the last decades, e.g. Vardoulakis (1980), Tatsuoka et al. (1990) and Desrues et al. (1996). It is shown that shear banding can take place in both contractive and dilative specimens, but for the latter the onset of localization is delayed until cavitation takes place in the pore-fluid (Mokni and Desrues (1998)). Moreover, it was found that strain localization is affected by various factors, such as the mean diameter of the particles, the confining stress, the density and the shear conditions and that in axisymmetric tests strain localization may remain more or less hidden inside the specimen and therefore a single well-defined shear band rarely develops (Lade, 1982 and Alshibli et al., 2003). Therefore, most of the experimental campaigns

on localization have been performed in biaxial apparatus, where this latter process is clearly evidenced.

From a mechanical standpoint, localization in geomaterials is analysed as a material instability which starts to grow within a small part of a body and then may propagate until the global behaviour is strongly affected. In such a case, the constitutive relationship violates the stability criterion (Hill, 1958) which states that the inner product of the stress rate and the strain rate must be positive.

As it is well known, this inner product becomes negative when, in a uniaxial tension or compression test, the slope of the homogenized axial stress-axial strain curve is negative; the so-called strain softening phenomenon. However, apart from softening behaviour, the use of a non-associated flow rule may contribute to material instability as well, as clearly indicated by Rudnicki and Rice (1975). As a consequence of the aforementioned behaviour, the homogeneous deformation state which can be observed at the beginning of the loading, swaps into an inhomogeneous state indicated by the occurrence of shear bands, Figure 1.2 (Desrues and Viggiani, 2004).

Furthermore, the loss of positive definiteness of the second order work criterion is governed by the symmetry properties of the stiffness matrix (**D)** and according to Imposimato and Nova (1998) the Hill's criterion can be violated for the first time when the determinant of the symmetric part of the stiffness matrix becomes zero. It is interesting to observe that when the flow rule is non-associated, the loss of positive definiteness of the symmetric part of the stiffness matrix ($\det\mathbf{D}^s = 0$) will occur while the determinant of the stiffness matrix is still positive ($\det\mathbf{D} > 0$). This is because non-associativeness implies non-symmetry of the stiffness matrix and this in turn implies that the uniqueness of the incremental response can be lost even in the hardening regime, i.e. before the conventional limit locus under stress control is attained.

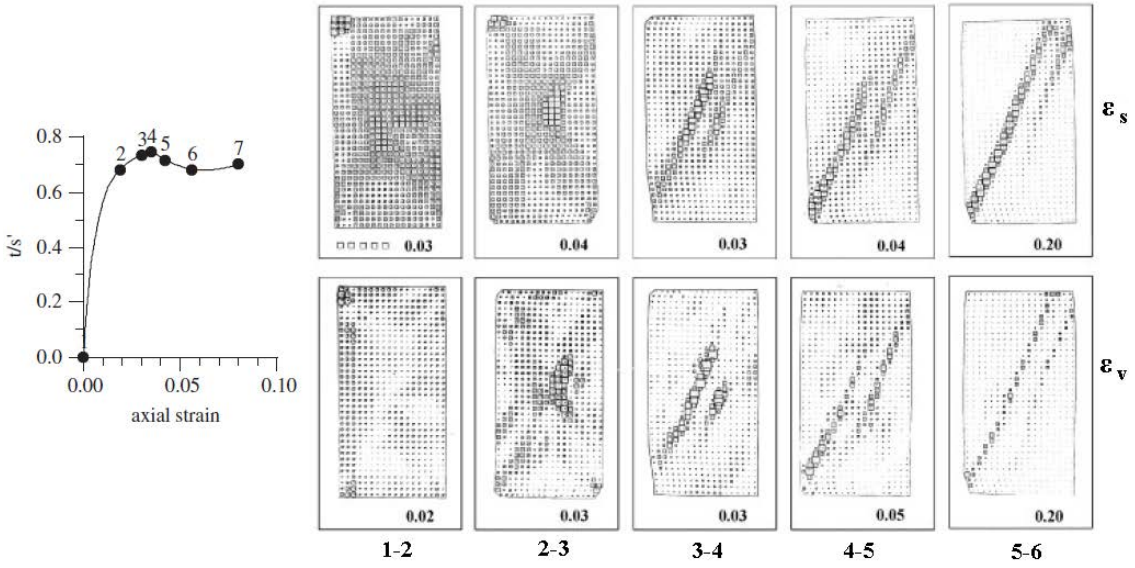

Figure 1.2: Stress-strain response of dense Hostun sand (test shf06) and stereophotogrammetry-based incremental fields of shear strain (top row) and volumetric strain (bottom row) [40].

The bifurcation analysis is a widely recognized theory for strain localization, which specifies the condition for the emergence of a shear band within a homogeneous stress and strained media. It is important to underline that this classical theory has three major drawbacks. First of all it analyses the emergence but not the development of shear band. Secondly, it does not guarantee that the shear band will actually emerge and finally, it does not give the thickness of the shear band and it precludes post-localization analysis (Bardet, 1990). Moreover, classical theory of plasticity applied to the simulation of localization phenomena leads to ill-posed problems due to the absence of an internal length scale.

More specifically, in quasi-static rate-boundary value problem the governing partial differential equations are elliptic prior to localization and exclude discontinuous solutions. At the onset of localization, as a consequence of material instability, these equations are changing type from elliptic to hyperbolic. Slip-lines and shear-bands are thus identified with the characteristic lines of the governing hyperbolic partial differential equations (Exadaktylos & Vardoulakis, 2007). Ellipticity is a necessary condition for well-posedness of the rate boundary value problem, in the sense that a finite number of linearly independent solutions are admitted, continuously depending on the data and not involving discontinuities (Benallal et al., 1991). Mathematically, loss of ellipticity occurs when the tangent modulus ceases to be positive and the acoustic tensor becomes singular (that is the determinant of the acoustic tensor is equal to zero). It is emphasized that ellipticity is a local condition and is one of the three conditions that are necessary for the well-posedness of the rate boundary value problem. The other two conditions are the satisfaction of the boundary complementing condition and the satisfaction of the interfacial boundary condition when the solid is heterogeneous.

Similarly, in dynamic problems, the governing equations of motion cease to be hyperbolic and become elliptic. In this case, the domain is split up into an elliptic part, in which waves have imaginary wave speeds and are not able to propagate (standing waves), and into a hyperbolic part with propagating waves (Sluys, 1992). Thus, the initial value problem becomes ill-posed and can no longer be a proper description of the underlying physical problem. Because of the inability of the standing waves to propagate, localization is then possible in a so-called set of measure zero, with no energy consumption.

As a consequence, in computations using finite element methods, the finite element model attempts to simulate the localization zone of zero thickness resulting in pathological dependence on discretization and in excessive mesh sensitivity. Obviously, such a behaviour leads to unphysical results, as from experimental investigations it can be seen that the width of the shear band is directly connected with a micro-structural length scale. For example, Roscoe (1970) based on direct experimental observations, proposed that the width of shear bands is about 10 times the averaged grain diameter. It is emphasized that the same problem is present in all discretization methods, for instance in the (meshless) finite difference method the spacing of nodes determines the width of a simulated localization zone.

To overcome this pathological mesh sensitivity and to ensure objectivity of the numerical results, the ill-posed problem has to be regularized and, therewith, to be transferred into a well-posed problem. Two main categories of methodologies can be found in the literature.

The first is to simulate the formation and propagation of such discontinuities via suitable enrichment functions and is the concept of the so-called extended finite elements, XFEM, (e.g. Babuška and Melenk 1997). The XFEM takes the advantage of the partition of unity property of finite elements, which allows a global enrichment to be incorporated locally. The standard approximation is enriched in a region of interest by a suitable global function multiplied by a linear combination of the standard shape functions associated with the nodes in that region.

The other solution is to exploit enhanced continuum theories. These theories contain an internal length scale which is an additional material parameter related to the shear band width and removes the spurious mesh sensitivity of the numerical simulation results.

Along these lines, various modifications and generalizations of standard continuum plasticity have been proposed to avoid the mesh-sensitivity problem in localization simulation of single phase materials. One of these is the so-called gradient plasticity, where higher order gradients of the plastic strain are considered in the material model, e.g. Mühlhaus and Aifantis (1991), de Borst and Mühlhaus (1992), Sluys et al. (1993) and Voyiadjis et al. (2001). The constitutive model involves the second gradient of the plastic strain measure in the yield or potential function and results in a well-posed set of partial differential equations.

In contrast to this mainly numerical motivated regularization technique, a regularization of the ill-posed localization problem can also be obtained by a detailed consideration of the material properties; Needleman (1988), Loret and Prevost (1990), Sluys (1992) and Oka et al. (1995) and (2002) introduced rate-dependence in their constitutive models. As indicated by the above authors and by Wu and Freund (1984) and Sluys and de Borst (1991), rate-dependence naturally introduces a length scale parameter, even though the constitutive equations do not contain a material parameter with dimension of length. It is noteworthy, that for dynamic analysis the width of the localization band can be predicted *a priori* as a function of material parameters, Sluys (1992). The stress waves, that produce loading and unloading paths, travel at a celerity which depends only on the material parameters, thus the band width depends on the stress wave celerity and the viscous effects. Moreover, Wang (1997) investigate the width of the localization zone in viscoplastic solid under dynamic loading and he alleged that, in the absence of imperfections, the key parameters which determine the width of the localization band are the viscosity and the softening modulus. An increase of viscosity or a less negative value of softening (for less brittle behaviour) leads to a widening of the localization zone. In contradiction, in quasi-static analysis (inertia effects are not considered) the velocity governing the loading and unloading, is no longer the stress wave celerity but the external load velocity. Therefore, the band width is not governed exclusively by the material parameters but it mostly depends on the load velocity. Indeed, Needleman (1988) demonstrated that in case of one-dimensional problems the

load velocity plays a crucial role in the resulting band width. Moreover, as it is discussed in Diéz et al. (2000) when the load velocity decreases, the viscoplastic solution tends to the elastoplastic one. Thus, if loading velocity is very small the band width is very narrow and the viscoplastic solution has the same deficiencies as the elastoplastic one (e.g. pathological mesh dependent results). Nevertheless, for quasi-static or dynamic problems, viscoplastic models still considered as a powerful tool for the regularization procedure.

In the case of granular material, the micropolar properties of the underlying microstructure can be taken into account with the application of the Cosserat or micropolar theory. This approach goes back to the Cosserat brothers in 1909. A first application of the Cosserat theory to the regularization of ill-posed localization problems is demonstrated in papers by Mühlhaus (1986), Mühlhaus and Vardoulakis (1987) and de Borst (1991). The basic idea of this extended continuum theory is to assign to each material point rotational degrees of freedom in addition to the standard translational degrees of freedom. The regularizing effect is due to the additional quantities of couple stress and curvature, which are related to each other by a constitutive relation containing usually an internal length scale. However, the application of the Cosserat theory significantly increases the numerical effort of solving a boundary-value problem, because of the introduction of the rotations as additional degrees of freedom.

Finally, another possibility for the regularization is the averaging of strain measures over a finite region, which yields to the so-called integral or non-local continua, e.g. Bažant and Lin (1988), Brinkgreve (1994) and Jirásek (2002). The non-local theory is based on the idea that the response of the material at a point is determined not only by the state at that point but also by the state of its neighboring points. In this approach, the averaging function contains the internal length by which the influence of the regularization method on the numerical solution is established. Moreover, the application of the non-local model is not restricted with respect to certain types of boundary-value problems or specific materials. An excellent overview on the physical motivations of non-locality and related numerical issues can be found in Bažant and Jirásek (2002).

An increasing number of papers related to strain localization problems in multiphase porous media have been published in recent years due to the importance of considering the fluid-solid interaction for the better understanding of the phenomenon. The general behaviour of the medium depends not only on the skeleton response (solid phase) to a given loading path, but also on the interactions occurring between the different phases of the medium (i.e. water, gas, oil). Capillary effects, temperature variations, chemical reactions induce specific behaviours, which have to be modeled by multiphysical constitutive laws. The numerical tools for the modeling of post failure problems have thus to be extended to this multiphysic context and questions concerning the interactions between localization and physical processes (like cavitation) can be answered.

According to Schrefler et al. (1996), Zhang et al. (1999) and Schrefler et al. (2006) in the numerical simulation of strain localization on multiphase materials an internal length scale may be naturally

introduced through Darcy's law and the related constitutive relationship for permeability. It has been shown by the same authors that this internal length scale may confer a regularization effect on the numerical solution in dynamic localization analysis only for axial waves, whereas this is not valid under quasi-static conditions where the internal length scale associated with permeability disappears. Reliable experimental observations have been difficult and the physical understanding of the nature of the problem is not yet satisfactory.

In the framework of multiphase porous media the aforementioned regularization techniques such as gradient plasticity models (e.g. Zhang and Schrefler (2000)), rate-dependent constitutive models (e.g. Loret and Prevost (1991), Liu (2003), Ehlers et al. (2004)) or micropolar continua (Ehlers and Volk (1998)) are usually adopted. The integral or non-local continuum, to the best of the author's knowledge, has not been commonly used as an alternative solution for regularization in the context of multiphase porous media.

Apart from the still posed question of the mesh dependency on the development of shear bands, another important issue is the constitutive modelling of the mechanical behaviour of variably saturated soils in the context of coupled hydro-mechanical analysis.

A large number of constitutive models can now be found in the literature that consider fundamental issues associated with the unsaturated soil behaviour, like the volume change and shear strength behaviour with suction or saturation changes. Partially saturated soils may either expand or collapse upon wetting depending on the stress level, and it is also possible that a soil might experience a reversal in the volumetric behaviour during wetting (initial expansion followed by collapse). Shear strength of soils also changes dramatically with changes on the degree of saturation, and a related engineering problem is slope failures caused by rainfall. There are several state of the art reviews over the last years for studying the topic (see e.g. Cui and Sun (2009), Gens (2010), Sheng (2011) etc.) that usually provide a thorough discussion of the stress state, the advantages and disadvantages of specific constitutive models as well as the latest developments in the area of unsaturated soil modelling.

It is now generally accepted that two independent constitutive stress quantities are necessary for the description of the mechanical behaviour of partially saturated soils. One of the most commonly used pair is the net total stress ($\boldsymbol{\sigma} - p^g$) and the suction ($p^g - p^w$), e.g. Alonso et al. (1990), Wheeler and Sivakumar (1995), Cui and Delage (1996). Another common choice is the average skeleton stress ($\boldsymbol{\sigma}' = \boldsymbol{\sigma} - \mathbf{1}[(1- S_w)p^g + S_w p^w$) together with the suction, e.g. Jommi and di Prisco (1994), Bolzon et al. (1996), Jommi (2000), Sheng et al. (2004), Borja (2006), Della Vecchia et al. (2013).

Borja (2004) has combined this effective stress formulation with the strain localization theory, elucidating the key role of suction and drainage conditions on the mechanics of shear failure. More recently, Borja et al. (2013) emphasized the importance of mechanical and hydrologic heterogeneities on triggering strain localization, using a 'nonstandard' critical state model for sand. Buscarnera and Nova (2011) and Mihalache and Buscarnera (2014) combined an elastoplastic constitutive model for

unsaturated soils with the concept of controllability, providing a unified strategy for tackling both diffused and localized failure modes on the material point level.

Concluding this state of the art, it is clear that the understanding of the fundamental mechanisms of localization phenomena is a wide field in the current research and it is also the motivation of the present work.

1.2 Basic Features

The goal of this contribution is to develop efficient numerical techniques and constitutive models for the objective simulation of strain localization in the framework of coupled hydro-mechanical analysis. To accomplish this task, throughout this thesis viscoplasticity is adopted as regularization technique in the post bifurcation regime.

The consideration of rate-dependency has been proved to be an appropriate solution, by introducing implicitly a characteristic length through the viscous parameter, without adding extra degrees of freedom in an existing finite element code. Moreover, according to experimental evidence (e.g., di Prisco and Imposimato (1996)), the mechanical response of granular materials is very rapid but not instantaneous, setting the physical background for the application of viscoplasticity. However, di Prisco et al. (2002) admit that in case of weakly rate-sensitive materials artificial viscosities have to be chosen to obtain objective finite element results. To ensure a regularized numerical solution physically based and following di Prisco et al. (2002), the viscoplastic model is expanded with respect to another regularization technique, namely the non-local approach. The physical interpretation of the non-local approach stems from the fact that no real material is an ideal continuous medium and the evolution of the microstructure at one point influences the surrounding points when irreversible strains take place. Moreover, to the author's knowledge, the non-local approach has not been commonly used in the context of the multiphase porous media, which intrigued its application in the context of this thesis.

Classical viscoplasticity (which from this point on will be referred as local to distinguish from non-local) and its non-local version are formulated and implemented in the finite element code Comes-geo (Gawin and Schrefler (1996), Gawin and Sanavia (2009), Gawin and Sanavia (2010), Sanavia et al. (2006) and Sanavia et al. (2008)) based on the multiphase porous media model developed in Lewis and Schrefler (1998) and are then applied to a plane-strain compression test in case of dense Hostun RF sand. The examined problem was first simulated in Sanavia et al. (2006) where a rate-independent behaviour for the soil skeleton was assumed. The goal was to emphasize the benefits of using a multiphase model to study phase change phenomena, such as that of cavitation (experimentally observed in Mokni and Desrues (1998)) at strain localization and therefore a suitable mesh was used to avoid excessive mesh dependency. Herein, the mesh dependence of the elastoplastic solution of the previous work is first illustrated and the regularizing effect of local and non-local viscoplastic models on the respective numerical simulations is investigated. Two types of viscoplastic models are applied;

the Perzyna (1966) and the Duvaut-Lions (1972). The validation of the implementation is presented and an extensive discussion about the parameters important for the strain localization development and the formation of localization pattern follows. The models are then used to investigate the hydro-mechanical coupling in a slope stability problem.

The second aim of this research is to use advanced constitutive models for sands to study strain localization at a constitutive level. The part of this work has been done in collaboration with Professor Claudio di Prisco from Politecnico di Milano and Assistant Professor Federico Pisanò from Delft University of Technology. An advanced elastoplastic constitutive model for sands allowing for hydraulic bonding and debonding effects (Buscarnera and Nova (2009)) is implemented and validated in the finite element code Comes-geo. The model is then extended to viscoplasticity and the novelty of the formulation is enhanced with the dependence of the constitutive parameters on the relative density. This enrichment allows for modeling the transition from dense to loose states and vice versa. The viscoplastic model is also implemented in the Comes-geo code and validated with results from the literature. The verification of the viscoplastic model is finalized with the simulation of triaxial compression tests; the onset of shear strain localization is studied and the finite element results are compared with the results of a theoretical stability analysis.

Finally, the advanced elastoplastic and elasto-viscoplastic models for unsaturated soils are implemented and validated in PLAXIS commercial finite element analysis software. This practice is in the scope of linking academia (UNIPD) and industry (BAUGRUND DRESDEN) and the transfer of knowledge within the MuMoLaDe research project.

1.3 Thesis Layout

The thesis is divided into seven main chapters with the following content.

In **Chapter 2** the mathematical model for describing the thermo-hydro-mechanical behaviour of variably saturated porous medium is presented. This includes the balance equations and the constitutive assumptions. The set of equations resulting from the introduced model are then discretized in both space and time. A brief description of the finite element code Comes-geo is also given.

The mathematical model is completed in **Chapter 3** with the constitutive models adopted for the solid skeleton of the multiphase medium. The mechanical behaviour of the soil is described in the framework of elasto-viscoplasticity and the generalized effective stress is limited with a Drucker-Prager yield criterion as a first approximation. The basic features on the theoretical background of local (Perzyna and Duvaut-Lions) and non-local viscoplasticity (only Perzyna) are presented along with the algorithmic treatment of the constitutive equations. The chapter closes with the merits and drawbacks of each regularization model.

Chapter 4 shows the validation and the regularization capabilities of the three implemented models by simulating strain localization in a biaxial plane-strain compression test from the literature. Mesh

sensitivity analysis is conducted and the influence of factors such as, loading rate, soil permeability, suction, draining conditions and internal lengths interaction on the initiation and formation of localization pattern is presented in detail. The remaining part of the chapter is devoted to the numerical investigations of a slope failure by means of porous media mechanics.

Chapter 5 of the thesis is subdivided into two main parts. The first part describes the main features of an existing elastoplastic constitutive model capable of capturing the behaviour of variably saturated soils. The validation of the implementation in Comes-geo code is performed through single element analyses and comparison of the results with data taken from the literature. The second part includes the derivation, formulation and implementation of the viscoplastic model developed during this research as an extension of the previous described elastoplastic model. The viscoplastic model is validated through creep tests and triaxial compression tests on different sand densities. Particular emphasis is given to the definition of viscous nucleus. These analyses also highlight the model features. The chapter closes with the verification of the viscoplastic model with a numerical example and a considerable effort is made to illustrate the ability of the model to describe the onset of the localized failure.

This thesis is concluded with the implementation and validation of the advanced elastoplastic and elasto-viscoplastic models for unsaturated sands in PLAXIS commercial finite element analysis software in **Chapter 6**. The effectiveness of the viscoplastic model is displayed by numerical simulations of a partially saturated slope failure of the laboratory scale.

Finally, **Chapter 7** introduces a brief summary, conclusions, and proposals for future developments of the presented research work.

Chapter 2

Mechanics of Porous Media: Mathematical Model and Numerical Treatment

Chapter 2: Mechanics of Porous Media: Mathematical Model and Numerical Treatment

2.1 Introduction

The mathematical model to simulate the thermo-hydro-mechanical behaviour of fully and partially saturated porous media was developed within the Hybrid Mixture Theory (HMT) by Lewis and Schrefler (1998) and Schrefler (2002) using averaging theories according to Hassanizadeh and Gray (1979, 1980) with balance laws upscaled from micro-scale to macro-scale and thermodynamic statements at the macroscopic level. An alternative would be the adoption of the Thermodynamically Constrained Averaging Theory (TCAT) of Gray and Miller (2013, 2014) which upscale also thermodynamics from the micro-scale but the formalism makes a rather difficult comparison. Hybrid Mixture Theory is maintained in this thesis because it was deemed sufficient for our purpose.

This chapter is concerned with the description of partially saturated porous media mainly at the macroscopic level. Therefore, fundamentals of mechanics of multiphase porous media are briefly introduced. This includes the averaging process principles and the balance relations in a general and a specific form presented both for dynamic and quasi-static loading conditions. The mathematical modelling is completed by introducing the constitutive relations, which are able to describe the fluids response whereas the constitutive equations for the solid skeleton of the material are presenting in Chapters 3 and 5. The discretization of the governing equations both in space and time and the linearization of the final set of equations close this chapter.

2.2 Preliminaries and Assumptions

In the framework of realistic description of natural geomaterials it is necessary to proceed from an unsaturated soil based on a multiphase model. Therefore, the variably saturated porous medium is treated as a multiphase system composed of the solid skeleton (*s*) and open pores filled with liquid water (*w*) and gas (*g*). The gas phase is assumed to behave as an ideal mixture of dry air (non-condensable gas, *ga*) and water vapour (condensable gas, *gw*). At the macroscopic level the porous material is modelled by a substitute continuum of volume Ω with boundary Γ that simultaneously fills the entire domain, instead of the real fluids and the solid which each fill only a part of it.

In this substitute continuum each constituent $\pi = 1,2, \ldots, k$ has a reduced density which is obtained by means of the volume fraction concept. Volume fractions are given by the ratio of the volume of the constituents to the volume of the control space:

$$\eta^{\pi}\left(\boldsymbol{x},t\right) = dv^{\pi}/dv = \frac{1}{dv}\int_{dv}\gamma^{\pi}\left(\mathbf{r},t\right)dv_{\mathrm{m}} \tag{2.1}$$

In Equation (2.1) dv is the volume of the representative elementary volume, REV, of the porous medium and dv^{π} is the volume occupied by the constituent π in dv, $\boldsymbol{x}$ is the vector of the spatial

coordinates, t is the current time, $\gamma^{\pi}(\mathbf{r},t)$ is a phase distribution function, Equation (2.2), while r indicates the position of a microscopic volume element dv_{m}.

$$\gamma^{\pi}(\mathbf{r},t)=\begin{cases}1 \text{ per } \mathbf{r} \in dv^{\pi} \\ 0 \text{ per } \mathbf{r} \in dv^{\alpha} \quad \alpha \neq \pi\end{cases} \tag{2.2}$$

It is recalled that a REV (Figure 2.1) is an averaging volume that can be centered at each point in the system and always contain both the solid phase and the porous space. The size of the REV is an important choice. Average quantities have to be independent of the size of the REV and continuous in space and time. Thus the size of the REV has to be small enough to be considered as infinitesimal (i.e. the partial derivatives appearing in the governing equations must make sense) and, at the same time, must be large enough, with respect to the heterogeneities of the material, to provide average quantities without fluctuations (Figure 2.2).

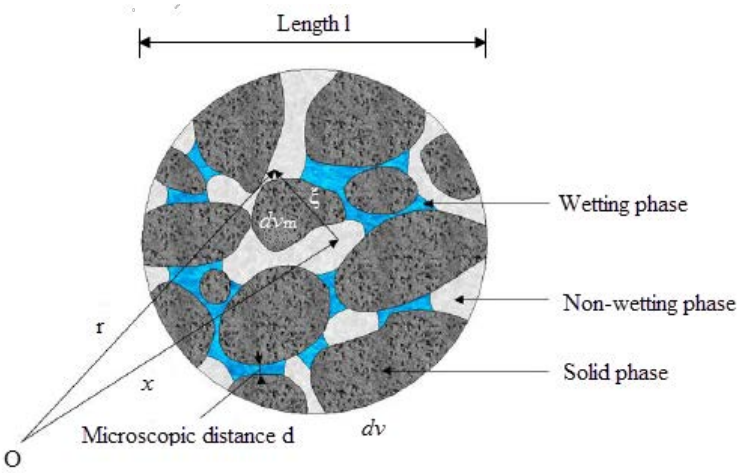

Figure 2.1: Typical averaging volume dv of porous medium consisting of three constituents [93].

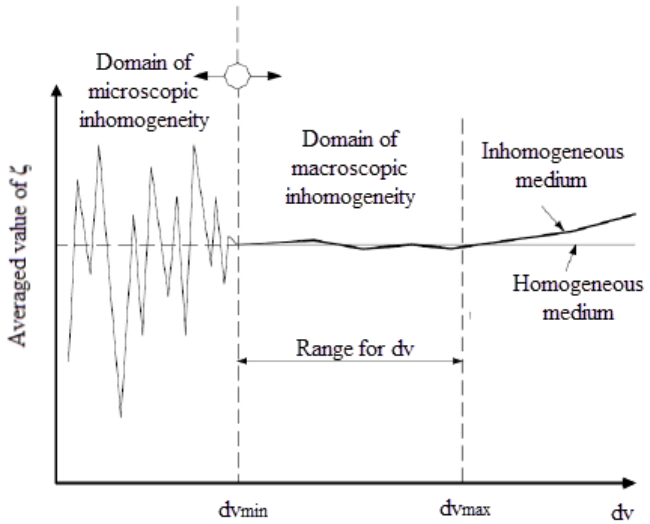

Figure 2.2: Averaged value of ζ versus size of the average volume *dv* [93].

To obtain meaningful average values, the characteristic length l of the average volume must satisfy the inequality d << l << L and l depends on the specific material which constitutes the medium. Typical values of the size of the REV can be found in Lemaitre and Chaboche (1988) i.e. 0.5mm for metals and 10mm for wood. Usually there are no boundary conditions associated with a REV, except in the case of the megascopic level or in the case of a medium with periodic structure.

In the following, averaged quantities are obtained by integrating a microscopic quantity over the volume, *dv*, of a REV resulting in a field of macroscopic variables where the average volume, *dv*, is associated with material points. In particular, the following average operators are defined and applied to a function, $\zeta(\mathbf{r},t)$, which is a microscopic field variable.

First the *volume average operators* are illustrated. The phase average is:

$$\langle \zeta \rangle_{\pi}(\mathbf{x},t) = \frac{1}{dv}\int_{dv} \zeta(\mathbf{r},t)\,\gamma^{\pi}(\mathbf{r},t)\,dv_{\mathrm{m}} \tag{2.3}$$

and the intrinsic phase average is:

$$\langle \zeta \rangle_{\pi}^{\pi}(\mathbf{x},t) = \frac{1}{dv^{\pi}}\int_{dv} \zeta(\mathbf{r},t)\,\gamma^{\pi}(\mathbf{r},t)\,dv_{\mathrm{m}} \tag{2.4}$$

From the definition of volume fraction (Equation (2.1)) it follows that:

$$\langle \zeta \rangle_{\pi}(\mathbf{x},t) = \eta^{\pi}(\mathbf{x},t)\langle \zeta \rangle_{\pi}^{\pi}(\mathbf{x},t) \tag{2.5}$$

The *mass average operator*, with $\rho(\mathbf{r},t)$ microscopic mass density as weighting function, is:

$$\overline{\zeta}^{\pi}(\mathbf{x},t) = \frac{\int_{dv} \rho(\mathbf{r},t)\,\zeta(\mathbf{r},t)\,\gamma^{\pi}(\mathbf{r},t)\,dv_{\mathrm{m}}}{\int_{dv} \rho(\mathbf{r},t)\,\gamma^{\pi}(\mathbf{r},t)\,dv_{\mathrm{m}}} \tag{2.6}$$

The *area average operator* is:

$$\overline{\overline{\zeta}}^{\pi}(\mathbf{x},t) = \frac{1}{da}\int_{da} \zeta(\mathbf{r},t)\cdot\mathbf{n}\;\gamma^{\pi}(\mathbf{r},t)\,da_{\mathrm{m}} \tag{2.7}$$

with **n** the outward normal unit vector of an area element da_{m}.

2.3 Microscopic Balance Equations

The microscopic situation of any π phase is described by the classical balance equations of continuum mechanics. At the interfaces with other constituents, the material properties and thermodynamic quantities may present step discontinuities.

For a generic conserved variable, ψ, the conservation equation within the π phase may be written as:

$$\frac{\partial(\rho\psi)}{\partial t} + \mathrm{div}(\rho\psi\dot{\mathbf{r}}) - \mathrm{div}\,\mathbf{i} - \rho\,\mathrm{b} = \rho\,\mathrm{G} \tag{2.8}$$

where $\dot{\mathbf{r}}$ is the local value of the velocity field of the π phase at a fixed point in space, **i** is the flux vector associated with ψ, b is the external supply and G is the net production of ψ.

The particular balance laws will be obtained by substituting the proper variables for ψ, **i** and b depending on the type of phenomenon being considered. The general balance law Equation (2.8) is not valid at a surface of discontinuity and in particular at the interfaces. At the interface between two constituents π and α, the jump condition holds:

$$\left[\rho\psi\left(\mathbf{w}-\dot{\mathbf{r}}\right)+\mathbf{i}\right]\Big|_{\pi}\cdot\mathbf{n}^{\pi\alpha}+\left[\rho\psi\left(\mathbf{w}-\dot{\mathbf{r}}\right)+\mathbf{i}\right]\Big|_{\alpha}\cdot\mathbf{n}^{\alpha\pi}=0 \tag{2.9}$$

where **w** is the velocity of the interface, $\mathbf{n}^{\alpha\pi}$ is the unit normal vector pointing out of the π phase and into the α phase with $\mathbf{n}^{\pi\alpha} = -\mathbf{n}^{\alpha\pi}$ and $\big|_{\pi}$ symbol indicates that the preceding terms in the square brackets must be evaluated with respect to the π phase.

No thermomechanical properties are attributed to these interfaces. This assumption does not exclude the possibility of exchange of mass, momentum or energy between the constituents. Moreover the local thermodynamic equilibrium hypothesis is assumed to hold because the time scale of the modelled phenomena is substantially larger than the relaxation time required to reach equilibrium locally.

The general form of conservation equations for mass, momentum, energy and entropy is given by Equation (2.8). The variables introduced in Table 2.1 may be substituted into Equations (2.8) and (2.9) to obtain individual microscopic balance equations for each microscopic quantity. As an example by replacing the corresponding values of the first row of Table 2.1 into Equation (2.8), the π-phase mass balance equation is derived:

$$\frac{\partial\rho}{\partial t}+\operatorname{div}\left(\rho\ \dot{\mathbf{r}}\right)=0 \tag{2.10}$$

Table 2.1: Thermodynamic properties for the microscopic mass balance equations.

Quantity	ψ	i	b	G
Balance of mass	1	0	0	0
Balance of linear momentum	$\dot{\mathbf{r}}$	$\mathbf{t}_m$	**g**	0
Balance of energy	E+0.5 $\dot{\mathbf{r}}\cdot\dot{\mathbf{r}}$	$\mathbf{t}_m\,\dot{\mathbf{r}}-\mathbf{q}$	$\mathbf{g}\cdot\dot{\mathbf{r}}+h$	0
Entropy inequality	λ	**Φ**	s	φ

In Table 2.1, E is the specific intrinsic energy, λ the specific entropy, $\mathbf{t}_m$ the microscopic stress tensor, **q** a heat flux vector, **Φ** the entropy flux, **g** the external momentum supply related to gravitational effects, *h* the intrinsic heat source, s an intrinsic entropy source and φ denotes an increase of entropy. The constituents are assumed to be microscopically non polar, hence the angular momentum balance equation has been omitted.

The microscopic equations are then integrated over the REV, using spatial averaging operators, to give the macroscopic balance equations.

2.4 Macroscopic Balance Equations

In this section the macroscopic balance equations for mass, linear momentum, angular momentum and energy as well as the entropy inequality for a deforming porous material are presented. The starting points are the microscopic balance equations (Equation (2.8)) where, for each constituent, the generic thermodynamic variable, ψ, is replaced by appropriate microscopic quantities, suitable for a microscopic non-polar material. The macroscopic equations have been obtained by systematically applying the averaging procedures to the microscopic balance equations.

For a proper description of the non-isothermal unsaturated porous medium we need to take into account not only heat conduction and vapour diffusion, but also heat convection, liquid water flow due to pressure gradients or capillary effects and latent heat transfer due to water phase change (evaporation and condensation) inside the pores. Furthermore the solid is deformable, resulting in coupling of the fluid, the solid and the thermal fields.

The constituents are assumed to be isotropic, homogeneous, immiscible except for dry air and water vapour, and chemically non-reacting. At micro level, solid and liquid water are incompressible, while gas is compressible. All fluid phases are in contact with the solid phase. Dissolution of air in water is here neglected. Because of the local thermodynamic equilibrium hypothesis, the temperatures of each constituent at a point in the multiphase medium are taken to be equal. This does not mean that the temperature is uniform throughout the medium but only that at each point one temperature is sufficient to characterize the state. Momentum exchanges due to mechanical interaction are independent of the temperature gradient.

It is noteworthy that in this section the formulation is still material free and no specific assumptions for the material behaviour have been introduced so far, except for the earlier general assumptions. Appropriate constitutive relations will be introduced in section 2.5. For the sake of brevity, the kinematic description is omitted here. For the interested reader it can be found in Lewis and Schrefler (1998).

In the following, stress is defined as tension positive for the solid phase, while pore pressure is defined as compressive positive for the fluids.

2.4.1 Mass Balance Equations

The volume fractions, η^{π} of the constituents are defined as follows:

For solid:

$\eta^{s} = 1- n$ where $n = (dv^{w} + dv^{g})/dv$ is the porosity and dv^{π} is the volume of constituent π within a REV.

For water:

$\eta^{w} = nS_{w}$ where $S_{w} = dv^{w}/(dv^{w} + dv^{g})$ is the degree of water saturation.

For gas:

$\eta^{g} = nS_{g}$ with $S_{g} = dv^{g}/(dv^{w} + dv^{g})$ the degree of gas saturation.

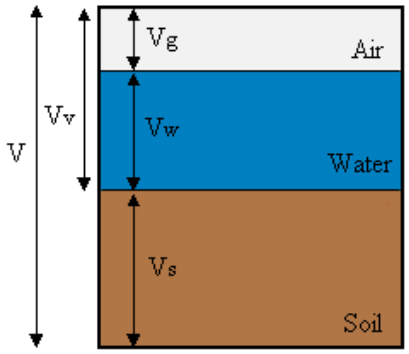

Figure 2.3: Soil composition.

It follows immediately that

$$S_g + S_w = 1 \tag{2.11}$$

- *Solid phase*

The macroscopic mass balance equation for the solid phase reads:

$$\frac{D^s\left[(1-n)\rho^s\right]}{Dt} + \rho^s(1-n)\,\mathrm{div}\,\bar{\mathbf{v}}^s = 0 \tag{2.12}$$

where ρ^s is the intrinsic phase averaged solid density and $\bar{\mathbf{v}}^s$ is the mass averaged solid velocity. The same simplified notation will be used for the other constituents, once π is accordingly specified.

It is reminded that the intrinsic phase averaged density of a phase is linked to its phase averaged density ρ^π by $\rho^\pi = \eta^\pi\rho^\pi$ and that the operator D^s / Dt is the material time derivative with respect to the solid skeleton (and is defined in the same way for other π phases).

- *Liquid phase: water*

The macroscopic mass balance equation for water has the following form:

$$\frac{D^w\rho^w}{Dt} + \rho^w div\,\bar{\mathbf{v}}^w = \rho^w e^w(\rho) \tag{2.13}$$

where the term $\rho^w e^w(\rho)$ is non-zero, because water may change into vapour or vice versa. Hence we have that:

$$\rho^w e^w(\rho) = -\dot{m} \tag{2.14}$$

and is the quantity of water per unit time and volume, lost through evaporation.

- *Gaseous phase: dry air and vapour*

The gaseous phase here is a multi-component material, composed of two different species: dry air and vapour. These species are miscible and therefore have the same volume fraction nS_g. For vapour (π = gw) the mass balance equation is written as:

$$\frac{D^{g}}{Dt}(nS_{g}\rho^{gw}) + \operatorname{div}(nS_{g}\rho^{gw}\mathbf{u}^{gw}) + nS_{g}\rho^{gw}\operatorname{div}\overline{\mathbf{v}}^{g} = \dot{m} \tag{2.15}$$

where $\mathbf{u}^{\pi} = \overline{\mathbf{v}}^{\pi g} = \overline{\mathbf{v}}^{\pi} - \overline{\mathbf{v}}^{g}$, is the macroscopic diffusive dispersive velocity.

We introduce now the diffusive-dispersive mass flux of component gw as follows (Eringen and Suhubi (1964)):

$$\mathbf{J}_{g}^{gw} = nS_{g}\rho^{gw}\mathbf{u}^{gw} \tag{2.16}$$

which allows us to write Equation (2.15) as:

$$\frac{D^{g}}{Dt}(nS_{g}\rho^{gw}) + \operatorname{div}(\mathbf{J}_{g}^{gw}) + nS_{g}\rho^{gw}\operatorname{div}\overline{\mathbf{v}}^{g} = \dot{m} \tag{2.17}$$

The mass balance equation for dry air is given by Equation (2.18) with appropriate superscripts and subscripts (π = ga), and an exchange term equal to zero.

$$\frac{D^{ga}}{Dt}(nS_{g}\rho^{ga}) + nS_{g}\rho^{ga}\operatorname{div}\overline{\mathbf{v}}^{ga} = 0 \tag{2.18}$$

The mass balance equation for the whole gaseous phase (mixture of vapour and dry air) is obtained by summing the macroscopic balance equations of the two species and using appropriate definitions for bulk properties of the gaseous phase (Hassanizadeh (1986)):

$$\frac{D^{g}}{Dt}(nS_{g}\rho^{g}) + nS_{g}\rho^{g}\operatorname{div}\overline{\mathbf{v}}^{g} = \dot{m} \tag{2.19}$$

where the density of gas ρ^{g} is the sum of the densities of dry air ρ^{ga} and vapour ρ^{gw}.

2.4.2 Linear Momentum Balance Equation

The linear momentum balance equation for the π phase has the following general form:

$$\operatorname{div}\mathbf{t}^{\pi} + \rho_{\pi}\left(\overline{\mathbf{g}}^{\pi} - \overline{\mathbf{a}}^{\pi}\right) + \rho_{\pi}\left[\mathbf{e}^{\pi}\left(\rho\dot{\mathbf{r}}\right) + \hat{\mathbf{t}}^{\pi}\right] = 0 \tag{2.20}$$

where $\mathbf{t}^{\pi}$ is the macroscopic stress tensor in the π phase, $\bar{\mathbf{g}}^{\pi}$ is the external momentum supply, $\rho^{\pi}\bar{\mathbf{a}}^{\pi}$ is the volume density of the inertia force, $\rho^{\pi}\,\mathbf{t}^{\pi}$ is the volumetric exchange term of linear momentum with other phases due to mechanical interaction and $\rho^{\pi}\mathbf{e}^{\pi}(\rho\ \dot{\mathbf{r}})$ is due to phase changes or chemical reactions.

In the following we make a further assumption that $\rho^{\pi}\mathbf{e}^{\pi}(\rho\ \dot{\mathbf{r}}) \neq 0$ only for the fluid phases. Therefore the linear momentum balance equation for the solid phase is according to Equation (2.21) while for the fluid phase has the form of Equation (2.20).

$$\operatorname{div}\mathbf{t}^{s} + \rho_{s}\left(\overline{\mathbf{g}}^{s} - \overline{\mathbf{a}}^{s}\right) + \rho_{s}\hat{\mathbf{t}}^{s} = 0 \tag{2.21}$$

The average linear momentum balance equations are subjected to the constraint:

$$\sum_{\pi} \rho_{\pi} \left[\mathbf{e}^{\pi} \left(\rho \dot{\mathbf{r}} \right) + \hat{\mathbf{t}}^{\pi} \right] = 0 \tag{2.22}$$

2.4.3 Angular Momentum Balance Equation

As indicated in section 2.3, all phases of the semi-saturated porous medium are considered microscopically non-polar. The volume averaged angular momentum balance equations shows that, for non-polar media, partial stress tensor is symmetric also at macroscopic level (Hassanizadeh and Gray (1979)):

$$\mathbf{t}^{\pi} = \left(\mathbf{t}^{\pi} \right)^{\mathrm{T}} \tag{2.23}$$

2.4.4 Energy Balance Equation

The macroscopic energy balance equation for the generic π phase can be written as:

$$\rho_{\pi} \frac{\overset{\pi}{D} \overline{E}^{\pi}}{Dt} = \mathbf{t}^{\pi} : \mathbf{D}^{\pi} + \rho_{\pi} h^{\pi} - \operatorname{div} \tilde{\mathbf{q}}^{\pi} + \rho_{\pi} R^{\pi} \tag{2.24}$$

where

$$\rho_{\pi} R^{\pi} = \rho_{\pi} \left[e^{\pi} \left(\rho \hat{E} \right) - e^{\pi} \left(\rho \right) \overline{E}^{\pi} + Q^{\pi} \right] \tag{2.25}$$

represents the exchange of energy between π phase and other phases of the medium due to phase change and mechanical interaction; $\tilde{\mathbf{q}}^{\pi}$ is a macroscopic heat flux vector, h^{π} results from the heat sources and D^{π} is the spatial rate of the deformation tensor. E^{π} accounts for the specific internal energy of the volume element. Equation (2.24) coincides with the energy balance equation in the mixture theory as shown in de Boer et al. (1991).

The energy balance equations have the form:

$$\sum_{\pi} \rho_{\pi} \left[e^{\pi} \left(\rho \hat{E} \right) + e^{\pi} \left(\rho \tilde{\dot{\mathbf{r}}} \right) \cdot \overline{\mathbf{v}}^{\pi} + \frac{1}{2} e^{\pi} \left(\rho \right) \overline{\mathbf{v}}^{\pi} \cdot \overline{\mathbf{v}}^{\pi} + \hat{\mathbf{t}}^{\pi} \cdot \overline{\mathbf{v}}^{\pi} + Q^{\pi} \right] = 0 \tag{2.26}$$

and physically mean that the total balance of energy exchange between all the phases is zero. Phase change and the corresponding supply terms will be considered in the following, only for the fluid phases.

2.4.5 Balance of Entropy

Exploitation of entropy inequality is a tool for developing constitutive equations in a systematic manner, leading to a consistent thermodynamic description of the material behaviour at macro-scale. The use of entropy inequality further assures that the second law of thermodynamics is not violated. The procedure was proposed by Coleman and Noll (1963) and has been exploited by Sampaio and Williams (1979) and recently by Gray and Hassanizadeh (1979) for the development of constitutive

equations for unsaturated flow in dry or partially saturated soil, including interfacial phenomena. The second law of thermodynamics states that the sum of the entropies of all bodies taking part in the process is increased for irreversible process. In the limit, i.e. for irreversible processes, the sum of the entropies remains unchanged (in other words the entropy production is zero).

Unlike the other balance principles, the entropy is expressed by an inequality, which serves as a mathematical restriction on the constitutive equations governing the reversible (e.g. elastic deformation) and the irreversible (e.g. plastic deformation due to internal dissipative mechanisms) processes in the system.

Recalling the formulation in Table 2.1 the microscopic balance equation receives the following form:

$$\frac{\partial(\rho\lambda)}{\partial t} + \operatorname{div}(\rho\lambda\dot{\mathbf{r}}) - \operatorname{div}\boldsymbol{\Phi} - \rho s = \rho\varphi \tag{2.27}$$

This equation may be transformed in the usual manner, also making use of the mass balance equation to obtain:

$$\rho\frac{D\lambda}{Dt} - \operatorname{div}\boldsymbol{\Phi} - \rho s = \rho\varphi \tag{2.28}$$

Substituting the entropy flux, $\boldsymbol{\Phi}$, and the entropy source, s, with the energy flux vector $\mathbf{q}$ and the energy source h respectively and both divided by the absolute temperature, θ (de Boer et al. (1991)), Equation (2.28) is written as:

$$\rho\frac{D\lambda}{Dt} + \operatorname{div}\frac{1}{\theta}\mathbf{q} - \frac{1}{\theta}\rho h = \rho\varphi \tag{2.29}$$

According to the second law of thermodynamics, the entropy is zero for reversible processes, whereas for irreversible processes is positive:

$$\rho\varphi \geq 0 \tag{2.30}$$

Equations (2.29) and (2.30) yield the entropy inequality for single component media:

$$\rho\frac{D\lambda}{Dt} + \operatorname{div}\frac{1}{\theta}\mathbf{q} - \frac{1}{\theta}\rho h \geq 0 \tag{2.31}$$

The entropy inequality for the mixture, which is the quantity of interest here, finally becomes:

$$\sum_{\pi}\left[\rho_{\pi}\frac{\overset{\pi}{D}\overline{\lambda}^{\pi}}{Dt} + \rho_{\pi}e^{\pi}(\rho)\overline{\lambda}^{\pi} + \operatorname{div}\left(\frac{1}{\theta^{\pi}}\mathbf{q}^{\pi}\right) - \frac{1}{\theta^{\pi}}\rho_{\pi}h^{\pi}\right] \geq 0 \tag{2.32}$$

Again, this corresponds to the form used in the mixture theory as shown in de Boer et al. (1991).

A visual summary of the general form of macroscopic balance equations is presented in Table 2.2. Inserting the terms of Table 2.2 into the form [Accumulation term] = - div [Flux] + [Source] results in

the balance equations described in this section (§2.4). Before making further transformations of the macroscopic balance equations, the constitutive equations for the constituents are introduced.

Table 2.2: A general form of macroscopic balance equations.

Balance Equation	Accumulation term	Fluxes	Volumic source
Mass of solid skeleton	$\frac{D^{s}\left[(1-n)\rho^{s}\right]}{Dt}$	Deformation : $\rho^{s}(1-n)\operatorname{div}\overline{\mathbf{v}}^{s}$	No source
Mass of dry air	$\frac{D^{g}}{Dt}(nS_{g}\rho^{ga})$	Advective : $nS_{g}\rho^{ga}\operatorname{div}\overline{\mathbf{v}}^{g}$ Diffusional : $\operatorname{div}\left(nS_{g}\rho^{ga}\mathbf{u}^{ga}\right)$	No source
Mass of vapour	$\frac{D^{g}}{Dt}(nS_{g}\rho^{gw})$	Advective : $nS_{g}\rho^{gw}\operatorname{div}\overline{\mathbf{v}}^{g}$ Diffusional : $\operatorname{div}\left(nS_{g}\rho^{gw}\mathbf{u}^{gw}\right)$	Evap./Cond.: $\dot{m}$
Mass of liquid water	$\frac{D^{w}\rho^{w}}{Dt}$	Advective : $\rho^{w}div\,\overline{\mathbf{v}}^{w}$	Evap./Cond.: $\dot{m}$
Linear momentum	No term	Stress tensor : $\mathbf{t}^{\pi}$	Mass forces : $-\rho_{\pi}\overline{\mathbf{g}}^{\pi}$ Inertia forces : $+\rho_{\pi}\overline{\mathbf{a}}^{\pi}$
Energy	$\rho_{\pi}\frac{\overset{\pi}{D}\overline{E}^{\pi}}{Dt}$	Heat cond. : $\tilde{\mathbf{q}}^{\pi}$ $\mathbf{t}^{\pi}:\mathbf{D}^{\pi}$	Heat source : $\rho_{\pi}h^{\pi}$ Exhange energy : $\rho_{\pi}R^{\pi}$

2.5 Constitutive Equations

To complete the description of the mechanical behaviour, the constitutive equations have to be specified. The balance equations developed in the previous sections allow for the introduction of quite elaborate constitutive theories, especially if the balance equations presented in the previous sections for the bulk material are extended to the interfaces, as done by Gray and Hassanizadeh in [68-69] for the aspects concerning multiphase flow. For the solid phase, second-grade material theories are also possible, where the gradients of relevant thermodynamic properties, such as densities, are considered as independent variables (de Boer et al. (1991)). However, since this thesis is application oriented, i.e. we aim at the quantitative solution of real engineering problems, we make a different choice.

Constitutive models which are based on quantities currently measurable in laboratory or field experiments, and which have been extensively validated both with reference to known exact solutions and to experiments, are selected. Many of these constitutive models correspond to linearization of more complex arguments.

The properties of the fluid phases are presented first, and the solid phase is only briefly outlined here, as Chapters 3 and 5 are mainly devoted to this subject.

2.5.1 Stress Tensor in the Fluid Phases

By applying entropy inequality (Equation (2.32)) for the bulk material, it can be shown that the stress tensor in the fluid phases, appearing in Equation (2.20)is:

$$\mathbf{t}^{\pi} = -\eta^{\pi} p^{\pi} \mathbf{I} \tag{2.33}$$

where **I** is the identity tensor. This operator is equivalent to the Kronecker symbol δ. Quantity p^{π} is the macroscopic pressure of the π phase. The volume fraction η^{π} appears in Equation (2.33) because $\mathbf{t}^{\pi}$ is the force exerted on the fluid phase per unit area of multiphase medium. It should be noted that the stress vector in the fluid phase does not have any dissipating part. The macroscopic effects of deviatoric stress components will be accounted for in linear momentum balance equations through momentum exchange terms.

2.5.2 Gaseous Mixture of Dry Air and Water Vapour

The moist air in the pore system is usually assumed to be a perfect mixture of two ideal gases, i.e. dry air and water vapour. Hence the ideal gas law, relating the partial pressure $p^{g\pi}$ of species π, the mass concentration $\rho^{g\pi}$ of species π in the gas phase and the absolute temperature T, is used. The equations of state of a perfect gas, applied to dry air (ga), vapour (gw) and moist air (g) are:

$$\begin{aligned} p^{ga} &= \rho^{ga} \mathrm{T} R / M_{\mathrm{a}} \\ p^{gw} &= \rho^{gw} \mathrm{T} R / M_{\mathrm{w}} \\ \rho^{g} &= \rho^{ga} + \rho^{gw} \end{aligned} \tag{2.34}$$

$$\begin{aligned} p^{g} &= p^{ga} + p^{gw} \\ M_{\mathrm{g}} &= \left(\frac{\rho^{gw}}{\rho^{g}} \frac{1}{M_{\mathrm{w}}} + \frac{\rho^{ga}}{\rho^{g}} \frac{1}{M_{\mathrm{a}}} \right)^{-1} \end{aligned} \tag{2.35}$$

where M_{π} is the molar mass of constituent π and R is the universal gas constant. The second Equation of (2.35) expresses Dalton's law (Moran and Shapiro 1993). For the averaging process it is reminded that dry air, vapour and moist air occupy the same volume fraction nS_{g}.

2.5.3 Sorption Equilibrium

If an oven-dry porous medium is exposed to moist air, the weight of such solid increases because the moisture is adsorbed on the inner surfaces of the pores starting with the finest ones. In the cases of interest here, the water is present as a condensed liquid that (because of the surface tension) is separated from its vapour by a concave meniscus (capillary water). There is then a relationship between the relative humidity, the water content (saturation) and the capillary pressure (also known as matrix suction) in the pores.

The capillary pressure is defined as the pressure difference between the gas phase and the liquid phase, by the capillary pressure equation:

$$p^{\mathrm{c}} = p^{\mathrm{g}} - p^{\mathrm{w}} \tag{2.36}$$

where p^{w} is the pressure of liquid water. Gray and Hassanizadeh (1991) showed that Equation (2.36) is not just a definition but a derived relationship between two independent quantities (p^{c} and p^{g} - p^{w}) at equilibrium.

A model of the capillary pressure in a gas/water system is shown in Figure 2.4. If the end of a narrow capillary tube is placed in a wetting fluid net adhesive forces draw the fluid into the tube. The wetting phase rises in the capillary above the original interface or free surface until adhesive and gravitational forces are balanced (Equation (2.37)).

$$2\pi R T \cos\theta - \pi R^2 \rho^{\mathrm{w}} \mathrm{g}\, p^{\mathrm{c}} = 0 \tag{2.37}$$

Because the wetting and non-wetting (gas) fluids have different densities, they also have different pressure gradients. Capillary pressure is defined as the difference in pressure across the meniscus in the capillary tube. In other words, capillary pressure is the amount of extra pressure required to force the non-wetting phase to displace the wetting phase in the capillary and can be calculated as follows:

$$p^{\mathrm{c}} = \frac{T}{\rho^{\mathrm{w}} \mathrm{g} R} \tag{2.38}$$

Since the pores in a soil are different in sizes the capillary tubes are different in diameter, causing different surface tension values. The smaller the tube is and therefore the smaller the radius, the larger the surface tension occurs.

For the relationship between the relative humidity (RH) and the capillary pressure in the pores, Kelvin-Laplace law is assumed to be valid as:

$$\mathrm{RH} = \frac{p^{\mathrm{gw}}}{p^{\mathrm{gws}}} = \exp\left(\frac{p^{\mathrm{c}} M_{\mathrm{w}}}{\rho^{\mathrm{w}} R \mathrm{T}} \right) \tag{2.39}$$

The water vapour saturation pressure p^{gws}, which is a function of the temperature only, can be obtained from the Clausius-Clapeyron equation indicated in section 2.5.4, or from empirical formulas such as the one proposed by Hyland and Wexler (ASHRAE, 1993).

The aforementioned considerations are applicable if the water is present in the pores, as a condensed liquid (capillary region). When, instead, the water is present as one or more molecular layers adsorbed on the surface of a solid because of the Van der Waals and/or other interactions, the capillary pressure no longer has an obvious meaning, even if it can be retained, referring to the broader concept of water potential or moisture stress. In this case, a direct relationship between the water content and the relative humidity is assumed to hold such as the BET equation (ASHRAE, 1993).

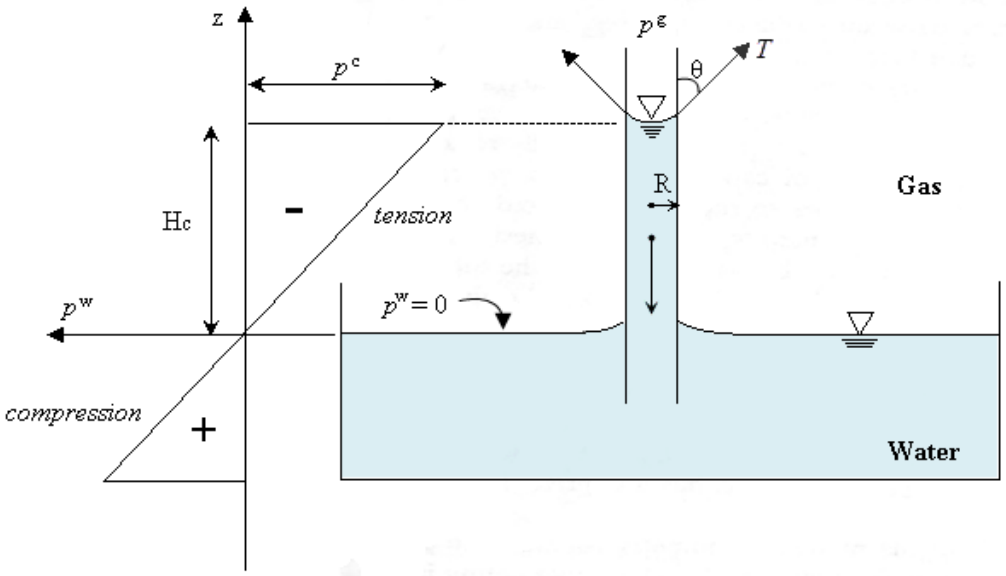

Figure 2.4: Capillary rise in a small tube.

The capillary pressure-saturation relationship is obtained through experimental tests. Numerous approaches (empirical and physical models) have been suggested for mathematical representation of this relationship. Frequently used empirical models are that by Brooks and Corey (1966), Safai and Pinder (1979), van Genuchten (1980) and Fredlund & Xing (1994). All these models are not capable to predict hysteresis or scanning curves in the suction water content relationship and for each drainage or imbibition cycle different set of parameters has to be provided.

Two of the above mentioned equations are explained in the following and will be used in the numerical analyses of this thesis.

- *Safai and Pinder (1979)*

Safai and Pinder suggested the following relationship for relating water saturation to matric suction:

$$S_w = \frac{\theta_r}{\theta_s} + \left(1 - \frac{\theta_r}{\theta_s}\right)\left\{1 + \left(\beta \left|h_w\right|\right)^{\nu}\right\}^{-\alpha} \tag{2.40}$$

In Equation (2.40) α, β (in cm^{-1}), ν are parameters characteristic of the soil. The residual moisture content of the soil is given by θ_r and θ_s is the saturated moisture content. h_w is the pressure head (in cm) and is related to the fluid pressure (p^w) in the water phase by:

$$h_w = \frac{p^w}{\gamma_w} \tag{2.41}$$

where γ_w is the specific weight of water.

To show the shape of the curve in Figure 2.5 experimental results from drainage for dense Hostun sand as found in Lins (2009) are fitted using the abovementioned equation. It is noted that the shape of the soil-water characteristic curve is related to the void ratio of the sample and to the hydraulic loading path direction i.e. whether it is drainage or imbibition path.

- *Van Genuchten (1980)*

A well-known and frequently used sigmoidal type equation is that given by van Genuchten (1980) and is similar in form with the one of Safai and Pinder:

$$S_w = \left\{1 + (\alpha \cdot s)^n\right\}^{-m} \tag{2.42}$$

where s is suction (in kPa) and a (in kPa^{-1}), n, and m are curve fitting soil parameters. Burdine (1953) suggested that m be calculated as m = 1 – 2/ n and Mualem (1976) suggested that m be calculated as m = 1 – 1/n. These assumptions reduce the accuracy of the suction-water content curve fit but allow the relative hydraulic conductivity function to be represented as a closed-form equation.

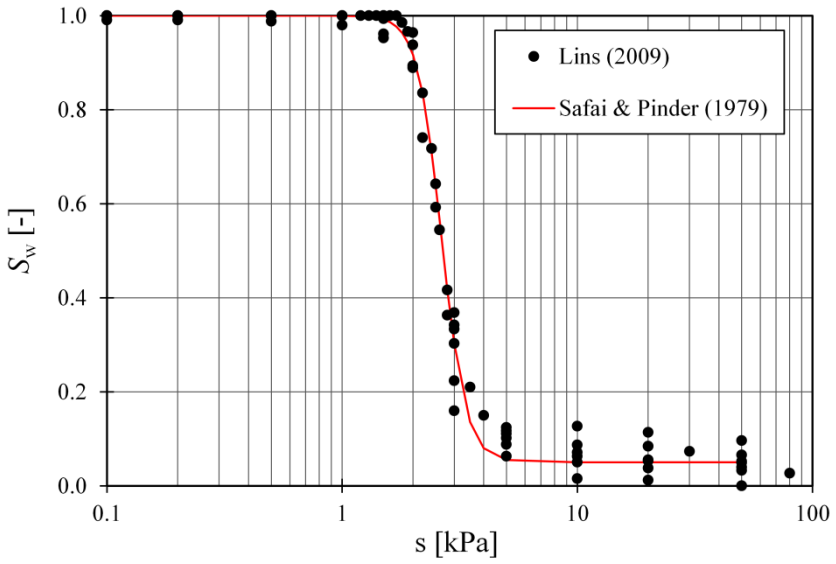

Figure 2.5: SWCC for dense Hostun sand: Experimental results from Lins (2009) and fitted results using Safai and Pinder (1979) model.

2.5.4 Clausious-Clapeyron Equation

As indicated above, this equation links the water vapour saturation pressure with temperature:

$$p^{gws}(T) = p^{gws0} \exp\left[-\frac{M_w \Delta H_{gw}}{R}\left(\frac{1}{T} - \frac{1}{T_0}\right)\right] \tag{2.43}$$

where T_0 is a reference temperature, p^{gws} is the water vapour saturation pressure at T, p^{gws0} is the water vapour saturation pressure at T_0 and ΔH_{gw} is the specific enthalpy of evaporation. The equation is obtained from the second law of thermodynamics and is valid in the vicinity of T_0.

2.5.5 Darcy's Law

Darcy's law, generalized to allow for relative permeability, is assumed valid for the transport of both water and gas in slow phenomena:

$$\eta^{\pi}\overline{\mathbf{v}}^{\pi s} = \frac{k^{r\pi}\mathbf{k}}{\mu^{\pi}}(-\mathrm{grad}p^{\pi} + \rho^{\pi}\mathbf{g}) \tag{2.44}$$

In Equation (2.44) $\mathbf{k}$ is the permeability tensor of the medium (also called intrinsic permeability), μ is the dynamic viscosity and $k^{r\pi}$ is the relative permeability, a dimensionless parameter varying from zero to one.

At a macroscopic level we assume that the resulting permeability, $\mathbf{k}^{\pi}$ is the product of the intrinsic permeability times the relative permeability:

$$\mathbf{k}^{\pi} = k^{r\pi}\mathbf{k} \tag{2.45}$$

The intrinsic permeability varies with the void ratio and with the degree of saturation. For many situations the change of void ratio may be of secondary importance and the intrinsic permeability may be satisfactory defined as a function of the degree of saturation. For each particular porous medium, the relations $k^{r\pi}$ (S_w) are either predicted by models based on some more or less realistic capillary assumption or experimentally determined in laboratory as well as field conditions.

Numerous equations have been proposed by several researchers to predict the relative hydraulic conductivity function from the soil-water characteristic curve. A suitable closed-form equation was given by Safai and Pinder (1979) and is adopted here:

$$k^{rw} = \left\{1 + \left(a|h_w|\right)^b\right\}^{-\alpha} \tag{2.46}$$

where α, b and a (in cm^{-1}) are parameters characteristic of the soil

The relative permeability of the water equals to unity at fully saturated states and reduces to zero before the saturation reaches the value zero. The water saturation at which the relative permeability goes to zero is termed the residual water saturation or displacement residual water saturation.

Among the relationships used here are those proposed by Brooks and Corey (1966) for the wetting phase, Equation (2.47), and for the non-wetting phase (air), Equation (2.48), respectively:

$$k^{rw} = S_e^{\frac{2+3\lambda}{\lambda}} \tag{2.47}$$

where $S_e = \dfrac{S_w - S_{wc}}{1 - S_{wc}}$ is the effective saturation, S_{wc} is the irreducible saturation and λ the pore size distribution.

$$k^{ra} = (1 - S_e)^2\left(1 - S_e^{\frac{2+\lambda}{\lambda}}\right) \tag{2.48}$$

Typical curves of relative permeability of water and air for sand are presented in Figure 2.6.

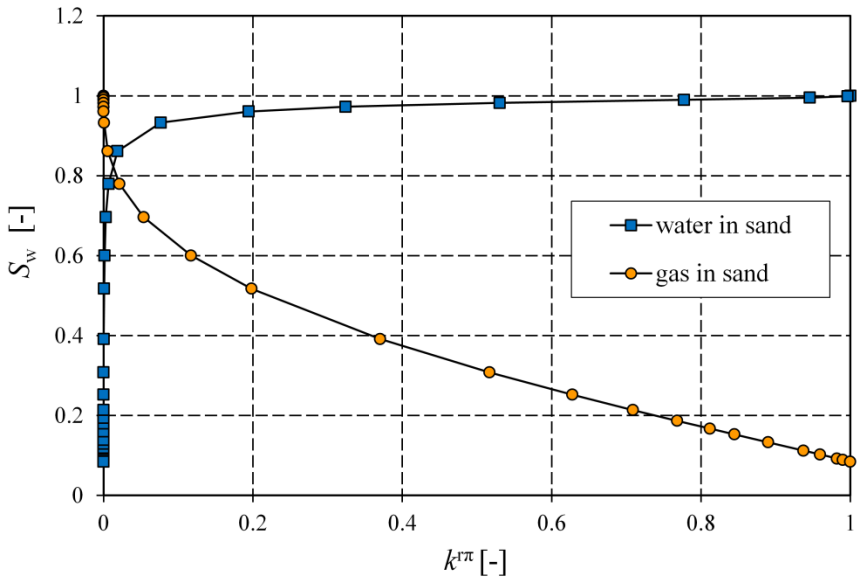

Figure 2.6: Relative hydraulic conductivity curves for sand using Brooks and Corey (1966) relations.

2.5.6 Fick's Law

Diffusive-dispersive mass flux is governed by Fick's law; it postulates that the flux goes from region of higher concentration to regions of lower concentration, with a magnitude that is proportional to the concentration gradient:

$$\mathbf{J}_a^\pi = -\rho^a \mathbf{D}_a^\pi \mathrm{grad}\left(\frac{\rho^\pi}{\rho^a}\right) \tag{2.49}$$

where $\mathbf{D}_a^\pi$ is the effective dispersion tensor, π is the diffusing phase and a is the phase in which diffusion takes place (a = w, g). $\mathbf{D}_a^\pi$ is a function of the tortuosity factor, which accounts for the tortuous nature of the pathway in soil; because of mechanical dispersion, $\mathbf{D}_a^\pi$ is also correlated with seepage velocity.

For dry air and water vapour (binary system) we have in particular that:

$$\mathbf{J}_{\mathrm{g}}^{ga} = -\rho^{\mathrm{g}} \frac{M_a M_{\mathrm{w}}}{M_{\mathrm{g}}^2} \mathbf{D}_{\mathrm{g}} \mathrm{grad}\left(\frac{p^{ga}}{p^{\mathrm{g}}}\right) = -\rho^{\mathrm{g}} \frac{M_a M_{\mathrm{w}}}{M_{\mathrm{g}}^2} \mathbf{D}_g \mathrm{grad}\left(\frac{p^{gw}}{p^{\mathrm{g}}}\right) = -\mathbf{J}_{\mathrm{g}}^{gw} \tag{2.50}$$

It is worthwhile to emphasize that gas diffusion can take place even in the absence of a gas pressure gradient, i.e. when its mass weighted velocity $\overline{\mathbf{v}}^g$, is zero.

2.5.7 Fourier's Law

A constitutive assumption for the heat flux is the generalized Fourier's Law:

$$\tilde{\mathbf{q}} = -\chi_{\mathrm{eff}} \mathrm{grad} T \tag{2.51}$$

where $\boldsymbol{\chi}_{\text{eff}}$ is the effective thermal conductivity tensor and $\tilde{\mathbf{q}}$ is the heat flux of the multiphase medium, sum of the partial heat fluxes $\tilde{\mathbf{q}}^{\pi}$. For isotropic media the generalized Fourier's Law becomes the well-known empirical Fourier's Law:

$$q = -\chi_{\text{eff}} \operatorname{grad} T \tag{2.52}$$

where χ_{eff} is the effective thermal conductivity and can be determined theoretically or experimentally.

For instance, in case of porous building materials the following linear relationship may be used, which represents with sufficient accuracy the data by Bomberg and Shirtliffe (1978):

$$\chi_{\text{eff}} = \chi_{\text{dry}} \left(1 + 4 \frac{n S^{\text{w}} \rho^{\text{w}}}{(1-n)\rho^{\text{g}}} \right) \tag{2.53}$$

2.5.8 Stress Tensor in the Solid Phase

From the entropy inequality written in Hassanizadeh and Gray (1990) for unsaturated flow, including interfacial phenomena, it can be shown that the total stress tensor of the solid phase is defined as:

$$\mathbf{t}^{\text{s}} = (1-n)\left(\mathbf{t}_{\text{e}}^{\text{s}} - \mathbf{I} p^{\text{s}} \right) \tag{2.54}$$

where p^{s} is the solid phase pressure and is actually the pressure exerted on the solid phase by the surrounding fluid:

$$p^{\text{s}} = p^{\text{w}} S_{\text{w}} + p^{\text{g}} S_{\text{g}} \tag{2.55}$$

and the effective stress is given by:

$$\boldsymbol{\sigma}' = (1-n)\mathbf{t}_{\text{e}}^{\text{s}} \tag{2.56}$$

Introduction of Equation (2.55) into (2.54) yields:

$$\mathbf{t}^{\text{s}} = (1-n)\left[\mathbf{t}_{\text{e}}^{\text{s}} - \mathbf{I}\left(S_{\text{w}} p^{\text{w}} + S_{\text{g}} p^{\text{g}} \right) \right] \tag{2.57}$$

The volume fraction (1 - n) indicates that $\mathbf{t}^{\text{s}}$ is the stress exerted on the solid phase per unit area of a multiphase medium. For $S_{\text{w}} = 1$ Equation (2.57) resembles the Terzaghi stress concept.

The sum of Equation (2.57) and (2.33) written for gas and for water gives the total stress $\boldsymbol{\sigma}$ acting on a unit area of a multiphase medium:

$$\begin{aligned} \boldsymbol{\sigma} &= \mathbf{t}^{s} + \mathbf{t}^{w} + \mathbf{t}^{g} = (1-n)\left[\mathbf{t}_{\text{e}}^{\text{s}} - \mathbf{I}\left(S_{\text{w}} p^{\text{w}} + S_{\text{g}} p^{\text{g}} \right) \right] - S_{\text{w}} n \mathbf{I} p^{\text{w}} - S_{\text{g}} n \mathbf{I} p^{\text{g}} \\ &= (1-n)\mathbf{t}_{\text{e}}^{\text{s}} - \mathbf{I}\left(S_{\text{w}} p^{\text{w}} + S_{\text{g}} p^{\text{g}} \right) \end{aligned} \tag{2.58}$$

This can be put in the usual soil mechanics form, by means of Equation (2.56), as:

$$\boldsymbol{\sigma} = \boldsymbol{\sigma}' - \mathbf{I}\left(S_{\text{w}} p^{\text{w}} + S_{\text{g}} p^{\text{g}} \right) \tag{2.59}$$

or in terms of effective stress:

$$\boldsymbol{\sigma}' = \boldsymbol{\sigma} + \mathbf{I}\left(S_{\mathrm{w}} p^{\mathrm{w}} + S_{\mathrm{g}} p^{\mathrm{g}}\right) \tag{2.60}$$

or using the Equation (2.36):

$$\boldsymbol{\sigma}' = \boldsymbol{\sigma} + \mathbf{I}\left(p^{\mathrm{g}} - S_{\mathrm{w}} p^{c}\right) \tag{2.61}$$

From Equation (2.60) it follows that the relationship between effective stress and total stress, in partially saturated porous media, is no longer independent of the soil type because of the saturations. Whereas in fully saturated soils (where $S_{\mathrm{g}} = 0$ and $S_{\mathrm{w}} = 1$), the effective stress principle (Equation (2.60)) is unique for all soil types.

An expression of the form of Equation (2.60) was obtained by Bishop and Blight (1963) using a phenomenological approach and the same equation was obtained by Schrefler et al. (1990) using volume averaging.

The effective stress is responsible for all major deformations in the skeleton and is linked to the strain rate tensor $\mathbf{D}^{\mathrm{s}}$ by means of a constitutive relationship:

$$\frac{D\boldsymbol{\sigma}'}{Dt} = \mathbf{D}_{\mathrm{T}}\left[\left(\mathbf{D}^{\mathrm{s}} - \mathbf{D}_0^{\mathrm{s}}\right)\right] \tag{2.62}$$

where

$$\mathbf{D}_{\mathrm{T}} = \mathbf{D}_{\mathrm{T}}\left(\mathbf{D}^{\mathrm{s}}, \boldsymbol{\sigma}', T\right) \tag{2.63}$$

is a fourth-order tensor and $\mathbf{D}_0^{\mathrm{s}}$ represnts the increment of all other strains not directly associated with stress changes.

Assuming small strains, it follows that:

$$\mathbf{D}^{\mathrm{s}} = \boldsymbol{\varepsilon}\, dt \tag{2.64}$$

2.6 General Field Equations

In this section the general field equations obtained by introducing the constitutive equations of section 2.5 into the transformed macroscopic balance laws, are presented. The averaging symbol (overbar) is omitted in the remainder of this thesis, because all quantities belong to the macroscopic situations.

2.6.1 Mass Balance Equations

2.6.1.1 Solid phase

The macroscopic mass balance equation for the solid phase (Equation (2.12)), divided by ρ^{s} is

$$\frac{1-n}{\rho^{\mathrm{s}}}\frac{D^{\mathrm{s}}\rho^{\mathrm{s}}}{Dt} - \frac{\overset{\mathrm{s}}{D}\, n}{Dt} + \left(1-n\right)\operatorname{div}\mathbf{v}^{\mathrm{s}} = 0 \tag{2.65}$$

2.6.1.2 Liquid phase

Upon introduction of the relative velocity and the material time derivative with respect to the moving solid Equation (2.13) for liquid water becomes:

$$\frac{D^{\mathrm{s}}\rho^{\mathrm{w}}}{Dt}+\mathbf{v}^{\mathrm{ws}}\cdot\mathrm{grad}\rho^{\mathrm{w}}+\rho^{\mathrm{w}}\mathrm{div}\left(\mathbf{v}^{\mathrm{s}}+\mathbf{v}^{\mathrm{ws}}\right)=-\dot{m} \tag{2.66}$$

Introduction of intrinsic phase averaged densities with the appropriate volume fractions, use of vector identity written for water and division by $S_w\rho^w$ allows us to transform the last equation into:

$$\frac{D^{\mathrm{s}}n}{Dt}+\frac{n}{\rho^{w}}\frac{D^{\mathrm{s}}\rho^{w}}{Dt}+\frac{n}{S_{\mathrm{w}}}\frac{D^{\mathrm{s}}S_{\mathrm{w}}}{Dt}+\frac{1}{S_{\mathrm{w}}\rho^{w}}\mathrm{div}(nS_{\mathrm{w}}\rho^{w}\mathbf{v}^{\mathrm{ws}})+n\mathrm{div}\,\mathbf{v}^{\mathrm{s}}=-\frac{\dot{m}}{S_{\mathrm{w}}\rho^{w}} \tag{2.67}$$

Summation with Equation (2.65), to eliminate $\frac{D^{\mathrm{s}}n}{Dt}$ gives:

$$\frac{1-n}{\rho^{\mathrm{s}}}\frac{D^{\mathrm{s}}\rho^{\mathrm{s}}}{Dt}+\mathrm{div}\,\mathbf{v}^{\mathrm{s}}+\frac{n}{\rho^{w}}\frac{D^{\mathrm{s}}\rho^{w}}{Dt}+\frac{n}{S_{\mathrm{w}}}\frac{D^{\mathrm{s}}S_{\mathrm{w}}}{Dt}+\frac{1}{S_{\mathrm{w}}\rho^{w}}\mathrm{div}(nS_{\mathrm{w}}\rho^{w}\mathbf{v}^{\mathrm{ws}})=-\frac{\dot{m}}{S_{\mathrm{w}}\rho^{w}} \tag{2.68}$$

Introduction of the material derivatives of the solid and water densities and along with Equation (2.55) gives:

$$\begin{aligned}&\frac{\alpha-n}{K_{\mathrm{s}}}\frac{D^{\mathrm{s}}}{Dt}(p^{\mathrm{w}}S_{\mathrm{w}}+p^{\mathrm{g}}S_{\mathrm{g}})-\beta_{\mathrm{s}}(\alpha-n)\frac{D^{\mathrm{s}}T}{Dt}+\alpha\mathrm{div}\,\mathbf{v}^{\mathrm{s}}+n\left(\frac{1}{K_{\mathrm{w}}}\frac{D^{\mathrm{s}}p^{\mathrm{w}}}{Dt}-\beta_{\mathrm{w}}\frac{D^{\mathrm{s}}T}{Dt}\right)\\&+\frac{n}{S_{\mathrm{w}}}\frac{D^{\mathrm{s}}S_{\mathrm{w}}}{Dt}+\frac{1}{S_{\mathrm{w}}\rho^{w}}\mathrm{div}(nS_{\mathrm{w}}\rho^{w}\mathbf{v}^{\mathrm{ws}})=-\frac{\dot{m}}{S_{\mathrm{w}}\rho^{w}}\end{aligned} \tag{2.69}$$

where p^{w}, p^{g} and T are independent variables and $\beta_{\mathrm{sw}}=S_w\left[(\alpha-n)\beta_{\mathrm{s}}+n\beta_{\mathrm{w}}\right]$.

For incompressible grains ($\alpha = 1$ and $1/K_s = 0$) this equation may be simplified as follows:

$$\frac{nS_{\mathrm{w}}}{K_{\mathrm{w}}}\frac{D^{\mathrm{s}}p^{\mathrm{w}}}{Dt}+S_{\mathrm{w}}\mathrm{div}\,\mathbf{v}^{\mathrm{s}}-\beta_{\mathrm{sw}}\frac{D^{\mathrm{s}}T}{Dt}+n\frac{D^{\mathrm{s}}S_{\mathrm{w}}}{Dt}+\frac{1}{\rho^{w}}\mathrm{div}(nS_{\mathrm{w}}\rho^{w}\mathbf{v}^{\mathrm{ws}})=-\frac{\dot{m}}{\rho^{w}} \tag{2.70}$$

2.6.1.3 Gaseous phase

The mass balance equation for gas as a mixture of dry air and vapour is presented in the following. In the same mode of the liquid phase, starting from Equation (2.15) we obtain:

$$\frac{\alpha-n}{K_s}S_w S_g\frac{D^s p^w}{Dt}+\frac{\alpha-n}{K_s}S_g^2\frac{D^s p^g}{Dt}+\alpha S_g \operatorname{div}\mathbf{v}^s+\frac{nS_g}{\rho^g}\frac{D^s\left[\frac{1}{\theta R}\left(p^{ga}M_a+p^{gw}M_w\right)\right]}{Dt}+$$
$$-\left(\frac{\alpha-n}{K_s}p^c S_g+n\right)\frac{D^s S_w}{Dt}+\frac{1}{\rho^g}\operatorname{div}(nS_g\rho^g\mathbf{v}^{gs})-\beta_s(\alpha-n)S_g\frac{D^s T}{Dt}=\frac{\dot{m}}{\rho^g} \tag{2.71}$$

where p^w, p^g and T are independent variables

For incompressible solid grains this equation may be simplified to:

$$-n\frac{D^s S_w}{Dt}-\beta_s(\alpha-n)S_g\frac{D^s T}{Dt}+S_g\operatorname{div}\mathbf{v}^s+\frac{nS_g}{\rho^g}\frac{D^s\left[\frac{1}{\theta R}\left(p^{ga}M_a+p^{gw}M_w\right)\right]}{Dt}$$
$$+\frac{1}{\rho^g}\operatorname{div}(nS_g\rho^g\mathbf{v}^{gs})=\frac{\dot{m}}{\rho^g} \tag{2.72}$$

For heat transfer analysis, in partially saturated porous media, it is more convenient to consider the mass balance equation for dry air separately from that of vapour (Gawin et al. (1995)) and to sum the mass balance equations for water species, liquid water and water vapour. In this way, the mass rate of water evaporation, $\dot{m}$, disappears from the mass balance equations. An evolution equation needed and this will be given by the energy balance equation. Note that, in this way, no constitutive model for the mass rate of water evaporation is needed.

2.6.1.4 Gaseous phase: dry air

The mass balance equation for dry air is transformed in the following equation:

$$\frac{D^g(nS_g\rho^{ga})}{Dt}+\operatorname{div}\mathbf{J}_g^{ga}+nS_g\rho^{ga}\operatorname{div}\mathbf{v}^g=0 \tag{2.73}$$

The resulting equation is divided by $\rho^{ga}S_g$ and summed with Equation (2.65) we obtained:

$$\frac{\alpha-n}{K_s}S_w S_g\frac{D^s p^w}{Dt}+\frac{\alpha-n}{K_s}S_g^2\frac{D^s p^g}{Dt}+\alpha S_g\operatorname{div}\mathbf{v}^s+\frac{nS_g}{\rho^{ga}}\frac{D^s\rho^{ga}}{Dt}+\frac{1}{\rho^{ga}}\operatorname{div}\mathbf{J}_g^{ga}+$$
$$-\left(\frac{\alpha-n}{K_s}p^c S_g+n\right)\frac{D^s S_w}{Dt}+\frac{1}{\rho^{ga}}\operatorname{div}(nS_g\rho^{ga}\mathbf{v}^{gs})-\beta_s(\alpha-n)S_g\frac{D^s T}{Dt}=0 \tag{2.74}$$

For incompressible solid grains this equation is simplifies to:

$$-n\frac{D^s S_w}{Dt}-\beta_s(1-n)S_g\frac{D^s T}{Dt}+S_g\operatorname{div}\mathbf{v}^s+\frac{nS_g}{\rho^{ga}}\frac{D^s\rho^{ga}}{Dt}+\frac{1}{\rho^{ga}}\operatorname{div}\mathbf{J}_g^{ga}+\frac{1}{\rho^{ga}}\operatorname{div}(nS_g\rho^{ga}\mathbf{v}^{gs})= \tag{2.75}$$

Introducing now the constitutive equations for ρ^{ga} (Equation (2.34)) and for $\mathbf{J}_g^{ga}$ (Equation (2.50)), one obtains:

$$-n\frac{D^{\mathrm{s}}S_{\mathrm{w}}}{Dt}-\beta_{\mathrm{s}}(1-n)S_g\frac{D^{\mathrm{s}}T}{Dt}+S_{\mathrm{g}}\mathrm{div}\,\mathbf{v}^{\mathrm{s}}+\frac{nS_{\mathrm{g}}}{\rho^{\mathrm{ga}}}\frac{D^{\mathrm{s}}\left[\frac{M_{\mathrm{a}}}{\theta R}p^{\mathrm{ga}}\right]}{Dt}$$
$$-\frac{1}{\rho^{\mathrm{ga}}}\mathrm{div}\left[\rho^{\mathrm{g}}\frac{M_{\mathrm{a}}M_{\mathrm{w}}}{M_g^2}\mathbf{D}_{\mathrm{g}}\mathrm{grad}\left(\frac{p^{\mathrm{ga}}}{p^{\mathrm{g}}}\right)\right]+\frac{1}{\rho^{\mathrm{ga}}}\mathrm{div}(nS_{\mathrm{g}}\rho^{\mathrm{ga}}\mathbf{v}^{\mathrm{gs}})=0 \tag{2.76}$$

2.6.1.5 Gaseous phase: vapour

The way to derive the mass balance equation for vapour is identical to that of dry air and for the case of incompressible solid grains it results in:

$$-n\frac{D^{\mathrm{s}}S_{\mathrm{w}}}{Dt}-\beta_{\mathrm{s}}(1-n)S_g\frac{D^{\mathrm{s}}T}{Dt}+S_{\mathrm{g}}\mathrm{div}\,\mathbf{v}^{\mathrm{s}}+\frac{nS_{\mathrm{g}}}{\rho^{\mathrm{gw}}}\frac{D^{\mathrm{s}}\left[\frac{M_{\mathrm{w}}}{\theta R}p^{\mathrm{gw}}\right]}{Dt}$$
$$-\frac{1}{\rho^{\mathrm{gw}}}\mathrm{div}\left[\rho^{\mathrm{g}}\frac{M_{\mathrm{a}}M_{\mathrm{w}}}{M_g^2}\mathbf{D}_{\mathrm{g}}\mathrm{grad}\left(\frac{p^{\mathrm{gw}}}{p^{\mathrm{g}}}\right)\right]+\frac{1}{\rho^{\mathrm{gw}}}\mathrm{div}(nS_{\mathrm{g}}\rho^{\mathrm{gw}}\mathbf{v}^{\mathrm{gs}})=\frac{\dot{m}}{\rho^{\mathrm{gw}}} \tag{2.77}$$

This equation is now multiplied by ρ^{gw} and added to the mass balance equation of liquid water (Equation (2.70)), in turn multiplied by ρ^{w}. This sum gives the mass balance equation for the water species, liquid and vapour, without mass rate of water evaporation as:

$$n(\rho^{w}-\rho^{\mathrm{gw}})\frac{D^{\mathrm{s}}S_{\mathrm{w}}}{Dt}-\beta_{\mathrm{swg}}\frac{D^{\mathrm{s}}T}{Dt}+(\rho^{\mathrm{gw}}S_g+\rho^{w}S_{\mathrm{w}})\mathrm{div}\,\mathbf{v}^{\mathrm{s}}+\frac{n\rho^{w}S_{\mathrm{w}}}{K_{\mathrm{w}}}\frac{D^{\mathrm{s}}p^{\mathrm{w}}}{Dt}+nS_{\mathrm{g}}\frac{D^{\mathrm{s}}\left[\frac{M_{\mathrm{w}}}{\theta R}p^{\mathrm{gw}}\right]}{Dt}$$
$$-\mathrm{div}\left[\rho^{\mathrm{g}}\frac{M_{\mathrm{a}}M_{\mathrm{w}}}{M_g^2}\mathbf{D}_{\mathrm{g}}\mathrm{grad}\left(\frac{p^{\mathrm{gw}}}{p^{\mathrm{g}}}\right)\right]+\mathrm{div}(nS_{\mathrm{g}}\rho^{\mathrm{gw}}\mathbf{v}^{\mathrm{gs}})+\mathrm{div}(nS_{\mathrm{w}}\rho^{w}\mathbf{v}^{\mathrm{ws}})=0 \tag{2.78}$$

where:

$$\beta_{\mathrm{swg}}=\beta_{\mathrm{s}}(1-n)(\rho^{\mathrm{gw}}S_g+\rho^{w}S_{\mathrm{w}})+n\beta_{\mathrm{w}}S_{\mathrm{w}}\rho^{w} \tag{2.79}$$

In these equations Darcy's law for the fluid velocities relative to the solid has still to be introduced. This law was introduced in Section 2.5.5 Darcy's law and will be derived again in its generalized form in the next section from the linear momentum balance equations.

2.6.2 Linear momentum balance equation

2.6.2.1 Fluids

A more suitable form for the linear momentum balance equation for the fluid-phases is now obtained by introducing kinematic equations and constitutive relationships.

$$\mathbf{a}^{\pi}=\mathbf{a}^{\mathrm{s}}+\mathbf{a}^{\pi\mathrm{s}}+\mathbf{v}^{\pi\mathrm{s}}\cdot\mathrm{grad}\mathbf{v}^{\pi} \tag{2.80}$$

where $\mathbf{a}^{\pi\mathrm{s}}$ is the relative acceleration.

Introduction in Equation (2.20) of (2.80) and (2.33) and the intrinsic phase averaged density yields:

$$-\eta^{\pi}\rho^{\pi}\left(\mathbf{a}^{s}+\mathbf{a}^{\pi s}+\mathbf{v}^{\pi s}\cdot\mathrm{grad}\mathbf{v}^{\pi}\right)-\mathrm{div}(\eta^{\pi}p^{\pi}\mathbf{I})+\eta^{\pi}\rho^{\pi}e^{\pi}(\rho\dot{\mathbf{r}})+\eta^{\pi}\rho^{\pi}\mathbf{g}-\mathrm{R}^{\pi}\eta^{\pi}\mathbf{v}^{\pi s}=0 \tag{2.81}$$

By neglecting the term that depends on the gradient of the fluid velocity, the effects of phase change and by applying a vector identity, for the divergence of the stress tensor in the fluid-phase, the relative velocity of the fluid is obtained:

$$\eta^{\pi}\mathbf{v}^{\pi s}=(\mathrm{R}^{\pi})^{-1}\eta^{\pi}[-\mathrm{grad}p^{\pi}+\rho^{\pi}(\mathbf{g}-\mathbf{a}^{s}-\mathbf{a}^{\pi s})] \tag{2.82}$$

$$\eta^{\pi}\mathbf{v}^{\pi s}=\frac{\mathbf{k}k^{r\pi}}{\mu}[-\mathrm{grad}p^{\pi}+\rho^{\pi}(\mathbf{g}-\mathbf{a}^{s}-\mathbf{a}^{\pi s})] \tag{2.83}$$

Finally, neglecting the soil acceleration and the relative acceleration terms, it yields Darcy's law in the form of Equation (2.44):

$$\eta^{\pi}\mathbf{v}^{\pi s}=\frac{\mathbf{k}k^{r\pi}}{\mu}(-\mathrm{grad}p^{\pi}+\rho^{\pi}\mathbf{g}) \tag{2.84}$$

Due to the simplifications introduced, this law is valid as a first approximation for slow flow of a macroscopically inviscid fluid through a porous medium with incompressible grains.

2.6.2.2 Solid-phase

Taking into account Equations (2.54), (2.55) and (2.56), the linear momentum balance equation for the solid-phase becomes:

$$\begin{aligned}&\mathrm{div}\left[\boldsymbol{\sigma}'-\mathbf{I}(1-n)\left(S_{w}p^{w}+S_{g}p^{g}\right)\right]+(1-n)\rho^{s}\mathbf{g}\\&-(1-n)\rho^{s}\mathbf{a}^{s}+\mathbf{R}^{w}\eta^{w}\mathbf{v}^{ws}+\mathbf{R}^{g}\eta^{g}\mathbf{v}^{wg}=0\end{aligned} \tag{2.85}$$

2.6.2.3 Multiphase medium

Through summing the momentum balance equations, written for water and gas-phase in section 2.6.2.1, with that of the solid phase in section 2.6.2.2, by taking into account the definition of total stress, assuming continuity of stress at the fluid-solid interfaces and by introducing the averaged density of the multiphase medium

$$\rho=(1-n)\rho^{s}+nS_{w}\rho^{w}+nS_{g}\rho^{g} \tag{2.86}$$

the linear momentum balance equation for the whole multiphase medium is obtained:

$$-\rho\mathbf{a}^{s}-nS_{w}p^{w}[\mathbf{a}^{ws}+\mathbf{v}^{ws}\cdot\mathrm{grad}\mathbf{v}^{w}]-nS_{g}\rho^{g}[\mathbf{a}^{gs}+\mathbf{v}^{gs}\cdot\mathrm{grad}\mathbf{v}^{g}]+\mathrm{div}(\boldsymbol{\sigma})+\rho\mathbf{g}=0 \tag{2.87}$$

2.6.3 Energy balance equation

The energy balance equation for the single phase is:

$$\rho^{\pi} C_p^{\pi} \frac{D^{\pi}\theta^{\pi}}{Dt} = \rho^{\pi} h^{\pi} - \operatorname{div} \tilde{\mathbf{q}}^{\pi} + \rho^{\pi} R^{\pi} - \rho^{\pi} e^{\pi} \left(\rho\right) H^{\pi} \tag{2.88}$$

The specific enthalpy of the phase π, is a function of the absolute temperature and the pressure

$$H^{\pi} = H^{\pi}(\overline{\rho}^{\pi}, \theta^{\pi}) \tag{2.89}$$

and $C_p^{\pi} = \left(\frac{\partial H^{\pi}}{\partial \theta^{\pi}} \right)_{\overline{p}}$ is the specific heat at constant pressure.

For the continuum multiphase, imposing the thermodynamic equilibrium, the energy balance equation can be written as:

$$\left(\rho C_p\right)_{eff} \frac{\partial T}{\partial t} + \left(\rho_{\mathrm{w}} C_p^{\mathrm{w}} \mathbf{v}^{\mathrm{w}} + \rho_{\mathrm{g}} C_p^{\mathrm{g}} \mathbf{v}^{\mathrm{g}}\right) \cdot \operatorname{grad} T - \operatorname{div}\left(\chi_{eff} \operatorname{grad} T\right) = -\dot{m} \Delta H_{\mathrm{vap}} \tag{2.90}$$

where:

$\left(\rho C_p\right)_{eff} = \rho_{\mathrm{s}} C_p^{\mathrm{s}} + \rho_{\mathrm{w}} C_p^{\mathrm{w}} + \rho_{\mathrm{g}} C_p^{\mathrm{g}}$

$\chi_{eff} = \chi^{s} + \chi^{w} + \chi^{g}$

$\Delta H_{\mathrm{vap}} = H^{\mathrm{gw}} - H^{\mathrm{w}}$

2.6.4 Governing equations

The governing equations that will be used in the context of this thesis are briefly presented in the following sections for the dynamic and quasi-static conditions.

2.6.4.1 Dynamic case

Neglecting the relative acceleration of the fluids, the convective terms and the dynamic seepage forcing term in the governing equations of Lewis and Schrefler (1998), a reduced form of the balance equations for the porous medium has been obtained and the respective balance equations are shown next. For more details the interest reader is referred to Passarotto (2013) and Cao et al. (2015).

Linear momentum balance equation

The linear momentum balance equation of the mixture for the reduced formulation is:

$$\operatorname{div}(\boldsymbol{\sigma}) + \rho \mathbf{g} - \rho \mathbf{a}^{\mathrm{s}} = 0 \tag{2.91}$$

where ρ(x, t) is the averaged density of the multiphase medium defined as, $\rho = [1 - n]\, \rho_{\mathrm{s}} + n\, S_{\mathrm{w}}\, \rho_{\mathrm{w}} + n\, S_{\mathrm{g}}\, \rho_{\mathrm{g}}$ and n the porosity, $\mathbf{a}^{\mathrm{s}}(x, t)$ is the acceleration of solid phase, $\mathbf{g}$ is the acceleration of gravity, $\rho_{\mathrm{s}}(x, t)$ the density of the solid grain, $\rho_{\mathrm{w}}(x, t)$ the density of liquid water and $\rho_{\mathrm{g}}(x, t)$ the density of gas.

The total Cauchy stress $\boldsymbol{\sigma}(x, t)$ of variably saturated porous media can be expressed through the concept of generalized effective stress (Schrefler (1984)) as:

$$\boldsymbol{\sigma} = \boldsymbol{\sigma}' + \mathbf{I}\alpha\left(S_{\mathrm{w}}\, p^{\mathrm{w}} + S_{\mathrm{g}}\, p^{\mathrm{g}}\right) \tag{2.92}$$

where $\boldsymbol{\sigma}'(x, t)$ is the generalized effective Cauchy stress tensor, $\mathbf{I}$ the second order identity tensor and α the Biot coefficient defined as $\alpha = 1 - K_t / K_s$, with $K_t(x, t)$ being the bulk modulus of the porous medium. Assuming incompressibility of the solid grain at microscopic level, $K_s \longrightarrow \infty$, the Biot coefficient equals to 1.

Mass balance equations

The sum of the mass balance equation for the water species and the solid for the reduced formulation is written as:

$$\begin{aligned}
&\mathrm{div}\left(\rho^{\mathrm{w}}\frac{k^{\mathrm{rw}}\boldsymbol{k}}{\mu^{\mathrm{w}}}\left(-\mathrm{grad}p^{\mathrm{w}} + \rho^{\mathrm{w}}\boldsymbol{g}\right)\right) + \mathrm{div}\left(\rho^{\mathrm{gw}}\frac{k^{\mathrm{rg}}\boldsymbol{k}}{\mu^{\mathrm{g}}}\left(-\mathrm{grad}p^{\mathrm{gw}} + \rho^{\mathrm{gw}}\boldsymbol{g}\right)\right)\\
&-\mathrm{div}\left[\rho^{\mathrm{g}}\frac{M_{\mathrm{a}}M_{\mathrm{w}}}{M_{\mathrm{g}}^2}\boldsymbol{D}_{\mathrm{g}}^{\mathrm{gw}}\mathrm{grad}\left(\frac{p^{\mathrm{gw}}}{p^{\mathrm{g}}}\right)\right] + \left(\rho^{\mathrm{w}}S_{\mathrm{w}} + \rho^{\mathrm{gw}}S_{\mathrm{g}}\right)\alpha\,\mathrm{div}\mathbf{v}^{\mathrm{s}}\\
&-\left[\rho^{\mathrm{w}}\beta_{\mathrm{sw}} + \rho^{\mathrm{gw}}\beta_{\mathrm{s}}\left(\alpha - n\right)S_{\mathrm{g}}\right]\dot{T} + \left[n\rho^{\mathrm{w}} - n\rho^{\mathrm{gw}}\right]\dot{S}_{\mathrm{w}}\\
&+nS_{\mathrm{g}}\dot{\rho}^{\mathrm{gw}} + \left[\rho^{\mathrm{w}}\frac{nS_{\mathrm{w}}}{K_{\mathrm{w}}}\right]\dot{p}^{\mathrm{w}} = 0
\end{aligned} \tag{2.93}$$

where, $k^{\mathrm{w}}(x, t)$ and $k^{\mathrm{g}}(x, t)$ are the intrinsic permeability tensors of liquid water and gas, $k^{\mathrm{rw}}(x, t)$ and $k^{\mathrm{rg}}(x, t)$ the liquid water and gas relative permeability, $\mu^{\mathrm{w}}(x, t)$ and $\mu^{\mathrm{g}}(x, t)$ the liquid water and gas viscosity, $\beta_{\mathrm{sw}} = S_{\mathrm{w}}[1 - n]\beta_{\mathrm{s}}$ with β_{s} the thermal expansion coefficient for solid articles; K_{w} is the bulk modulus of water, $\boldsymbol{D}_{\mathrm{g}}^{\mathrm{gw}}(x)$ the effective diffusivity tensor of water vapour in the gas phase, and $M_{\mathrm{a}}(x)$, $M_{\mathrm{w}}(x)$ and $M_{\mathrm{g}}(x, t)$ the molar mass of dry air, liquid water and the gas mixture, respectively (see Equation (2.94)).

$$M_{\mathrm{g}} = \left(\frac{\rho^{\mathrm{gw}}}{\rho^{\mathrm{g}}}\,\frac{1}{M_{\mathrm{w}}} + \frac{\rho^{\mathrm{ga}}}{\rho^{\mathrm{g}}}\,\frac{1}{M_{\mathrm{a}}}\right)^{-1} \tag{2.94}$$

Similarly, the sum of the mass balance equation for dry air and for solid in the reduced formulation reads:

$$\begin{aligned}
&\mathrm{div}\left\{\rho^{\mathrm{ga}}\frac{k^{\mathrm{rg}}\boldsymbol{k}}{\mu^{\mathrm{g}}}\left(-\mathrm{grad}p^{\mathrm{g}} + \rho^{\mathrm{g}}\boldsymbol{g}\right)\right\} + \mathrm{div}\left[\rho^{\mathrm{g}}\frac{M_{\mathrm{a}}M_{\mathrm{w}}}{M_{\mathrm{g}}^2}\boldsymbol{D}_{\mathrm{g}}^{\mathrm{ga}}\mathrm{grad}\left(\frac{p^{\mathrm{ga}}}{p^{\mathrm{g}}}\right)\right]\\
&+\rho^{\mathrm{ga}}\alpha S_{\mathrm{g}}\mathrm{div}\mathbf{v}^{\mathrm{s}} + nS_{\mathrm{g}}\rho^{\mathrm{ga}} - \rho^{\mathrm{ga}}n\dot{S}_{\mathrm{w}} - \rho^{\mathrm{ga}}\beta_{\mathrm{s}}\left(\alpha - n\right)S_{\mathrm{g}}\dot{T} = 0
\end{aligned} \tag{2.95}$$

where $\boldsymbol{D}_{\mathrm{g}}^{\mathrm{ga}}(x)$ is the effective diffusivity tensor of dry air in water vapour. The mass balance equation of solid phase has been summed to that of the other phases to eliminate the time derivative of the

porosity (Lewis and Schrefler (1998)). In Equations (2.93) and (2.95), the advective fluxes have been described by using Darcy's law for liquid water and gas, while the diffusion of vapour in the gas phase has been modelled with Fick's law (see Section 2.5.5 and 2.5.6, respectively).

Energy balance equation

The energy balance equation of the porous medium for the reduced formulation is:

$$\begin{aligned}
&\left[C_p^{\mathrm{w}} \rho^{\mathrm{w}} \frac{k^{\mathrm{rw}} \boldsymbol{k}}{\mu^{\mathrm{w}}} \left(-\mathrm{grad} p^{\mathrm{w}} + \rho^{\mathrm{w}} \boldsymbol{g} \right) + C_p^{\mathrm{g}} \rho^{\mathrm{g}} \frac{k^{\mathrm{rg}} \boldsymbol{k}}{\mu^{\mathrm{g}}} \left(-grad p^{\mathrm{g}} + \rho^{\mathrm{g}} \boldsymbol{g} \right) \right] \cdot \mathrm{grad}\, T \\
&+ \left(\rho C_p \right)_{eff} \dot{T} - \mathrm{div} \left(\chi_{eff} \mathrm{grad} T \right) - \rho^{\mathrm{w}} \frac{n S_{\mathrm{w}}}{K_{\mathrm{w}}} \dot{p}^{\mathrm{w}} \Delta H_{\mathrm{vap}} - \rho^{\mathrm{w}} S_{\mathrm{w}} \alpha\, \mathrm{div} \mathbf{v}^{\mathrm{s}} \Delta H_{\mathrm{vap}} \\
&+ \beta_{\mathrm{sw}} \dot{T} \Delta H_{\mathrm{vap}} - n \left(\rho^{\mathrm{w}} - \rho^{\mathrm{gw}} \right) \dot{S}_{\mathrm{w}} \Delta H_{\mathrm{vap}} - \mathrm{div} \left(\rho^{\mathrm{w}} \frac{k^{\mathrm{rw}} \boldsymbol{k}}{\mu^{\mathrm{w}}} \left(-\mathrm{grad} p^{\mathrm{w}} + \rho^{\mathrm{w}} \boldsymbol{g} \right) \right) \Delta H_{\mathrm{vap}} = 0
\end{aligned} \tag{2.96}$$

where $\Delta H_{\mathrm{vap}}(\mathrm{x}, \mathrm{t})$ is the latent heat, $(\rho C_p)_{eff}(\mathrm{x}, \mathrm{t})$ the effective heat capacity of the porous medium, $C_p^{\mathrm{w}}(\mathrm{x})$ and $C_p^{\mathrm{g}}(\mathrm{x})$ are the specific heat of liquid water and the gas mixture respectively, and $\chi_{eff}(\mathrm{x}, \mathrm{t})$ is the effective thermal conductivity of the porous medium.

2.6.4.2 Quasi static case

Equilibrium equation

The equilibrium equation of the mixture in terms of generalized effective Cauchy's stress tensor $\boldsymbol{\sigma}'(\mathrm{x}, \mathrm{t})$ assumes the form:

$$\mathrm{div}(\boldsymbol{\sigma}' - \left[p^g - S_w p^c \right] \mathbf{1}) + \rho \mathbf{g} = 0 \tag{2.97}$$

where as for the dynamic case $\rho = [1 - n]\, \rho_{\mathrm{s}} + n\, S_{\mathrm{w}}\, \rho_{\mathrm{w}} + n\, S_{\mathrm{g}}\, \rho_{\mathrm{g}}$ is the mass density of the overall medium, $n(\boldsymbol{x}, t)$ is the porosity, $S_w(\boldsymbol{x}, t)$ and $S_g(\boldsymbol{x}, t)$ are respectively the water and gas degree of saturation, $\mathbf{g}$ is the gravity acceleration vector and $\mathbf{1}$ is the second order identity tensor. The form of Equation (2.97) assumes incompressible grains, which is common in soil mechanics. To consider compressible grains, the Biot coefficient should be set in front of the solid pressure (this becomes important when dealing with rock and concrete).

Mass balance equations

The mass balance equation for the mixture of solid phase, liquid water and its vapour is:

$$
\begin{aligned}
&n\left[\rho^{w}-\rho^{gw}\right]\left[\frac{\partial S_{w}}{\partial t}\right]+\left[\rho^{w}S_{w}+\rho^{gw}\left[1-S_{w}\right]\right]\mathrm{div}\left(\frac{\partial \mathbf{u}}{\partial t}\right)+\left[1-S_{w}\right]n\frac{\partial \rho^{gw}}{\partial t}\\
&-\mathrm{div}\left(\rho^{g}\frac{M_{\mathrm{a}}M_{w}}{M_{g}^{2}}\boldsymbol{D}_{\mathrm{g}}^{\mathrm{gw}}\mathrm{grad}\left(\frac{p^{gw}}{p^{g}}\right)\right)+\mathrm{div}\left(\rho^{w}\frac{\mathbf{k}^{\mathrm{w}}k^{rw}}{\mu^{w}}\left[-\mathrm{grad}(p^{g})+\mathrm{grad}(p^{c})+\rho^{w}\mathbf{g}\right]\right)\\
&+\mathrm{div}\left(\rho^{gw}\frac{\mathbf{k}^{\mathrm{g}}k^{rg}}{\mu^{g}}\left[-\mathrm{grad}(p^{g})+\rho^{g}\mathbf{g}\right]\right)-\beta_{swg}\frac{\partial T}{\partial t}=0
\end{aligned}
\tag{2.98}
$$

where $\mathbf{k}^{\pi}(\boldsymbol{x}, t) = k^{\pi}(\boldsymbol{x}, t)\mathbf{1}$ is the intrinsic permeability tensor of the porous matrix in π-fluid saturated condition, which is assumed to be isotropic, $k^{r\pi}(\boldsymbol{x},t)$ is the fluid relative permeability parameter and $\mu^{\pi}(\boldsymbol{x}, t)$ is the dynamic viscosity of the fluid, with π= w, g. $\boldsymbol{D}_{\mathrm{g}}^{\mathrm{gw}}$ is the effective diffusivity tensor of water vapour in the gas phase contained within the pore space and $\beta_{swg} = \beta_s(1 - n)\cdot(S_g\,\rho^{gw} + \rho^{w}S_w)$ with $\beta_s(\boldsymbol{x},t)$ the cubic thermal expansion coefficient and M_a, M_w and $M_g(\boldsymbol{x},t)$ are the molar mass of dry air, liquid water and gas mixture, respectively.

Similarly, the sum of the mass balance equation for the dry air and that of the solid phase is:

$$
\begin{aligned}
&-n\rho^{\mathrm{g}\alpha}\left[\frac{\partial S_{w}}{\partial t}\right]+\rho^{\mathrm{g}\alpha}\left[1-S_{w}\right]\mathrm{div}\left(\frac{\partial \mathbf{u}}{\partial t}\right)+n\left[1-S_{w}\right]\frac{\partial \rho^{\mathrm{g}\alpha}}{\partial t}\\
&-\mathrm{div}\left(\rho^{g}\frac{M_{\mathrm{a}}M_{w}}{M_{g}^{2}}\mathbf{D}_{\mathrm{g}}^{\mathrm{g}\alpha}\mathrm{grad}\left(\frac{p^{\mathrm{g}\alpha}}{p^{g}}\right)\right)+\mathrm{div}\left(\rho^{\mathrm{g}\alpha}\frac{\mathbf{k}^{\mathrm{g}}k^{rg}}{\mu^{g}}\left[-\mathrm{grad}(p^{g})+\rho^{g}\mathbf{g}\right]\right)\\
&-\left[1-n\right]\beta_{s}\rho^{\mathrm{g}\alpha}\left[1-S_{w}\right]\frac{\partial T}{\partial t}=0
\end{aligned}
\tag{2.99}
$$

Enthalpy balance equation

The enthalpy balance equation of the mixture has the following form:

$$
\begin{aligned}
&\left(\rho C_{p}\right)_{eff}\frac{\partial T}{\partial \mathrm{t}}+\rho^{\mathrm{w}}C_{p}^{\mathrm{w}}\left[\frac{\mathbf{k}^{\mathrm{w}}k^{\mathrm{rw}}}{\mu^{\mathrm{w}}}\left[-\mathrm{grad}(p^{\mathrm{g}})+\mathrm{grad}(p^{\mathrm{c}})+\rho^{\mathrm{w}}\mathbf{g}\right]\right]\cdot\mathrm{grad}T\\
&+\rho^{\mathrm{g}}C_{p}^{g}\left[\frac{\mathbf{k}^{\mathrm{g}}k^{\mathrm{rg}}}{\mu^{\mathrm{g}}}\left[-\mathrm{grad}(p^{\mathrm{g}})+\rho^{\mathrm{g}}\mathbf{g}\right]\right]\cdot\mathrm{grad}T-\mathrm{div}\left(\chi_{eff}\mathrm{grad}T\right)=-\dot{m}_{\mathrm{vap}}\Delta H_{\mathrm{vap}}
\end{aligned}
\tag{2.100}
$$

where, $\rho(C_p)_{eff}$ is the effective thermal capacity of the porous medium, $C_p^{\mathrm{w}}(\boldsymbol{x},t)$ and $C_p^{\mathrm{g}}(\boldsymbol{x},t)$ are the specific heat of the water and gas mixture respectively, and $\chi_{eff}(\boldsymbol{x}, t)$ is the effective thermal conductivity of the porous medium. The right hand side term of Equation (2.100) considers the contribution of the evaporation and condensation.

2.7 Initial and Boundary Conditions

The final mathematical model consists of the following balance equations: mass conservation of solid skeleton, mass conservation of dry air, mass conservation of the water species, enthalpy

conservation of the whole medium and linear momentum of the multiphase system. They are completed by an appropriate set of constitutive and state equations, as well as some thermodynamic relationships.

The governing equations of the model are expressed in terms of the chosen state variables: gas pressure p^g, capillary pressure p^c, temperature T and displacement vector of the solid matrix $\mathbf{u}$.For the model closure the initial and boundary conditions are needed. The initial conditions specify the full fields of primary state variables at time instant $t = t_0$, in the whole analyses domain Ω and on its boundary Γ, ($\Gamma = \Gamma_\pi \cup \Gamma_\pi^q$, π = g, c, T, $\mathbf{u}$):

$$p^{\mathrm{g}} = p_0^{\mathrm{g}},\ p^{\mathrm{c}} = p_0^{\mathrm{c}},\ T = T_0,\ \mathbf{u} = \mathbf{u}_0 \text{ on } (\Omega \cup \Gamma) \tag{2.101}$$

The boundary conditions (BCs) can be of Dirichlet's type on Γ_π for $t \geq t_0$:

$$\begin{aligned} p^{\mathrm{g}} &= \hat{p}^{\mathrm{g}} \quad \text{on } \Gamma_{\mathrm{pg}} \\ p^{\mathrm{c}} &= \hat{p}^{\mathrm{c}} \quad \text{on } \Gamma_{\mathrm{pc}} \\ T &= \hat{T} \quad \text{on } \Gamma_T \\ \mathbf{u} &= \hat{\mathbf{u}} \quad \text{on } \Gamma_{\mathrm{u}} \end{aligned} \tag{2.102}$$

or of Cauchy's type (the mixed BCs) on Γ_π^q for $t \geq t_0$:

$$\begin{aligned} &(nS_{\mathrm{g}}\rho^{\mathrm{ga}}\mathbf{v}^{\mathrm{gs}} + \mathbf{J}_d^{\mathrm{ga}}) \cdot \mathbf{n} = q^{\mathrm{ga}} && \text{on } \Gamma_{\mathrm{g}}^q \\ &(nS_{\mathrm{w}}\rho^{\mathrm{w}}\mathbf{v}^{\mathrm{ws}} + nS_{\mathrm{g}}\rho^{\mathrm{gw}}\mathbf{v}^{\mathrm{gs}} + \mathbf{J}_d^{\mathrm{gw}}) \cdot \mathbf{n} = q^{\mathrm{gw}} + q^{\mathrm{w}} + \beta_c(\rho^{\mathrm{gw}} - \rho_\infty^{\mathrm{gw}}) && \text{on } \Gamma_{\mathrm{c}}^q \\ &(nS_{\mathrm{w}}\rho^{\mathrm{w}}\mathbf{v}^{\mathrm{ws}}\Delta H_{\mathrm{vap}} - \chi_{eff}\, grad T) \cdot \mathbf{n} = q^T + a_c(T - T_\infty) + e\sigma_0(\mathrm{T}^4 - \mathrm{T}_\infty^4) && \text{on } \Gamma_T^q \\ &\boldsymbol{\sigma}' \cdot \mathbf{n} = \bar{\mathbf{t}} && \text{on } \Gamma_{\mathrm{u}}^q \end{aligned} \tag{2.103}$$

where $\mathbf{n}$ is the unit normal vector, pointing toward the surrounding gas, q^{ga}, q^{gw}, q^{w} and q^T are, respectively, the imposed fluxes of dry air, vapour, liquid water and the imposed heat flux, $\bar{\mathrm{t}}$ is the imposed traction, $\rho_\infty^{\mathrm{gw}}$ and T_∞ are the mass concentration of water vapour and the temperature in the far field of undisturbed gas phase, e is emissivity of the interface, σ_0 the Stefan-Boltzmann constant, while α_c and β_c are convective heat and mass exchange coefficients.

The boundary conditions with only imposed fluxes are called Neumann's BCs while the purely convective boundary conditions for heat and moisture exchange are also called Robin's BCs.

2.8 Finite Element Formulation

Discretization in space of the governing equations in their weak form is performed by means of the finite element method (Zienkiewicz and Taylor (2000)). The unknown primary variables are expressed in the whole domain by global shape functions matrices and the nodal value vectors:

$$p^{\mathrm{g}}(t)=\mathbf{N}_p\overline{\mathbf{p}}^{\mathrm{g}}(t),\qquad p^{\mathrm{c}}(t)=\mathbf{N}_p\overline{\mathbf{p}}^{\mathrm{c}}(t)$$
$$T(t)=\mathbf{N}_t\overline{\mathbf{T}}(t),\qquad \mathbf{u}(t)=\mathbf{N}_u\overline{\mathbf{u}}(t) \tag{2.104}$$

In particular, the finite element model is derived by applying the Galerkin procedure for the spatial integration and the Generalized Trapezoidal Method for the time integration of the weak form of the balance equations of section 2.6.4. After spatial discretization within the isoparametric formulation the following non-symmetric, non-linear and coupled system of equation is obtained:

$$\mathbf{C}_{ij}(\mathbf{x})\frac{\partial\mathbf{x}}{\partial t}+\mathbf{K}_{ij}(\mathbf{x})\mathbf{x}-\mathbf{f}_t(\mathbf{x})=0 \tag{2.105}$$

with

$$\mathbf{C}_{ij}=\begin{bmatrix}\mathbf{C}_{gg} & \mathbf{C}_{gc} & \mathbf{C}_{gt} & \mathbf{C}_{gu}\\ 0 & \mathbf{C}_{cc} & \mathbf{C}_{ct} & \mathbf{C}_{cu}\\ 0 & \mathbf{C}_{tc} & \mathbf{C}_{tt} & \mathbf{C}_{tu}\\ 0 & 0 & 0 & 0\end{bmatrix},\ \mathbf{K}_{ij}=\begin{bmatrix}\mathbf{K}_{gg} & \mathbf{K}_{gc} & \mathbf{K}_{gt} & 0\\ \mathbf{K}_{cg} & \mathbf{K}_{cc} & \mathbf{K}_{ct} & 0\\ \mathbf{K}_{tg} & \mathbf{K}_{tc} & \mathbf{K}_{tt} & 0\\ \mathbf{K}_{ug} & \mathbf{K}_{uc} & \mathbf{K}_{ut} & \mathbf{K}_{uu}\end{bmatrix},\ \mathbf{f}_t=\begin{bmatrix}\mathbf{f}_g\\ \mathbf{f}_c\\ \mathbf{f}_t\\ \mathbf{f}_u\end{bmatrix} \tag{2.106}$$

where $\mathbf{x}=\left[\overline{\mathbf{p}}^{g},\overline{\mathbf{p}}^{c},\overline{\mathbf{T}},\overline{\mathbf{u}}\right]^{\mathrm{T}}$ and the non-linear matrix coefficients $\mathbf{C}_{ij}$ ($\mathbf{x}$), $\mathbf{K}_{ij}$ ($\mathbf{x}$) and $\mathbf{f}_j$ ($\mathbf{x}$) are defined in detail in Sanavia et al. (2006).

Finite differences in time are used for the solution of the initial value problem over a finite time step $\Delta t = t_{\mathrm{n+1}} - t_{\mathrm{n}}$. Following the Generalized Trapezoidal Method, Equation (2.105) is rewritten at time $t_{\mathrm{n+1}}$ using the relationships:

$$\left(\frac{\partial\mathbf{x}}{\partial t}\right)_{n+\theta}=\frac{\mathbf{x}_{n+1}-\mathbf{x}_n}{\Delta t},\quad \mathbf{x}_{n+\theta}=(1-\theta)\mathbf{x}_n+\theta\mathbf{x}_{n+1}\quad \text{with } \theta=[0,\,1] \tag{2.107}$$

where n is the time step number, $\mathbf{x}_{\mathrm{n}}$ and $\mathbf{x}_{\mathrm{n+1}}$ are the state vectors at times $\mathbf{t}_{\mathrm{n}}$ and $\mathbf{t}_{\mathrm{n+1}}$, thus obtaining:

$$\mathbf{G}(\mathbf{x}_{n+1})=\left[\mathbf{C}+\theta\Delta t\mathbf{K}\right]_{n+\theta}\mathbf{x}_{n+1}-\left[\mathbf{C}-(1-\theta)\Delta t\mathbf{K}\right]_{n+\theta}\mathbf{x}_n-\Delta t\mathbf{f}_{n+\theta}=0 \tag{2.108}$$

Linearized analysis of accuracy and stability suggest the use of $\theta \geq$ ½ and herein an implicit one-step time integration ($\theta = 1$) has been performed.

After time integration the non-linear system of equation is linearized, thus obtaining the equations system that can be solved numerically (in compact form):

$$\left.\frac{\partial\mathbf{G}}{\partial\mathbf{x}}\right|_{\mathbf{x}^k_{n+1}}\Delta\mathbf{x}^{k+1}_{n+1}\cong-\mathbf{G}(\mathbf{x}^k_{n+1}) \tag{2.109}$$

with the symbol $(\bullet)^{k+1}_{n+1}$ indicating the current iteration (k+1) in the current time step (n+1) and with the following form for the Jacobian matrix:

$$\left.\frac{\partial \mathbf{G}}{\partial \mathbf{x}}\right|_{\mathbf{x}_{n+1}^{k}} = \left[\begin{array}{cccc} \dfrac{\partial \mathrm{G}^{g}}{\partial \overline{\mathbf{p}}^{g}} & \dfrac{\partial \mathrm{G}^{g}}{\partial \overline{\mathbf{p}}^{c}} & \dfrac{\partial \mathrm{G}^{g}}{\partial \mathbf{T}} & \dfrac{\partial \mathrm{G}^{g}}{\partial \overline{\mathbf{u}}} \\ \dfrac{\partial \mathrm{G}^{c}}{\partial \overline{\mathbf{p}}^{g}} & \dfrac{\partial \mathrm{G}^{c}}{\partial \overline{\mathbf{p}}^{c}} & \dfrac{\partial \mathrm{G}^{c}}{\partial \mathbf{T}} & \dfrac{\partial \mathrm{G}^{c}}{\partial \overline{\mathbf{u}}} \\ \dfrac{\partial \mathrm{G}^{t}}{\partial \overline{\mathbf{p}}^{g}} & \dfrac{\partial \mathrm{G}^{t}}{\partial \overline{\mathbf{p}}^{c}} & \dfrac{\partial \mathrm{G}^{t}}{\partial \mathbf{T}} & \dfrac{\partial \mathrm{G}^{t}}{\partial \overline{\mathbf{u}}} \\ \dfrac{\partial \mathrm{G}^{u}}{\partial \overline{\mathbf{p}}^{g}} & \dfrac{\partial \mathrm{G}^{u}}{\partial \overline{\mathbf{p}}^{c}} & \dfrac{\partial \mathrm{G}^{u}}{\partial \mathbf{T}} & \dfrac{\partial \mathrm{G}^{u}}{\partial \overline{\mathbf{u}}} \end{array}\right]_{\mathbf{x}_{n+1}^{k}} \tag{2.110}$$

The increment vector of the primary variables is:

$$\Delta \mathbf{x}_{n+1}^{k} = \left[(\Delta \overline{\mathbf{p}}^{\mathrm{g}})_{n+1}^{k}, (\Delta \overline{\mathbf{p}}^{\mathrm{c}})_{n+1}^{k}, \Delta \overline{\mathbf{T}}_{n+1}^{k}, \Delta \overline{\mathbf{u}}_{n+1}^{k} \right]^{\mathrm{T}} \tag{2.111}$$

Owing to the strong coupling between the mechanical, thermal and the pore fluids problem, a monolithic solution of Equation (2.109) is preferred using a Netwon-Rapshon scheme. Finally, the solution vector $\mathbf{x} = \left[\overline{\mathbf{p}}^{g}, \overline{\mathbf{p}}^{c}, \overline{\mathbf{T}}, \overline{\mathbf{u}} \right]^{\mathrm{T}}$ is updated by the incremental relationship:

$$\mathbf{x}_{n+1}^{k+1} = \mathbf{x}_{n+1}^{k} + \Delta \mathbf{x}_{n+1}^{k} \tag{2.112}$$

The convergence and error analysis of the method applied here can be found in Gawin and Schrefler (1996).

During computations a problem arises when the medium is fully saturated because in this case the gas pressure, p^{g}, is undefined and the capillary pressure, p^{c}, has no physical meaning. On the other hand, the state of the liquid water in the medium is described by two variables (since in such situation there are only two degrees of freedom on top of solid displacements: liquid pressure and temperature).

The problem is treated with a formal modification of the relationship between saturation and capillary pressure: when the saturation becomes equal to one, the sign of the capillary pressure is formally set negative and the value equal to the pressure in the liquid above gas pressure. The fully saturated state is detected by monitoring the sign of the capillary pressure: when such a condition is reached, the dry air conservation equation is dropped and the gas pressure is set to equal to the atmospheric pressure. Thus we perform "switching", element by element, from fully saturated to partially saturated state equations (or vice versa) when capillary pressure reaches the bubbling pressure value (also called air entry value).

In practice, capillary and gas pressure oscillations may arise when this switch is performed. As already pointed out in Gawin et al. (1995), these oscillations are possibly due to the sudden switch of element behaviour (there is a change in governing equations) in a part of the domain, which in turn causes different convergence to solution in fully saturated and partially saturated zone of the domain and produces oscillations in the Newton iteration procedure (Forsyth and Simpson (1991)). Another reason is occurrence in the matrices C and K (Equation (2.105)) of very small diagonal terms related to gas pressure (because of very low value of gas relative permeability), which create numerical

problems. An efficient way of avoiding the mentioned oscillations is assumption of a lower limit for the value of relative permeability of gas phase (e.g. 0.0001), what seems to be physically admissible.

Based on the described discretization, the Comes-geo research computer code has been developed.

- *The Comes-geo code*

Geomaterials (soils, rocks, concrete) are the most common examples of porous media. The general purpose codes, currently available in the market, do not deal with more than a single fluid phase. Therefore it is not possible to carry out realistic numerical studies of porous materials structures in partially saturated conditions as: seismic analysis of soil dams where in the upper part wide zones, containing pores filled with air and water, are present; stability analysis of soil slopes; simulation of the subsidence phenomena in presence of gas extraction from deep reservoirs (in this case water and different gases are present in the pores).

Comes-geo is a software, written in Fortran90, for the solution of the non-linear and non-symmetrical system of equations governing heat and mass transfer in a deformable porous medium. The model makes use of the generalized effective stress concept together with the capillary pressure relationship.

The problem unknowns are the following: temperature, capillary pressure, gas pressure and displacements. These data allow the calculation of interesting derived outputs (i.e. saturation, stress-strain fields). To reach the solution of the problem using the considered model, four balance equations are imposed: mass of the dry air, mass of the water species (both liquid water and vapour; phase changes are considered); energy conservation of the mixture and the linear momentum of the multiphase medium. They are completed by an appropriate set of constitutive and state equations, as well as some thermodynamic relationships, as reported in the previous sections of this chapter. Comes-geo allows any finite element analysis in plane-strain and axialsymmetric conditions, using four nodes bilinear elements or Serendipity eight nodes elements or Lagrange nine nodes elements.

The system of algebraic equations obtained through the space-time discretization is solved following the flowchart given in Figure 2.7. The subroutine VARCA2 is the main subroutine which contains the Newton-Raphson loop. In VARCA2, there is the loop over the elements within which ABFOR5 is called: this subroutine computes, for each element, the left and the right hand side vector of the linearized system of equations. Through ABFOR5 the necessary subroutines are called in order to compute the constitutive and thermodynamic relationships for the description of thermo-hydro-mechanical state of the porous medium:

WATPROP: defines the physical properties of liquid water;

PRVAP: evaluates the vapour pressure, the vapour density and the relative humidity;

MATPROP: computes the material properties of the soil and calls also the subroutine which evaluates gas and water relative permeability and the one which evaluates the saturation for the porous material;

FORMBE: computes the strain–displacement matrix;

FORMDE: computes the elastic stress-strain matrix and calls the subroutine of the constitutive model for soils in which the effective stress and the stress-strain tensor are computed;

PRMEFF: evaluates the effective diffusivity of vapour inside the pores of partially saturated medium and its effective thermal conductivity.

Finally, ABFOR calls BFLUX5, which contains the boundary conditions formulation for gas pressure, capillary pressure, temperature and displacements.

The BMMFRONT is the frontal solver: the function of this subroutine is to assemble the contribution of each element to the global load vector and to solve the resulting set of simultaneous equations by Gaussian direct elimination. Once the convergence is achieved, the primary variables are updated and the mechanical stresses and strains are computed.

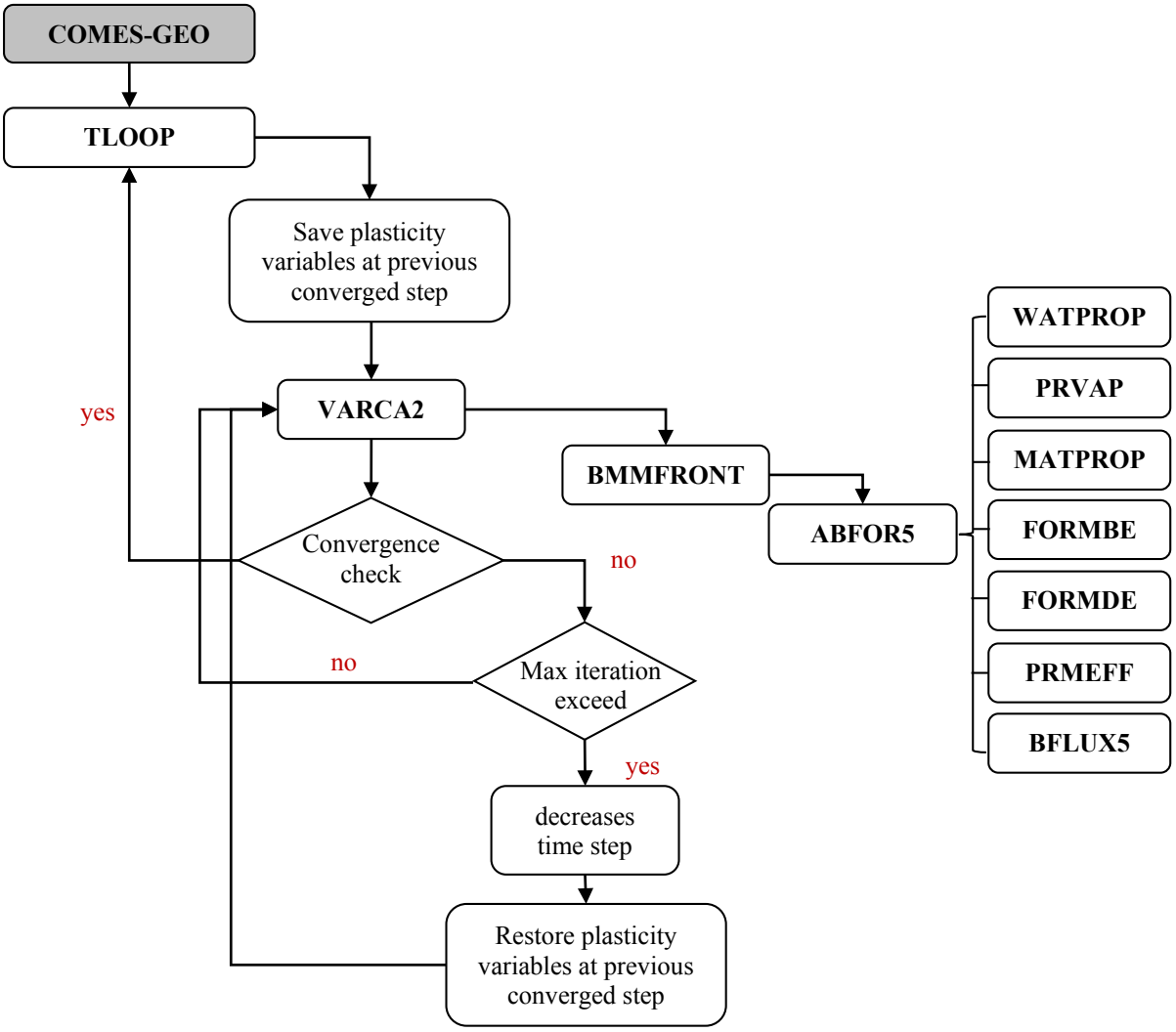

Figure 2.7: Comes-geo flowchart with the main subroutines.

2.9 Concluding Remarks

In this Chapter, the porous medium was postulated to be composed of a mixture of three interacting constituents: solid, liquid water and gas. By using the concept of volume fractions, appropriate average quantities for describing the behaviour of a porous medium were developed and balance laws for the mixture were derived in the light of HMT. These equations, combined with appropriate constitutive equations, constitute the general governing field equations that can be utilized to simulate the dynamic or quasi-static behaviour of fully or partially saturated porous media.

Chapter 3

Constitutive Modelling of Solid Phase from the Regularization Perspective: Governing Equations and Numerical Aspects

Chapter 3: Constitutive Modelling of Solid Phase from the Regularization Perspective: Governing Equations and Numerical Aspects

3.1 Introduction

The mechanical behaviour of the solid skeleton of the multiphase system is here described in the framework of elasto-viscoplasticity. This implies a time-delayed inelastic response of the material, which is accordingly referred to as rate-sensitive or time-dependent.

The observed behaviour of real materials is generally time dependent; that is the stress response always depends on the rate of loading and the time scale considered. In soil mechanics, the mechanical behaviour of granular materials is usually assumed as time-independent. Experimental evidence (e.g. di Prisco and Imposimato, (1996), Pham Van Bang et al. (2007)) however, shows that the mechanical response of granular material is rapid but not instantaneous. Microfabric rearrangement, associated with the development of irreversible deformations, takes place with time which depends on the type of the material taken into consideration and may vary between few minutes (sand) and several days (clay) (di Prisco and Imposimato, (1996)). These experimental observations motivate the application of viscoplasticity in such materials on a physical basis and led to consider viscoplasticity as an appropriate constitutive framework and as a tool for the theoretical interpretation of several unstable phenomena (e.g. Oka et al., (1994), di Prisco and Imposimato (1997)).

Apart from the physical soundness, the use of viscoplasticity is supported by a further numerical motivation, that it can be viewed as a regularization technique of the elasto-plastic ill-posed problem. The occurrence of localization raises the problem of the objectivity of numerical results and in viscoplastic model a length scale emerges (although the constitutive equations do not explicitly contain a parameter with the dimension of length) that mitigates the mesh dependence effects arising from such a bifurcation response.

Nowadays, the main approaches for modelling rate effects are those proposed by Perzyna (1966) and Duvaut and Lion (1972). A third model, the so-called consistency model has been more recently proposed in Wang et al. (1997) and Heeres et al. (2002). At variance with standard elasto-plasticity, both Perzyna's and Duvaut-Lion's models allow the stress point to lie outside the yield locus, whereas in the former such states are not permitted. Therefore, the well-known Kuhn-Tucker conditions are not applicable in viscoplastic models. By abolishing the consistency rule, the yield function may be positive or negative without any constraint. If the external loading remains constant, the stresses return to the yield surface as a function of time and because of this feature viscoplastic theories are often called overstress laws, Figure 3.1. The two approaches basically differ in the definition of the viscoplastic strain rate they adopt. Conversely, consistency models maintain the usual consistency constraint for the stress point, while the material time-sensitiveness is modelled by assuming a rate-dependent evolution of the plasticity locus.

Henceforth, Perzyna's and Duvaut-Lion's viscoplasticity will be considered and the main features in terms of analytical formulation and numerical treatment are summarized in Section 3.3 and 3.4, respectively. In Section 3.5 a non-local viscoplastic approach of Perzyna is explored to deal with weakly rate sensitive materials, where viscoplasticity is not sufficient to suit numerical requirements. After a brief introduction on the key points of non-local method, this section reviews the non-local formulation and its FEM implementation. The merits and drawbacks of each regularization model are summarized in the last section of this chapter.

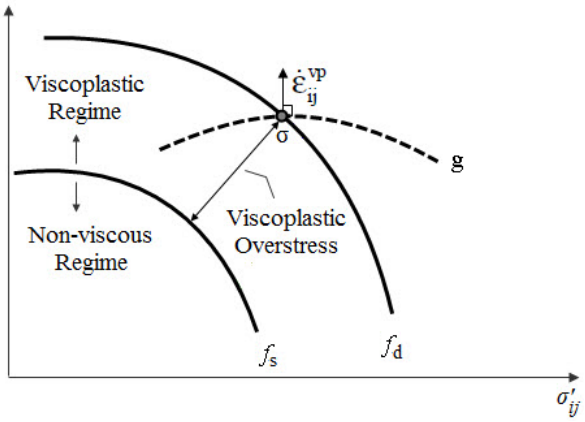

Figure 3.1: The concept of overstress viscoplastic model (from [94]).

3.2 Yield Criterion for Granular Soil

The elasto-viscoplastic behaviour of soil is described by the classical rate-dependent theory for geometrically linear problems. The yield function restricting the generalized effective stress is assumed in the form of Drucker-Prager to take into account the dilatant/contractant behaviour of sands:

$$f\left(\mathrm{p}',\mathbf{s},\xi\right)=3\alpha_f \mathrm{p}'+\left\|\mathbf{s}\right\|-\beta_f\sqrt{\frac{2}{3}}\left[\mathrm{c}+\mathrm{h}\xi^{\mathrm{vp}}\right] \tag{3.1}$$

In Equation (3.1) p' = (1/3)tr**σ'** is the mean pressure, ||**s**|| is the norm of the deviatoric part of the stress tensor, c is the suction dependent cohesion (Equation (3.2)), α_f and β_f are two material parameters related to the friction angle, φ, of the soil defined by Equation (3.3), h (Figure 3.2) is the hardening (h > 0) or softening (h < 0) modulus and ξ^{vp} is the equivalent viscoplastic strain (with the superscript p, instead of vp, stands for the equivalent plastic strain in elastoplasticity i.e. ξ^{p}).

According to Fredlund et al. (1978), c is the intercept of the extended Mohr-Coulomb failure envelope with the shear stress axis at a specific matric suction and zero net normal stress and it can be referred to as the 'total cohesion intercept':

$$\mathrm{c}=\mathrm{c}_0+p^{\mathrm{c}}\cdot\tan\varphi^{\mathrm{b}} \tag{3.2}$$

where c_0 is the apparent saturated cohesion, p^c is the capillary pressure (or matric suction) and φ^b is the angle of friction accounting for the matric suction contribution to the shear strength. It is

remarkable that at very high suctions as the soil becomes completely dry, the increase of apparent cohesion due to suction tends to zero (Escario and Juca (1989)).

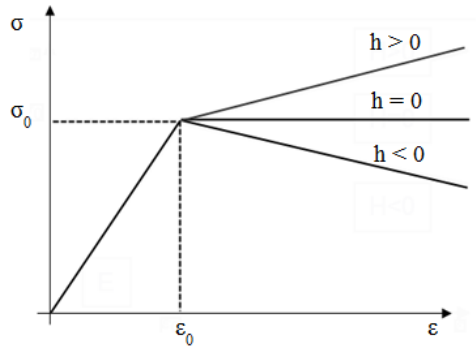

Figure 3.2: Different types of material behaviour: hardening, perfectly plastic and softening behaviour (post bifurcation response).

The flow rule is of non-associated type and takes the direction of the plastic strain rate to be normal to the plastic flow potential function. A non-associated flow rule has been shown to be capable of fitting experimental data more accurately than an associative model, which generally overpredict the amount of plastic dilatation, and therefore is adopted here.

The plastic potential function, g (p',**s**,ξ), has the same expression as for the yield function (Equation (3.1)) but with the dilatancy angle, ψ, substituting the friction angle, φ, in Equation (3.3).

$$\alpha_f = 2\frac{\sqrt{2/3}\sin\varphi}{3-\sin\varphi} \quad , \quad \beta_f = 2\frac{6\cos\varphi}{3-\sin\varphi} \tag{3.3}$$

Of course, there is the possibility of having the same parameters for α_f, β_f and α_g, β_g, encompassing in such a way also the case of an associated flow rule.

The Drucker–Prager yield criterion is a simple modification of the J2 von Mises criterion, in which the hydrostatic stress component is also included to introduce pressure-sensitivity. The yield surface in the principal stress space is represented by a circular cone around the hydrostatic axis, Figure 3.3.

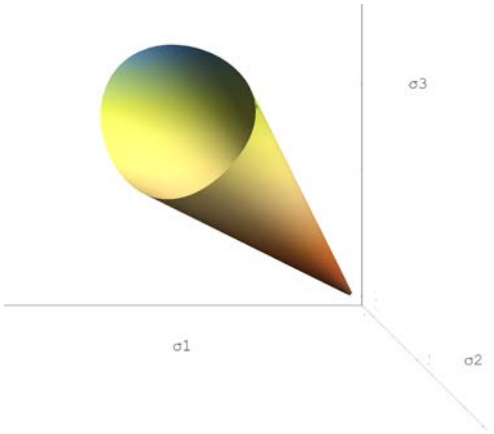

Figure 3.3: Drucker-Prager yield surface.

In the following, direct notation is adopted and more information on the adopted convention can be found in **Nomenclature**.

3.3 Elasto-Viscoplastic Model of Perzyna

A widespread strategy to include rate-dependent plastic material behaviour in a continuum mechanical model is the approach suggested by Perzyna in the middle of 60s of the last century. The mathematical structure of the viscoplastic constitutive equations can be easily explained by means of a one-dimensional treatment using the rheological model in Figure 3.4.

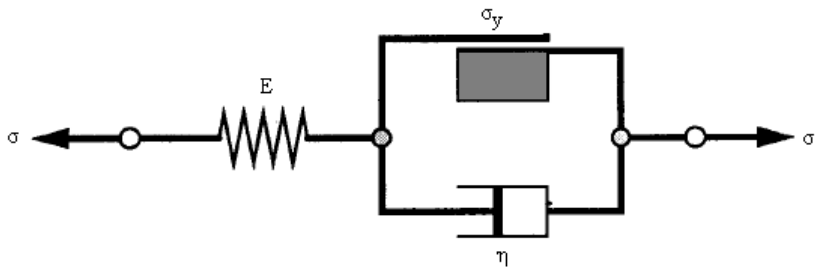

Figure 3.4: Rheological model for one-dimensional viscoplastic solid [140].

The model consists of a spring with elastic constant E, which is serially connected to the inelastic part. The inelastic part contains a dashpot with constant η and a coulombic frictional device with constant σ_y. Let σ be the applied stress on the device, and let ε be the total strain. As in rate-independent plasticity we assume the additive decomposition of the total strain:

$$\varepsilon = \varepsilon^{e} + \varepsilon^{vp} \tag{3.4}$$

where ε^{e} is the strain in the spring and ε^{vp} is the viscoplastic strain in the inelastic element, so that:

$$\sigma = E\varepsilon^{e} = E\left(\varepsilon - \varepsilon^{vp}\right) \tag{3.5}$$

As in standard plasticity the solid remains elastic when the stress σ is smaller than the absolute value of the yield stress σ_y. Hence, the loading function is defined as:

$$f\left(\sigma\right) = \left|\sigma\right| - \sigma_{y} \tag{3.6}$$

The extra stress, σ_{ex}, that may occur and can only be carried by the dashpot, is given as:

$$\sigma_{ex} = \left\{\begin{matrix} \sigma - \sigma_{y} & \text{if } \sigma \geq \sigma_{y} \\ \sigma + \sigma_{y} & \text{if } \sigma \leq -\sigma_{y} \end{matrix}\right\} = \left(\left|\sigma\right| - \sigma_{y}\right)\text{sign}\left(\sigma\right) \tag{3.7}$$

The daspot reacts according to the viscous relation:

$$\sigma_{ex} = \eta\dot{\varepsilon}^{vp} \tag{3.8}$$

in which η is the viscosity parameter. We can rewrite Equation (3.8) with Equation (3.7) which yields:

$$\dot{\varepsilon}^{vp} = \frac{1}{\eta} f\left(\sigma\right)\text{sign}\left(\sigma\right) \quad \text{if} \quad f\left(\sigma\right) \geq 0 \tag{3.9}$$

Equation (3.9) is the one-dimensional viscoplastic constitutive equation of the Perzyna type. Instead of a viscosity parameter η we can define a time constant $\tau = \eta / E$. One can refer to τ as the relaxation time of the model and its physical significance is illustrated in the example (relaxation test) below.

At time $t = 0$ an instantaneous strain ε_0, which is held constant throughout time, is applied on the device in Figure 3.4. The strain jump is chosen such that $\varepsilon_0 > \sigma_y / E$ and viscoplasticity is initiated. The stress $\sigma_0 = E\varepsilon_0$ at $t = 0$ is larger than the yield stress. To compute the stress history, we need to integrate the constitutive model as follows.

The rate form of Equation (3.5) reads:

$$\dot{\sigma} = E\left(\dot{\varepsilon} - \dot{\varepsilon}^{vp}\right) \tag{3.10}$$

substituting $\tau = \eta / E$ and from Equation (3.9) results in:

$$\dot{\varepsilon}^{vp} = \frac{1}{\tau} E^{-1}\left(\sigma - \sigma_y\right) \quad \text{if} \quad \sigma \geq \sigma_y \tag{3.11}$$

Combining Equations (3.10) and (3.11) gives:

$$\dot{\sigma} + \frac{1}{\tau}\sigma = E\dot{\varepsilon} + \frac{1}{\tau}\sigma_y \tag{3.12}$$

A closed-form solution of the Equation (3.12) can be obtained using the integrating factor method.

Assuming as integrating factor the $e^{t/\tau}$ and since in this relaxation test $\dot{\varepsilon}(t) = 0$ one obtains:

$$\sigma(t) = \left(E\varepsilon_0 - \sigma_y\right)e^{-t/\tau} + \sigma_y \tag{3.13}$$

The stress response is plotted in Figure 3.5. The material data are as follows: Young's modulus E = 1000 N/mm^2, σ_y = 1 N/mm^2, the imposed strain is $\varepsilon_0 = 0.0015$ and varying the relaxation time τ. The absolute time t can be regarded as short or long when compared to τ. So, the ratio of the viscosity η in the dashpot over the stiffness E in the spring is therefore called the relaxation time.

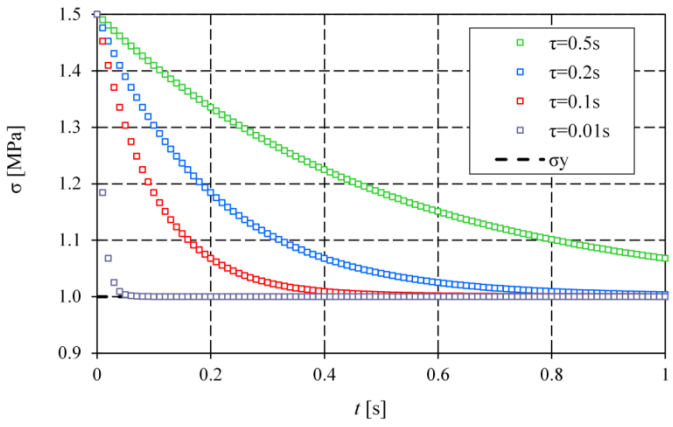

Figure 3.5: Relaxation test: stress response with varying relaxation time.

Next, the extension to three-dimensional model is treated along with some algorithmic aspects concerning its numerical implementation.

3.3.1 Analytical Formulation in Rate Form

In the representation of stress and strain states, use will be made of the following invariant quantities:

$$p' := \frac{1}{3}\mathrm{tr}(\boldsymbol{\sigma}') \qquad q := \sqrt{\frac{3}{2}}\|\mathbf{s}\| \tag{3.14}$$

where p' is the mean pressure, q the deviatoric stress and **s** is the deviatoric part of the stress tensor:

$$\mathbf{s} := \boldsymbol{\sigma}' - \frac{1}{3}\mathrm{tr}(\boldsymbol{\sigma}')\mathbf{1} \tag{3.15}$$

and:

$$\varepsilon_v := \boldsymbol{\varepsilon} : \mathbf{1} \quad \varepsilon_s := \sqrt{\frac{2}{3}}\|\mathbf{e}\| \quad \dot{\varepsilon}_v := \dot{\boldsymbol{\varepsilon}} : \mathbf{1} \quad \dot{\varepsilon}_s := \sqrt{\frac{2}{3}}\|\dot{\mathbf{e}}\| \tag{3.16}$$

where $\boldsymbol{\varepsilon}$ is the strain tensor, ε_v the volumetric strain, ε_s the deviatoric strain and **e** is the deviatoric part of the strain tensor:

$$\mathbf{e} := \boldsymbol{\varepsilon} - \frac{1}{3}\mathrm{tr}(\boldsymbol{\varepsilon})\mathbf{1}, \quad \dot{\mathbf{e}} := \dot{\boldsymbol{\varepsilon}} - \frac{1}{3}\mathrm{tr}(\dot{\boldsymbol{\varepsilon}})\mathbf{1} \tag{3.17}$$

with **1** being the second order identity tensor.

Analogous to the additive decomposition in elastoplasticity, the total strain rate in an elasto-viscoplastic material is decomposed into an elastic ($\boldsymbol{\varepsilon}^e$) and a viscoplastic part ($\boldsymbol{\varepsilon}^{vp}$):

$$\dot{\boldsymbol{\varepsilon}} = \dot{\boldsymbol{\varepsilon}}^e + \dot{\boldsymbol{\varepsilon}}^{vp} \tag{3.18}$$

where the superimposed dot denotes time derivative. Considering linear elasticity (which is also adopted in the Duvaut-lions model and in non-local approach as presented in the following Sections 3.4 and 3.5), the stress rate is related to the strain rate via the following constitutive relation:

$$\dot{\boldsymbol{\sigma}}' = \mathbf{D}^e : \left(\dot{\boldsymbol{\varepsilon}} - \dot{\boldsymbol{\varepsilon}}^{vp}\right) \tag{3.19}$$

where double dots " : " denote the doubly contracted tensor product and $\mathbf{D}^e$ is the fourth-order elasticity tensor, which can be formulated in general form as:

$$\mathbf{D}^e = K\mathbf{1}\otimes\mathbf{1} + 2G\mathbf{I}_{dev} \tag{3.20}$$

In Equations (3.20), $\mathbf{I}_{dev}$ is the fourth-order deviatoric tensor (defined in **Nomenclature)**, K stands for the bulk modulus, while G denotes the shear modulus.

Their connections to the Young's modulus, E, and to the Poisson's ratio, ν, are:

$$K = \frac{E}{3(1-2\nu)} \qquad G = \frac{E}{2(1+\nu)} \tag{3.21}$$

In the viscoplastic model according to Perzyna, the viscoplastic strain rate is determined by the gradient of a plastic potential function calculated at the current stress point and is directly linked to the yield function through the viscous nucleus:

$$\dot{\boldsymbol{\varepsilon}}^{vp} = \gamma \Phi(f) \frac{\partial g}{\partial \boldsymbol{\sigma}'} \tag{3.22}$$

with f and g being the yield function and the plastic potential respectively (associative flow is invoked by f = g), Φ the viscous nucleus and γ the "fluidity parameter" which depends on the viscosity, η, of the material ($\gamma=1/\eta$) and can be constant or a function of the stress or strain rate.

The positive constitutive parameter γ influences the strain rate and consequently the rapidity with which the asymptotic strain value is reached. In Figure 3.6 some axial strain-time curves, associated to the same instantaneous axial stress increments but to different γ values, are schematically drawn. By increasing the γ value, the initial curve slopes become steeper: when $\gamma \rightarrow \infty$ the mathematical response is instantaneous.

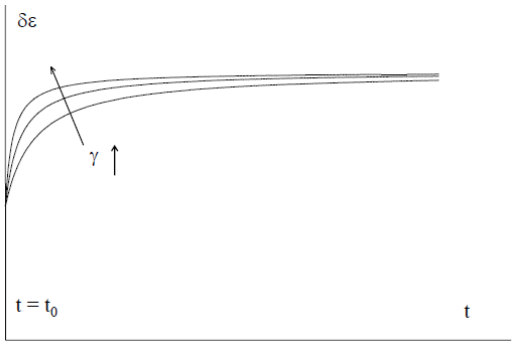

Figure 3.6: Theoretical material's strain response obtained by introducing different values of γ [45].

Moreover, the time dependency is introduced by modifying the flow rule and by abolishing the consistency rule. The plastic potential defines the direction of the viscoplastic strain rate tensor while the yield function influences its modulus by means of the viscous nucleus.

The viscous nucleus quantifies the "overstress" (i.e. $f(\boldsymbol{\sigma}') > 0$) and the choice of its form determines the regularizing effect of the viscoplastic model. A linear relation for the viscous nucleus is obviously the simplest and probably quite adequate to describe the behaviour of many materials and therefore the following linear form will be assumed:

$$\Phi = \left\langle \left(\frac{f}{f_0} \right) \right\rangle^N \tag{3.23}$$

In Equation (3.23), f_0 is introduced as a fixed reference value making the viscous nucleus dimensionless and N is a calibration parameter, $N \geq 1$ (herein N = 1 for the sake of simplicity). In the literature (e.g. Desai and Zhang (1987), Sluys (1992), Wang et al. (1997), Dìez et al. (2000) etc.), f_0 is commonly chosen as the initial yield stress however the normalization of the yield locus should be

done with respect to the isotropic mean pressure when dealing with frictional (cohesionless) materials (e.g. Pisanò (2011)). In above equation, " $< \bullet >$ " are the McCauley brackets, such that:

$$\left\langle \Phi\left(f\right)\right\rangle = \begin{cases} \Phi\left(f\right) & \text{if } \Phi\left(f\right) \geq 0 \\ 0 & \text{if } \Phi\left(f\right) < 0 \end{cases} \tag{3.24}$$

When $f < 0$ only elastic strains are possible, otherwise both elastic and viscoplastic effects are exhibit. Moreover, according to Simo (1989), the overstress function Φ must fulfill the following conditions so that a rate-independent elastoplastic model is recovered if viscosity reaches zero:

$$\begin{aligned} &\Phi \text{ is continuous in } \left[0,\infty\right], \\ &\Phi \text{ is convex in } \left[0,\infty\right], \\ &\Phi\left(0\right) = 0 \end{aligned} \tag{3.25}$$

It is also remarkable that in the viscoplastic approach the plastic multiplier, λ, in the flow rule (Equation (3.22)), is directly given by Equation (3.26) instead of the Kuhn-Tucker conditions; thus it allows for overstress, the amount of which depends on the values chosen for the viscoplastic material parameters (η and N).

$$\lambda = \gamma \Phi\left(f\right) \tag{3.26}$$

Now, invoking the viscoplastic model of Perzyna with the plastic potential function and applying the chain rule of partial differentiation, the flow rule specifies to:

$$\dot{\boldsymbol{\varepsilon}}^{\mathrm{vp}} = \gamma \Phi\left(f\right) \left\{ \frac{\partial \mathrm{g}}{\partial \mathrm{p}'} : \frac{\partial \mathrm{p}'}{\partial \boldsymbol{\sigma}'} + \frac{\partial \mathrm{g}}{\partial \mathbf{s}} : \frac{\partial \mathbf{s}}{\partial \boldsymbol{\sigma}'} \right\} \tag{3.27}$$

and leads to:

$$\dot{\boldsymbol{\varepsilon}}^{\mathrm{vp}} = \lambda \left\{ \alpha_{\mathrm{g}} \mathbf{1} + \mathbf{n} \right\} \tag{3.28}$$

where $\mathbf{n} = \mathbf{s} / \|\mathbf{s}\|$ is the unit normal field.

Accordingly, the equivalent viscoplastic strain rate is defined in terms of the viscoplastic strain rate, as follows:

$$\dot{\xi}^{\mathrm{vp}} = \left\| \dot{\boldsymbol{\varepsilon}}^{\mathrm{vp}} \right\| \tag{3.29}$$

and considered the definition of the Euclidean norm of a second order tensor, one obtains:

$$\dot{\xi}^{\mathrm{vp}} = \gamma \Phi\left(f\right) \left\{ \left(\alpha_{\mathrm{g}} \mathbf{1} + \mathbf{n} \right) : \left(\alpha_{\mathrm{g}} \mathbf{1} + \mathbf{n} \right) \right\}^{1/2} = \gamma \Phi\left(f\right) \sqrt{3\alpha_{\mathrm{g}} + 1} \tag{3.30}$$

3.3.2 Integration Algorithm

To illustrate the computational implementation of the viscoplastic regularization procedure discussed previously, this section presents the algorithm for the viscoplastic model of Perzyna combined with a Drucker-Prager yield surface (assuming non-associated flow rule and linear isotropic

hardening). In Table 3.1 the numerical algorithm for Perzyna's viscoplastic model is outlined, highlighting the essential steps of the numerical implementation.

3.3.2.1 Fully Implicit Backward Euler Scheme

In displacement-based finite element method the update of stresses takes place at Gauss points. Assuming that at time t_n the value of total and viscoplastic strains is known, the stress state is known as well. Then suppose that an increment in total strain ($\Delta\varepsilon$) is given which drives the state to time $t_{n+1} = t_n + \Delta t$. The incremental strain, $\Delta\varepsilon = \varepsilon_{n+1} - \varepsilon_n$, is used to update the stress at time t_{n+1}.

A trial and error strain driven process is adopted, in which an elastic trial step is first assumed by freezing the viscoplastic flow (Equation (3.31)) to distinguish between elastic and viscoplastic loading.

$$\boldsymbol{\varepsilon}_{n+1}^{vp,trial} = \boldsymbol{\varepsilon}_n^{vp} \qquad \xi_{n+1}^{vp,trial} = \xi_n^{vp} \tag{3.31}$$

Then, the trial stress (Equations (3.32) and (3.33)) is tested to see if it is inside or outside the yield surface (Equation (3.34)).

$$p'^{tr}_{n+1} = p'_n + Ktr\Delta\boldsymbol{\varepsilon}^{el,tr}_{n+1} = Ktr(\boldsymbol{\varepsilon}_{n+1} - \boldsymbol{\varepsilon}^{vp}_n) \tag{3.32}$$

$$\mathbf{s}^{tr}_{n+1} = \mathbf{s}_n + 2G\Delta\mathbf{e}^{el,tr}_{n+1} = 2G(\mathbf{e}_{n+1} - \mathbf{e}^{vp}_n) \tag{3.33}$$

$$f^{tr}_{n+1} = 3\alpha_f p'^{tr}_{n+1} + \left\|\mathbf{s}^{tr}_{n+1}\right\| - \beta_f\sqrt{2/3}\left(c + h\xi^{vp}_n\right) \tag{3.34}$$

If it falls within or is on the yield surface the process is elastic and the trial state $(\bullet)^{tr}$ represents the actual final state of the material. Otherwise, the process is viscoplastic and the viscoplastic strain increment is computed by integrating Equation (3.28) with the unconditionally stable Backward Euler scheme:

$$\boldsymbol{\varepsilon}^{vp}_{n+1} = \boldsymbol{\varepsilon}^{vp}_n + \Delta\lambda_{n+1}\left\{\alpha_g\mathbf{1} + \mathbf{n}_{n+1}\right\} \tag{3.35}$$

The unit normal $\mathbf{n}_{n+1}$ is determined exclusively in terms of the trial elastic stress (Simo and Hughes (1998)):

$$\mathbf{n}_{n+1} = \frac{\mathbf{s}_{n+1}}{\left\|\mathbf{s}_{n+1}\right\|} = \frac{\mathbf{s}^{tr}_{n+1}}{\left\|\mathbf{s}^{tr}_{n+1}\right\|} \tag{3.36}$$

In the absence of the consistency rule, the inelastic multiplier is directly computed as:

$$\Delta\lambda_{n+1} = \frac{f^{tr}_{n+1}}{\frac{\eta f_0}{\Delta t} + 9\alpha_f\alpha_g K + 2G + \sqrt{\frac{2}{3}}\beta_f h\sqrt{3\alpha_g^2 + 1}} \tag{3.37}$$

Subsequently, from the knowledge of $\Delta\lambda_{n+1}$, the components of the stress tensor and the equivalent viscoplastic strain can be updated:

$$p'_{n+1} = p'^{tr}_{n+1} - 3K\Delta\lambda_{n+1}\alpha_g \tag{3.38}$$

$$\mathbf{s}_{n+1} = \mathbf{s}^{tr}_{n+1} - 2G\Delta\lambda_{n+1}\mathbf{n}_{n+1} \tag{3.39}$$

$$\boldsymbol{\sigma}'_{n+1} = p'_{n+1}\mathbf{1} + \mathbf{s}_{n+1} = \boldsymbol{\sigma}'^{tr}_{n+1} - 3K\Delta\lambda_{n+1}\alpha_g\mathbf{1} - 2G\Delta\lambda_{n+1}\mathbf{n}_{n+1} \tag{3.40}$$

$$\xi^{vp}_{n+1} = \xi^{vp}_{n} + \Delta\lambda_{n+1}\sqrt{\left(3\alpha_g^2 + 1\right)} \tag{3.41}$$

Finally, the algorithmic procedure is completed with the derivation of the algorithmic (consistent) viscoplastic tangent modulus, which is presented in the next section.

It is noteworthy that, by selecting $\alpha_f = \alpha_g = 0$ and $\beta_f = 1$ the algoritmh reduces to the one of the von Mises model reported in Simo and Hughes (1998).

Table 3.1: Numerical algorithm for local Perzyna model.

1. Compute trial elastic state

$p'^{tr}_{n+1} = Ktr(\boldsymbol{\varepsilon}_{n+1} - \boldsymbol{\varepsilon}^{vp}_{n})$; $\mathbf{s}^{tr}_{n+1} = 2G(\mathbf{e}_{n+1} - \mathbf{e}^{vp}_{n})$

2. Check viscoplastic flow potential

$$f^{tr}_{n+1} = 3\alpha_f p'^{tr}_{n+1} + \left\|\mathbf{s}^{tr}_{n+1}\right\| - \beta_f\sqrt{2/3}\left(c + h\xi^{vp}_{n}\right)$$

IF: $f^{tr}_{n+1} \le 0 \rightarrow$ elastic step $\rightarrow$ Set $(\bullet)_{n+1} = (\bullet)^{tr}_{n+1}$ & EXIT

else go to 3

3. Compute $\Delta\lambda_{n+1}$: $\Delta\lambda_{n+1} = \dfrac{f^{tr}_{n+1}}{\dfrac{\eta f_0}{\Delta t} + 9\alpha_f\alpha_g K + 2G + \sqrt{\dfrac{2}{3}}\beta_f h\sqrt{3\alpha_g^2 + 1}}$

4. Update viscoplastic strain and stress

$$\boldsymbol{\varepsilon}^{vp}_{n+1} = \boldsymbol{\varepsilon}^{vp}_{n} + \Delta\lambda_{n+1}\left(\alpha_g\mathbf{1} + \mathbf{n}_{n+1}\right)$$

$$\xi^{vp}_{n+1} = \xi^{vp}_{n} + \Delta\lambda_{n+1}\sqrt{\left(3\alpha_g^2 + 1\right)}$$

$$\boldsymbol{\sigma}'_{n+1} = p'_{n+1}\mathbf{1} + \mathbf{s}_{n+1}$$

5. Compute consistent viscoplastic tangent moduli, → Eq. (3.47)

3.3.2.2 Consistent Tangent Operator

Consistent tangent matrix, which leads to faster convergence rate in case of Newton–Raphson algorithms (Simo and Taylor (1985)), is derived for the viscoplastic formulation. In viscoplasticity, '*the use of consistent tangent moduli is not only desirable but also necessary*' as remarked in Ju (1990). This necessity stems from the fact that in viscoplastic models a continuum tangent stiffness operator does not exist, as a result of abolishing the consistency condition which prevents a direct incremental relationship to be established between the stress and the total strain increments.

By differentiating the algorithm discussed in the previous section, one obtains the algorithmic consistent viscoplastic tangent moduli. In particular, the linearization of the computed Cauchy stress tensor gives:

$$\mathbf{C}^{\mathrm{vp}}_{\mathrm{n+1}} = \frac{\partial \boldsymbol{\sigma}'_{\mathrm{n+1}}}{\partial \boldsymbol{\varepsilon}_{\mathrm{n+1}}} = \frac{\partial \boldsymbol{\sigma}'_{\mathrm{n+1}}}{\partial \boldsymbol{\varepsilon}^{\mathrm{el,tr}}_{\mathrm{n+1}}} \tag{3.42}$$

and using Equation (3.40), one obtains:

$$\mathbf{C}^{\mathrm{vp}}_{\mathrm{n+1}} = \frac{\partial \boldsymbol{\sigma}'^{\,\mathrm{tr}}_{\mathrm{n+1}}}{\partial \boldsymbol{\varepsilon}^{\mathrm{el,tr}}_{\mathrm{n+1}}} - 3\mathrm{K}\Delta\lambda_{\mathrm{n+1}}\alpha_{\mathrm{g}}\mathbf{1}\otimes\frac{\partial \Delta\lambda_{\mathrm{n+1}}}{\partial \boldsymbol{\varepsilon}^{\mathrm{el,tr}}_{\mathrm{n+1}}} - 2\mathrm{G}\mathbf{n}_{\mathrm{n+1}}\otimes\frac{\partial \Delta\lambda_{\mathrm{n+1}}}{\partial \boldsymbol{\varepsilon}^{\mathrm{el,tr}}_{\mathrm{n+1}}} - 2\mathrm{G}\Delta\lambda_{\mathrm{n+1}}\otimes\frac{\partial \mathbf{n}_{\mathrm{n+1}}}{\partial \boldsymbol{\varepsilon}^{\mathrm{el,tr}}_{\mathrm{n+1}}} \tag{3.43}$$

in which the partial derivatives are defined as follows:

$$\frac{\partial \boldsymbol{\sigma}^{\mathrm{tr}}_{\mathrm{n+1}}}{\partial \boldsymbol{\varepsilon}^{\mathrm{el,tr}}_{\mathrm{n+1}}} = \mathrm{K}\mathbf{1}\otimes\mathbf{1} + 2\mathrm{G}\mathbf{I}_{\mathrm{dev}} = \mathbf{D}^{\mathrm{e}} \tag{3.44}$$

$$\frac{\partial \Delta\lambda_{\mathrm{n+1}}}{\partial \boldsymbol{\varepsilon}^{\mathrm{el,tr}}_{\mathrm{n+1}}} = \frac{1}{\mathrm{d}}\frac{\partial f^{\mathrm{tr}}_{\mathrm{n+1}}}{\partial \boldsymbol{\varepsilon}^{\mathrm{el,tr}}_{\mathrm{n+1}}} = \frac{1}{\mathrm{d}}\left\{3\alpha_f\mathrm{K}\mathbf{1} + 2\mathrm{G}\mathbf{n}_{\mathrm{n+1}}\right\} \tag{3.45}$$

$$\begin{aligned}\frac{\partial \mathbf{n}_{\mathrm{n+1}}}{\partial \boldsymbol{\varepsilon}^{\mathrm{el,tr}}_{\mathrm{n+1}}} = \frac{\partial \mathbf{n}_{\mathrm{n+1}}}{\partial \mathbf{s}^{\mathrm{tr}}_{\mathrm{n+1}}} : \frac{\partial \mathbf{s}^{\mathrm{tr}}_{\mathrm{n+1}}}{\partial \boldsymbol{\varepsilon}^{\mathrm{el,tr}}_{\mathrm{n+1}}} &= \frac{1}{\left\|\mathbf{s}^{\mathrm{tr}}_{\mathrm{n+1}}\right\|}\left\{\mathbf{I} - \mathbf{n}_{\mathrm{n+1}}\otimes\mathbf{n}_{\mathrm{n+1}}\right\} : 2\mathrm{G}\mathbf{I}_{\mathrm{dev}} \\ &= \frac{2\mathrm{G}}{\left\|\mathbf{s}^{\mathrm{tr}}_{\mathrm{n+1}}\right\|}\mathbf{I}_{\mathrm{dev}} - \frac{2\mathrm{G}}{\left\|\mathbf{s}^{\mathrm{tr}}_{\mathrm{n+1}}\right\|}\mathbf{n}_{\mathrm{n+1}}\otimes\mathbf{n}_{\mathrm{n+1}}\end{aligned} \tag{3.46}$$

The consistent viscoplastic tangent operator takes the final form:

$$\begin{aligned}\mathbf{C}^{\mathrm{vp}}_{\mathrm{n+1}} = &\left(1 - \frac{9\alpha_{\mathrm{g}}\alpha_f\mathrm{K}}{\mathrm{d}}\right)\mathrm{K}\mathbf{1}\otimes\mathbf{1} + 2\mathrm{G}\mathbf{I}_{\mathrm{dev}}\left(1 - \frac{2\mathrm{G}\Delta\lambda_{\mathrm{n+1}}}{\left\|\mathbf{s}^{\mathrm{tr}}_{\mathrm{n+1}}\right\|}\right) - \frac{6\mathrm{KG}\alpha_{\mathrm{g}}}{\mathrm{d}}\mathbf{1}\otimes\frac{\mathbf{s}_{\mathrm{n+1}}}{\left\|\mathbf{s}_{\mathrm{n+1}}\right\|} \\ &- \frac{6\mathrm{KG}\alpha_f}{\mathrm{d}}\frac{\mathbf{s}_{\mathrm{n+1}}}{\left\|\mathbf{s}_{\mathrm{n+1}}\right\|}\otimes\mathbf{1} - 4\mathrm{G}^2\left(\frac{1}{\mathrm{d}} - \frac{\Delta\lambda_{\mathrm{n+1}}}{\left\|\mathbf{s}^{\mathrm{tr}}_{\mathrm{n+1}}\right\|}\right)\frac{\mathbf{s}_{\mathrm{n+1}}}{\left\|\mathbf{s}_{\mathrm{n+1}}\right\|}\otimes\frac{\mathbf{s}_{\mathrm{n+1}}}{\left\|\mathbf{s}_{\mathrm{n+1}}\right\|}\end{aligned} \tag{3.47}$$

In Equations (3.45) and (3.47) $\mathrm{d} = \frac{\eta f_0}{\Delta \mathrm{t}} + 9\alpha_{\mathrm{g}}\alpha_f\mathrm{K} + 2\mathrm{G} + \sqrt{\frac{2}{3}}\beta_f \mathrm{h}\sqrt{3\alpha_{\mathrm{g}}^2 + 1}$ and it can be inferred that the viscoplastic modulus tends to the elastoplastic limit as viscosity (η) tends to zero.

3.4 Elasto-Viscoplastic Model of Duvaut-Lions

A different viscoplastic model, which its elaboration is more closely connected to the rate-independent plasticity theory, has been proposed by Duvaut- Lions on 1972.

A strong advantage of the Duvaut-Lions model is that once it has been implemented in a FEM code it can then be used for any existing elastoplastic models. This feature arises naturally from the dependence of the viscoplastic solution on the existence of the elastoplastic one.

Furthermore, Duvaut-Lions model becomes more attractive when a yield surface with an apex or a non-smooth one is considered, as it avoids the difficulties encountered by the Perzyna-type model in such non-smooth corner regions (see, e.g., Simo et al. (1988b), Ju (1990)). In fact, as the viscosity parameter approaches zero, the Perzyna type models do not reduce to the rate-independent plasticity formulation in the case of non-smooth multi-surface models. To remedy this shortcoming an alternative viscoplastic formulation was proposed by Duvaut-Lions.

3.4.1 Evolution Equations

The Duvaut-Lions model is based on the difference in response between the viscoplastic material and the rate-independent one. This is in contrast with the model proposed by Perzyna in which the value of the yield surface determines the viscoplastic strain rate.

In the case of the Duvaut-Lions formulation the viscoplastic strain rate is related to the difference between the current viscoplastic stress, $\boldsymbol{\sigma}'$, and the contribution of the elastoplastic material, $\overline{\boldsymbol{\sigma}}'$, which can be viewed as a projection of the current stress to the yield surface (also called as inviscid back-bone model (Sluys (1992)):

$$\dot{\boldsymbol{\varepsilon}}^{\mathrm{vp}} = \frac{1}{\tau}\left[\mathbf{D}^{\mathrm{e}}\right]^{-1}\left(\boldsymbol{\sigma}' - \overline{\boldsymbol{\sigma}}'\right) \tag{3.48}$$

In a similar fashion the hardening rate is given as:

$$\dot{\mathrm{q}} = -\frac{1}{\tau}\left(\mathrm{q} - \overline{\mathrm{q}}\right) \tag{3.49}$$

where the overbarred quantities represent solutions of the inviscid elastoplastic problem. The quantities q consern internal hardening variables associated with the grotwh of the yield surface.

In Equations (3.48) and (3.49), τ is the relaxation time of the material and, in general, is strain and strain-rate dependent.

3.4.2 Derivation of Duvaut-Lions Algorithm

The viscoplastic strain rate, Equation (3.48), is time discretized through the Backward Euler algorithm:

$$\Delta\boldsymbol{\varepsilon}^{\mathrm{vp}}_{\mathrm{n+1}} = \frac{\Delta t}{\tau}\left[\mathbf{D}^{\mathrm{e}}\right]^{-1}\left(\boldsymbol{\sigma}'_{\mathrm{n+1}} - \overline{\boldsymbol{\sigma}}'_{\mathrm{n+1}}\right) \tag{3.50}$$

Similarly, the hardening law is defined as:

$$\begin{aligned} q_{n+1} &= q_n + \Delta t\left(-\frac{1}{\tau}q_{n+1} + \frac{1}{\tau}\overline{q}_{n+1}\right) \\ &= q_n - \frac{\Delta t}{\tau}q_{n+1} + \frac{\Delta t}{\tau}\overline{q}_{n+1} \\ &= \frac{\tau}{\tau+\Delta t}q_n + \frac{\Delta t}{\tau+\Delta t}\overline{q}_{n+1} \end{aligned} \tag{3.51}$$

Then, the tangential stiffness relation (Equation (3.19) is recalled:

$$\begin{aligned} \Delta\boldsymbol{\sigma}'_{n+1} &= \mathbf{D}^e : \left(\Delta\boldsymbol{\varepsilon}_{n+1} - \Delta\boldsymbol{\varepsilon}^{vp}_{n+1}\right) \\ &= \mathbf{D}^e : \Delta\boldsymbol{\varepsilon}_{n+1} - \frac{\Delta t}{\tau}\mathbf{D}^e : \left[\mathbf{D}^e\right]^{-1}\left(\boldsymbol{\sigma}'_{n+1} - \overline{\boldsymbol{\sigma}}'_{n+1}\right) \\ &= \mathbf{D}^e : \Delta\boldsymbol{\varepsilon}_{n+1} - \frac{\Delta t}{\tau}\left(\boldsymbol{\sigma}'_{n+1} - \overline{\boldsymbol{\sigma}}'_{n+1}\right) \end{aligned} \tag{3.52}$$

After some algebra one obtains the following expression for the new stress state:

$$\boldsymbol{\sigma}'_{n+1} = \frac{\tau}{\tau+\Delta t}\left(\boldsymbol{\sigma}'_n + \mathbf{D}^e\Delta\varepsilon_{n+1}\right) + \frac{\Delta t}{\tau+\Delta t}\overline{\boldsymbol{\sigma}}'_{n+1} \tag{3.53}$$

In the case of the Duvaut-Lions model the stress update is carried out in two steps. Firstly, the inviscid elastoplastic stress is computed, using a classical return mapping algorithm and then the viscoplastic update of Equations (3.50), (3.51) and (3.53) is applied (Table 3.2) . In fact as also stated by Schwer (1994), to convert an existing elastoplastic constitutive algorithm to a viscoplastic one, a simple stress update loop through the integration points is required at the end of the existing routine. After their update, both viscoplastic stress and strain are stored for each integration point, to be used in the subsequent time steps.

The algorithmic tangent operator at $t = t_{n+1}$ is given in Equation (3.54) and involves the evaluation of both the elastic and the rate-independent operators (Ju (1990)). Moreover, it indicates that in the limiting condition $\Delta t/\tau \to 0$ the viscoplastic model reduces to the elastic case, while for $\Delta t/\tau \to \infty$ to the elastoplastic one. This illustrates that in the Duvaut-Lions formulation, appropriate limiters between the time interval and the relaxation time must be taken into account to obtain objective (viscoplastic) predictions of the failure zone when dealing with strain localization problems.

$$\mathbf{C}^{vp}_{n+1} = \frac{\tau}{\tau+\Delta t}\left[\mathbf{D}^e + \frac{\Delta t}{\tau}\mathbf{D}^{ep}_{n+1}\right] \tag{3.54}$$

Herein, the elasto-viscoplastic model of Duvaut-Lions constitutes an extension of the elastoplastic version of Drucker-Prager model where a special treatment of the corner region (for the apex of the cone) was taken into account. Description of the elastoplastic model is given in the sequel for a better overview of the reader and a more comprehensive presentation can be found in Sanavia et al. (2006).

Algorithmic formulation for elastoplasticity

The plastic flow direction, based on the yield function of the Drucker-Prager elastoplasticity model, is defined by the non-associated flow rule:

$$\dot{\boldsymbol{\varepsilon}}^{\mathrm{p}} = \dot{\lambda}\left\{\alpha_{\mathrm{g}}\mathbf{1} + \mathbf{n}\right\} \tag{3.55}$$

The loading/unloading conditions can be expressed in the Kuhn-Tucker form as:

$$\dot{\lambda} \geq 0, \quad f \leq 0, \quad \dot{\lambda} f = 0 \tag{3.56}$$

The problem of the calculation of strain and stress is typically solved by an operator split into an elastic predictor and a plastic corrector.

The trial elastic state $(\bullet)^{\mathrm{tr}}$ is based on freezing the plastic flow at time t_{n+1}. If this trial state is admissible it does not violate the inequality $f^{\mathrm{tr}}_{n+1} \leq 0$ and the stress state is hence already computed. Otherwise, the return mapping or plastic corrector algorithm is applied to compute the inelastic multiplier, $\Delta\lambda_{n+1}$, satisfying the consistency condition.

$$\begin{aligned} f_{n+1} &= 3\alpha_f p'^{\mathrm{tr}}_{n+1} - 9\alpha_f\alpha_{\mathrm{g}}\mathrm{K}\Delta\lambda_{n+1} + \left\|\mathbf{s}^{\mathrm{tr}}_{n+1}\right\| - 2\mathrm{G}\Delta\lambda_{n+1} - \beta_f\sqrt{2/3}\left(\mathrm{c} + \mathrm{h}\xi^{\mathrm{p}}_{n}\right) - \Delta\lambda_{n+1}\sqrt{\frac{2}{3}}\beta_f \mathrm{h}\sqrt{3\alpha_{\mathrm{g}}^2 + 1} \\ &= f^{\mathrm{tr}}_{n+1} - \Delta\lambda_{n+1}\left(9\alpha_f\alpha_{\mathrm{g}}\mathrm{K} + 2\mathrm{G} + \sqrt{\frac{2}{3}}\beta_f \mathrm{h}\sqrt{3\alpha_{\mathrm{g}}^2 + 1}\right) \end{aligned} \tag{3.57}$$

The plastic multiplier can be derived from the consistency condition, $f_{n+1} = 0$:

$$\Delta\lambda_{n+1} = \frac{f^{\mathrm{tr}}_{n+1}}{9\alpha_f\alpha_{\mathrm{g}}\mathrm{K} + 2\mathrm{G} + \sqrt{\frac{2}{3}}\beta_f \mathrm{h}\sqrt{3\alpha_{\mathrm{g}}^2 + 1}} \tag{3.58}$$

From the knowledge of $\Delta\lambda_{n+1}$ the plastic strain is computed by the backward Euler integration of Equation (3.55):

$$\boldsymbol{\varepsilon}^{\mathrm{p}}_{n+1} = \boldsymbol{\varepsilon}^{\mathrm{p}}_{n} + \Delta\lambda_{n+1}\left\{\alpha_{\mathrm{g}}\mathbf{1} + \mathbf{n}_{n+1}\right\} \tag{3.59}$$

and the stress tensor can be updated as well:

$$\boldsymbol{\sigma}'_{n+1} = p'_{n+1}\mathbf{1} + \mathbf{s}_{n+1} \tag{3.60}$$

The method is then extended to take into account a special treatment of the corner region based on the concept of multi-surface plasticity developed in Hofstetter and Taylor (1991). It is mentioned that the return mapping algorithm developed without any special treatment of the apex region, leads to physically meaningless results (i.e. $||\mathbf{s}_{n+1}|| < 0$) for a certain range of trial elastic stress. This happens when the following relationship obtained from the updated deviatoric components of the stress tensor is violated:

$$\left\|\mathbf{s}_{n+1}\right\| = \left\|\mathbf{s}^{\mathrm{tr}}_{n+1}\right\| - 2\mathrm{G}\Delta\lambda_{n+1} \geq 0 \tag{3.61}$$

Without getting into details, violation of the abovementioned inequality and the consistency condition define the inequality for which the return mapping needs to be modified:

$$p'^{tr}_{n+1} > \frac{3\alpha_g K}{2G}\left\|\mathbf{s}^{tr}_{n+1}\right\| + \frac{\sqrt{\frac{2}{3}}\beta_f}{3\alpha_f}\left\{\frac{\left\|\mathbf{s}^{tr}_{n+1}\right\|}{2G}h\sqrt{3\alpha_g^2+1} + c + h\xi^p\right\} \tag{3.62}$$

To simplify matters, if the inequality (3.62) holds, the classical return mapping will produce a physical solution and no special treatment is needed. As soon as the inequality in (3.62) is violated, the procedure described below is followed for the update of stress and strain at each gauss point.

In this case, the stress region characterized by Equation (3.62) may be treated like a corner region in non-smooth multi-surface plasticity. To this end a second yield function f_2 is introduced in addition to Equation (3.1) as:

$$f_2\left(p',\xi\right) = 3\alpha_f p' - \beta_f\sqrt{\frac{2}{3}}\left[c + h\xi^p\right] \tag{3.63}$$

in which $\|\mathbf{s}\| = 0$ and the plastic evolution equations need to be modified following Koiter's generalisation, introducing a second plastic multiplier λ_2.

$\Delta\lambda_{1,n+1}$ occurs from Equation (3.61) with the condition $\mathbf{s}_{n+1} = 0$ and $\Delta\lambda_{2,n+1}$ is obtained enforcing the constancy condition $f_2 = 0$ and is computed iteratively via a Newton scheme. Once the two plastic multipliers have been computed the components of the Cauchy stress tensor $\boldsymbol{\sigma}'$, the elastic strain tensor $\boldsymbol{\varepsilon}^e$ and the plastic strain tensor $\boldsymbol{\varepsilon}^p$, can be updated.

In particular, the Cauchy stress tensor in case of the non-corner region is:

$$\overline{\boldsymbol{\sigma}}'_{n+1} = p'^{tr}_{n+1} - 3K\alpha_g\Delta\lambda_{n+1} + \left[1 - \frac{2G\Delta\lambda_{n+1}}{\left\|\mathbf{s}^{tr}_{n+1}\right\|}\right]\mathbf{s}^{tr}_{n+1} \tag{3.64}$$

and for the corner zone is:

$$\overline{\boldsymbol{\sigma}}'_{n+1} = p'^{tr}_{n+1} - 3K\alpha_g\left[\Delta\lambda_1 + \Delta\lambda_2\right]_{n+1} \tag{3.65}$$

The plastic strain is computed from Equation (3.59) for the non-corner zone. Otherwise, is given from the following equation:

$$\boldsymbol{\varepsilon}^p_{n+1} = \boldsymbol{\varepsilon}^p_n + \alpha_g\left[\Delta\lambda_1 + \Delta\lambda_2\right]_{n+1}\mathbf{1} + \left[\Delta\lambda_1\right]_{n+1}\mathbf{n}_{n+1} \tag{3.66}$$

Finally, the computed algorithmic tangent moduli for the two cases are respectively:

- for the non-corner zone:

$$\begin{aligned}\mathbf{D}^{ep}_{n+1} = {} & \left(1 - \frac{9\alpha_g\alpha_f K}{c_1}\right)K\mathbf{1}\otimes\mathbf{1} + 2G\mathbf{I}_{dev}\left(1 - \frac{2G\Delta\lambda_{n+1}}{\left\|\mathbf{s}^{tr}_{n+1}\right\|}\right) - \frac{6KG\alpha_g}{c_1}\mathbf{1}\otimes\frac{\mathbf{s}^{tr}_{n+1}}{\left\|\mathbf{s}^{tr}_{n+1}\right\|} \\ & - \frac{6KG\alpha_f}{c_1}\frac{\mathbf{s}^{tr}_{n+1}}{\left\|\mathbf{s}^{tr}_{n+1}\right\|}\otimes\mathbf{1} - 4G^2\left(\frac{1}{c_1} - \frac{\Delta\lambda_{n+1}}{\left\|\mathbf{s}^{tr}_{n+1}\right\|}\right)\frac{\mathbf{s}^{tr}_{n+1}}{\left\|\mathbf{s}^{tr}_{n+1}\right\|}\otimes\frac{\mathbf{s}^{tr}_{n+1}}{\left\|\mathbf{s}^{tr}_{n+1}\right\|}\end{aligned} \tag{3.67}$$

with $c_1 = 2G + 9K\alpha_g\alpha_f + \beta_f h\sqrt{\frac{2}{3}\left(1+3\alpha_g^2\right)}$

- for the corner zone:

$$\mathbf{D}_{n+1}^{ep} = c_2 K \mathbf{1}\otimes\mathbf{1} + \frac{c_2 K}{2G\alpha_g \left[\Delta\lambda_1 + \Delta\lambda_2\right]_{n+1}} \mathbf{1}\otimes\mathbf{s}_{n+1}^{tr} \tag{3.68}$$

in which the coefficient c_2 equals to:

$$c_2 = \alpha_g \beta_f \sqrt{\frac{2}{3}} h \left[\Delta\lambda_1 + \Delta\lambda_2\right]_{n+1} \Big/ 3\alpha_f K \sqrt{\left[\Delta\lambda_1\right]_{n+1}^2 + 3\alpha_g^2 \left[\Delta\lambda_1 + \Delta\lambda_2\right]_{n+1}^2} + \alpha_g \beta_f \sqrt{\frac{2}{3}} h \left[\Delta\lambda_1 + \Delta\lambda_2\right]_{n+1}$$

Table 3.2: Numerical algorithm for local Duvaut-Lions model.

1. Compute trial elastic state

$$p'^{tr}_{n+1} = K\,tr(\boldsymbol{\varepsilon}_{n+1} - \boldsymbol{\varepsilon}^p_n)\ ;\ \mathbf{s}^{tr}_{n+1} = 2G(\mathbf{e}_{n+1} - \mathbf{e}^p_n)$$

2. Check flow potential

$$f^{tr}_{n+1} = 3\alpha_f p'^{tr}_{n+1} + \left\|\mathbf{s}^{tr}_{n+1}\right\| - \beta_f \sqrt{2/3}\left(c + h\xi^p_n\right)$$

IF: $f^{tr}_{n+1} \le 0 \rightarrow$ elastic step $\rightarrow$ Set $(\bullet)_{n+1} = (\bullet)^{tr}_{n+1}$ & EXIT

else go to 3

3. Compute elastoplastic stress and strain $\bar{\boldsymbol{\sigma}}_{n+1}, \bar{q}_{n+1}, \bar{\varepsilon}^p_{n+1} \rightarrow$ Eq. (3.64) or (3.65) and (3.59) or (3.66)

4. Update viscoplastic strain and stress

$$\boldsymbol{\sigma}'_{n+1} = \frac{\tau}{\tau + \Delta t}\left(\boldsymbol{\sigma}'_n + \mathbf{D}^e \Delta\varepsilon_{n+1}\right) + \frac{\Delta t}{\tau + \Delta t}\bar{\boldsymbol{\sigma}}'_{n+1}$$

$$\boldsymbol{\varepsilon}^{vp}_{n+1} = \boldsymbol{\varepsilon}^{vp}_n + \frac{\Delta t}{\tau}\left[\mathbf{D}^e\right]^{-1}\left(\boldsymbol{\sigma}'_{n+1} - \bar{\boldsymbol{\sigma}}'_{n+1}\right)$$

$$q_{n+1} = \frac{\tau}{\tau + \Delta t} q_n + \frac{\Delta t}{\tau + \Delta t}\bar{q}_{n+1}$$

5. Compute consistent viscoplastic tangent moduli, $\rightarrow$ Eq. (3.54) in combination with Eq. (3.20) & (3.67) or (3.68)

3.5 Non-Local Enhancement of the Viscoplastic Approach

It is very well known fact that, in the case of slightly viscous materials, the regularizing effect of viscosity vanishes, so that the employment of more advanced constitutive theories is recommended. Along this direction, a non-local enhancement of the initial viscoplastic model of Perzyna presented in Section 3.3 is introduced and analyzed in terms of regularizing performance.

Non-local models can be grouped into gradient type models that apply differential operators, and into integral type models that use weighted spatial averages. On expanding a non-local model in Taylor series and omitting the high-order derivatives, one obtains a strain-gradient model; hence, a strain-gradient model can be seen as a particular case of a non-local one. This thesis is dealing only with the integral type of non-locality and always in combination with the viscoplastic approach.

Furthermore, it is evident from the literature that formulations based on non-local averaging are widely used in single phase materials, whereas they have not been fully investigated in the context of multiphase porous media motivating the non-local application within the context of this thesis.

3.5.1 Preface and Definitions

The first publications with the integral-type models date back to the late sixties of the last century and focus on non-local formulations for elasticity e.g. Kröner (1967) and Eringen and Edelen (1972). The extension of the integral-type non-local models to plasticity was proposed by Eringen. He developed non-local formulations of isotropically hardening plasticity in strain space (Eringen (1981)), perfect plasticity with associated flow, and deformation theory of plasticity (Eringen (1983)). The model was first applied as a regularization method in the context of damage models by Pijaudier-Cabot and Bažant (1987) and for strain-softening problems by Bažant et al. (1987). In Strömberg and Ristinmaa (1996) a detailed description of a possible numerical solution procedure for an integral-type non-local plasticity model within the FE method is presented. Initially conceived for concrete and rock-like materials, the integral non-local approach has been then extended to granular soils as well (see e.g. di Prisco et al. 2002).

Generally speaking, the non-local theory is based on the idea that the response of the material at a point is determined not only by the state at that point but also by the state of its neighboring points. In the application of non-local averaging, the local results of a specific integration point will be averaged by considering the results of the integration points in a certain radius resulted from the characteristic length (points in neighborhood). For this reason this method is known as non-local integral type averaging method.

Following Jirásek (2002) in non-local approach, a certain variable is substituted with its non-local counterpart obtained by weighted averaging over a spatial neighborhood of each point under consideration. If f(**x**) is a "local" field, the corresponding non-local field is defined as:

$$\overline{f}(\mathbf{x}) = \int_V \alpha(\mathbf{x},\boldsymbol{\xi})\, f(\boldsymbol{\xi}) d\boldsymbol{\xi} \tag{3.69}$$

where $\alpha(\mathbf{x},\boldsymbol{\xi})$ is a given non-local weight function of the point under consideration located at **x** and the neighboring (or distributing) points located at $\boldsymbol{\xi}$ and V is the volume of the entire body.

For an infinite body the weight function depends only on the distance $r = \|\mathbf{x} - \boldsymbol{\xi}\|$ and can be expressed as $\alpha(\mathbf{x},\boldsymbol{\xi}) = \alpha_0(\|\mathbf{x} - \boldsymbol{\xi}\|)$ where α_0 is a function of r. For a finite body, the weight function is usually adjusted such that the non-local field corresponding to a constant local field remains constant even in the vicinity of a boundary. This is guaranteed if the weight function satisfies the normalizing condition:

$$\int_V \alpha(\mathbf{x},\boldsymbol{\xi})\, d\boldsymbol{\xi} = 1 \;\forall\; \mathbf{x} \in V \tag{3.70}$$

This condition can be achieved by imposing that the weight function is expressed by:

$$\alpha(\mathbf{x},\boldsymbol{\xi}) = \frac{\alpha_0\left(\left\|\mathbf{x}-\boldsymbol{\xi}\right\|\right)}{\int_V \alpha_0\left(\left\|\mathbf{x}-\boldsymbol{\zeta}\right\|\right) d\boldsymbol{\zeta}} \tag{3.71}$$

where α_0 is the basic weight function.

Key points for the formulation and implementation of an integral non-local approach are the shape function for the averaging, the non-local variable and its discretization. In the following, these factors are discussed in detail.

Basic shape function

The weight function always contains at least one parameter with the dimension of length which incorporates, in the simplest possible way, information about the microstructure and controls the size of the localized plastic zone (Jirásek and Rolshoven (2003)).

For the basic weighting function, α_0, several choices can be found in the literature on non-local theories. Some of the most commonly used averaging functions are:

- Gaussian function (Jirásek (2002)):

$$\alpha_0(r) = \exp\left(-\frac{r^2}{2l^2}\right) \tag{3.72}$$

where l is the internal length of the non-local continuum.

- Bell-shaped truncated polynomial function (Rolshoven and Jirásek (2003)):

$$\alpha_0^{\text{bell}}(r) = \begin{cases} \frac{1}{c}\left(1-\frac{r^2}{R^2}\right)^2 & \text{if } |r| \le R \\ 0 & \text{if } |r| > R \end{cases} \tag{3.73}$$

where R is the interaction radius representing a parameter linked to the internal length.

- Exponential Gaussian bell-shaped function (Ammann (2005)):

$$\alpha_0(\mathbf{x}-\boldsymbol{\xi}) = \frac{1}{l\sqrt{\pi}}\exp\left(-\frac{(\mathbf{x}-\boldsymbol{\xi})\cdot(\mathbf{x}-\boldsymbol{\xi})}{l^2}\right) \tag{3.74}$$

- Bi-linear exponential function (Lu et al. (2012)):

$$\alpha_0(r) = \begin{cases} \exp\left(-\frac{r}{l}\right) & \text{if } |r| \le R \\ 0 & \text{if } |r| > R \end{cases} \tag{3.75}$$

where R is the radius of effective zone which can be determined by l.

The Gauss-like weight function (Equation (3.72)) has an unbounded support, which means that the nonlocal interaction theoretically takes place at an arbitrary long distance. Since the decay of α_0 with

increasing r = l is very fast, in practical applications it is possible to truncate the function at a finite distance.

The bell-shaped function (Equation (3.73)) has a bounded support and vanishes at distances r exceeding the interaction radius R. In this equation the scaling factor c depends on the dimension of the problem and equals to 16R/15 for one dimension, $\pi R^2/3$ for two dimensions and $32\pi R^3/105$ for three dimensions (Rolshoven and Jirásek (2003)).

A bi-linear exponential function with bounded support was selected by Lu et al. (2012). The influence area in which the non-local variable was weighted, had a radius R = 6l.

Ammann (2005) used an exponential Gaussian bell-shaped function (Equation (3.74)) which has a maximum at y = x, it is symmetric about this point and depends on the internal length scale l.

In Figure 3.7 this function is plotted within an 1-D example for different values of l, at the position x = 0.1m. It can be observed that the influence of the weighting function increases with increasing values of the internal length scale. In the same figure (Figure 3.7b), it is emphasized that for relative small values of the internal length, the representative volume results in the constant value 1.0, except close to the boundaries where the value decreases to 0.5. As a result, values of fields that are to be averaged at points close to the boundaries are more weighted (Figure 3.8), since they do not get contributions from the points outside the boundaries (Strömberg and Ristinmaa (1996)). Modifications on the description of the non-local field so as to overcome boundary problems have been proposed by Bažant et al. (2010) and Giry et al. (2011).

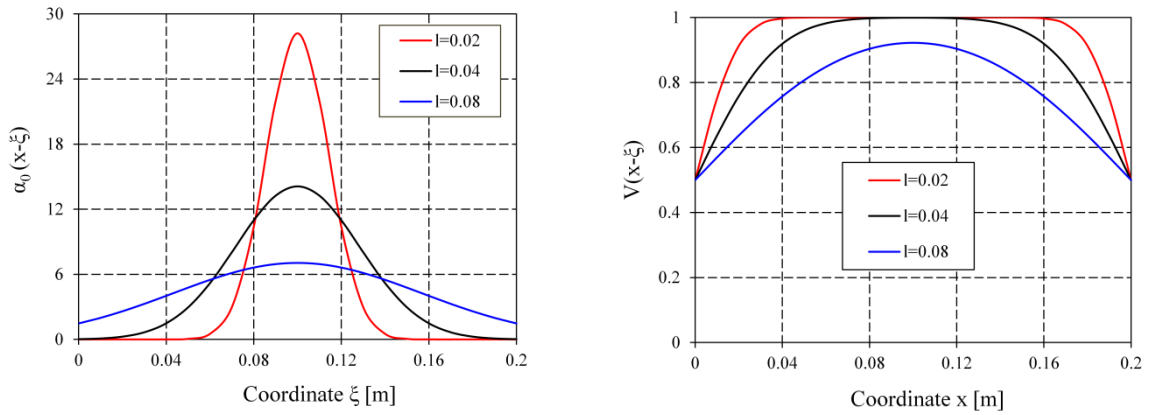

(a) (b)

Figure 3.7: 1-D example of the (a) weight function and (b) representative volume adopted in Ammann (2005) varying the internal length l.

The same author showed that using the aforementioned averaging procedure, for small enough values of the internal length, the non-local function equals to the local one.

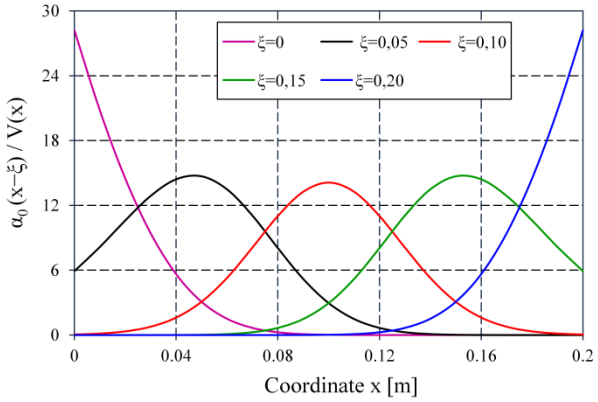

Figure 3.8: The weight function over the representative volume as a function of x, for constant l=0.04m and varying ξ.

A comparison between the four abovementioned weight functions is presented in Figure 3.9. For an identical scale parameter l, the bi-linear exponential function and the Gauss distribution function are similar, while the unbounded bell-shaped function gives a wider influence zone.

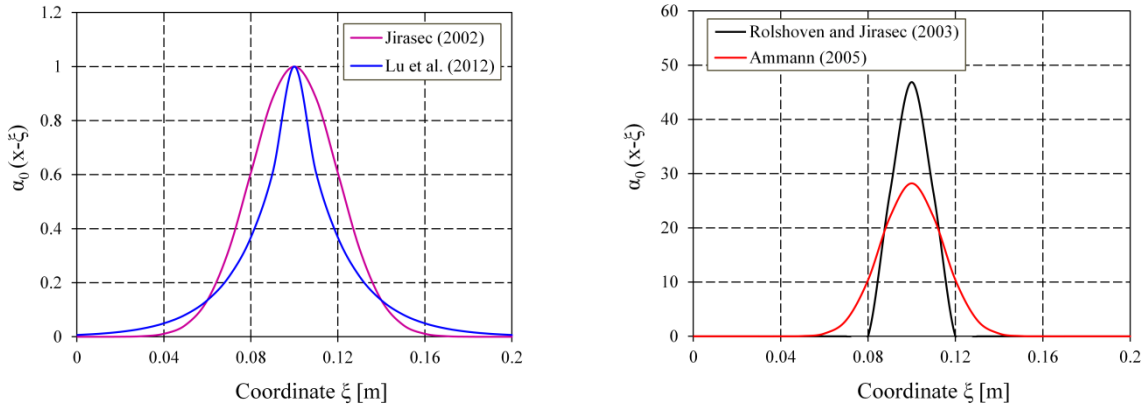

(a) (b)

Figure 3.9: Comparison between the weight functions used by (a) Jirásek (2002) and Lu et al. (2012) and (b) Ammann (2005) and Rolshoven and Jirásek (2003). Parameters l and R are set to 0.02m for fixed position x=0.1m.

Non-local variable

In non-local theories, an internal length enters as a material parameter by allowing a dependency on the so-called non-local variables in the constitutive equations. A non-local variable is a weighted average of the local variable over all the material points in the body, and the length parameter determines how the value of the variable at a certain point is weighted.

The way non-locality is introduced into the constitutive equations is dominant because an inappropriate treatment of the non-local variable, may lead to instability of the numerical analysis.

According to Jirásek (2002), the choice of the variable to be averaged remains to some extent arbitrary, whereby at least one basic requirement has to be satisfied:

1. The generalized model should exactly agree with the standard "local" elastic continuum as long as the material behaviour remains in the elastic range. Except for the case of homogeneous strain, non-local strain differs from the local one, leading to a different model behaviour already for purely elastic deformations. For this reason, it is not possible to simply replace the local strain by nonlocal strain and apply the usual constitutive law.
2. The model should give a realistic response in simple loading situations such as uniaxial tension.

In a fully integral non-local model, a relation is established between average stresses and average strains. Instead of considering a fully non-local stress-strain relationship, it is convenient to consider only a particular strain measure as non-local, whereas general stresses and strains remain local (Bažant et al. (1987)). This enables a near-local treatment of the constitutive equation.

In rate-independent plasticity theory, such a model obtained by formulating the hardening parameter as a non-local quantity. A disadvantage of rate-independent non-local models is that the determination of the plastic multiplier results in an integro-differential equation due to the consistency rule. Strömberg and Ristinmaa (1996) proposed an integration algorithm using a Backward-Euler method, in which the consistency condition resulted in a Fredholm integral equation of the second kind for the determination of the plastic multiplier. The authors declared that in non-local theory is not possible to derive a point-wise relation between the stress rate and strain rate as in local theory, because in the former the consistency condition is an integral equation that involves all the material points within the body. Indeed, this would give complex numerical procedures, however the procedures can be simplified by adopting suitable approximations of the hardening parameter in terms of total strains instead of plastic strains as for example in Brinkgreve (1994).

Another choice for the non-local variable is the scalar value of the plastic strain tensor (the equivalent or accumulated plastic strain) which is incorporated in the softening law, or the plastic strain itself. However, as it has been first demonstrated by Brinkgreve (1994), a classical non-local model is not always effective as a regularization method and a modified (also called over-non-local model in Luzio and Bažant (2005), Lu et al. (2012) and mixed local and non-local model in Strömberg and Ristinmaa (1996)) non-local model has to be adopted.

di Prisco et al. (2002) combined the non-local approach with rate-dependency and chose the yield function as non-local variable. This combination excludes the problems arising with the consistency condition in rate-independent non-local models. Moreover, if the viscoplastic constitutive law is of Perzyna type, it is very convenient to be extended to non-local approach, by redefining the flow rule and assuming that the viscous nucleus depends on the non-local yield function. The simplicity of the proposed method is further highlighted by the addition, on the original viscoplastic approach, of a single constitutive parameter to account for the non-local effects. This parameter can be calibrated by either experimentally estimating the shear band thickness during a biaxial test or by assuming that such thickness is empirically correlated to the mean grain size of the material.

Discretization of the non-local variable

The non-local variable of Equation (3.69) is evaluated using Gauss quadrature. The Gaussian integration process allows the spatial integrals of a polynomial to be replaced with finite sums over a discrete set of integration points. In each element we perform Gauss integration. For details on this point the interest reader refers to Zienkiewicz and Taylor (2000). The numerical integration of spatial averaging is schematized in Figure 3.10.

$$\bar{f}(\mathbf{x}_i) = \frac{\sum_{e=1}^{el}\sum_{j=1}^{n} \omega_j^e \alpha\left(\left\|\mathbf{x}_i - \xi_j^e\right\|\right) \det\mathbf{J}_j^e f(\xi_j^e)}{\sum_{e=1}^{el}\sum_{j=1}^{n} \omega_j^e \alpha\left(\left\|\mathbf{x}_i - \xi_j^e\right\|\right) \det\mathbf{J}_j^e} \tag{3.76}$$

in which i is the integration point under consideration, j is the j^{th} Gauss point of element e; *el* is the total number of elements inside the interaction volume defined by a sphere centered at x with radius R (Figure 3.10), *n* is the number of Gauss points of this element inside the interaction volume; ω_j^e and $\mathbf{J}_j^e$ are, respectively, the weight and Jacobian matrix at Gauss point j of element e.

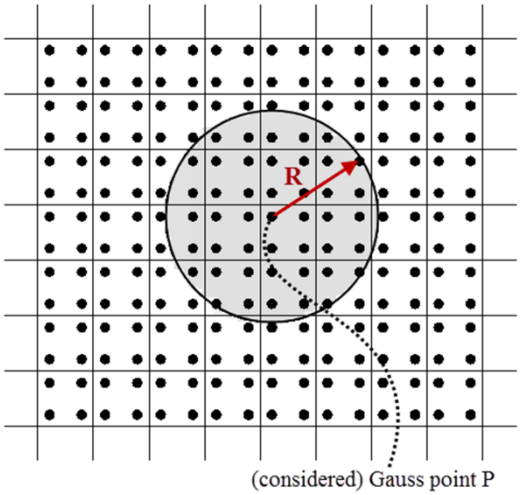

Figure 3.10: Area where the average is calculated. Gauss point P is the point under consideration where the non-local variable is calculated.

The above expression can be rewritten in compact form as:

$$\bar{f}_i = \sum_{j}^{NG_i} w_{ij} f_j \tag{3.77}$$

where NG_i is the total number of Gauss points inside the non-local interaction volume at point i and the weight w_{ij} for the interaction between points i and j has the form:

$$w_{ij} = \frac{\omega_j^e \alpha\left(\left\|\mathbf{x}_i - \xi_j^e\right\|\right) \det\mathbf{J}_j^e}{\sum_{e=1}^{el}\sum_{j=1}^{n} \omega_j^e \alpha\left(\left\|\mathbf{x}_i - \xi_j^e\right\|\right) \det\mathbf{J}_j^e} \tag{3.78}$$

3.5.2 Algorithmic Aspects

The non-local enhancement of the viscoplastic model is obtained by modifying the viscoplastic flow rule of Perzyna (presented in Section 3.3) and assuming the yield function as a non-local variable. Thus, the viscous nucleus in the flow rule is also redefined.

$$\dot{\boldsymbol{\varepsilon}}^{vp} = \gamma\Phi\left(\bar{f}\right)\frac{\partial g}{\partial \boldsymbol{\sigma}'} \tag{3.79}$$

where $\bar{f}$ is the non-local yield function defined as (Equation (3.69)):

$$\bar{f}(\mathbf{x}) = \int_V \alpha(\mathbf{x},\boldsymbol{\xi})\, f(\boldsymbol{\xi})\mathrm{d}\boldsymbol{\xi} \tag{3.80}$$

and is evaluated using Gauss quadrature as in Equation (3.76).

For the basic weighting function, α_0, a Gaussian weighting function with a bounded support is selected (Figure 3.11):

$$\alpha_0(\mathbf{x}-\boldsymbol{\xi}) = \begin{cases} \exp\left(-\dfrac{2(\mathbf{x}-\boldsymbol{\xi})}{l}\right)^2 & \text{if } \|\mathbf{x}-\boldsymbol{\xi}\| \le R \\ 0 & \text{if } \|\mathbf{x}-\boldsymbol{\xi}\| > R \end{cases} \tag{3.81}$$

The algorithmic treatment of the non-local approach and its implementation can be divided in two main steps.

In the first step the factors ω_j^e, $\mathbf{J}_j^e$ and $\alpha\left(\left\|\mathbf{x}_i - \boldsymbol{\xi}_j^e\right\|\right)$ of Equation (3.76) are computed. These factors depend on the finite element mesh itself and not on the material model considered. Therefore, this step is applied only once at the beginning of the analysis and the values of the calculated factors can be reused in the subsequent iterations, whenever the non-local formulation is activated. This fact has twofold advantage as it allows for non-local extension to more sophisticated yield criteria and in addition reduces significantly the computational burden.

Moreover, carrying out an integration over the whole domain with a relatively small value for the internal length l, may lead to the summation of zero values. This is because in such a case, the sphere of influence of the weighting function is only in the closest neighborhood of the regarded integration point. To prevent such an inefficient strategy, at the beginning of the calculation, the set of elements, which have an influence on the non-local quantity, are determined by calculating the distance between the respective points and comparing the distance with some reference value, which depends on the internal length.

Table 3.3 describes the first step of the numerical integration process. This procedure has been implemented as a separate subroutine in Comes-geo code and it therefore allows for non-local extension to more sophisticated yield criteria only by minor modifications in the local model.

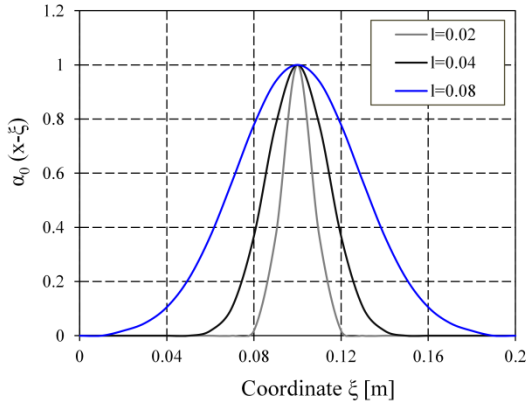

Figure 3.11: 1-D example of Gaussian weighting function for different values of the internal length scale l (l=0.02, 0.04 and 0.08m). The influence of the weighting function increases with increasing values of the internal length scale.

Table 3.3: Calculation of non-local factors at Gauss points.

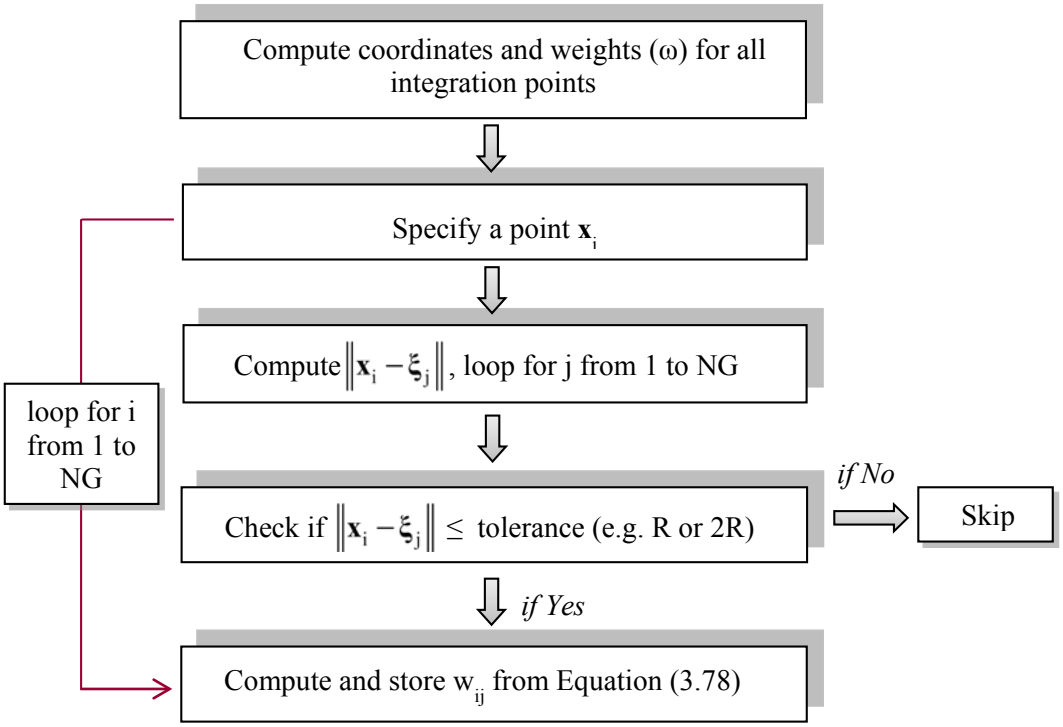

In the second step the non-local quantity and the integration of the non-local elasto-viscoplastic constitutive equations are computed.

In non-local context an implicit scheme is difficult to be applied, as the integration of the constitutive equations is no longer a local stage (Strömberg and Ristinmaa (1996)). For this purpose an explicit integration scheme is adopted only for the integration of non-local viscoplastic constitutive equations (whereas the rest of the algorithm operates implicitly) and the non-local values at the current time step are calculated from the local values of the previous time step. The employment of this semi-implicit algorithm implies the loss of unconditional stability, but overcomes the spatial

coupling in Equation (3.83). Due to its explicit nature, the stability of the algorithm is maintained using a relatively small time step.

Using forward Euler method for the integration of Equation (3.79) one obtains:

$$\boldsymbol{\varepsilon}_{n+1}^{vp} = \boldsymbol{\varepsilon}_{n}^{vp} + \Delta\bar{\lambda}_{n+1}\left\{\alpha_g \mathbf{1} + \mathbf{n}_n\right\} \tag{3.82}$$

in which the increment of the inelastic multiplier is obtained by integrating the non-local version of Equation (3.26):

$$\Delta\bar{\lambda}_{n+1} = \frac{\Delta t}{\eta f_0}\left(\bar{f}_n\right) \tag{3.83}$$

Having computed $\Delta\bar{\lambda}$, strain and stresses can be updated in a similar manner as shown in Section 3.3.2.

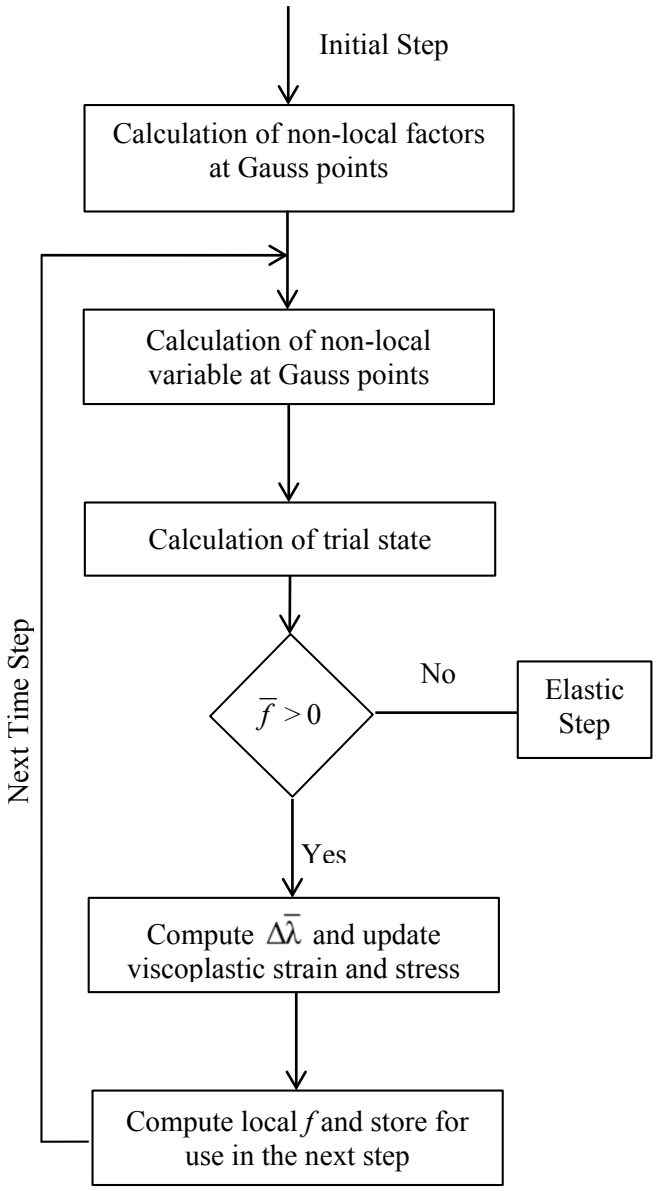

Figure 3.12: Flowchart of the non-local implementation in Comes-geo code.

Since this procedure uses the local values of the previous time step for the calculation of non-local values at the current time step, the local variable has to be stored and ensure that this information will be available in the next time step. In fact the local yield function, *f*, is a column matrix that collects the local values at all Gauss points.

Figure 3.12 summarizes the algorithm of non-local formulation, which extends the local stress update of the viscoplastic model of Perzyna.

3.6 Concluding Remarks

This Chapter contains the analytical formulation and the numerical treatment of the adopted regularization techniques that complete the multiphase model described in Chapter 2.

Having the combination of a regularized finite element solution and the multiphase material model describing the behaviour of soils, we will have a numerical tool capable of simulating strain localization phenomena in a realistic base.

Following this goal three viscoplastic models are theoretically employed and numerically implemented in the finite element Comes-geo code:

- Local viscoplastic model of Perzyna
- Local viscoplastic model of Duvaut-Lions
- Non-local viscoplastic model of Perzyna

For simplicity, a Drucker-Prager yield criterion was assumed and a more sophisticated yield criterion will be introduced in Chapter 5.

The merits and drawbacks of each regularization model are summarized in Table 3.4.

Table 3.4: Advantages and disadvantages of regularization models.

Viscoplastic model	Advantages	Disadvantages
Local Perzyna	New functional relationships, $\Phi(f)$ can be easily added	In multi-surface plasticity as $\eta \rightarrow 0$ do not reduce to the rate-independent plasticity
Duvaut-Lions	Easily adopted to existing elastoplastic material models	Regularization in a weak sense as viscoplastic solution lies between elastic and inviscid solution
Non-local Perzyna	A characteristic length is explicitly introduced (shear zone thickness depends on the R value)	A minimum mesh density is necessary to activate the nonlocal interaction

Chapter 4

Numerical Validation and Applications

Chapter 4: Numerical Validation and Applications

4.1 Introduction

The analysis of strain localization is of importance in engineering practice because localization is a precursor to sudden failure. Localized deformations in the form of narrow shear bands can be considered as a bifurcation from a smoothly varying pattern of deformation, which arises as a result of instability in the inelastic behaviour of the material. A strain-softening behaviour is expected to induce localization phenomena and, as is well-known, this poses the issue concerning the objectivity of the numerical results. When rate-independent elastoplastic solids are considered, the solutions of localization problems are mesh dependent and the width of the shear band is set by the finite element size.

In order to properly characterize the mechanisms of strain localization without mesh dependency, local and non-local viscoplasticity are introduced in the framework of multiphase porous media, as discussed in Chapter 3.

In this Chapter, the validation of the model's implementation in the Comes-geo code is presented along with two characteristic applications of strain localization to explore the regularization capabilities of the applied models.

More specifically, fully-coupled hydro-mechanical analysis of shear failure is performed for a case of an experimental plane-strain compression test and for a benchmark slope instability problem. These examples aimed at answering key questions, such as: what are the most significant influential factors in the development of strain localization for each regularization technique and which is the role of the fluid components in localization; is the viscosity of the soil affected by the presence of water and how does this fact influence the regularizing capabilities of the method; how do the internal lengths introduced by viscosity and non-locality interact with each other and under which circumstances is the one method preferable to the other?

This Chapter is structured as follows: In Section 4.2 the numerical results coming out from the simulation of a plane-strain compression test using local and non-local viscoplasticity are presented followed by the numerical simulation of a slope failure in Section 4.3. The conclusions drawn from these investigations are given in Section 4.4.

4.2 Strain Localization on Initially Saturated Dense Hostun Sand

In this section the regularization methods presented in Chapter 3, are applied to a plane-strain compression test and their effect on the respective numerical solution is discussed. It is about a biaxial compression test of initially water saturated globally undrained dense Hostun RF sand, inspired by the experimental work of Mokni and Desrues (1998). In globally undrained situations, relative drainage may appear between zones of the domain i.e. between shear bands and blocks as far as localization is concerned.

This example was previously studied by Sanavia et al. (2006), assuming a rate-independent behaviour for the description of the mechanical behaviour of sand. The goal was to emphasize the benefits of using a multiphase model to study phase change phenomena, such as that of cavitation at strain localization and therefore a suitable mesh was used to avoid excessive mesh dependency.

For clarity, a brief description of the simulated example, providing general assumptions and details, follows.

To begin with, mesh sensitivity of the numerical results is examined by using three different finite element discretizations. The meshes consist of 85, 340 and 1360 elements respectively, for a rectangular sample of homogeneous soil of 34 cm height and 10 cm width, sketched in Figure 4.1. The finite element mesh consists of eight node quadrilateral isoparametric elements with reduced Gaussian (2 x 2) integration scheme to eliminate shear locking (Owen and Hinton (1980)). The bottom of the sample is fixed and rough whereas the boundaries are impervious and adiabatic. Hydrostatic distribution of water pressure is assumed as initial condition.

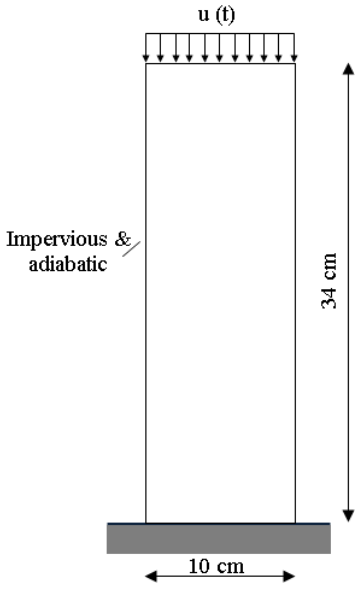

Figure 4.1: Description of the geometry, boundary and loading conditions.

Quasi-static loading conditions are assumed and gravity acceleration is taken into account. Axial compression is applied to the specimen by imposing vertical velocity (1.2 mm/s) on the top. No weak elements are specified since the boundary value problem inherently generates a non-uniform stress field. A non-associated plastic flow rule is adopted to simulate the material nonlinear response and the values of the mechanical and hydraulic properties used in the computations are presented in Table 4.1. The constitutive relationships for the water degree of saturation (Equation (2.40)) and the water relative permeability (Equation (2.46)) are of the type of Safai and Pinder. For the gas relative permeability the relationship of Brooks and Corey has been selected (Equation (2.48)).

Finally, for the sake of simplicity, the strain softening phenomenon is assumed to occur isothermally. In other words, the strain softening is executed at constant temperature and no temperature gradient is developed in the material during the deformation (uniform temperature distribution, no heat transfer due to conduction). It is important to note that thermal effects can cause the softening in plasticity regime, but they are out of scope of this study.

Table 4.1: Soil parameters used in the computation.

Parameter	Symbol	Value	SI unit
Young modulus	E	30	MPa
Linear softening modulus	h	-1	MPa
Initial apparent cohesion	c_0	0.5	MPa
Angle of internal friction	φ	30	(°)
Dilatancy angle	ψ	20	(°)
Poisson ratio	ν	0.4	[-]
Initial porosity	n	0.2	[-]
Solid density	ρ_s	2000	kg/m^3
Intrinsic water permeability	k	1.0E-14	m^2
Water unit weight	γ_w	10	kN/m^3
Gravity acceleration	g	9.81	m/s^2
Soil viscosity	η	variable	s
SWCC parameter	α	1	[-]
SWCC parameter	ν	5	[-]
SWCC parameter	β	0.0005	cm^{-1}

4.2.1 Plastic Mesh Dependence

The numerical results for the rate-independent plasticity model are first presented, where pathological mesh dependency is observed. For an evaluation of the posedness of the respective problem, FE calculations are carried out with different meshes.

The equivalent plastic strain profiles plotted in Figure 4.2 for the vertical centre cross-section of the specimen depicts that the width of the shear zone is bounded within the size of one element and the maximum value of the equivalent plastic strain significantly differs.

The contours of equivalent plastic strain reflect the difference in the computations with varying meshes; three different meshes are used and three different solutions are obtained; the numerical results indicate the accumulation of inelastic strains in narrow zones after 27 s, for the course and the intermediate mesh, as can be observed in Figure 4.2 a and b. The shear bands develop from the bottom surface because of the higher stress state due to gravity load and the constrained conditions.

When a finer mesh is used (20x68 mesh), the strong mesh dependence is shown with concentration of the equivalent plastic strain in the corners of the sample without propagation in shear bands. A non-acceptable numerical error develops and the analysis failed to converge at t= 9s as soon as strain localization appears.

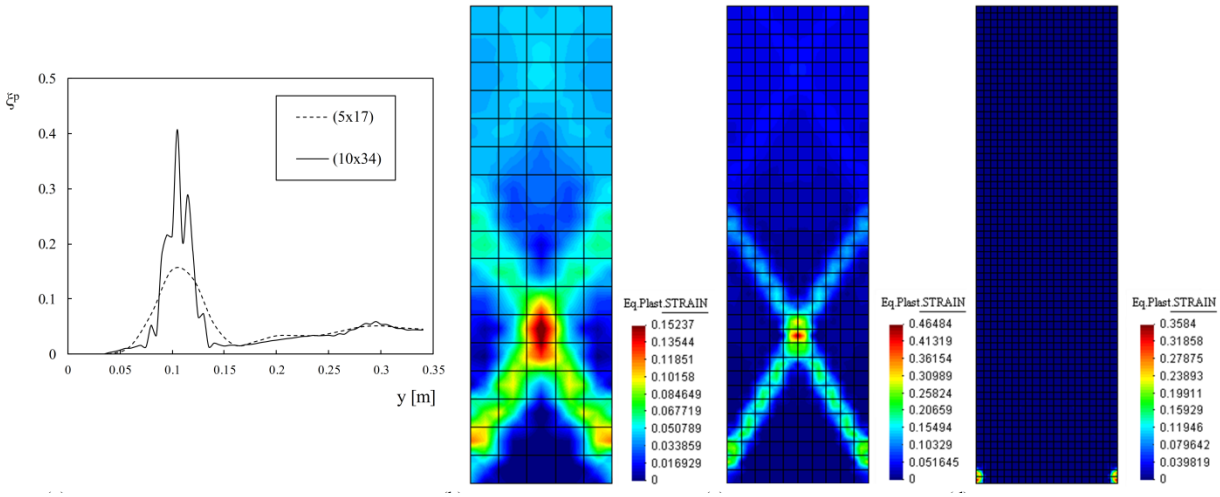

(a) (b) (c) (d)

Figure 4.2: Equivalent plastic strain (a) profiles and contours for (b) course (5 × 17) and (c) intermediate mesh (10 × 34) at t = 27 s and (d) fine mesh (20 × 68) at t=9s.

4.2.2 Viscous Regularization – Perzyna's Model

The local viscoplastic model of Perzyna described in Section 3.3 is now used to simulate the same plane-strain compression test.

- Validation in Comes-geo

The numerical validation of the model in the Comes-geo code is first presented and is conducted in two stages.

In the first stage, a nil value of viscosity is used. This is because for rather small values of viscosity elastoplastic limit is approached (Needleman (1988)). In Figure 4.3 are plotted the equivalent inelastic strains in the vertical section at the centre of the sample for both elastoplastic (solid black line) and elasto-viscoplastic (dashed red line) constitutive models. The comparison of the results shows the coincidence between the elastoplastic and the considered viscoplastic solution for nil viscosity value.

The second stage of validating the implementation of Perzyna's model in Comes-geo code regards the reproduction of the creep process. To this end, a creep test on loose Hostun sand published in di Prisco and Imposimato (1996) is simulated. A single element test is performed under drained conditions and the sample is gradually loaded until a deviatoric stress of 75 kPa is reached (Figure 4.4a). Then, the load is kept constant in time.

Figure 4.4c clearly shows that the material strain response to the instantaneous stress increment is delayed in time. Under a constant load (in the time period 200-1000 min) the axial strain slowly but continuously increases. The same curve is also reproduced in a semi-logarithmic scale Figure 4.4d. It

is important to underline that, this time-dependent behaviour is not due to the water flow within the sample (i.e. to the consolidation phenomenon), but uniquely to the material mechanical properties (the chosen viscous parameters are $\gamma=1\cdot10^{-8}$ s^{-1} and N=1).

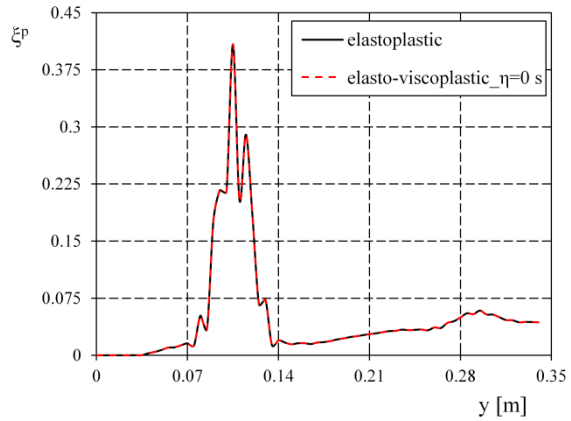

Figure 4.3: Equivalent inelastic strain profile for elastoplastic model and elasto-viscoplastic model in case of nil viscosity, for the intermediate mesh (10 × 34).

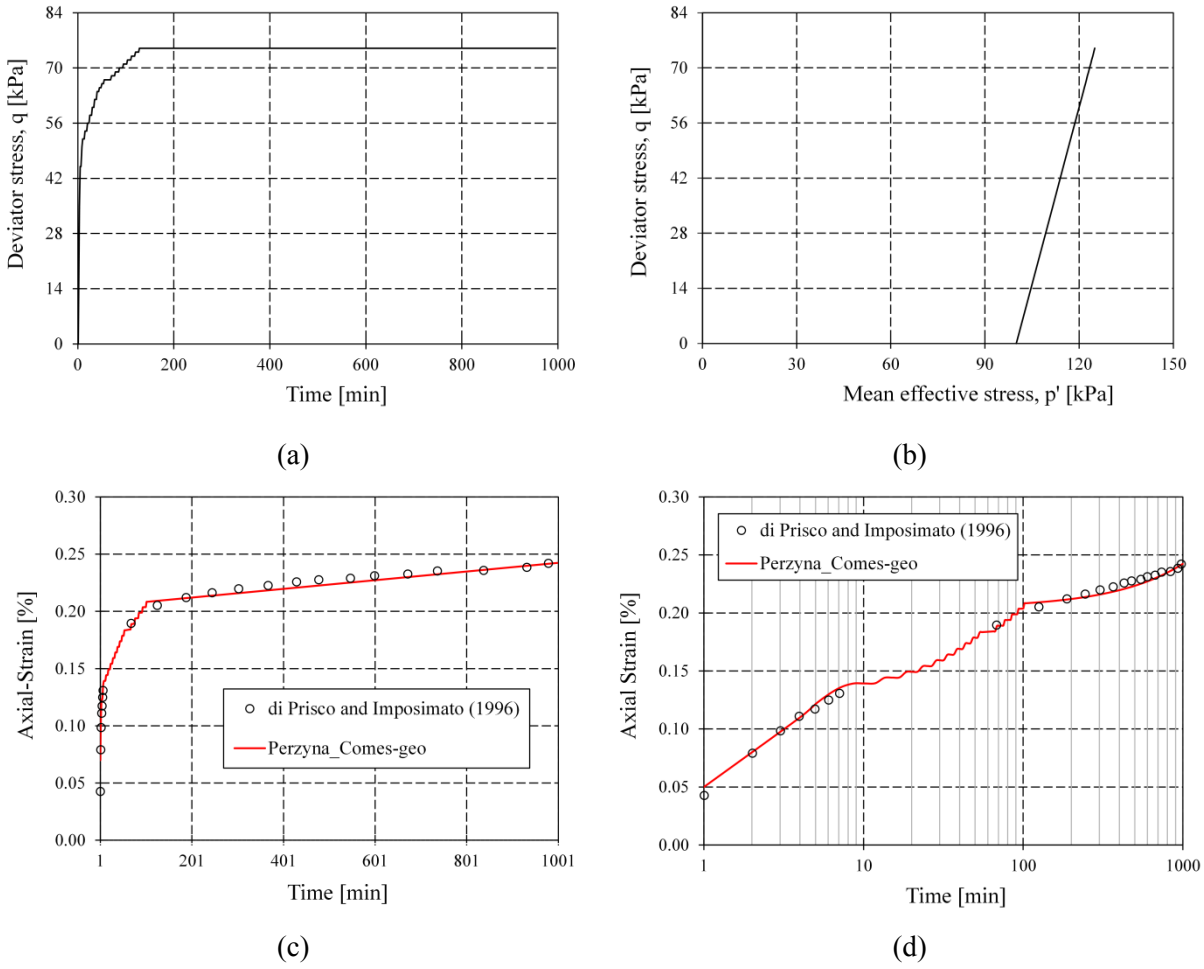

Figure 4.4: Creep test: (a) Axial load-time history and (b) effective stress path; material strain-time response: comparison between the experimental and the numerical results in (c) linear scale and (d) semi-logarithmic scale.

- Influence of viscosity

Coming back to the undrained plane-strain compression test on dense Hostun sand, a second value of viscosity, η= 30 s is used to detect mesh insensitive results, as depicted in Figure 4.5. In contrast to the elastoplastic solution, the mechanical response becomes more stable and the shear band width remains unaltered upon mesh refinement (Figure 4.5c and Figure 4.5d). In addition, the peak value of equivalent viscoplastic strain coincides for the intermediate and fine meshes whereas slightly deviates for the coarse mesh (Figure 4.5a).

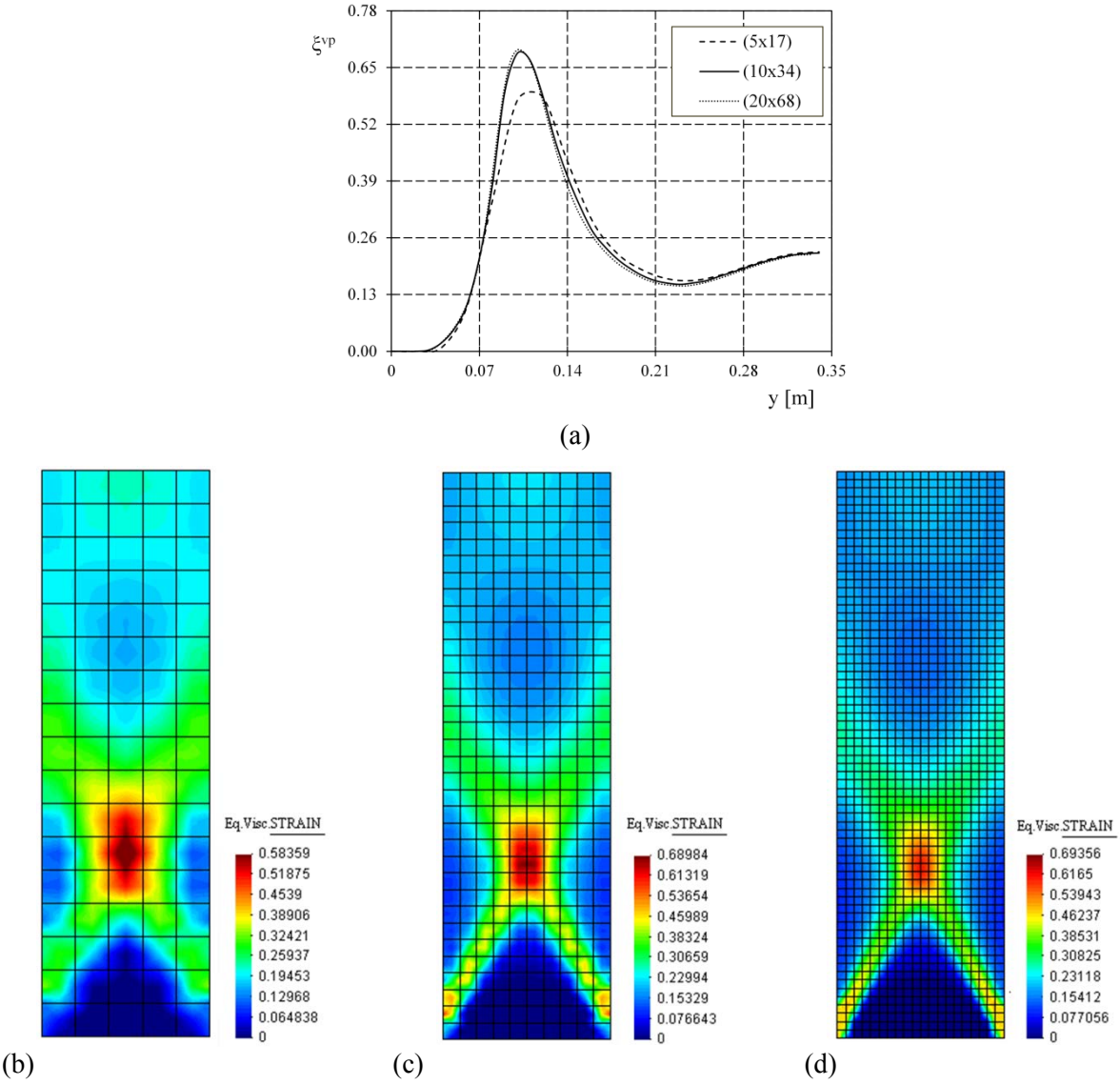

Figure 4.5: Equivalent viscoplastic strain profiles (a) and contours for (b) coarse mesh (5 × 17), (c) intermediate mesh (10 × 34) and (d) fine mesh (20 × 68), in case viscosity η=30 s.

The influence of varying the viscosity on the solution of the numerical simulation is illustrated in Figure 4.6, for a constant finite element mesh with 340 elements. A dependence of the shear zone on the viscosity is obtained, due to overstress coming along with the viscoplastic approach. Increasing the value of viscosity results in an increase of the shear band width and a simultaneously decrease of the maximum value of the equivalent viscoplastic strain. In addition, the larger the value of viscosity

is, the larger is the delay on the response of the viscoplastic model. Furthermore, for a rather large value of viscosity equal to 100 s (Figure 4.6f) the equivalent viscoplastic strains are distributed over the whole sample whereas for small value of viscosity, viscoplastic strains are mostly detected inside the shear bands.

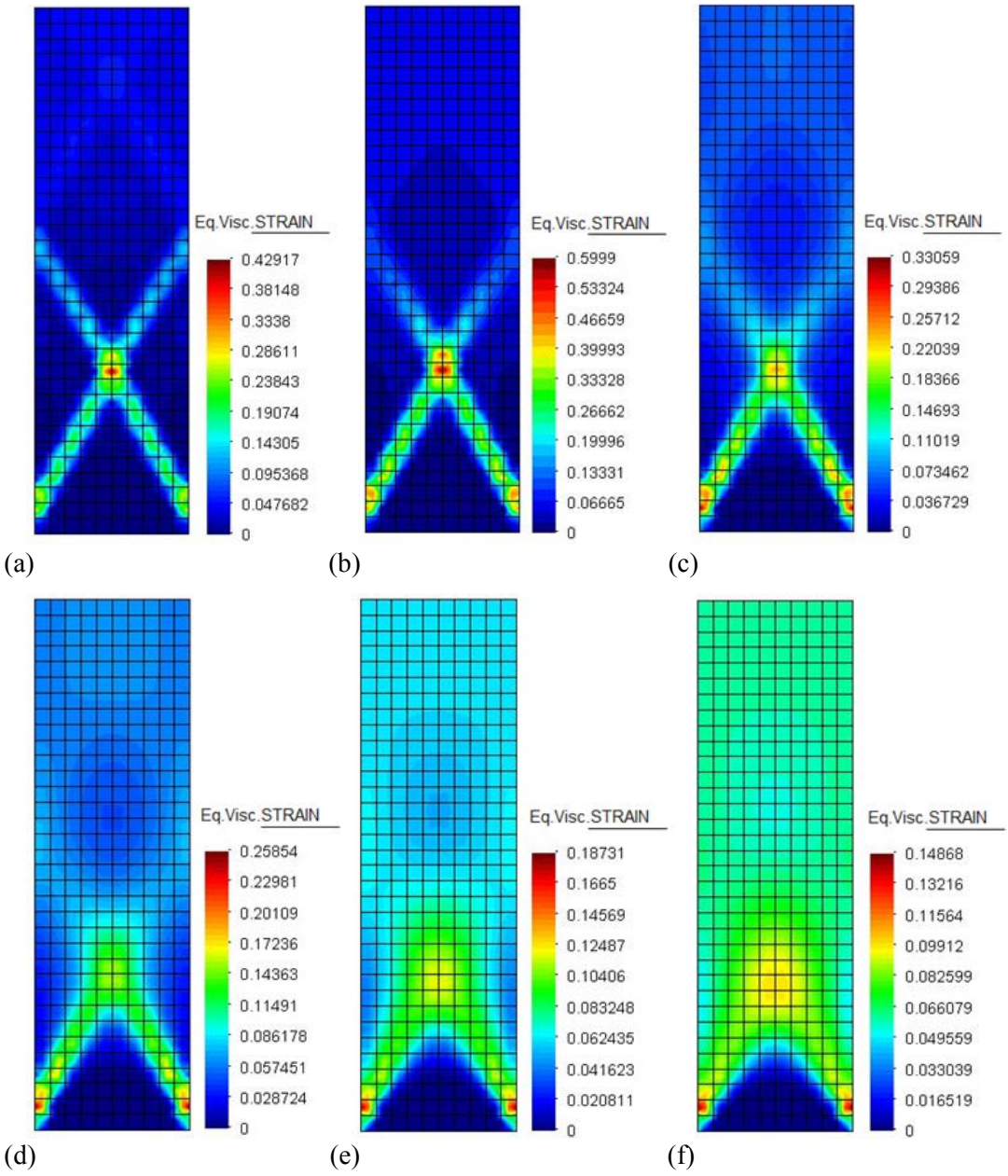

Figure 4.6: Equivalent viscoplastic strain contours varying viscosity (a) η=0 s, (b) η=5 s, (c) η=10 s, (d) η=20 s, (e) η=50 s and (f) η=100 s, for the intermediate mesh (10 × 34).

4.2.2.1 Major Factors Affecting Mesh Objectivity and Shear Band Evolution

In this subsection the factors having an important influence on the evolution of localization bands, always in conjunction with viscosity, are addressed and discussed in detail.

- Influence of Loading Velocity

To examine the influence of loading velocity on the viscous regularization of quasi-static process numerical simulations with velocity equal to 0.2 mm/s and 1.2 mm/s are performed.

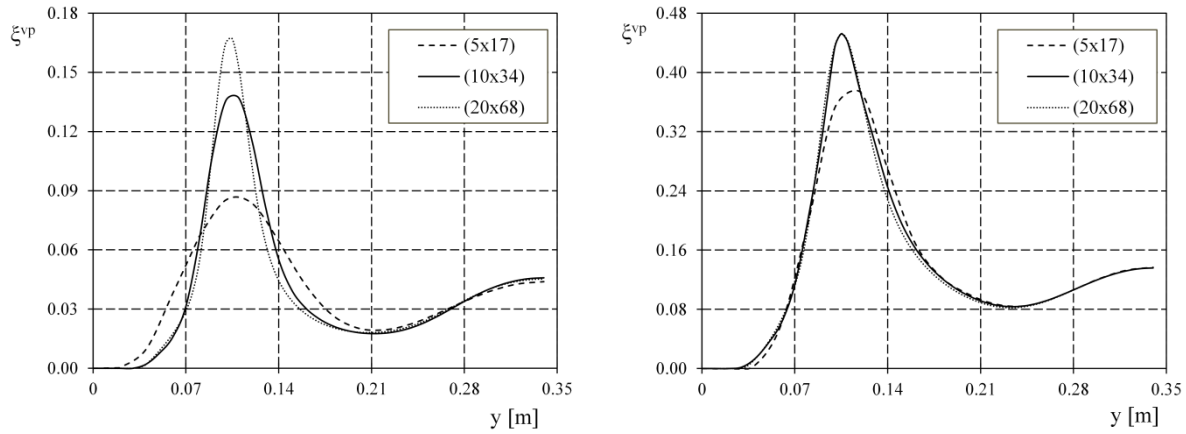

Figure 4.7: Distribution of the equivalent viscoplastic strains in the vertical centre section of the specimen for three meshes and loading velocity v=0.2 mm/s for viscosity (a) η=30 s and (b) η=110 s.

The importance of the considered viscous parameter and the crucial influence of the loading velocity on the material response, are evidence through Figure 4.7 and Figure 4.8. In particular, Figure 4.7a clearly shows the dependence upon mesh refinement of both the shear band width and maximum value of viscoplastic strain, when decreasing the loading velocity six times while keeping the viscous parameter (η=30 s) constant.

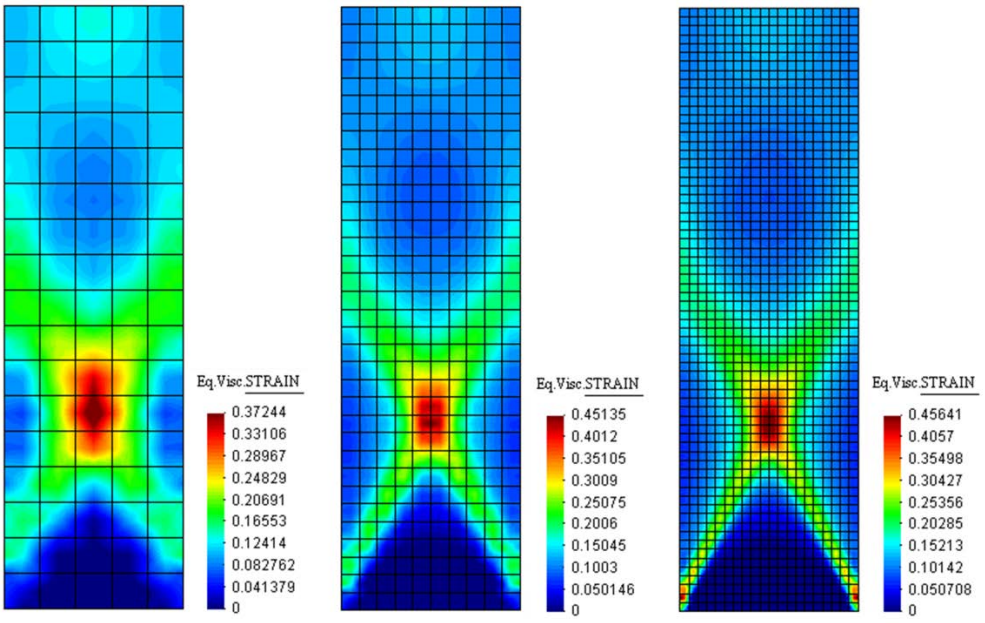

(a) (b) (c)

Figure 4.8: Equivalent viscoplastic strain contours in case v=0.2 mm/s and viscosity η=110 s for (a) coarse mesh (5 × 17), (b) intermediate mesh (10 × 34) and (c) fine mesh (20 × 68), respectively.

Indeed, when the load velocity decreases significantly, the viscoplastic solution tends to the elastoplastic and strong mesh-sensitivity and loss of mesh objectivity follows. In contrast to this mesh-dependent behaviour, the results coming from the simulations with increasing viscous parameter up to 110s show much better characteristics (Figure 4.7b and Figure 4.8). In these figures the equivalent viscoplastic strains in the vertical centre section of the sample and the corresponding contours are presented for the three discretizations, for η=110s and v=0.2mm/sec. No fundamental difference can be detected for results obtained from meshes with 340 or more elements. This leads to infer that the band width in quasi-static analysis is not exclusively governed by viscosity, but it also depends on the load velocity.

Figure 4.9 shows exemplary plot profiles of the computed volumetric strain and capillary pressure distribution for the applied loading velocities (v=1.2mm/s and 0.2mm/s) and the corresponding viscosity values that preserve regularization (η=30s and 110s respectively). The plotted results are obtained for the same deformation of the specimen thus in different time step values as the loading velocity changes.

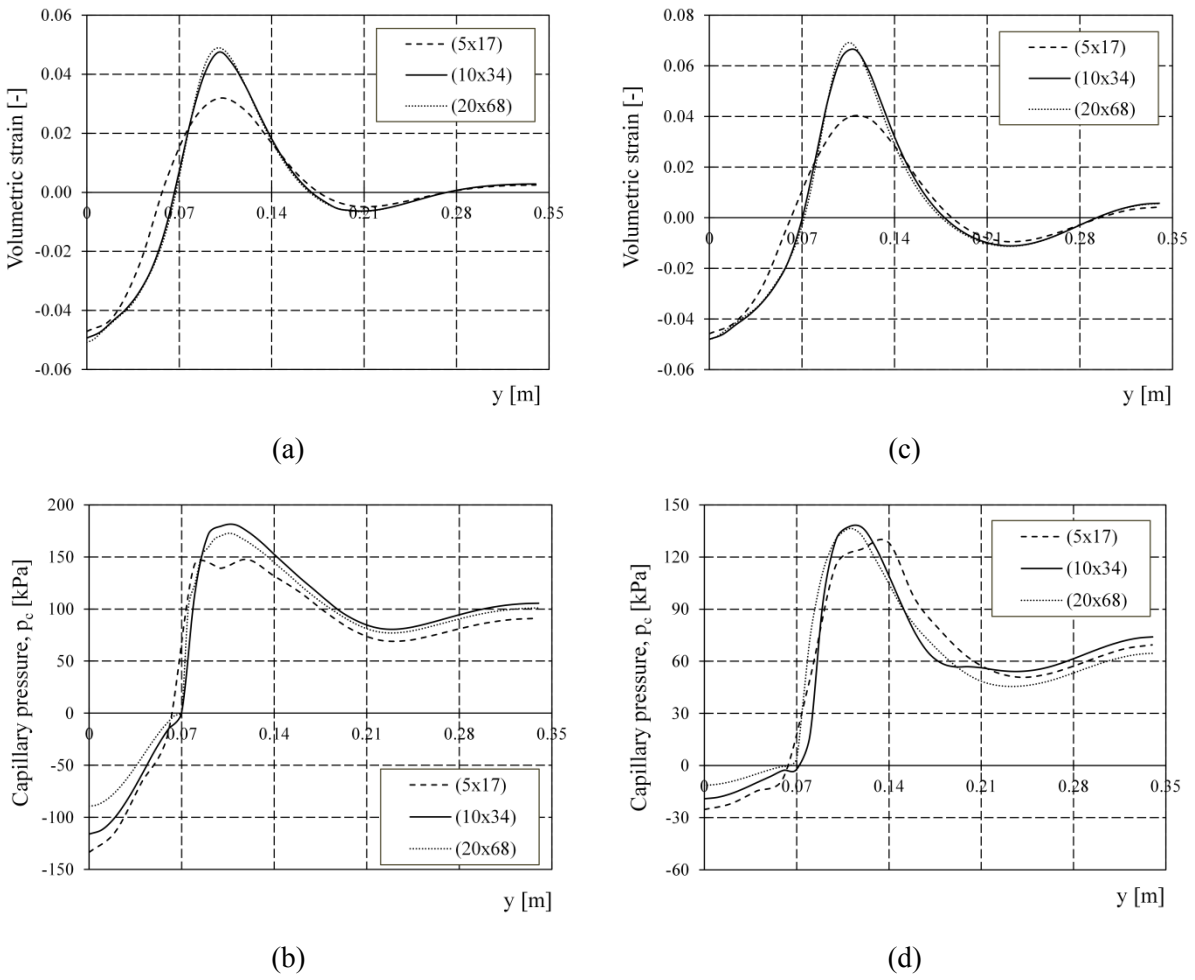

Figure 4.9: Profiles for volumetric strain (top) and capillary pressure (bottom) computed with v=1.2 mm/s and η=30 s (a), (b) and computed with v=0.2 mm/s and η=110 s (c) and (d), respectively.

According to laboratory observations, under globally undrained conditions, the increment of the void ratio due to volumetric plastic deformations will cause the water pressure to drop.

In both cases the positive values of the volumetric strains are accompanied by the development of capillary pressure desaturating the inelastic zones. Moreover, Figure 4.9 shows similar volumetric strain distribution for the two applied loading rates. The results indicate consistency between the developed viscoplastic deformation and the capillary pressure, as the higher values of the later are detected within the localization zone, as expected. Regularized behaviour is apparent also for the fluid part with the coarser mesh showing again slightly different results.

It is noteworthy that positive values of capillary pressure are observed on the upper part of the sample, while the volumetric strains are negative indicating absence of dilatancy. However in the adjacent sections excessive dilatant behaviour occurs explaining the development of capillary pressure. This excessive dilatant behaviour owes to the fact that when very large values of viscosity are considered to regularize the solution, the development of viscoplastic strains is delayed or rather suppressed and so higher deformation of the specimen are necessary to obtain the shear band. Dilatant behaviour occurs also outside of the shear zone and consequently almost all the sample becomes partially saturated at the end of the analysis.

- Influence of Permeability

A case of different permeability value under the same applied loading (v=1.2 mm/s) and the same viscosity (η=30 s) is studied to investigate the influence of soil permeability on the development of strain localization. The results are presented here only for the finer mesh.

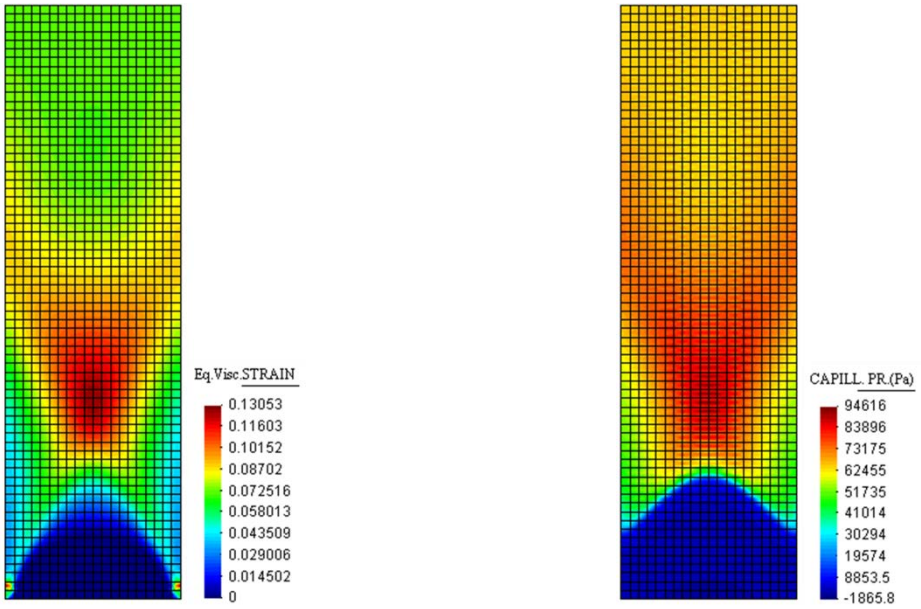

(a) (b)

Figure 4.10: Contours for the (a) equivalent viscoplastic strain and (b) capillary pressure, for the fine mesh (20 × 68), viscosity η=30 s and permeability $k=10^{-3}$ m/s.

Comparison between Figure 4.5d with the initial (lower) permeability ($k=10^{-7}$ m/s) and Figure 4.10a with $k=10^{-3}$ m/s, shows a diffused failure mode in the specimen with higher permeability. The plastic zone spreads over the whole structure owing to the fact that the pore fluid can easily escape from the domain into neighboring locations.

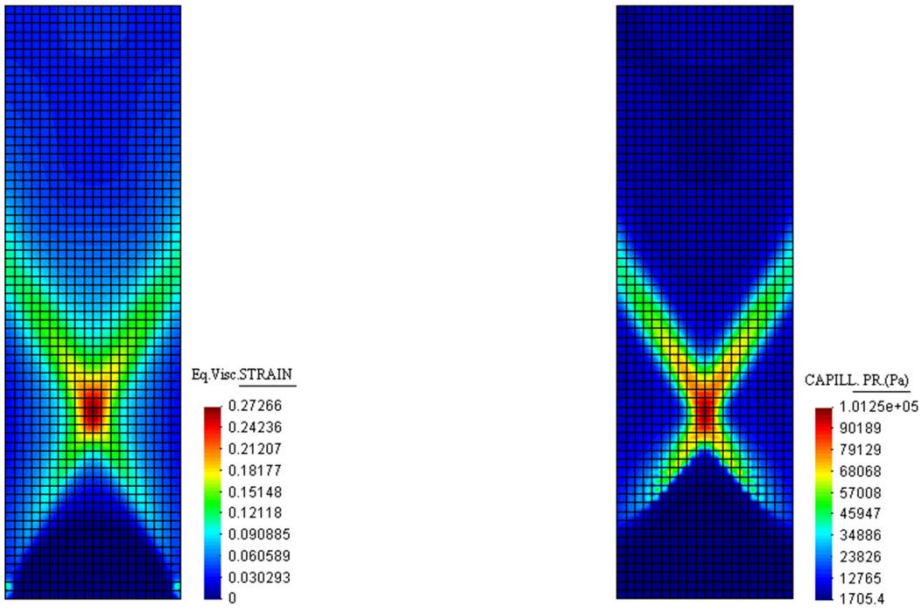

(a) (b)

Figure 4.11: Contours for the (a) equivalent viscoplastic strain and (b) capillary pressure, for the fine mesh (20 × 68), viscosity η=10 s and permeability k= 10^{-3} m/s.

The value of permeability affects the coupling between the solid and the fluid phases and in conjunction with the viscosity parameter influences the development of strain localization. In fact interpreting the figures above, it can be seen that permeability plays a role in defining the width of the inelastic zone acting as an additional internal length parameter.

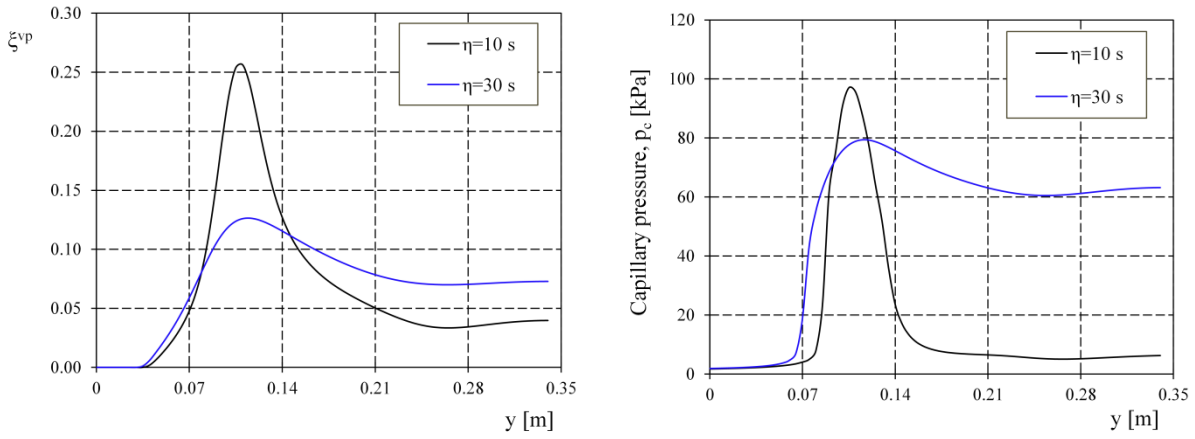

(a) (b)

Figure 4.12: Profiles of (a) equivalent viscoplastic strain and (b) capillary pressure in the vertical centre section of the specimen, for permeability k = 10^{-3} m/s and varying viscosity for (20 × 68) mesh.

Similar analyses were performed also for more permeability values within the presented limits and the results showed the same trend; therefore they are not presented for brevity.

This spreading of the plasticity zone caused by using higher permeability tends to disappear with reducing the value of viscosity thus approaching the elastoplastic limit. This is clearly demonstrated in Figure 4.11 and Figure 4.12 where the permeability is kept fixed to the higher value of 10^{-3} m/s and the viscosity is set equal to 10 s. In this case the viscoplastic zone is concentrated inside the shear bands and their width is mainly governed by viscosity. Further decrease of viscosity drives to mesh dependent solution, similar to the one depicted in Figure 4.2d, regardless of the value of permeability.

These results are in consistency with previous theoretical studies in Zhang et al. (1999), Zhang and Schrefler (2004). According to these authors, due to the presence of the gradient term in the fluid continuity equation through Darcy's law, an internal length scale is naturally introduced under dynamic loading. This internal length is mainly depended on permeability. However, this is not valid under quasi-static loading where without a regularization tool there is no internal length parameter naturally introduced by the multiphase model.

In particular, the numerical results presented in this sub-section showed that in quasi-static process the internal length scale given by the liquid water motion is evident only when the viscous effects are intense. Based on this, the more viscous the material, the stronger is the coupling with the value of permeability.

- Loading Rate Effect: Quasi-Static vs. Dynamic

Most factors affecting soil behaviour are equally important under both dynamic and quasi-static loading conditions. However, the significant characteristic of the dynamic response is the inertia force and its importance increases with the load application rapidity. To understand the dependency of the viscous regularization on the rate of the applied displacement the same example utilized in the previous sections is solved using the model described in Section 2.6.4.1. Dr. T. D. Cao.

A vertical displacement increment of 1.2 mm/s is applied on the top surface of the dense Hostun sand sample. Figure 4.13 and Figure 4.14 shows the equivalent viscoplastic strain profiles for a horizontal section at y=0.1 m and for a vertical centre section respectively, for two values of viscosity η=20 s and η=30 s. The value of 30 s seems to regularize the problem giving results that are mesh insensitive and objective. It should be noted that the same viscosity value leads to regularized solution also in the Quasi-Static solution.

The contours of the positive volumetric strain (Figure 4.15a,b,c) emphasizes the dilatant behaviour of the shear bands as positive values develop inside the inelastic zones. As a consequence, water pressure decreases inside the shear bands up to the development of capillary pressure (Figure 4.15d,e,f), desaturating the plastic zones.

To investigate further the effects of dynamics, Figure 4.16 presents a comparison with the corresponding quasi-static solution. In particular, Figure 4.16 shows the time histories of equivalent

viscoplastic strain, capillary pressure and liquid water saturation, inside the shear band at coordinates x=5 cm and y=10 cm. The dynamic solution is delayed in terms of equivalent viscoplastic strain as smaller values are observed in comparison with the corresponding of the quasi-static analysis.

Moreover, a significant difference is depicted between the dynamic and quasi-static solution for the fluid variables (capillary pressure and water degree of saturation). For the dynamic solution the capillary pressure occurs higher than in the quasi-static and a more profound decrease of the degree of saturation is observed. The response allows us to infer that the dynamic solution is smoother than the quasi-static one, which is attributed to the stabilizing effect of the mass matrix.

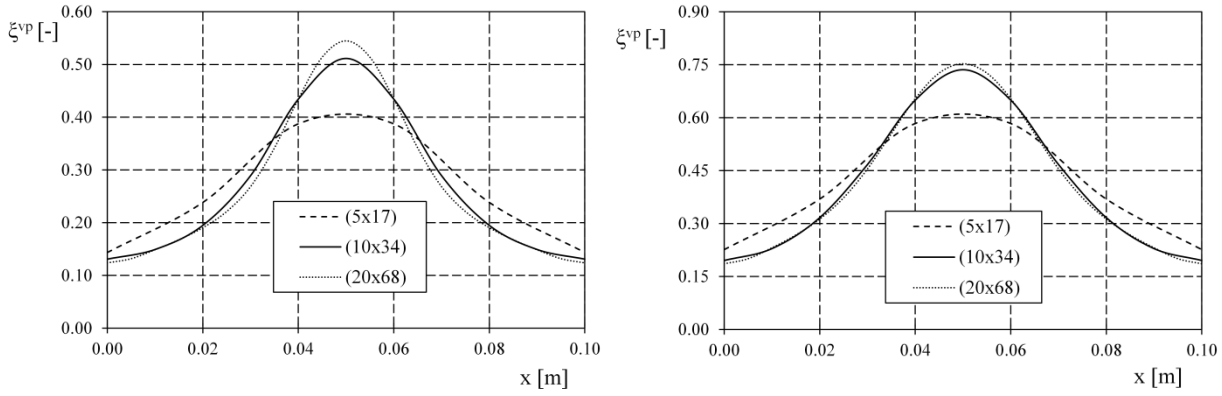

(a) (b)

Figure 4.13: Dynamic loading: Profiles of equivalent viscoplastic strain for (a) η=20 s and (b) η=30 s in the horizontal section (y=0.1 m) of the specimen, for the three meshes.

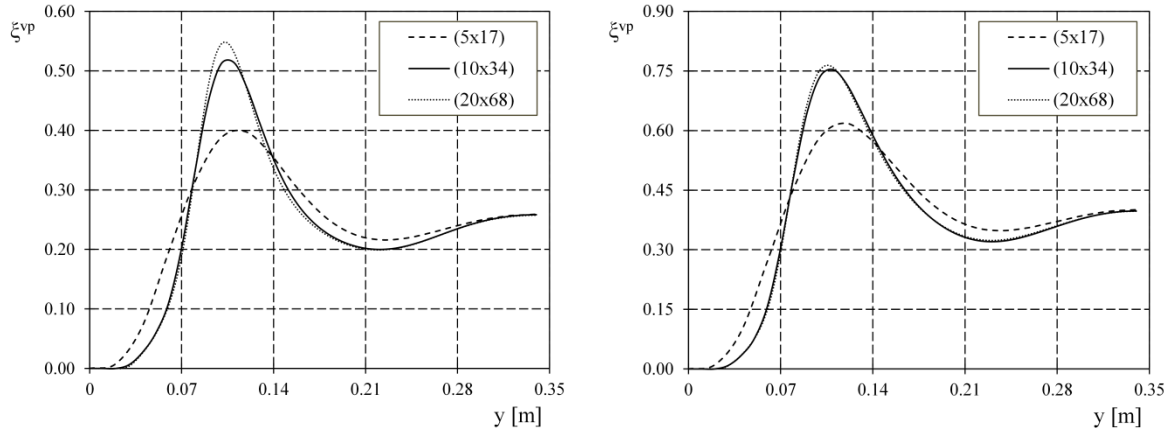

(a) (b)

Figure 4.14: Dynamic loading: Profiles of equivalent viscoplastic strain for (a) η=20 s and (b) η=30 s in the vertical centre section of the specimen, for the three meshes.

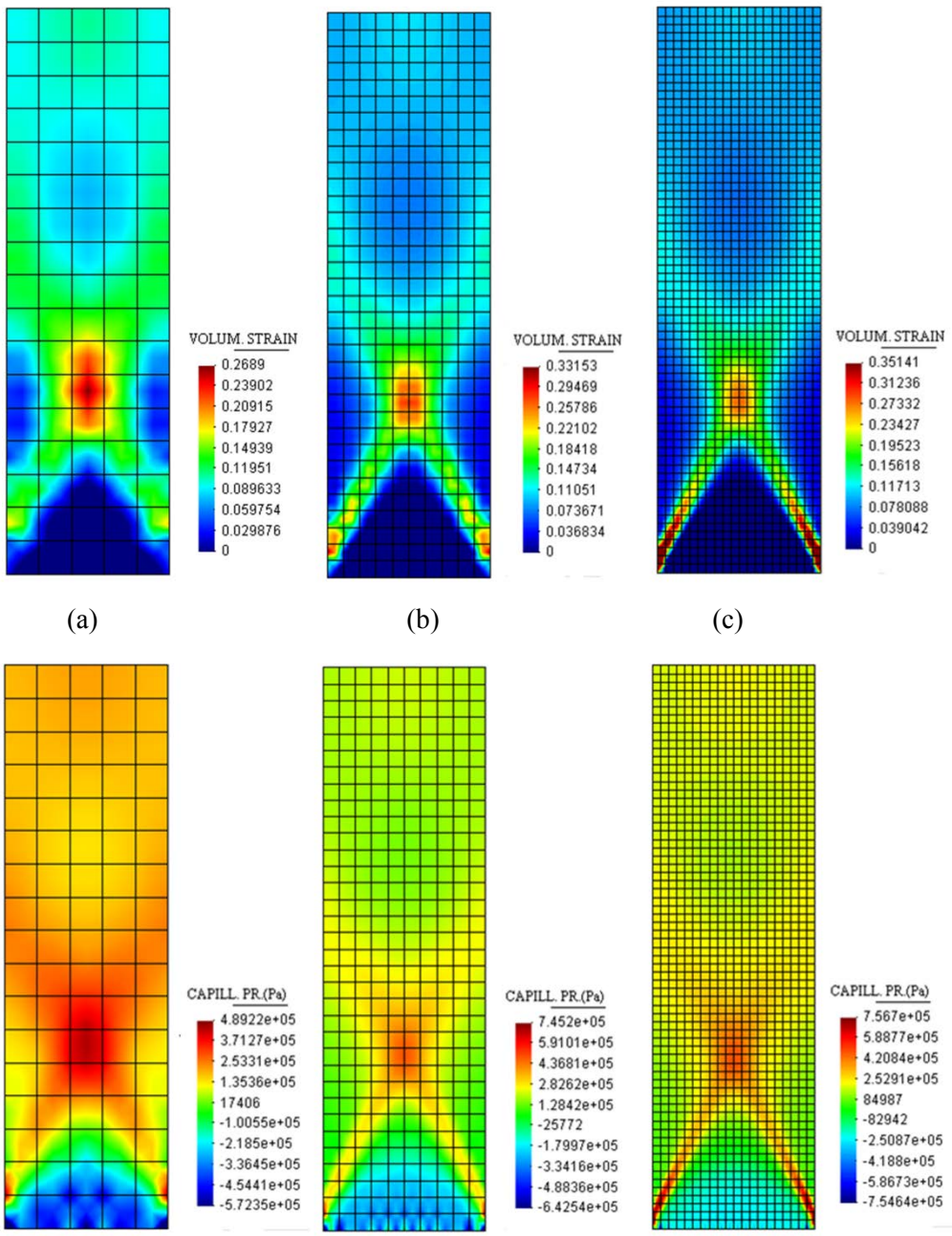

Figure 4.15: Dynamic loading: (a), (b), (c) volumetric strain and (d), (e), (f) capillary pressure contours in case viscosity is η=30 s for the three meshes, respectively.

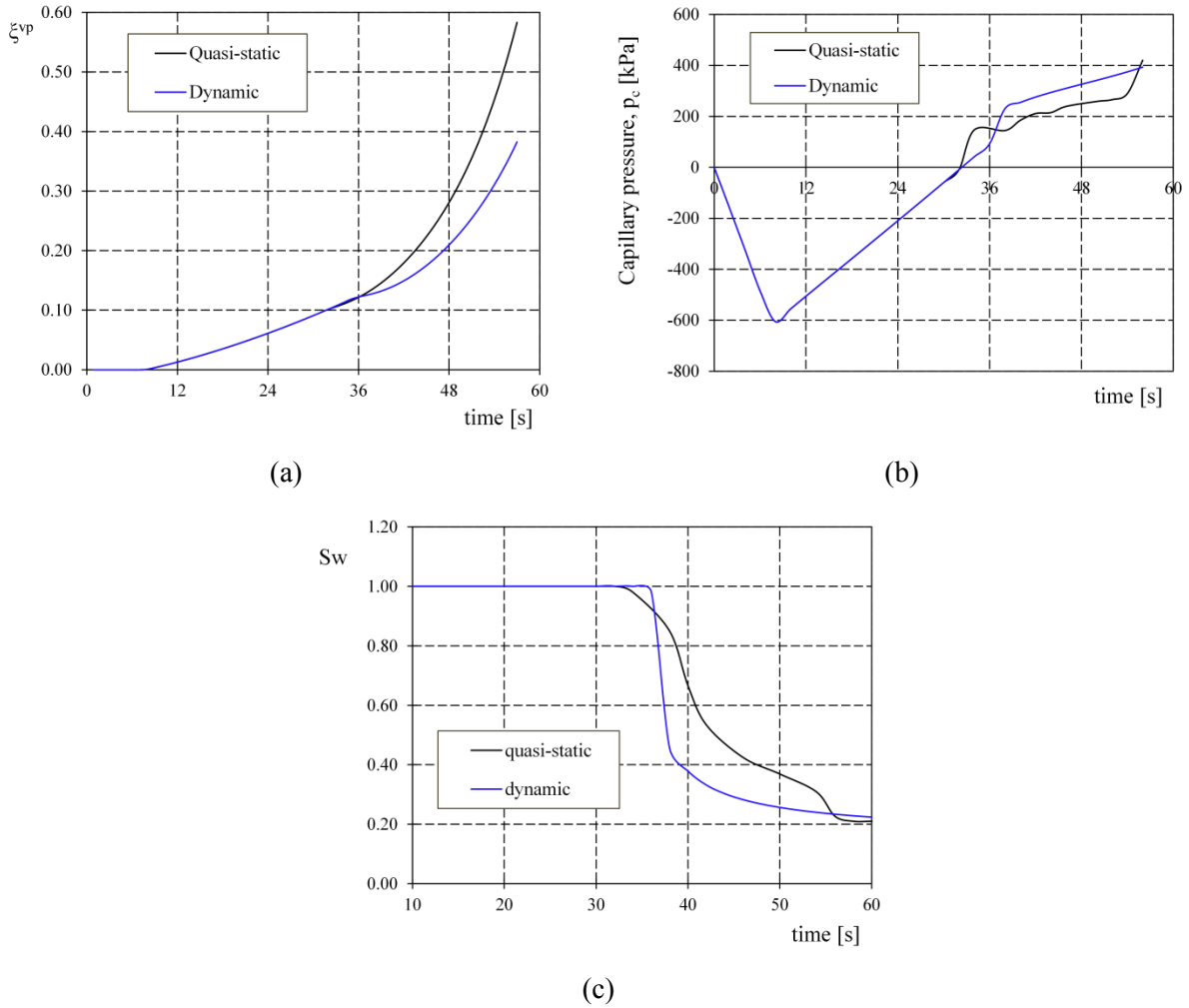

Figure 4.16: Comparison between dynamic and quasi-static solution inside the shear band for (a) equivalent viscoplastic strain, (b) capillary pressure and (c) liquid water saturation for (10 × 34) mesh.

- Effect of Drainage

From laboratory observations it is well known that the impose of drained or undrained conditions influences the onset and development of strain localization in the specimen. The fluid flow cause significant differences in the mechanical response depending on the drainage conditions.

In order to examine the effect of drainage conditions on viscous regularization, the exact same sample described on the introduction of Section 4.2 is used applying drained instead of undrained constrain.

From Figure 4.17, it can be observed that under drained conditions the formation of the shear band differs. In the undrained conditions the shear band reached the bottom of the specimen whereas in the drained conditions it is mostly concentrated in the middle. However the most important observation is that for viscosity greater or equal to 5 s a diffused deformation occurs and a regularized response is obtained for viscosity approximately 0.5 s. This is in contrast with the undrained conditions in which a viscosity of 30 s is needed for regularization purposes.

Thus in drained conditions a quite smaller value of viscosity seems to be needed to preserve regularization. Conclusively the value of viscosity for regularization of the problem is greatly affected by the response of the liquid phase.

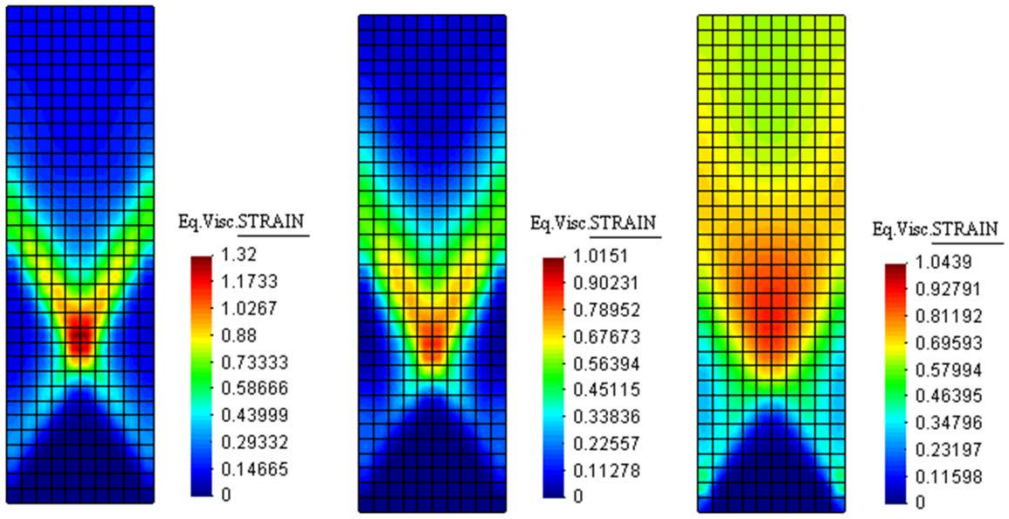

(a) (b) (c)

Figure 4.17: Drained conditions: Equivalent viscoplastic strain contours for viscosity (a) η=0.5 s, (b) η=1 s and (c) η=5 s, for the (10 × 34) mesh.

4.2.3 Viscous Regularization – Duvaut-Lions Model

In this section the viscoplastic model of Duvaut-Lions as described in Section 3.4 is applied and the regularization effect of model's formulation is examined.

As it has been mentioned the model possesses the same deficiencies of the inviscid material formulation when the limiting condition $\Delta t/\tau \to \infty$ (where τ the relaxation time of the material) is reached. Moreover, for $\Delta t/\tau \to 0$ the viscoplastic prediction approaches the elastic solution. These limits set the boundaries within which the viscoplastic solution affects the overall mesh dependent behaviour of the examined problem.

Herein, the relaxation time is varied over a very wide rage (from $1 \cdot 10^{-5}$s up to $5 \cdot 10^{4}$s), keeping all the other parameters the same as in the initial numerical example.

The numerical validation of the implementation of the model in Comes-geo code, is presented in Figure 4.18. This figure shows the contours of the volumetric and the equivalent plastic strain with varying the ratio $\Delta t/\tau$ towards the two limiting bounds (Figure 4.18a and Figure 4.18e). In case $\Delta t/\tau$ is set equal to $2 \cdot 10^{-7}$, (Figure 4.18b), the elastic solution is obtained and the volumetric strain is identical to the elastic case, Figure 4.18(a). In reverse, for a large value of $\Delta t/\tau$, (Figure 4.18d) the equivalent viscoplastic strain approaches the inviscid elastoplastic case, Figure 4.18e. The viscoplastic mesh insensitive solution is obtained for the intermediate value of $\Delta t/\tau$=0.033, for which the localization zone of the viscoplastic deformations exceeds the element size as indicated in Figure 4.18c.

The following figures illustrate the localization properties of the viscoplastic Duvaut-Lions model. To control rate effects one can either vary Δt while fixing τ, or vary the relaxation time while fixing Δt. Figure 4.19 shows the effect of varying the relaxation time in terms of equivalent viscoplastic strain and water degree of saturation when the intermediate mesh with 10x34 elements is used. Increasing the value of relaxation time τ, results in a delayed or rather suppressed response of the plastic deformation, which means lower values of equivalent viscoplastic strain for a given deformation level. Consistent response is also obtained for the water degree of saturation due to the coupling between solid and fluid phases (Figure 4.19b).

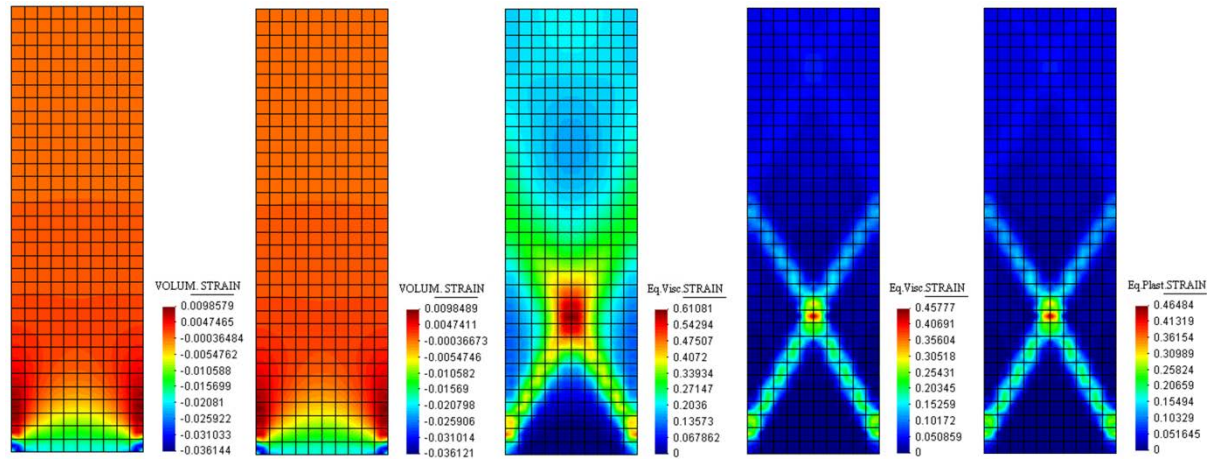

Figure 4.18: Contours for numerical validation of Duvaut-Lions model (a) elastic solution and viscoplastic solution with (b) $\Delta t/\tau = 2 \cdot 10^{-7}$, (c) $\Delta t/\tau = 0.033$ and (d) $\Delta t/\tau = 1000$ and (e) elastoplastic solution for the intermediate (10 × 34) mesh.

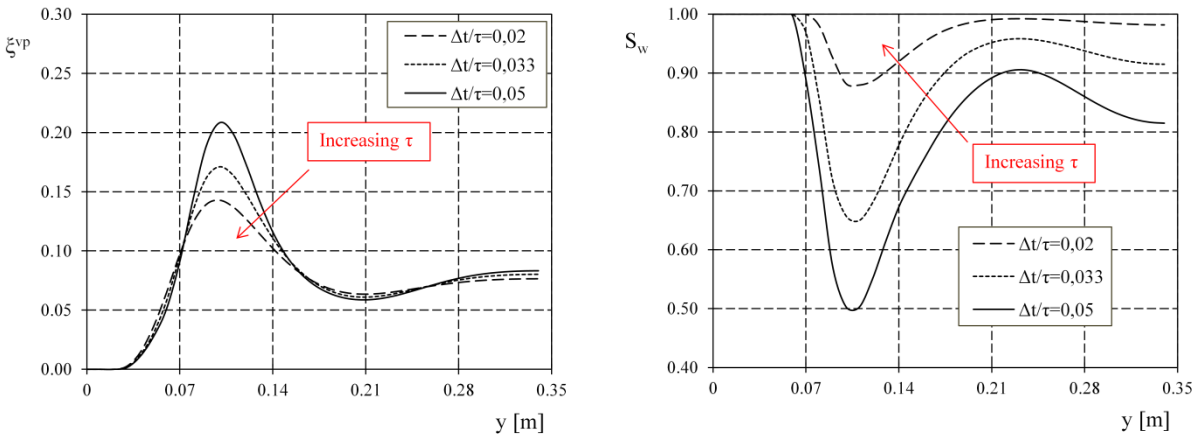

Figure 4.19: Profiles varying Δt/τ for (a) equivalent viscoplastic strain and (b) water degree of saturation.

The regularization capabilities of Duvaut-Lions viscoplasticity are illustrated in Figure 4.20 when the three different meshes are considered. The profiles in this figure show the distribution of equivalent plastic strain, capillary pressure and water degree of saturation respectively, along a

vertical section cut in the middle of the examined specimen, for $\Delta t/\tau$=0.033. The mesh refinement has no influence on the results obtained by meshes with 10x34 or more elements. The width of localization zone is almost identical and desaturation, following the pattern of viscoplastic strains, is depicted mainly in the same area.

It is also remarkable that the viscoplastic Duvaut-Lions model approximates the solution obtained by applying Perzyna's model when the relaxation time equals to $1/\eta$.

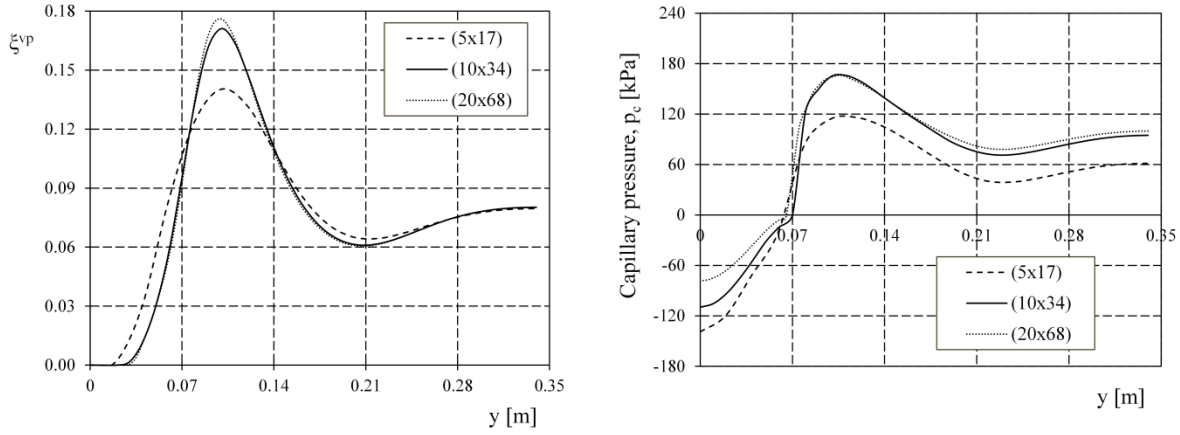

(a)

(b)

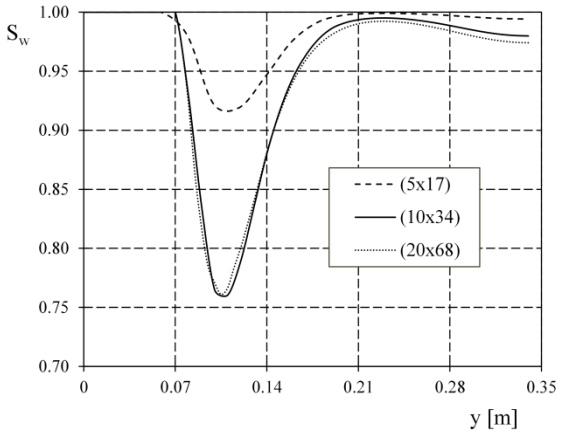

(c)

Figure 4.20: Profiles at $\Delta t/\tau$ = 0.033 for (a) equivalent viscoplastic strain, (b) capillary pressure and (c) water degree of saturation for three meshes.

4.2.4 Non-local Regularization

Discussing the regularization effect of the non-local approach three values of the internal length scale 7.5, 10 and 20 mm are used. The first value agrees with the thickness of the shear band experimentally measured by Mokni and Desrues in undrained plane-strain test on dense Hostun RF sand (SHFND02). The other two values are used to consider the influence of the non-local contribution on the solution by varying the internal length scale.

As far as the viscosity parameter is concerned, a value (η=10 s) resulting in a mesh dependent solution with the local viscoplastic model of Perzyna is firstly adopted to emphasize the effectiveness of the non-local application. Table 4.2 summarizes the set of non-local analyses performed with constant viscosity value. As with the simulations with the local viscoplastic regularization methods, calculations are carried out on different meshes consisting of 340 up to 5440 finite elements. For the coarse mesh (5 x 17) the distance between the gauss points is larger than the examined internal length (and subsequently the interaction radius R) and therefore this mesh will not be used in the nonlocal formulation. It can be observed that for small values of the non-local internal length l, the non-local solution approaches the local one. This effect is shown in Figure 4.21 where the difference between the non-local and the local solution tends to disappear for smaller values of l and is a form of numerical validation of the non-local model in the code.

Table 4.2: Non-local viscoplastic analyses for constant viscosity, η=10 s.

Meshes	10 x 34	20 x 68	40 x 136
Non local internal length l (m)	0.0001		
	0.002		
	0.0075	0,0075	0.0075
	0.01	0.01	0.01
	0.02	0.02	0.02

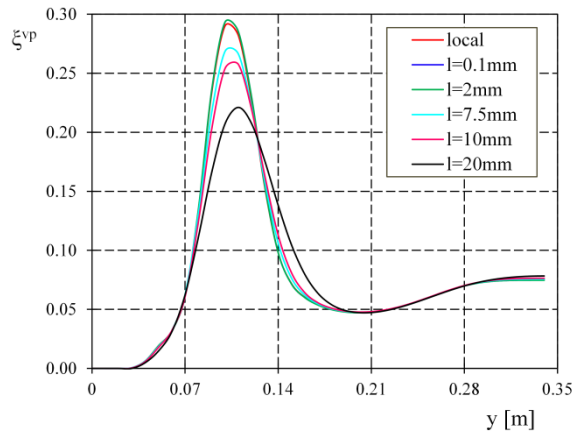

Figure 4.21: Non-local approach: distribution of equivalent viscoplastic strain, varying the internal length l for constant viscosity, η=10 s (10 × 34 mesh).

Again a mesh-insensitive behaviour can be recognized in Figure 4.22 where the contours for the equivalent viscoplastic strain are shown for the three meshes (top 10x34; middle 20x68; bottom 40x136) with varying internal length l. Starting the calculations with a spatial resolution of 340 elements each mesh refinement leads to almost equal results; increasing the values of the internal length the shear zone width increases up to the value of l and the maximum value of the viscoplastic strains decreases. This is not the case for the local viscoplastic analysis, in which the localization band width is limited to the size of the element once the discretization is refined.

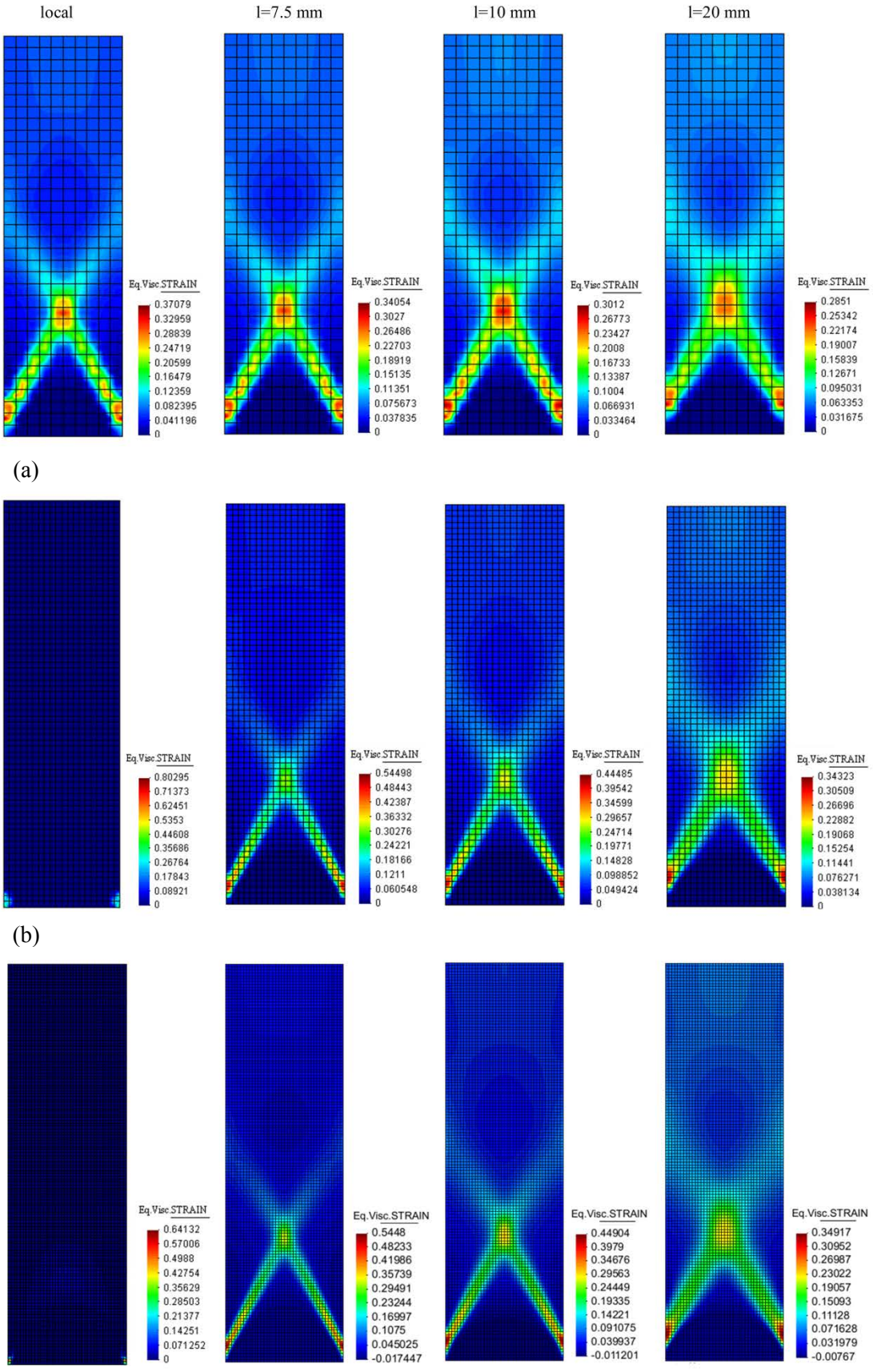

Figure 4.22: Non-local approach: equivalent viscoplastic strain contours, changing the internal length l, keeping constant η=10 s for (a) 10 × 34 mesh, (b) 20 × 68 mesh and (c) 40 × 136 mesh. Comparison with corresponding local solution.

In Figure 4.23, the time evolution of equivalent viscoplastic strain in the mid-point of the shear zone (coordinates: 0.05, 0.1) is illustrated, with different values of l and the three meshes examined. The response of the numerically simulated sample using different meshes is consistent for all meshes with element size less than the length scale l. If the element size is greater or equal to the characteristic nonlocal length scale, as in case of 10x34 mesh in Figure 4.23a and b, a non-adequate number of integration points fall in the shear zone and the solution deviates from the one depicted for sufficiently fine discretizations (Figure 4.23, meshes 20x34 and 40x136). This fact is recognized as the main obstacle in applying a non-local approach, because a minimum mesh density is necessary to activate the nonlocal interaction (Rolshoven and Jirásek (2003)).

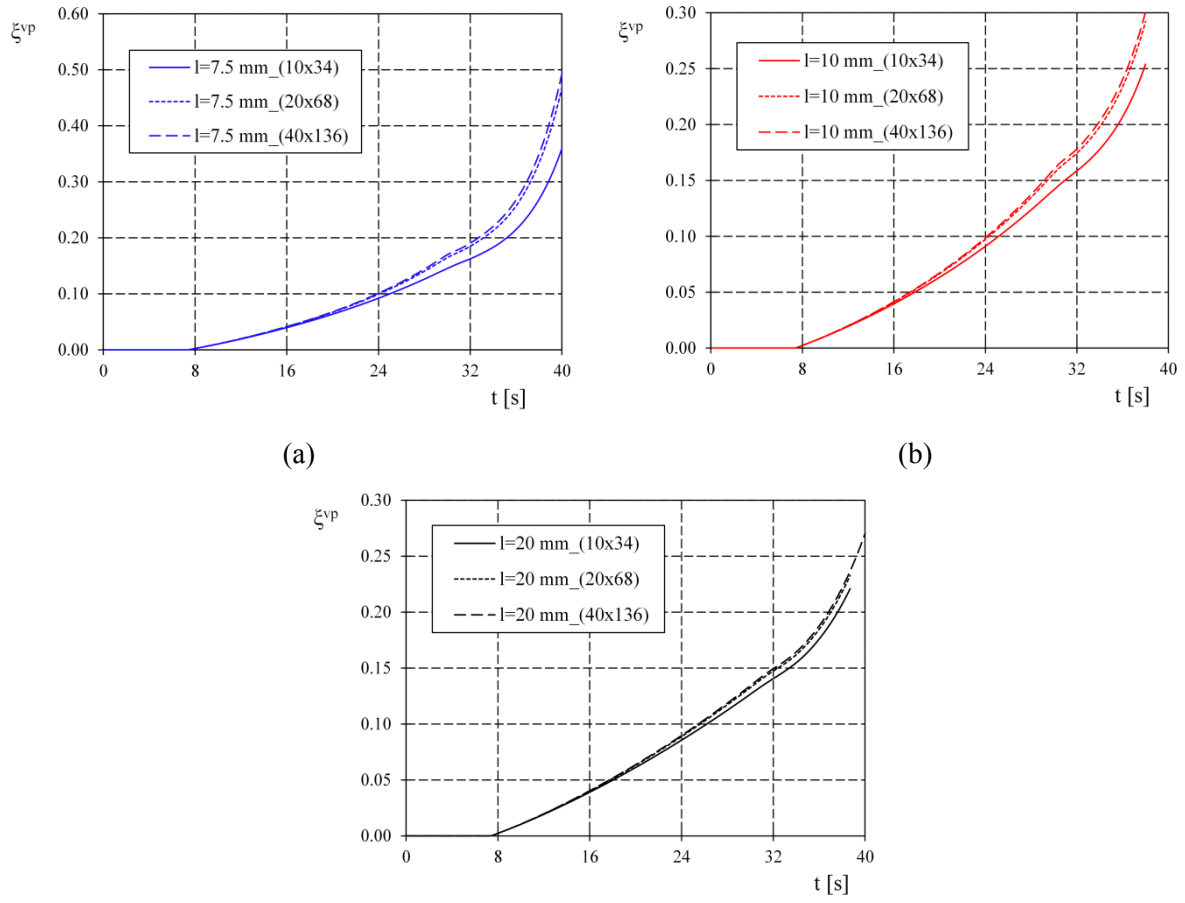

Figure 4.23: Non-local approach: time evolution of equivalent viscoplastic strain in the midpoint of shear band (coordinates: 0.05, 0.1) for (a) l=7.5 mm, (b) l=10 mm and (c) l=20 mm.

- Effect of Suction

In this subsection, the emphasis lies on the relation between water suction and strain localization occurrence within the non-local approach.

In Figure 4.24, the volumetric response as well as the time evolution of capillary pressure (which is actually the suction), vapour pressure and water degree of saturation within (Point A→ coordinates:

0.01, 0.03) and outside (Point B → coordinates: 0.05, 0.03) the shear band is illustrated, for two discretizations. For brevity, only the case with l=7.5mm is presented.

It is observed that, due to the contraction of sand at the beginning of the loading, negative capillary pressure is built initially. As soon as localization takes place the material dilates inside the shear zone whereas outside the shear zone it remains compressed as revealed by the negative values of the volumetric strain (Figure 4.24a). Pore water pressure decreases up to the development of capillary pressure (Figure 4.24b and Figure 4.25) accompanied by desaturation in the strain localized zones (Figure 4.24c and Figure 4.26).

As further novelty of the applied non-local model, cavitation (phase change of the liquid water to vapour) occurs at the point the water pressure decreases below the vapour saturation pressure (Figure 4.24d). Vapour can dilate almost freely and this results to pore volume increase in the specimen. In such conditions, the undrained specimen cannot be constrained to isochoric deformation.

It should be noted that once more the response of the points is identical regardless of the discretization.

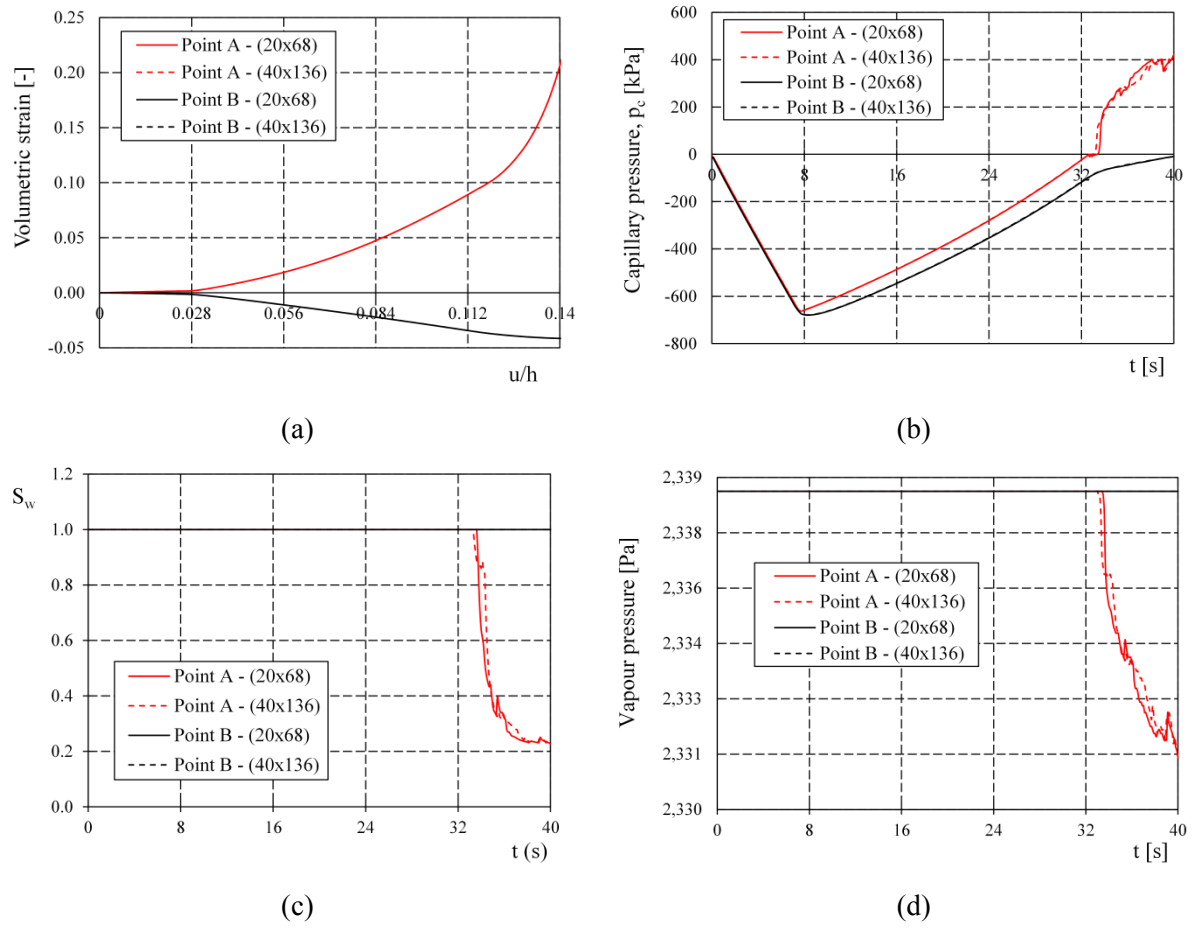

Figure 4.24: Non-local approach: (a) volumetric strain versus normalized vertical displacement, time evolution of (b) capillary pressure, (c) water degree of saturation and (d) vapour pressure, for points A (inside the shear band) and B (outside the shear band), for 20 × 68 and 40 × 136 meshes (l=7.5 mm and η=10 s).

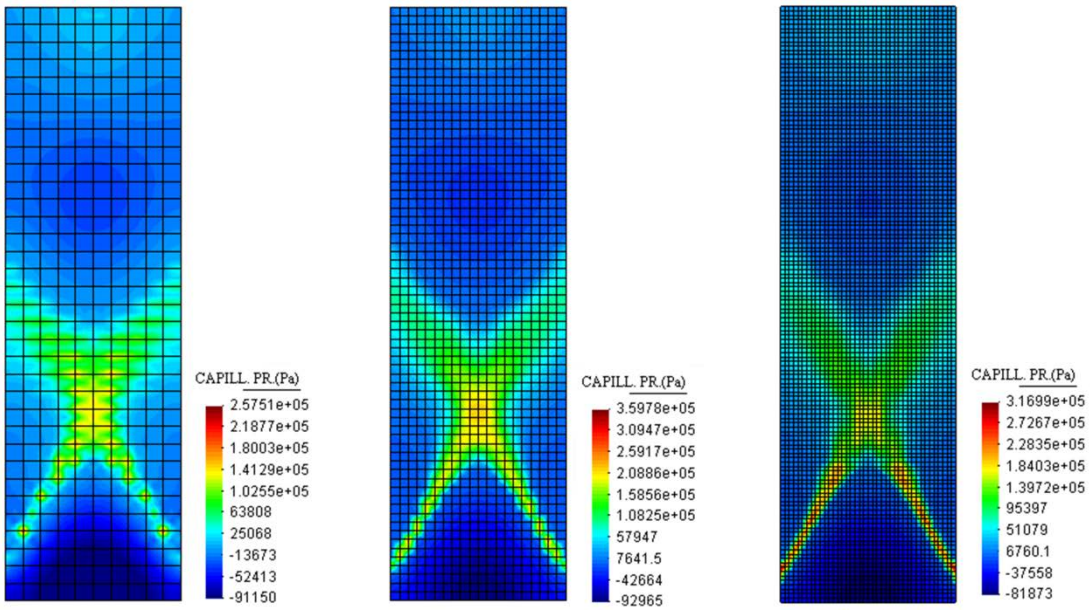

(a) (b) (c)

Figure 4.25: Non-local approach: capillary pressure contours for (a) 10 × 34 mesh, (b) 20 × 68 and (c) 40 × 136 mesh for l=7.5 mm and η=10 s.

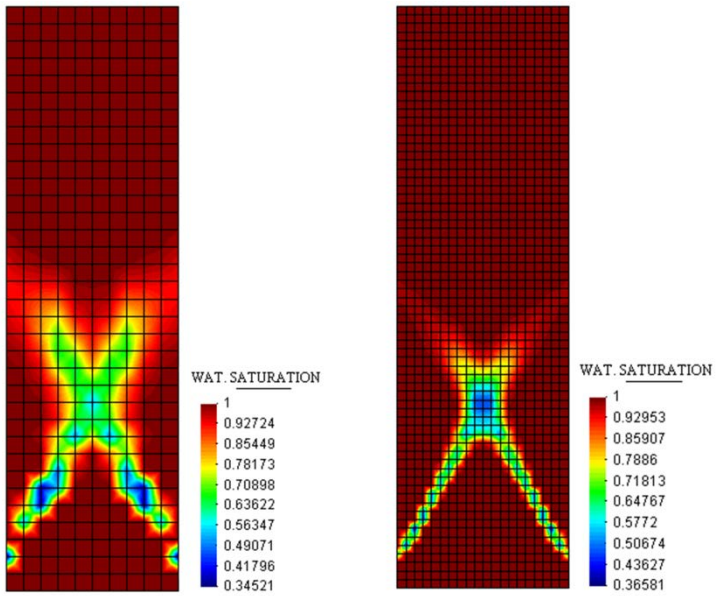

(a) (b)

Figure 4.26: Non-local approach: liquid water saturation contours for (a) 10 × 34 mesh and (b) 20 × 68 mesh for l=7.5 mm and η=10 s.

4.2.4.1 Internal Lengths Interaction

In Figure 4.27 the interaction between the characteristic lengths coming out from viscosity and non-locality is investigated. In Figure 4.27a, b and c the results for the simulations on the fine mesh (20x68) with different values of viscosity and constant internal length are illustrated. Increasing the viscous parameter the width of shear zone increases for all the internal lengths examined.

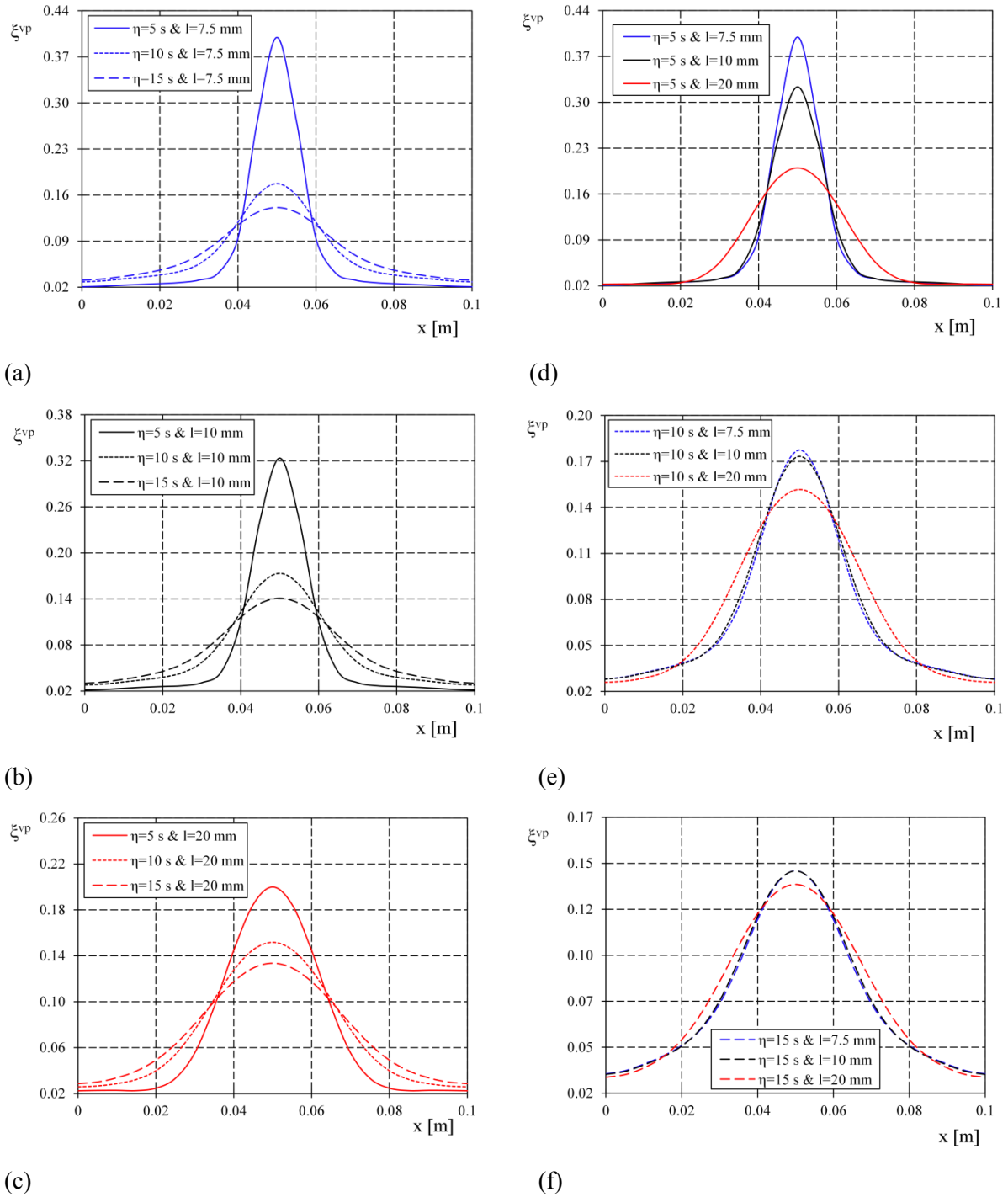

Figure 4.27: Non-local approach: equivalent viscoplastic strain in the horizontal section (y = 0.1 m) for varying (a), (b), (c) viscosity and (d), (e), (f) internal length (20 × 68 mesh).

In the same way, in Figure 4.27d, e and f viscoplastic strains are presented for different values of the internal length and constant viscosity. For small viscosity value (η=5 s), variation of the internal length leads to significant impact on the shear band width and the maximum value of the viscoplastic strain. This behaviour tends to disappear as viscosity increases. Indeed, in case viscosity is equal to 15 s the difference between the non-local solutions is almost negligible and the viscous regularization seems to dominate the non-local one. This leads to infer that the internal length implicitly introduced

by viscosity is larger than the internal lengths explicitly entered by the non-local contribution and therefore the solution coincides.

This is a very interesting result of the coupled use of viscosity and non-locality. This coupled implementation allows for the regularization of the solution with either one of the techniques when the other may become insufficient. The internal length may lead to loss of benefit from the non-local approach and in this case viscosity can be modified to obtain mesh insensitive results. On the other hand, the value of viscosity may describe the behaviour of the material but not lead to regularized solution. In this case the value of the internal length can be adjusted to benefit from the non-local approach.

4.3 Hydro-Mechanical Coupling in a Plane-Strain Slope Stability Test

Landslides and slope failures are of utmost important because they may cause loss of human life, injuries and economic devastation. There is a wide variety of types of landslides and slope failures, depending on the triggering mechanisms, the propagation and the materials involved. They are caused by changes of effective stress induced by external forces and/or variation of the pore pressure, variation of the material properties and changes in geometry. In some cases the failure mechanism consists of a clearly defined localized zone and the objective modelling of the initiation and propagation of such events is the motivation of this research.

A hydro-mechanical analysis of a benchmark slope stability problem, inspired by Regueiro and Borja (2001), is now presented to demonstrate the importance of adopting some kind of regularization technique for the numerical simulation of shear band evolution.

A process of progressive strain imposed at the boundary of a simple slope consisting of homogeneous soil is considered. The dimensions and boundary conditions of the problem are shown in Figure 4.28 whereas the soil parameters adopted in the analysis are indicated in Table 4.3.

The initial stress field of this slope is reproduced by increasing the gravity acceleration up to 9.81 m/s^2. At the end of the gravity loading stage, the resulting displacements and strains are reset to zero. Next, a downward displacement with a constant rate of 10^{-3} m/s is imposed on a portion of 4 m on the top slope surface (Figure 4.28). Two meshes with 400 and 1600 eight node quadrilateral isoparametric elements are used to analyze the problem. No weak elements are specified since the boundary value problem inherently generates a non-uniform stress field where, as expected, the element adjacent to the corner of the vertical load localizes first.

Two cases have been simulated, assuming the slope either fully or partially saturated. The constitutive relationship for the water degree of saturation is that of Safai and Pinder. For the water and gas relative permeability, the relationship of Brooks and Corey in isothermal conditions is selected. Plane-strain condition is assumed in the computations. The analyses are performed using: the elastoplastic model, the local elasto-viscoplastic model of Perzyna with viscosity η=100 s and the

non-local elasto-viscoplastic model with an internal length of l=0.8 m, to evidence the thickness of the shear zone.

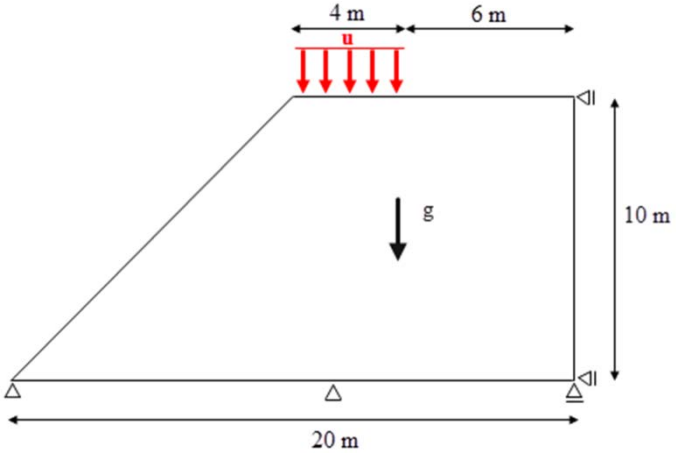

Figure 4.28: Slope stability problem. Geometry and boundary conditions.

Table 4.3: Material parameters for slope stability problem.

Parameter	Symbol	Value	SI unit
Young modulus	E	10	MPa
Linear softening modulus	h	-10	kPa
Initial apparent cohesion	c_0	40	kPa
Angle of internal friction	φ	10	(°)
Dilatancy angle	ψ	3	(°)
Poisson ratio	ν	0.4	[-]
Initial porosity	n	0.3	[-]
Solid density	ρ_s	2000	kg/m^3
Intrinsic water permeability	k	1.0E-10	m^2
Water unit weight	γ_w	10	kN/m^3
Gravity acceleration	g	9.81	m/s^2
Soil viscosity	η	100	s
SWCC parameter	α	1	[-]
SWCC parameter	ν	1.8	[-]
SWCC parameter	β	0.00007	cm^{-1}

Starting from a fully saturated state which describes the hydraulic conditions of the examined slope, the results for the three applied models are compared in Figure 4.29 in terms of equivalent (visco) plastic strain and in Figure 4.30 with the force-displacement plots.

The failure initiates in the element just to the right of the applied force and propagates in a manner depended on the angle of friction. When the elastoplastic constitutive model is used to solve this initial boundary value problem, a classical mesh dependent numerical solution is observed with the model being unable to simulate the failure process of the slope when the mesh is refined (Figure 4.29d). As is shown in Figure 4.29b, when the elasto-viscoplastic formulation of Perzyna is adopted, even if the number of elements is increased, the shear band formation and the force-displacement relationship (Figure 4.30b) are not affected by the element size. However, the peak value of the viscoplastic strain field depends on the element size of the mesh (Figure 4.29e). Finally, the non-local elasto-viscoplastic model is able to predict a clearly defined shear band and the slope's strain-softening response (Figure 4.30c) independently of the mesh adopted (Figure 4.29f).

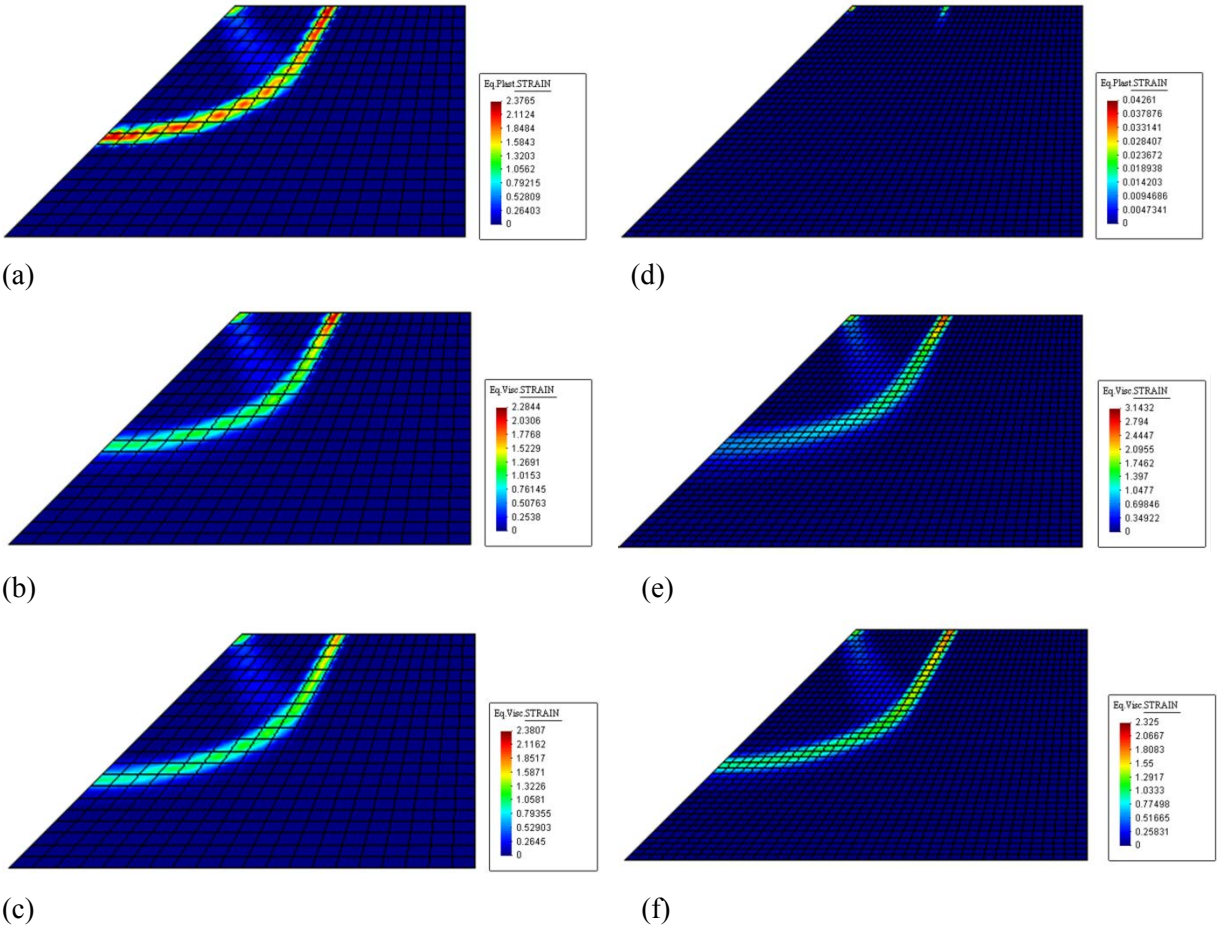

Figure 4.29: Equivalent visco-plastic strain contours as calculated using the elastoplastic, the local elasto-viscoplastic and the non-local elasto-viscoplastic model for a mesh consisting of 400 elements (a), (b) and (c) and for a mesh consisting of 1600 elements (d), (e) and (f), respectively.

As shown in Figure 4.29, the elastoplastic model can lead to the formation of a shear band failure for the coarser mesh used (with 400 elements). However, for the finer mesh (with 1600 elements) the solution is not acceptable and the analysis terminates with the concentration of plastic deformations in the vicinity of one, approximately, finite element. As in geotechnical engineering problems the size of the finite element mesh cannot be predefined in an ad-hoc manner, the need of the regularization

methods is clearly illustrated in this case. When applying the aforementioned regularization techniques, an objective solution is obtained regardless of the mesh adopted. This means that the shear band formation and the failure of the slope is the one expected, also for coarse and fine meshing.

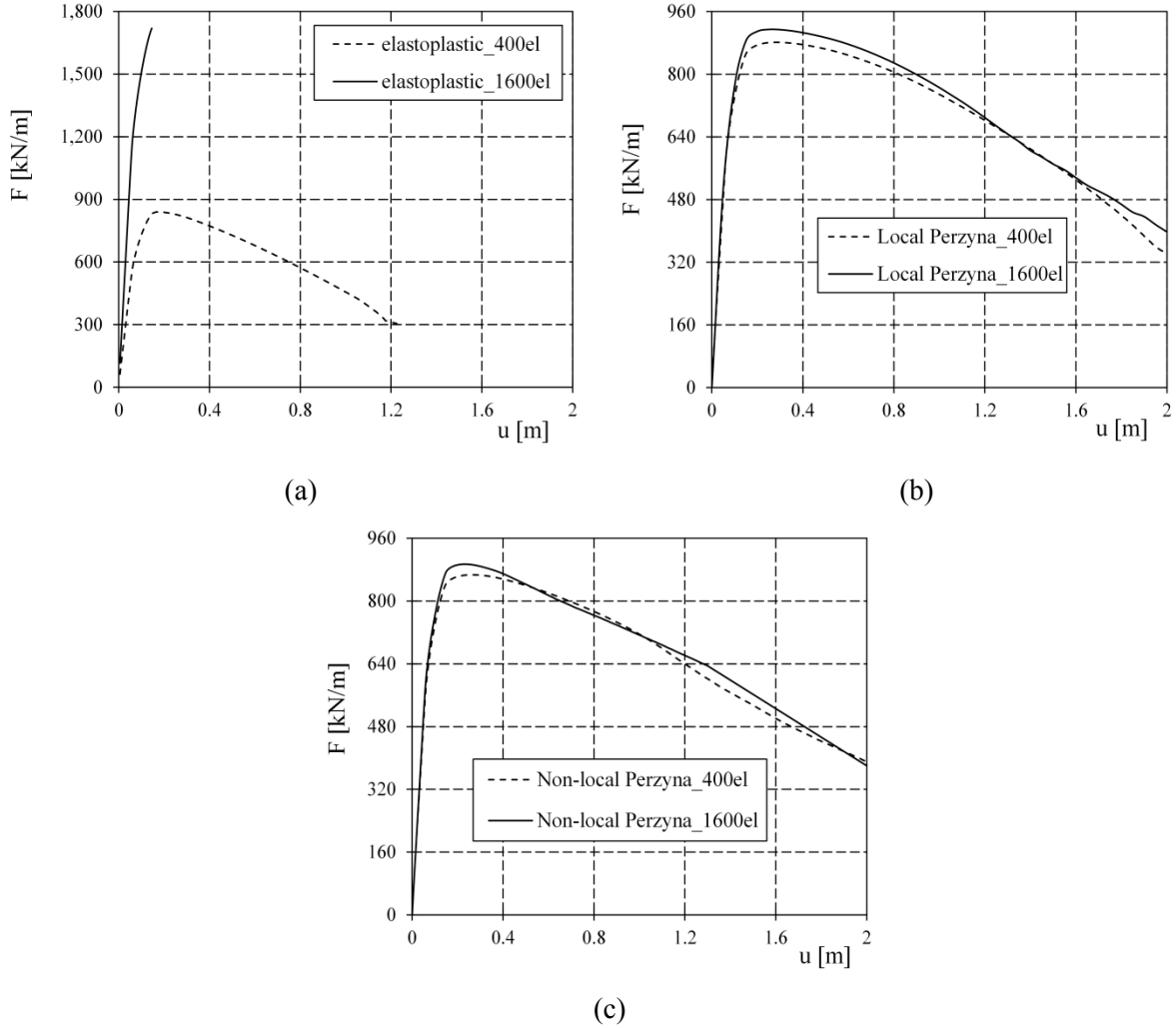

Figure 4.30: Force-displacement plots for the (a) elastoplastic model, (b) local elasto-viscoplastic model and (c) non-local elasto-viscoplastic model, for the two meshes.

After examining on the above the regularization capabilities of the applied models in the slope instability problem, in the following the response is studied under partially saturated conditions. For clarity, only the results for the non-local model are presented herein.

Figure 4.31 shows the results for the non-local Perzyna model for a coarser (with 400 elements) and a finer (with 1600 elements) mesh. In particular, the equivalent viscoplastic strain is plotted on the deformed mesh and the capillary pressure and water degree of saturation on the undeformed mesh at the same time step.

The equivalent viscoplastic strain (Figure 4.31a) has a lower maximum value in comparison to the fully saturated case (Figure 4.29c). This can be attributed to the strengthening of the material by the

presence of suction. Moreover, it is evident that the water suction occurs more pronounced into the localized shear zone (Figure 4.31b).

In Figure 4.32 the force-displacement plot is presented for the two meshes. It becomes directly apparent from the failure load that there is a significant influence of the variation of water saturation. In fact, comparing with the previous case (Figure 4.30c), there is an increase of the maximum load prior to failure of about 20% which is explained by the stabilizing effect of capillary pressure in the partially saturated zone.

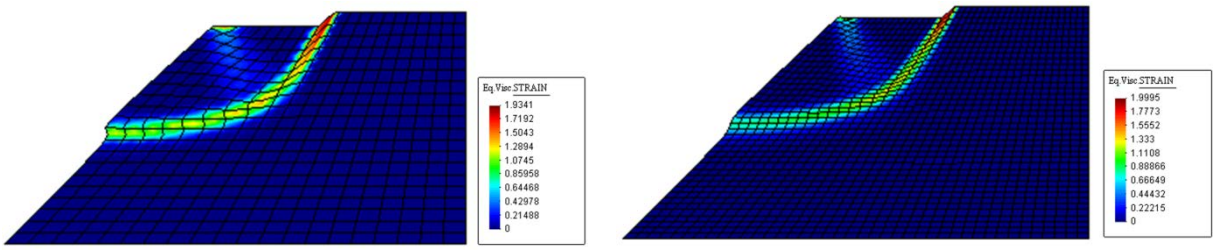

(a)

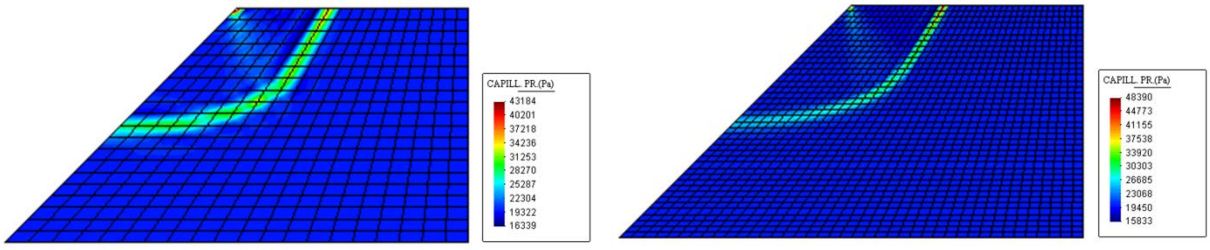

(b)

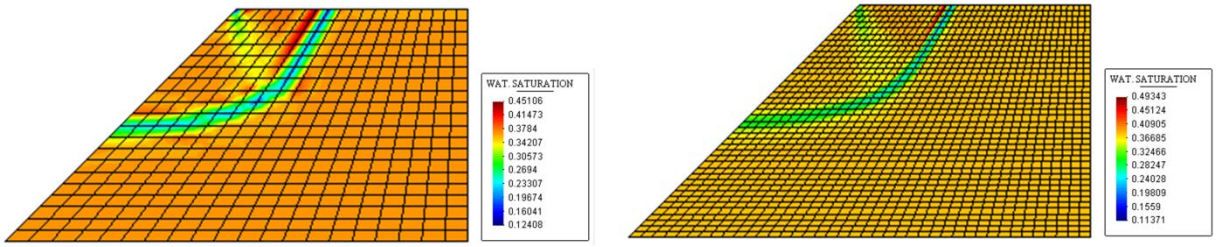

(c)

Figure 4.31: Non-local Perzyna model: (a) equivalent visco-plastic strain on the deformed mesh, (b) capillary pressure and (c) water degree of saturation for coarser (400 elements) and a finer (1600 elements) mesh.

As a closing remark, it is observed that despite the influence of the liquid phase on the response of the slope the non-local regularization is preserved.

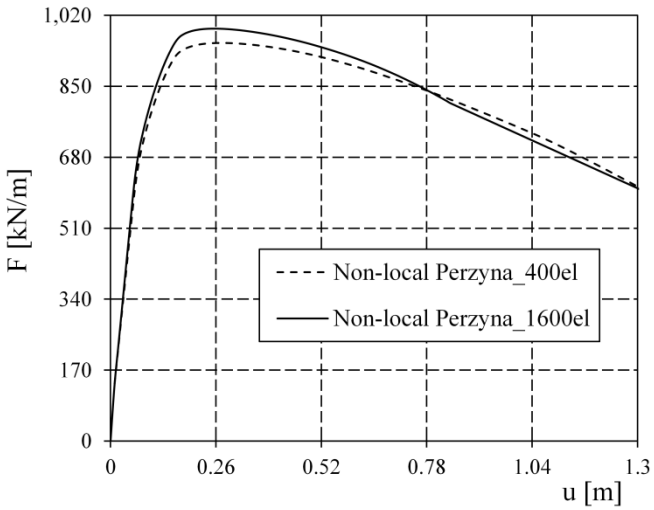

Figure 4.32: Force-displacement plot for the non-local elasto-viscoplastic model, for the two meshes.

4.4 Concluding Remarks

This Chapter discusses numerical aspects of strain localization analysis in multiphase porous media when local and non-local viscoplastic constitutive models are used for regularization purposes. The models are applied and their effectiveness is tested through a couple of numerical examples: an experimental plane-strain compression test on dense and isochoric sand and a slope failure problem.

The initiation and the propagation of the shear band are effectively described by means of FEM analysis, regardless of the mesh size adopted. The strain localization process realistically occurs within the shear band failure mode and its size is governed by the viscosity parameter and the internal length variable, which can be directly estimated by experimental tests.

Factors affecting the evolution of localization phenomena have been investigated in conjunction with viscous effects and the main conclusions can be drawn in the following:

1. The shear band width is not exclusively governed by the viscous parameter, but depends also on the applied loading velocity and soil permeability. These two factors delimit the value of viscosity which regularizes the numerical solution.
2. For a material characterized by a specific value of viscosity the effect of loading velocity is crucial for the regularization of the numerical solution. A relative low loading velocity demands high values of viscosity to obtain true mesh independence upon mesh refinement. The relationship between the loading velocity and the viscous regularization is linear and this can be attributed to the employed viscous nucleus.
3. Theoretical studies have underlined that in quasi-static processes, without a regularization tool, there is no internal length parameter naturally introduced by the multiphase model. In this work it is shown, that soil permeability plays a role in defining the width of the inelastic zone and interacts with viscoplasticity activating an internal length only when the regularizing influence of rate-

dependency is high. As soon as Perzyna's viscoplastic model approaches the elastoplastic limit the influence of permeability disappears and mesh sensitivity reemerges.

4. The viscosity governs the response of the specimen, causing a significant delay in the development of plastic strains and affects the evolution of water pressure due to the coupling between the solid and the fluid phase. Moreover, a different viscosity values seems to be needed to preserve regularization when drainage conditions change.
5. Viscoplasticity, in conjunction with the non-local approach governs the regularization process for high values of viscosity. On the contrary, the (explicit) internal length defined in the non-local approach overrides the influence of the viscoplastic internal length for small values of viscosity. Between these limiting conditions an interaction of the two length scales is observed.

As a final remark, it is worth to point out that viscoplasticity is an effective regularization method; however it does not lead to mesh insensitive results independently of the problem inputs. Soil permeability and loading velocity are of utmost importance and should be considered when viscoplasticity is used as a regularization technique of strain localization problem in the framework of multiphase porous media. Furthermore, viscosity and soil permeability are physical properties of the material and there is the possibility (depending on the examined material) when their real values is used, the regularization to be lost. In that case, the non-local approach is advisable.

Chapter 5

An Elasto-Viscoplastic Constitutive Model for Unsaturated Soil Behaviour

Chapter 5: An Elasto-Viscoplastic Constitutive Model for Unsaturated Soil Behaviour

5.1 Introduction

Mechanics of unsaturated soils has been an active field of research in the last few decades. Efficient constitutive models that take into account the partial saturation of soil are necessary to solve a number of engineering problems e.g. instability of slopes and cuts due to heavy rainfalls.

Even though the long-time debate on the most appropriate stress framework for unsaturated soils has eventually came to an end, evidencing the need for complete hydro-mechanical stress framework (Gens 1995; Jardine et al. 2004), several forms of adequate stress variables are still possible.

The stress parameter introduced by Bishop (1959) is primarily a function of the degree of saturation and was the first effort of explaining from a theoretical standpoint the mechanical behaviour of unsaturated soils. This simple approach was soon demonstrated to be unsuccessful on reproducing some features of the behaviour of partially saturated soils, such as wetting induced collapse, and the attention was focused on rather different hypotheses.

Fredlund and Morgenstern (1978) suggested that two pair of stress state variables should be adopted when describing partially saturated soil behaviour. Along these lines, there are constitutive models written in terms of the net total stress and the suction such as Barcelona Basic Model family (Alonso et al. 1990) or others (Wheeler and Sivakumar (1995), Cui and Delage (1996)) and constitutive models using the generalized effective stress and the suction as the two independent stress variables e.g. Jommi and di Prisco (1994), Bolzon et al. (1996), Nuth and Laloui (2008). Even though the original definition of the Bishop's generalized effective stress is due to Schrefler (1984), one of the first constitutive frameworks making use of this unified effective stress is that of Jommi and di Prisco (1994) and later reported by Jommi (2000) defined as the average soil skeleton stress.

Moreover, recently researches on partially saturated rockfill material (Oldecop and Alonso 2007) clearly show the effects of partial saturation states on the time dependent behaviour (particularly on creep phenomena) of geomaterials. Despite the significant practical interest, only few studies have focused on the coupling between partial saturation states and time effects on the behaviour of geomaterials.

In this Chapter an elasto-viscoplastic constitutive model for unsaturated soils is proposed and validated on the basis of experimental data. The model constitutes an extension of the model of Buscarnera and Nova (2009) which was based on the strain hardening elastoplastic approach proposed by Nova (2000), Tamagnini et al. (2002), and Nova et al. (2003) for modelling chemical degradation effects and the constitutive approach suggested by Jommi and di Prisco (1994). The novelty of the proposed viscoplastic formulation is enhanced with the dependence of the constitutive parameters on the relative density as an alternative of using the state parameter concept.

The work of the present Chapter is organized in two parts. The first part (Sections 5.2 and 5.3) focuses on the implementation in Comes-Geo code of the Buscarnera and Nova elastoplastic model for unsaturated soil, as part of this thesis. A description of the procedure is given and the validation of the implementation based on benchmark tests from the literature is presented. In the second part of this Chapter (Sections 5.4 − 5.6) the aforementioned model is extended to viscoplasticity. The detailed analytical formulation of the viscoplastic model and its implementation in Comes-Geo is discussed along with the validation of the code.

5.2 UNsand: An Elastoplastic Strainhardening Model for Soil Allowing for Hydraulic Bonding-Debonding Effects

Following the constitutive approach suggested by Jommi and di Prisco (1994), Buscarnera and Nova (2009) presented an elastoplastic strain-hardening constitutive model for unsaturated soil behaviour based on energy conjugated stress variables in the framework of superposed continua. The purpose was to develop a model able to deal with possible mechanical instabilities within a consistent energy framework.

The model shares the same conceptual structure of the elastoplastic laws proposed to deal with bonded geomaterials subject to weathering or diagenesis (e.g. Nova et al. (2003)) and is capable of modelling several kinds of instabilities induced by the loss of hydraulic bonding contributions.

To start with the description of the model, it is assumed that the material behaviour is isotropic. Moreover, all hydraulic effects, either due to a variation in suction or in degree of saturation, have simply been assumed to be isotropic. The stress responsible for straining the solid skeleton was in fact assumed to be defined as:

$$\boldsymbol{\sigma}' = \boldsymbol{\sigma} - S_{\mathrm{w}} p^{\mathrm{w}} \mathbf{I} - \left(1 - S_{\mathrm{w}}\right) p^{\mathrm{g}} \mathbf{I} \tag{5.1}$$

The constitutive modelling is based on an enlarged constitutive law, which considers the modified suction, $s^* = n \cdot s$ (n is the porosity of the material), as a further stress variable and the opposite of the rate of the degree of saturation as the corresponding hydraulic strain variable. The model neglects the hydraulic hysteresis effects and is formulated for general three-dimensional stress states.

The model as proposed by Buscarnera and Nova had to be amended to adapt in the finite element code Comes-geo. Thus, in the following are presenting the parts of the model that were actually implemented in the code.

5.2.1 Stored energy function and hyperelastic behaviour

Elasticity models are commonly incorporated into elastoplastic constitutive models through a hypoelastic formulation. However, extension of a hypoelastic formulation to the case of nonlinear elastic soil response could result, in some cases, in nonconservative models. For example, the formulation of Simpson (1973), in which the elastic bulk and shear moduli are linear functions of the

effective confining stress and related through a constant Poisson's ratio, leads to a model that does not conserve energy (Zytynski et al. (1978)). On the other hand, hyperelastic materials are those for which a stored energy function exists, and hence, are conservative.

Therefore, herein a hyperelastic reversible solid behaviour is assumed based on the existence of a stored energy function $\psi = \psi\left(\boldsymbol{\varepsilon}^{e}\right)$, such that:

$$\boldsymbol{\sigma}' := \frac{\partial \psi\left(\boldsymbol{\varepsilon}^{e}\right)}{\partial \boldsymbol{\varepsilon}^{e}} \tag{5.2}$$

Assuming small deformation, the strain rate is additively decomposed in an elastic, reversible part $\dot{\boldsymbol{\varepsilon}}^{e}$ and a plastic, irreversible part $\dot{\boldsymbol{\varepsilon}}^{p}$. Thus in turn, the hyperelastic constitutive equation in rate form can be written as:

$$\dot{\boldsymbol{\sigma}}' = \mathbf{D}^{e}\left[\dot{\boldsymbol{\varepsilon}} - \dot{\boldsymbol{\varepsilon}}^{p}\right] \tag{5.3}$$

where $\mathbf{D}^{e}$ is the fourth-order elastic stiffness tensor, given by:

$$\mathbf{D}^{e} := \frac{\partial^{2} \psi\left(\boldsymbol{\varepsilon}^{e}\right)}{\partial \boldsymbol{\varepsilon}^{e} \otimes \partial \boldsymbol{\varepsilon}^{e}} \tag{5.4}$$

In the development of the model, the stored energy function proposed in Borja et al. (1997), Tamagnini et al. (2002) and Nova et al. (2003) has been adopted. Accordingly, the function $\psi\left(\boldsymbol{\varepsilon}^{e}\right)$ is given by the following two-invariant expression:

$$\psi\left(\boldsymbol{\varepsilon}^{e}\right) = \overline{\psi}\left(\varepsilon_{v}^{e}, \varepsilon_{s}^{e}\right) = \tilde{\psi}\left(\varepsilon_{v}^{e}\right) + \frac{3}{2}\left[G_{0} + \frac{\alpha}{\hat{k}}\tilde{\psi}\left(\varepsilon_{v}^{e}\right)\right]\left(\varepsilon_{s}^{e}\right)^{2} \tag{5.5}$$

where:

$$\tilde{\psi}\left(\varepsilon_{v}^{e}\right) := \begin{cases} \hat{k} p_{r} \exp\left(\dfrac{\varepsilon_{v}^{e}}{\hat{k}} - 1\right), & \varepsilon_{v}^{e} \geq \hat{k} \left(\text{or } p' \geq p_{r}\right) \\ p_{r}\varepsilon_{v}^{e} + \dfrac{p_{r}\left(\varepsilon_{v}^{e} - \hat{k}\right)^{2}}{2\hat{k}}, & \varepsilon_{v}^{e} < \hat{k} \left(\text{or } p' < p_{r}\right) \end{cases} \tag{5.6}$$

This model produces pressure dependent elastic bulk and shear moduli. In Equations (5.5) and (5.6) and $G_{0}, \hat{k}, \alpha$ are constitutive parameters, p_{r} is a reference mean stress, while $\varepsilon_{v}^{e}, \varepsilon_{s}^{e}$ are the elastic volumetric strain and the second invariant of the elastic strain deviator, respectively (defined in the same way as in Equation (3.16)). When $p' < p_{r}$ the hyperelastic law predicts a linear elastic behaviour, whereas when $p' \geq p_{r}$ a fully non-linear pressure dependent behaviour is obtained. As a consequence, the parameter p_{r} can be selected in accordance to this observation. The absence of dependence on suction in Equation (5.5) implies that the suction stress does not influence the elastic response. By taking the first and the second derivative of Equation (5.5) with respect to $\boldsymbol{\varepsilon}^{e}$, the following expressions for the stress and the elastic stiffness tensor are obtained:

$$\boldsymbol{\sigma}' := \frac{\partial \psi\left(\boldsymbol{\varepsilon}^{e}\right)}{\partial \boldsymbol{\varepsilon}^{e}} = \left[1 + \frac{3\alpha}{2\hat{k}}\left(\varepsilon_{s}^{e}\right)^{2}\right]\theta_{\varepsilon}\mathbf{1} + 2\left(G_{0} + \frac{\alpha}{\hat{k}}\tilde{\psi}\right)\mathbf{e}^{e} \tag{5.7}$$

and:

$$\mathbf{D}^{e} = \left[1 + \frac{3\alpha}{2\hat{k}}\left(\varepsilon_{s}^{e}\right)^{2}\right]K_{\varepsilon}\mathbf{1}\otimes\mathbf{1} + 2\left(G_{0} + \frac{\alpha}{\hat{k}}\tilde{\psi}\right)\left[\mathbf{I} - \frac{1}{3}\mathbf{1}\otimes\mathbf{1}\right] + 2\left(\frac{\alpha}{\hat{k}}\right)\theta_{\varepsilon}\left(\mathbf{1}\otimes\mathbf{e}^{e} + \mathbf{e}^{e}\otimes\mathbf{1}\right) \tag{5.8}$$

where, $\mathbf{e}^{e} := \boldsymbol{\varepsilon}^{e} - \frac{1}{3}\mathrm{tr}(\boldsymbol{\varepsilon}^{e})\mathbf{1}$ is the deviatoric elastic strain and:

$$\theta_{\varepsilon} := \frac{\partial \tilde{\psi}\left(\varepsilon_{v}^{e}\right)}{\partial \varepsilon^{e}} = \begin{cases} p_{r}\exp\left(\frac{\varepsilon_{v}^{e}}{\hat{k}} - 1\right), & \varepsilon_{v}^{e} \geq \hat{k}\ \left(\text{or } p' \geq p_{r}\right) \\ p_{r}\frac{\varepsilon_{v}^{e}}{\hat{k}}, & \varepsilon_{v}^{e} < \hat{k}\ \left(\text{or } p' < p_{r}\right) \end{cases} \tag{5.9}$$

$$K_{\varepsilon} := \frac{\partial \theta_{\varepsilon}}{\partial \varepsilon^{e}} = \begin{cases} \frac{p_{r}}{\hat{k}}\exp\left(\frac{\varepsilon_{v}^{e}}{\hat{k}} - 1\right), & \varepsilon_{v}^{e} \geq \hat{k}\ \left(\text{or } p' \geq p_{r}\right) \\ \frac{p_{r}}{\hat{k}}, & \varepsilon_{v}^{e} < \hat{k}\ \left(\text{or } p' < p_{r}\right) \end{cases} \tag{5.10}$$

Another relevant feature of the hyperelastic model is related to the possibility of having volumetric-deviatoric coupling, governed by the parameter α on the last term on the RHS of Equation (5.8). This coupling effect disappears when α=0. In the latter case constant elastic shear modulus (G_0) is recovered (see Equation (5.5)).

5.2.2 Yield function and plastic potential

The model adopts yield surface and plastic potential expressions proposed by Lagioia et al. (1996).

Plastic Potential

The plastic potential is described by the following expression:

$$g = A_{g}^{K_{1g}/C_{g}} B_{g}^{-K_{2g}/C_{g}} p' - \tilde{p}_{s}' = 0 \tag{5.11}$$

where $\tilde{p}_{s}'$ is a dummy parameter (as only the derivatives of the equation are used) and:

$$K_{1g} := \frac{m_{g}\left(1-\alpha_{g}\right)}{2\left(1-m_{g}\right)}\left\{1 + \sqrt{1 - \frac{4\alpha_{g}\left(1-m_{g}\right)}{m_{g}\left(1-\alpha_{g}\right)^{2}}}\right\}$$

$$K_{2g} := \frac{m_{g}\left(1-\alpha_{g}\right)}{2\left(1-m_{g}\right)}\left\{1 - \sqrt{1 - \frac{4\alpha_{g}\left(1-m_{g}\right)}{m_{g}\left(1-\alpha_{g}\right)^{2}}}\right\} \tag{5.12}$$

and:

$$A_g := 1 + \frac{1}{K_{1g} M_g(S)} \frac{q}{p'}$$
$$B_g := 1 + \frac{1}{K_{2g} M_g(S)} \frac{q}{p'} \qquad (5.13)$$
$$C_g := (1 - m_g)(K_{1g} - K_{2g})$$

The function Mg(S) appearing in Equation (5.13) is given by the expressions suggested by Gudehus (1973):

$$M_g(S) = \frac{2cM_{cg}}{(1+c)-(1-c)S}, \qquad c = \frac{M_{eg}}{M_{cg}}, \qquad S := \sin(3\theta) = \sqrt{6}\frac{\mathrm{tr}(\mathbf{s}^3)}{\left[\mathrm{tr}(\mathbf{s}^2)\right]^{3/2}} \qquad (5.14)$$

in which M_c and M_e are the values of M(S) in triaxial compression and triaxial extension conditions, respectively and S is a function of the Lode angle θ.

Yield Surface

The analytical expression for the yield surface has been assumed to be characterized by the same expression as for the plastic potential, i.e:

$$f = A_f^{K_{1f}/C_f} B_f^{-K_{2f}/C_f} p' - p'_s = 0 \qquad (5.15)$$

where the Equations (5.12)-(5.14) hold also in this case. Having different constitutive parameters m_f, α_f, M_{ef} and M_{cf}, a non-associated flow rule is adopted and therefore different choices for the shape of the two surfaces. The variable p'_s in Equation (5.15) is the internal variable defining the size of the yield surface and responsible for its evolution in the skeleton stress space. In the present formulation of the constitutive model it has been neglected the possibility of including a mechanical bonding contribution (Castellanza (2002)). As a consequence, the only internal variable is the preconsolidation stress p'_s . The set of parameters of the constitutive model are summarized in

Table 5.1. Figure 5.1 shows a 3D visualization of the yield surface in the principal stress space.

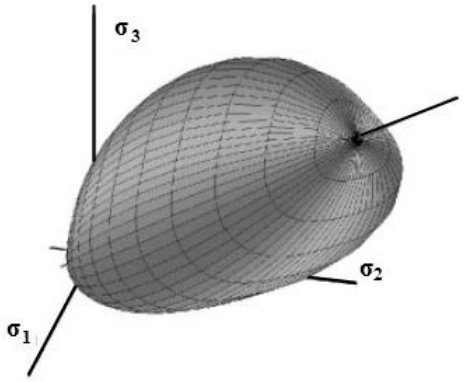

Figure 5.1: 3D visualization of the yield surface in the principal stress space [109].

5.2.3 Hardening law

The hardening law for the preconsolidation stress, p'_s the only internal variable considered in the model, is constituted by two separate contributions, a mechanical one and a hydraulic one (Figure 5.2). The analytical expression of the hardening law in rate form is:

$$\dot{p}'_s = \rho_s p'_s \left(\dot{\varepsilon}^p_v + \xi_s \dot{\varepsilon}^p_s\right) - r_{sw} p'_s \dot{S}_w \tag{5.16}$$

where ρ_s, ξ_s and r_{sw} are hardening constitutive parameters (

Table 5.1).

The first term in Equation (5.16) represents the mechanical contribution to the hardening law.

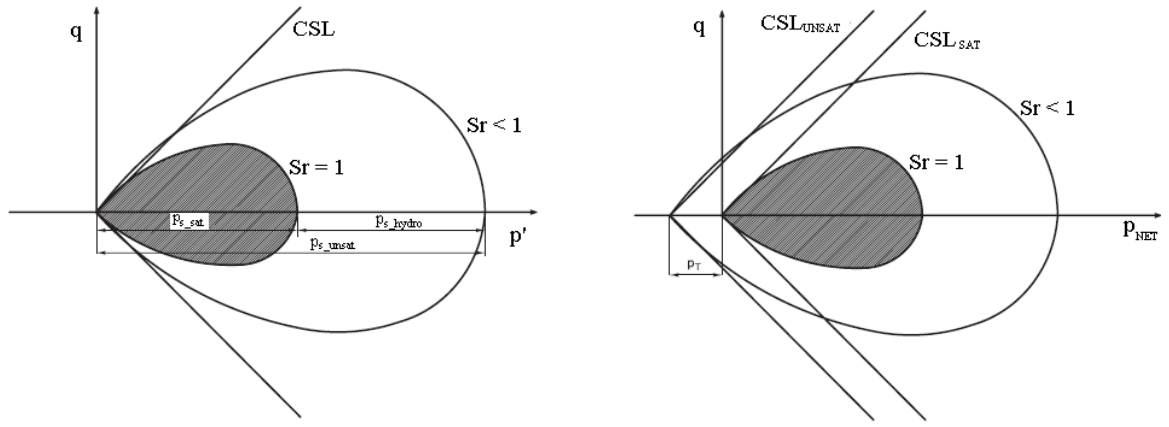

Figure 5.2: Yield surface in saturated and unsaturated conditions depicted in the (a) skeleton stress space and (b) net stress space [25].

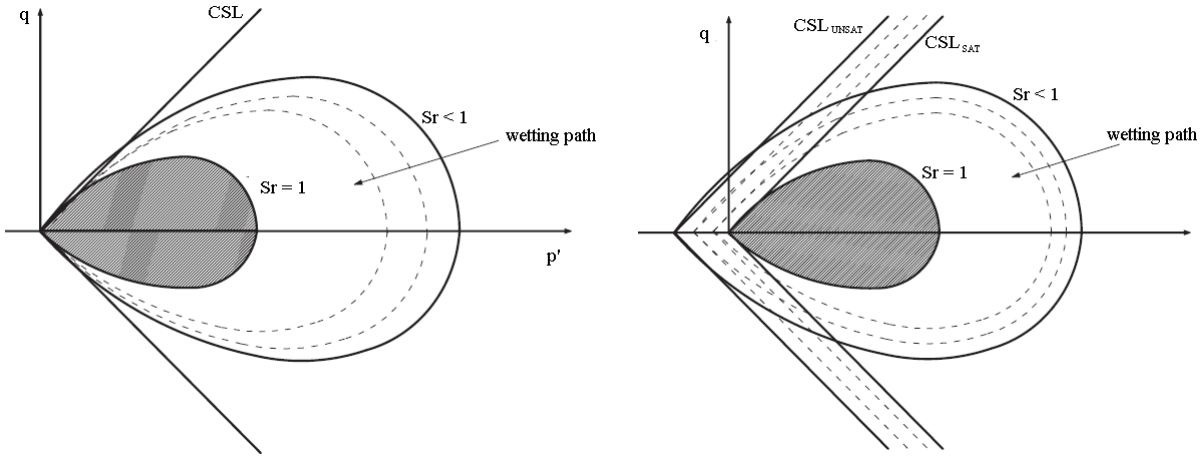

Figure 5.3: Contraction of yield surfaces upon wetting in the (a) skeleton stress space and (b) net stress space [25].

The second term is the mathematical form of the hydraulic bonding effect highlighting the dependence of the internal variable on the degree of saturation and therefore the expansion or

contraction of the yield surface upon drying or wetting process (Figure 5.3). It is thus clear that a hydraulic process can change the onset of yielding and the amount of plastic strains.

As in Tamagnini et al. (2002) the mechanical contribution of the hardening law can be rewritten as:

$$\dot{p}'_s = \dot{\lambda}\rho_s p'_s \left(\hat{T} + \xi_s \hat{N}\right) - r_{sw} p'_s \dot{S}_w$$

$$\hat{T} = \mathrm{tr}\left(\frac{\partial g}{\partial \boldsymbol{\sigma}'}\right), \quad \hat{N} = \sqrt{\frac{2}{3}}\left\|\mathrm{dev}\left(\frac{\partial g}{\partial \boldsymbol{\sigma}'}\right)\right\| \tag{5.17}$$

Table 5.1: List of constitutive parameters.

		Hyperelastic law
1	$\hat{k}$	slope of the swelling line in the lnυ-lnp' plane
2	G_0	shear modulus for p' =0
3	α	coupling parameter
4	p_r	reference pressure
		Yield surface
5	m_f	shape of yield function
6	α_f	shape of yield function
7	M_{cf}	slope of the line in the q-p plane for which $\partial f / \partial p = 0$ in compression triaxial ($\sigma_1 > \sigma_2 = \sigma_3$)
8	M_{ef}	slope of the line in the q-p plane for which $\partial f / \partial p = 0$ in extension triaxial ($\sigma_1 = \sigma_2 > \sigma_3$)
		Plastic potential surface
9	m_g	shape of plastic potential
10	α_g	shape of plastic potential
11	M_{cg}	slope of the line for which $\dot{\varepsilon}_v^p = 0$ in the triaxial plane (compression)
12	M_{eg}	slope of the line for which $\dot{\varepsilon}_v^p = 0$ in the triaxial plane (extension)
		Hardening law
13	ρ_s	$= 1/B_p$ in which B_p is the logarithmic volumetric compliance under isotropic loading
14	ξ_s	is the dilatancy at failure
15	r_{sw}	hydraulic hardening parameter

5.2.4 General formulation of the constitutive equation in rate from

Plastic strains are governed by the classical incremental flow rule for plastic deformations:

$$\dot{\boldsymbol{\varepsilon}}^{\mathrm{p}} = \dot{\lambda}\frac{\partial \mathrm{g}\left(\boldsymbol{\sigma}', \mathbf{q}\right)}{\partial \boldsymbol{\sigma}'} \tag{5.18}$$

where g(**σ'**,**q**) is the plastic potential function and λ is the plastic multiplier.

The hardening law is expressed in an incremental form as follows:

$$\dot{\mathbf{q}} = \dot{\lambda}\mathbf{h}\left(\boldsymbol{\sigma}', \mathbf{q}\right) - \dot{\mathrm{S}}_{\mathrm{w}}\boldsymbol{\eta}\left(\boldsymbol{\sigma}', \mathbf{q}\right) \tag{5.19}$$

where **h**(**σ'**,**q**) and **η**(**σ'**,**q**) are the mechanical and hydraulic function, respectively, influencing the evolution of the internal variables.

The loading and unloading conditions are expressed in terms of the Kuhn-Tucker complementarity conditions:

$$\dot{\lambda} \geq 0, \quad f\left(\boldsymbol{\sigma}', \mathbf{q}\right) \leq 0, \quad \dot{\lambda} f\left(\boldsymbol{\sigma}', \mathbf{q}\right) = 0 \tag{5.20}$$

In case of plastic loading, the following consistency condition must be satisfied:

$$\dot{f}\left(\boldsymbol{\sigma}', \mathbf{q}\right) = 0, \tag{5.21}$$

Taking into account the constitutive Equation (5.3) and the hardening law Equation(5.19), whenever plastic loading occurs then:

$$\begin{aligned} \dot{f} &= \frac{\partial f}{\partial \boldsymbol{\sigma}'} \cdot \boldsymbol{\sigma}' + \frac{\partial f}{\partial \mathbf{q}} \cdot \mathbf{q} \\ &= \frac{\partial f}{\partial \boldsymbol{\sigma}'} \cdot \mathbf{D}^{\mathrm{e}}\dot{\boldsymbol{\varepsilon}} - \frac{\partial f}{\partial \boldsymbol{\sigma}'} \cdot \mathbf{D}^{\mathrm{e}}\dot{\lambda}\frac{\partial \mathrm{g}}{\partial \boldsymbol{\sigma}'} + \frac{\partial f}{\partial \mathbf{q}} \cdot \dot{\lambda}\mathbf{h} - \frac{\partial f}{\partial \mathbf{q}} \cdot \dot{\mathrm{S}}_{\mathrm{w}}\boldsymbol{\eta} \end{aligned} \tag{5.22}$$

Imposing Equation (5.21), the plastic multiplier is expressed as follows:

$$\dot{\lambda} = \frac{1}{\mathrm{H} + \mathrm{H}_{\mathrm{c}}}\left\langle \frac{\partial f}{\partial \boldsymbol{\sigma}'} \cdot \mathbf{D}^{\mathrm{e}}\dot{\boldsymbol{\varepsilon}} - \left(\frac{\partial f}{\partial \mathbf{q}} \cdot \boldsymbol{\eta}\right)\dot{\mathrm{S}}_{\mathrm{w}} \right\rangle \tag{5.23}$$

where the symbol < > denotes the McCauley brackets, and

$$\mathrm{H} = -\frac{\partial f}{\partial \mathbf{q}}\mathbf{h} \tag{5.24}$$

is the hardening modulus and

$$\mathrm{H}_{\mathrm{c}} = \frac{\partial f}{\partial \boldsymbol{\sigma}'} \cdot \mathbf{D}^{\mathrm{e}}\frac{\partial \mathrm{g}}{\partial \boldsymbol{\sigma}'} \tag{5.25}$$

is the critical hardening modulus.

It can be noted that it is possible to decompose the plastic multiplier in two contributions, a mechanical one and a hydraulic one:

$$\dot{\lambda} = \dot{\lambda}_m + \dot{\lambda}_h \tag{5.26}$$

This means that plastic strain may develop even in the case of trial state, provided that the hydraulic debonding induced by a wetting process determines a sufficiently high contribution to the plastic multiplier.

Substituting Equation (5.23) into the stress rate (i.e. Equation (3.19)) one obtains:

$$\dot{\boldsymbol{\sigma}}' = \mathbf{D}_{\sigma\sigma}\dot{\boldsymbol{\varepsilon}} + \mathbf{D}_{\sigma w}\left(-\dot{S}_w\right) \tag{5.27}$$

where

$$\mathbf{D}_{\sigma\sigma} = \mathbf{D}^e - \frac{1}{H + H_c}\left(\mathbf{D}^e \frac{\partial g}{\partial \boldsymbol{\sigma}'}\right) \otimes \left(\frac{\partial f}{\partial \boldsymbol{\sigma}'}\mathbf{D}^e\right) \tag{5.28}$$

is the mechanical (continuum) elastoplastic constitutive matrix and

$$\mathbf{D}_{\sigma w} = -\frac{1}{H + H_c}\left(\frac{\partial f}{\partial \mathbf{q}} \cdot \boldsymbol{\eta}\right) \cdot \mathbf{D}^e \cdot \frac{\partial g}{\partial \boldsymbol{\sigma}'} \tag{5.29}$$

represents the mechanical effects of a hydraulic change of the saturation degree.

It should be noted that for the soil water retention curve the expression suggested by Van Genuchten (1980) was adopted. For validation purposes this relation is implemented in Comes-geo and the mathematical expression is given in Equation (2.42). However any other more suitable expressions could be employed.

The elastoplastic model as presented in Section 5.2 has been implemented in Comes-geo code with an explicit integration type algorithm. For the tangent of the linearized system of equations the elastoplastic continuum tangent operator was adopted.

It is noted that for brevity the implemented elastoplastic model for unsaturated soils is denoted as UNsand.

5.3 Validation of the Implementation of UNsand Model in Comes-geo F.E. Code

This section presents the validation of the implementation of the elastoplastic constitutive model for unsaturated soil behaviour in Comes-geo FEM code. The numerical validation is performed through single element analyses by using a single finite element with four nodes and 2 x 2 gauss points.

The validation process is carried out by simulating triaxial and oedometric tests with phases of drying and wetting and drained and undrained loading under axisymmetric and plane-strain conditions. Moreover, a series of drained and undrained triaxial tests with different initial densities are simulated. The results are compared with both numerical and experimental results taken from the literature.

5.3.1 Triaxial Tests at Constant Suction

To begin with a series of triaxial shear tests at constant suction, as in the work of Buscarnera and Nova (2009), are simulated.

The complete set of parameters along with the initial conditions and details for the soil water retention curve, are taken from Buscarnera and Nova (2009) and are detailed in Table 5.2. In this example a non-associated plastic flow rule is adopted.

The first simulation is a triaxial shearing of a saturated and unsaturated material. For the latter, the stress path followed is characterized by a first drying path, AB, up to a suction of 50 kPa under constant mean net stress and a second triaxial shearing path, BD, under constant suction (i.e. 50 kPa) and constant radial net stress (Figure 5.4).

Table 5.2: List of parameters adopted for triaxial shear tests at constant suction.

Elastic parameters	Yield surface parameters	Plastic potential	Hardening parameters	SWCC parameters	Initial state	Initial S_w & void ratio
α=0.0	α_f=0.63	α_g=0.63	r_s=1/0.038	α=0.43	p_0=10 kPa	S_{w0}=1.0
k=0.002	m_f=0.95	m_g=0.95	ξ_s=0.0	n=1.30	q_0=0 kPa	e_0=1.90
G_0=32MPa	M_{cf}=0.90	M_{cg}=1.37	r_{sw}=3.86	m=0.22	p_{s0}=10 kPa	
p_r=10 kPa	M_{ef}=0.70	M_{eg}=1.07				

Figure 5.5 shows the comparison of the saturated and unsaturated material in terms of deviatoric stress and volumetric strain with respect to deviatoric strain, for the published results by Buscarnera and Nova (black line) and the simulated with Comes-geo code (red line). The finite element results are in excellent agreement with the published and show the increase in stiffness and strength due to the hydraulic bonding effect caused by water menisci.

In sequence, similar simulations varying suction and net pressure are performed following the results given in Buscarnera and Nova and the experimental observations by Bilotta et al. (2005). Three different net confinement pressures and two suction levels are applied (Table 5.3). All tests are simulated imposing a first drying path at a low net confinement to establish a first suction equilibrium

stage. Afterwards, a constant suction triaxial compression stage is imposed under constant radial net stress.

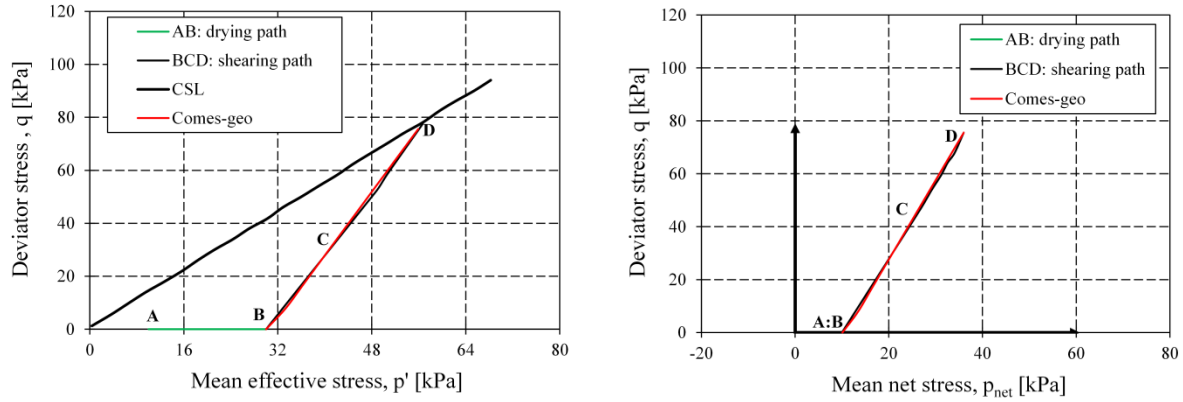

(a) (b)

Figure 5.4: UNsand validation - Stress path (a) in the skeleton and (b) net stress space for the unsaturated material.

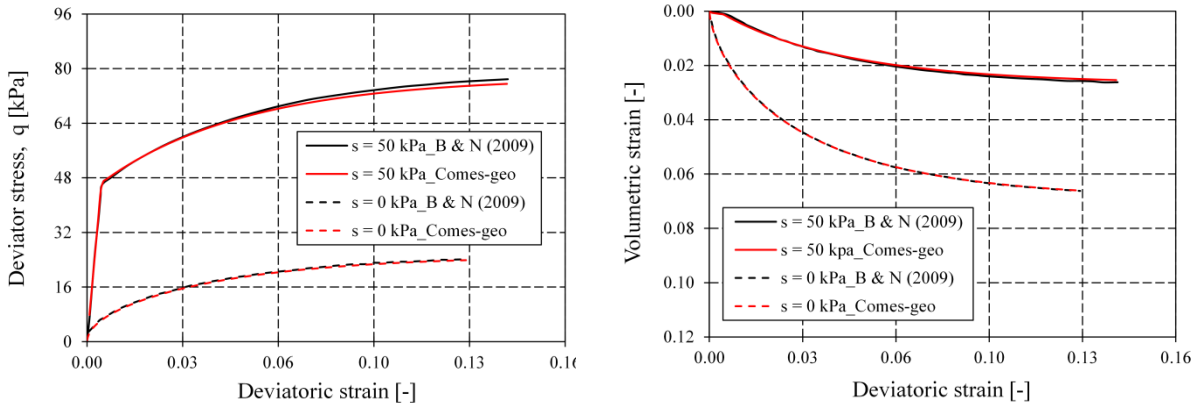

(a) (b)

Figure 5.5: UNsand validation - Comparison of the results of a triaxial test under saturated (s=0 kPa) and unsaturated (s=50 kPa) conditions: (a) deviatoric stress and (b) volumetric strain versus deviatoric strain.

Table 5.3: Triaxial tests at varying suction and net confinement pressure.

Simulation No	p_{net} [kPa]	s [kPa]
1	10	20
2	10	50
3	30	20
4	30	50
5	50	20
6	50	50

The results of the six simulations are depicted in Figure 5.6 and a very good agreement is verified. It is noteworthy that for specimens tested at a given mean net stress, higher suctions imply lower compressibilities and specimens tested at higher net confinements experience higher volumetric strains (Figure 5.6b).

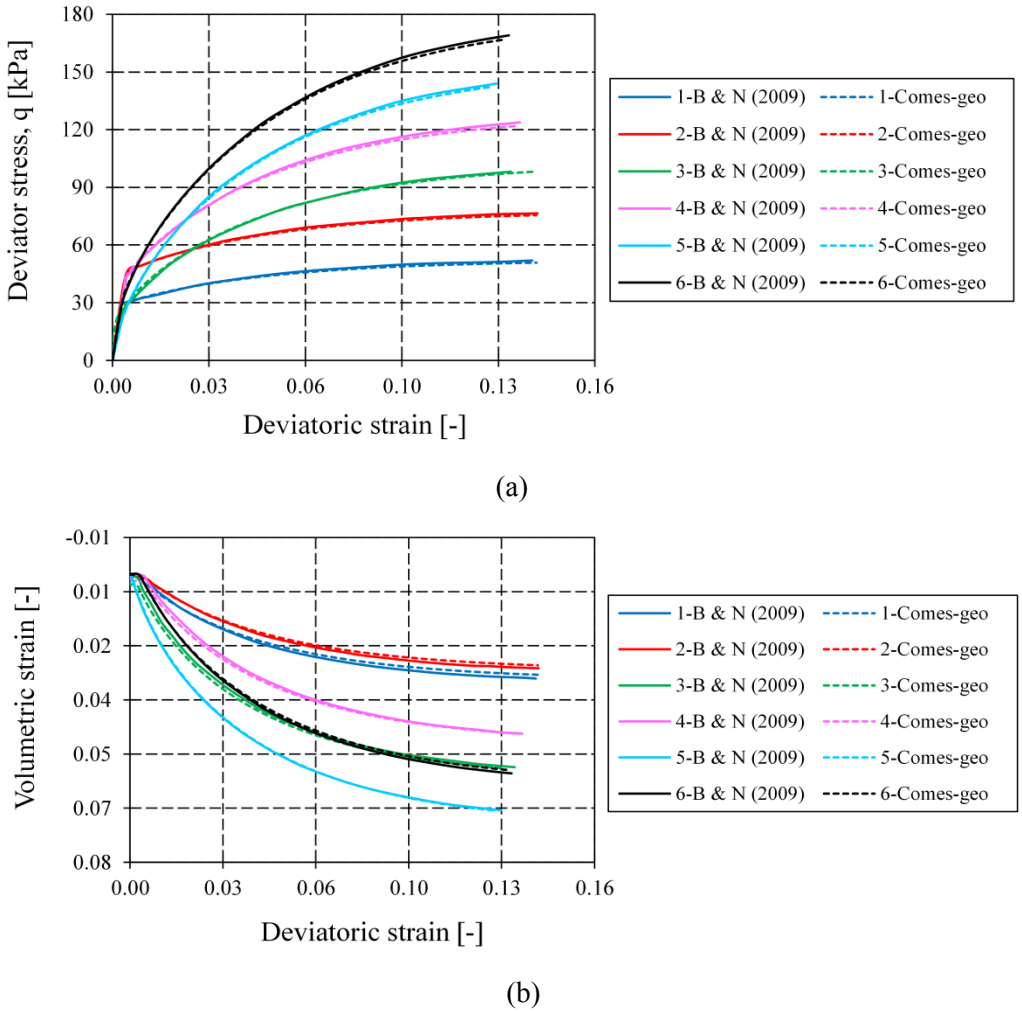

Figure 5.6: UNsand validation - Comparison of the results for the six simulations with varying suction and net confinement pressure: (a) deviatoric stress and (b) volumetric strain versus deviatoric strain.

5.3.2 Oedometric Test with Drying-Wetting Paths

The second example is an oedometric test performed on an ideal non-expansive material, imposing several drying and wetting paths. This validation test was also taken from the work of Buscarnera and Nova (2009). The soil properties used in the finite element analyses are listed in Table 5.1. In this example the flow rule is assumed to be associated.

As shown in Figure 5.7 the test is conducted starting from a saturated condition characterized by an isotropic stress of 200 kPa. An initial oedometric path, AB, is performed followed by a drying path, BC, up to a suction of 100 kPa at constant vertical net stress. Afterwards, a one-dimensional loading path, CE, under constant suction is applied. A final wetting stage, EF, follows holding fixed the

vertical net stress at 460 kPa, until a fully saturated state is reached. The stress path is given in Figure 5.8.

Table 5.4: List of parameters adopted for the oedometric test.

Elastic parameters	Yield surface parameters	Plastic potential	Hardening parameters	SWCC parameters	Initial state	Initial S_w & void ratio
α=0.0	α_f=0.63	α_g=0.63	r_s=1/0.1	α=0.0025	p_0=200 kPa	S_{w0}=1.0
k=0.01	m_f=0.95	m_g=0.95	ξ_s=0.0	n=1.42	q_0=0 kPa	e_0=0.90
G_0=20MPa	M_{cf}=0.75	M_{cg}=0.75	r_{sw}=5.35	m=0.6	p_{s0}=200 kPa	
p_r=200 kPa	M_{ef}=0.6	M_{eg}=0.6				

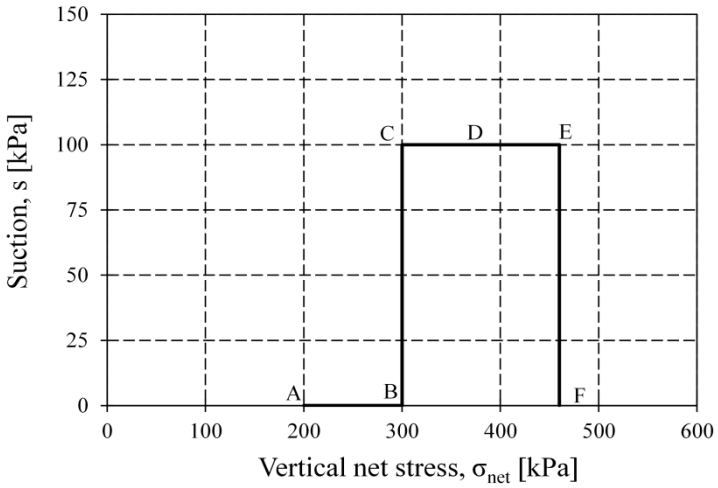

Figure 5.7: UNsand validation – Path followed in the oedometric test.

In this example two points will be raised and discussed. The first concerns the drying path BC. The presence of a plastic stage is evident in Figure 5.9 right at the onset of drying path. An elastic strain follows after 20 kPa of suction, until the point C. This behaviour is related to the fact that the hydraulic hardening is controlled by the degree of saturation, rather than by suction. As a result, since the soil is saturated at point B, a suction increase will generate an increase in mean stress together with negligible hardening and, hence, plastic loading up to a point when the degree of saturation is sufficiently low to generate appreciable hardening.

The second point deals with the ability of the model to describe the most relevant features of unsaturated soils such as the so-called wetting induced collapse. The volumetric compaction process is clearly shown in Figure 5.10; the specimen shows a significant reduction of the void ratio even though the vertical net stress is kept constant.

Finally, in Figures Figure 5.8-Figure 5.10, a perfect much between the Comes-geo results (red line) and those published by Buscarnera and Nova (black line), is obtained.

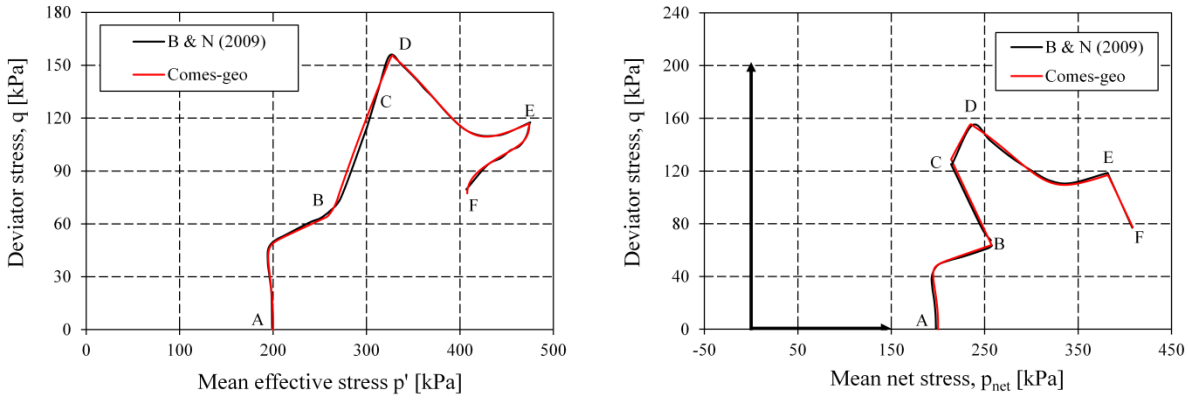

(a) (b)

Figure 5.8: UNsand validation – Results from the oedometer simulation: (a) effective stress path and (b) stress path in the net stress space.

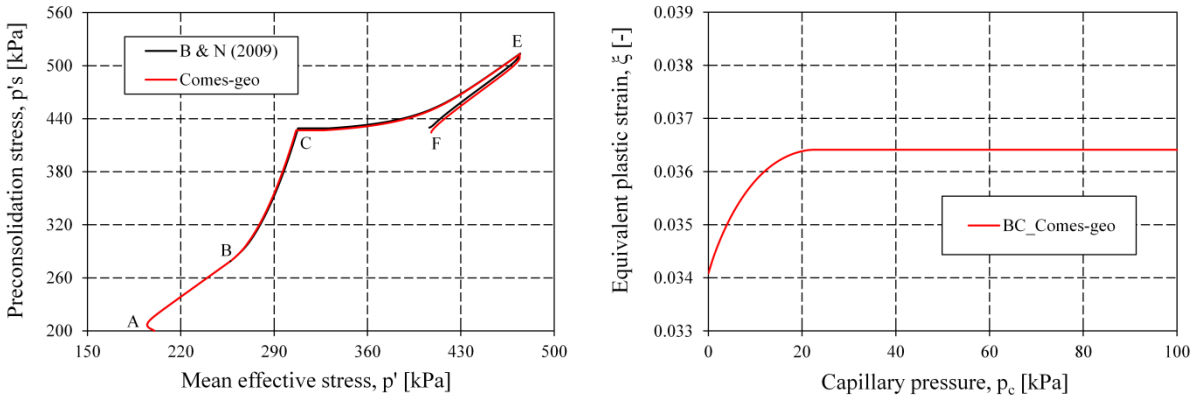

(a) (b)

Figure 5.9: UNsand validation – (a) Yield surface size evolution (data provided by C. Mihalache) and (b) evolution of equivalent plastic strain with suction for the drying path, BC.

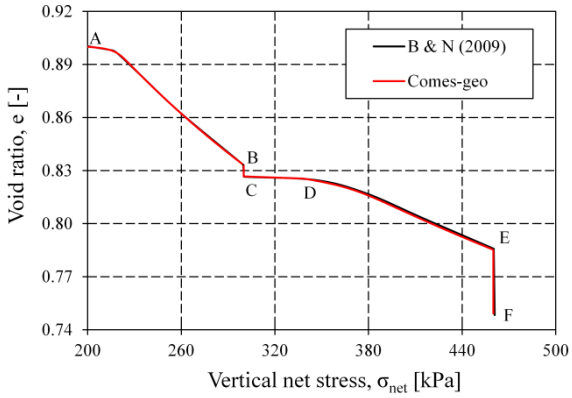

Figure 5.10: UNsand validation – Void ratio with respect to vertical net stress.

5.3.3 Drained and Undrained Plane-Strain Compression Tests on Loose Hostun Sand

In the previous sections the validation process included tests with complex loading paths and the finite element results indicated that both drying and wetting paths were properly and correctly captured.

To finalize the validation of the implementation, in this section standard drained and undrained compression tests under axisymmetric and plane-strain conditions are simulated for the case of a loose Hostun sand. The set of parameters that has been used for the following simulations is given in Table 2, according to Mihalache and Buscarnera (2014) and Ciceri (2014).

The Comes-geo results are compared with those published in Mihalache and Buscarnera (2014) for the triaxial compression tests (labeled as TXD and TXU for drained and undrained conditions respectively) in Figure 5.11 and for the plane-strain compression tests (labeled as PSD and PSU accordingly) in Figure 5.12 .

Table 5.5: List of model parameters for loose Hostun sand.

Elastic parameters	Yield surface parameters	Plastic potential	Hardening parameters	SWCC parameters	Initial state	Initial S_w & void ratio
α=0.0	α_f=0.9906	α_g=0.051	r_s=1/0.0074	α=0.8	p_0=300 kPa	S_{w0}=1.0
k=0.0046	m_f=1.146	m_g=0.98	ξ_s=0.0	n=1.8	q_0=0 kPa	e_0=0.945
G_0=14MPa	M_{cf}=0.52	M_{cg}=1.28	r_{sw}=5.45	m=1.9	p_{s0}=300 kPa	
p_r=1 kPa	M_{ef}=0.442	M_{eg}=1.0				

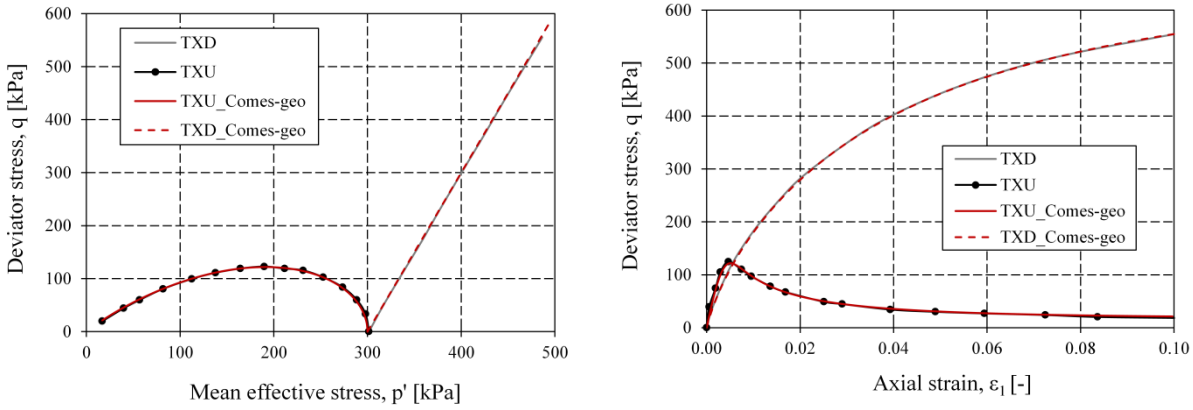

(a) (b)

Figure 5.11: UNsand validation – Comparison of the results of drained and undrained triaxial compression tests: (a) effective stress paths and (b) evolution of deviatoric stress with axial strain.

In both cases, the comparison shows a proper match thus validating the implementation of the model in Comes-geo.

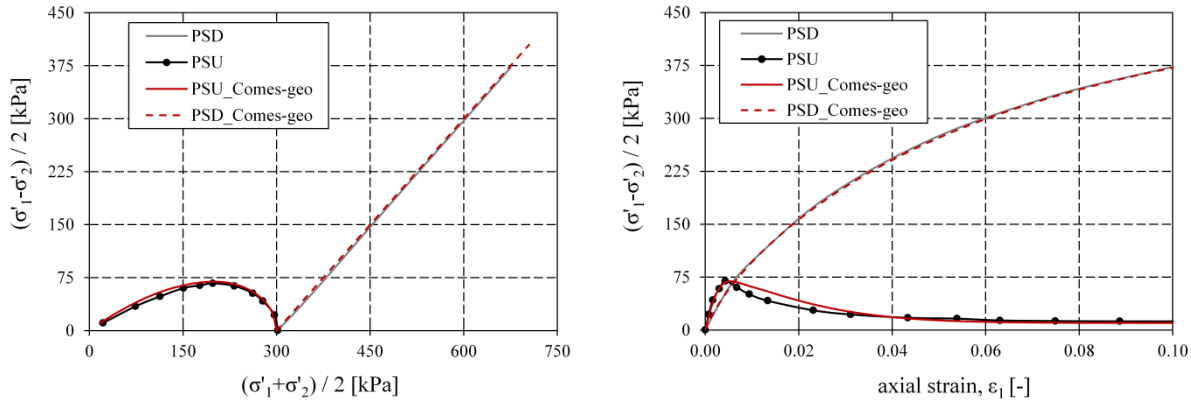

(a) (b)

Figure 5.12: UNsand validation – Comparison of the results of drained and undrained plane-strain compression tests: (a) effective stress paths and (b) evolution of deviatoric stress with axial strain.

5.3.4 Drained and Undrained Triaxial Compression Tests on Hostun Sand

In this section are presented the results for drained and undrained triaxial compression tests for loose, medium-dense and dense Hostun sand as in Gajo and Wood (1999). This last series of numerical simulations was mainly performed to 'double-check' the implementation of the model in Comes-geo code before the extension to viscoplasticity. These tests constitute the main core of the validation process of the viscoplastic model as it will be presented in Section 5.5. Therefore, the following results are not further discussed here and more details are given in the aforementioned section.

In the figures below the solid black line, denoted as 'driver', indicate the results from the numerical simulations performed by C. Mihalache (PhD student under the supervision of prof. Buscarnera) using material point driver. These data were provided in personal communication with C. Mihalache. The comparison indicates a perfect match with the results of the simulation in Comes-Geo.

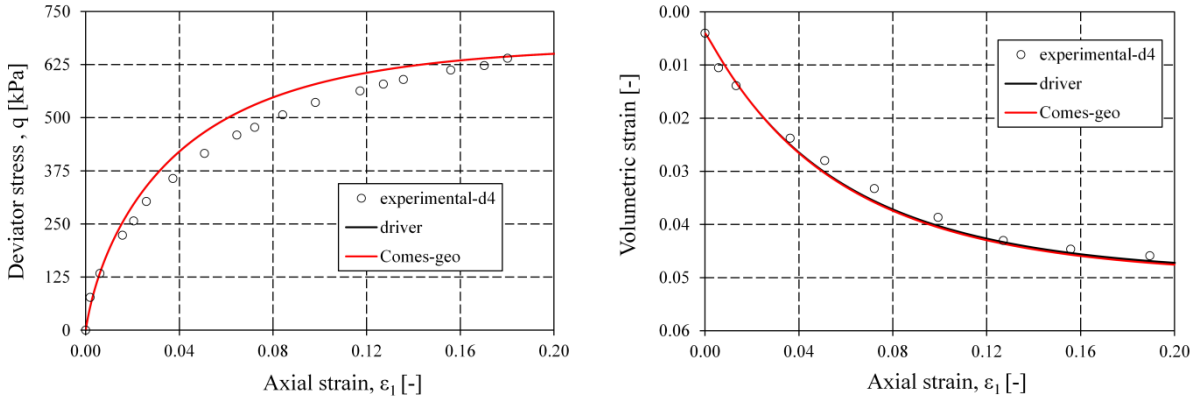

(a) loose sand (p_0=300 kPa, e_0=0.945)

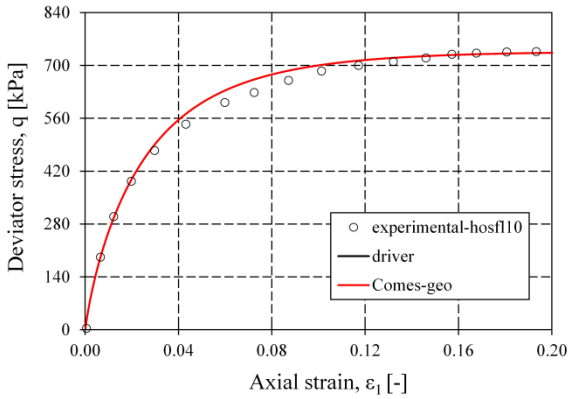

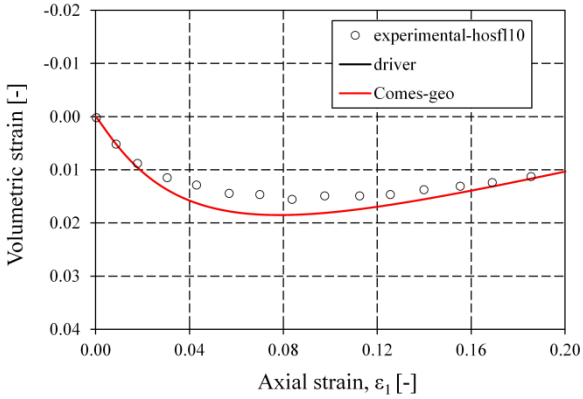

(b) medium-dense sand (p_0=300 kPa, e_0=0.800)

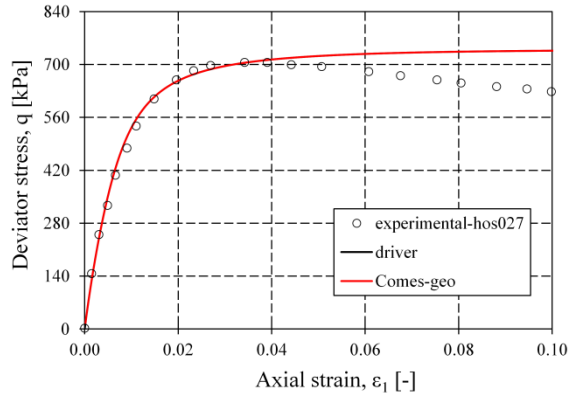

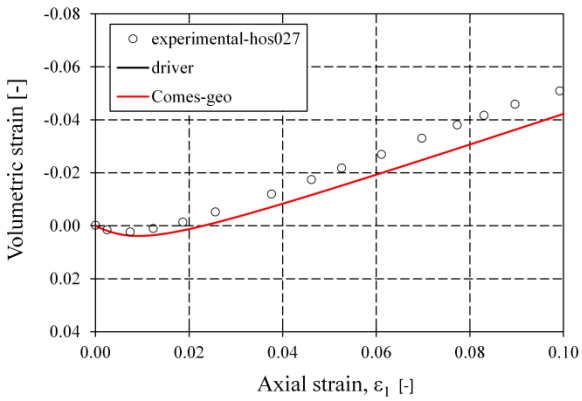

(c) dense sand (p_0=200 kPa, e_0=0.578)

Figure 5.13: UNsand validation – Model simulations of drained triaxial compression tests: evolution of deviatoric stress and volumetric strain with axial strain for (a) loose, (b) medium-dense and (c) dense Hostun sand.

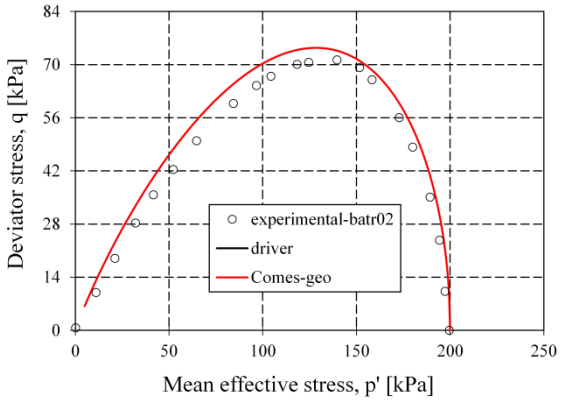

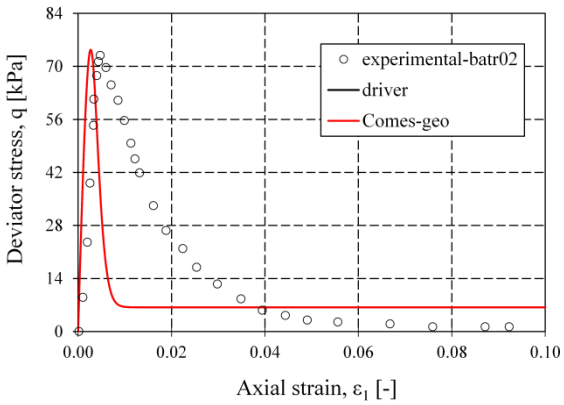

(a) loose sand (p_0=200 kPa, e_0=0.940)

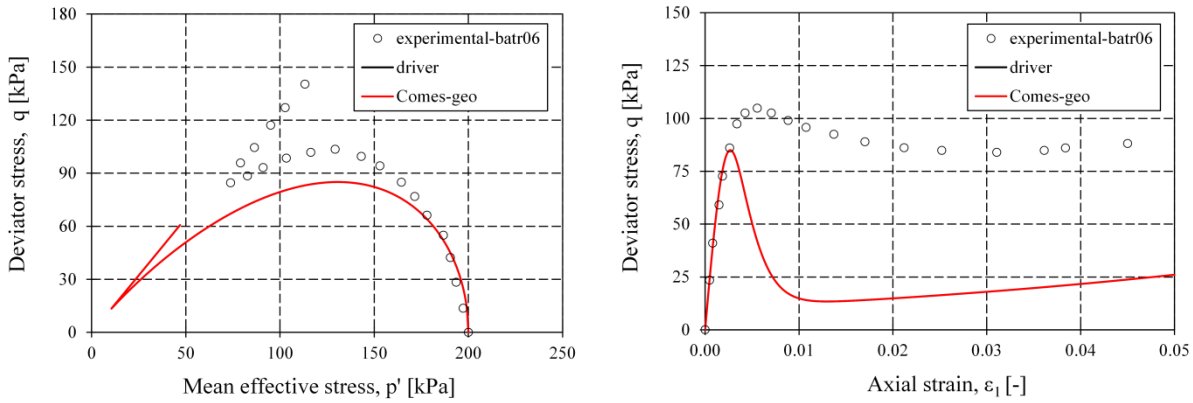

(b) medium-dense sand (p_0=200 kPa, e_0=0.830)

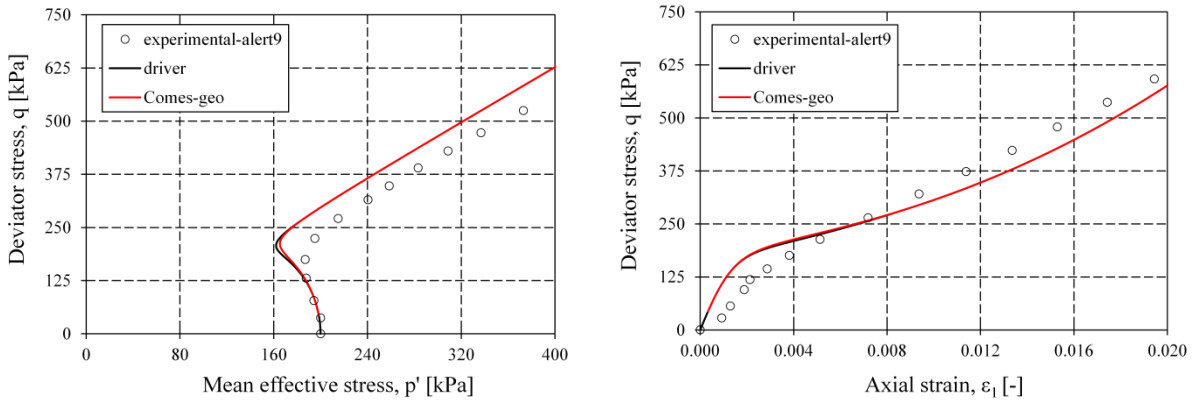

(c) dense sand (p_0=200 kPa, e_0=0.666)

Figure 5.14: UNsand validation – Model simulations of undrained triaxial compression tests: effective stress paths and evolution of deviatoric stress with axial strain for (a) loose, (b) medium-dense and (c) dense Hostun sand.

5.4 Extension to Viscoplasticity - The VISCUNsand Model

The second part of this Chapter is devoted to the proposed viscoplastic model for unsaturated soils. This section contains the analytical formulation of the viscoplastic model and its implementation in the Comes-geo code. The validation of the model and a few applications are discussed in Sections 5.5 and 5.6 respectively.

In the same manner as for the elastoplastic model, the elasto-viscoplastic model for unsaturated soils is denoted for simplicity as VISCUNsand.

5.4.1 Analytical Formulation of the Model

The basic elements of the considered elasto-viscoplastic model can be recognized as follows:

- The yield function that encompasses the elastic domain, expands with increasing suction and contracts upon wetting.
- A plastic potential function, which determines the relative magnitudes of the viscoplastic strains at each point of the yield surface as well as the position of the critical state line.

- The hardening/softening law which is constituted by two separate contributions. The first one describes the changes in the internal variables associated with viscoplastic deformations, while the second one accounts for the hydraulic hardening/softening process induced by a change on the water degree of saturation.
- The hyperelastic law that defines the elastic behaviour within the yield surface.
- The flow rule that describes the evolution of the viscoplastic strain.

As already mentioned the viscoplastic model constitutes an extension of the model of Buscarnera and Nova (2009) described in Section 5.2. Thus, from the above elements only the last one, the flow rule, changes and will be discussed here whereas the other elements remain the same as in Sections 5.2.1-5.23.

Flow rule:

According to Perzyna's approach, the evolution of viscoplastic strain is assumed to be delayed with time and is controlled by the following flow rule:

$$\dot{\boldsymbol{\varepsilon}}^{vp} = \gamma \left\langle \Phi(f) \right\rangle \frac{\partial g}{\partial \boldsymbol{\sigma}'} \tag{5.30}$$

with f and g being the yield function (Equation (5.15)) and the plastic potential (Equation (5.11)) respectively.

As already described in Section 3.3, Φ is the viscous nucleus and γ the "fluidity parameter" which depends on the viscosity, η, of the material and equals to $\gamma=1/\eta$.

For the viscous nucleus, two definitions are adopted; a linear and exponential:
Linear viscous nucleus (i.e. Pisanò (2011)):

$$\Phi(f) = \left(\frac{f}{|p'|} \right)^a \tag{5.31}$$

Exponential viscous nucleus (i.e. di Prisco and Imposimato (1996)):

$$\Phi(f) = e^{af} \tag{5.32}$$

where a is a constitutive parameter and f is the normalized yield function. In both cases the normalization of the yield function is done with respect to the isotropic mean pressure, which is necessary when dealing with cohesionless materials such as sands.

Derivatives of plastic potential with respect to effective stress:

For completeness sake, the mathematic derivation useful for the implementation of the model is presented here below.

The chain rule of differentiation gives:

$$\frac{\partial g}{\partial \boldsymbol{\sigma}'} = \frac{\partial g}{\partial p'} \frac{\partial p'}{\partial \boldsymbol{\sigma}'} + \frac{\partial g}{\partial q} \frac{\partial q}{\partial \boldsymbol{\sigma}'} + \frac{\partial g}{\partial S} \frac{\partial S}{\partial \boldsymbol{\sigma}'} \tag{5.33}$$

- Derivative of g with respect to p':

$$\begin{aligned}\frac{\partial g}{\partial p'} &= \frac{\partial}{\partial p'}\left\{A_g^{K_{1g}/C_g} B_g^{-K_{2g}/C_g} p' - \tilde{p}'_s\right\} \\ &= \left(A_g^{\frac{K_{1g}}{C_g}} B_g^{-\frac{K_{2g}}{C_g}}\right)\frac{\partial p'}{\partial p'} + \left(\frac{\partial}{\partial p'}\left\{A_g^{\frac{K_{1g}}{C_g}} B_g^{-\frac{K_{2g}}{C_g}}\right\}\right)p' \\ &= A_g^{\frac{K_{1g}}{C_g}} B_g^{-\frac{K_{2g}}{C_g}}\left\{1 + \frac{q}{p' C_g M_g(S)}\left(-A_g^{-1} + B_g^{-1}\right)\right\}\end{aligned} \tag{5.34}$$

- Derivative of p' with respect to **σ**':

$$\frac{\partial p'}{\partial \boldsymbol{\sigma}'} = \frac{\partial}{\partial \boldsymbol{\sigma}'}\left\{\frac{1}{3}\mathrm{tr}(\boldsymbol{\sigma}')\right\} = \frac{1}{3}\mathbf{1} \tag{5.35}$$

- Derivative of g with respect to q:

$$\begin{aligned}\frac{\partial g}{\partial q} &= \left[\frac{\partial}{\partial q}\left\{A_g^{\frac{K_{1g}}{C_g}}\right\}\right] B_g^{-\frac{K_{2g}}{C_g}} p' + A_g^{\frac{K_{1g}}{C_g}}\left[\frac{\partial}{\partial q}\left\{B_g^{-\frac{K_{2g}}{C_g}}\right\}\right] p' \\ &= \frac{K_{1g}}{C_g} A_g^{\frac{K_{1g}}{C_g}-1}\left[\frac{\partial}{\partial q}\{A_g\}\right] B_g^{-\frac{K_{2g}}{C_g}} p' - \frac{K_{2g}}{C_g} A_g^{\frac{K_{1g}}{C_g}} B_g^{-\frac{K_{2g}}{C_g}-1}\left[\frac{\partial}{\partial q}\{B_g\}\right] p' \\ &= A_g^{\frac{K_{1g}}{C_g}} B_g^{-\frac{K_{2g}}{C_g}} p'\left\{\frac{K_{1g}}{C_g} A_g^{-1}\left[\frac{\partial}{\partial q}\{A_g\}\right] - \frac{K_{2g}}{C_g} B_g^{-1}\left[\frac{\partial}{\partial q}\{B_g\}\right]\right\}\end{aligned} \tag{5.36}$$

The derivative in Equation (5.14) is needed for the $\partial_q\{A_g\}$ and $\partial_q\{B_g\}$:

$$\frac{\partial M_g(S)}{\partial q} = \frac{\partial}{\partial q}\left\{\frac{2cM_{cg}}{(1+c)-(1-c)\frac{27}{2}\frac{S^3}{q^3}}\right\} = -\frac{M_g(S)}{(1+c)-(1-c)\frac{27}{2}\frac{S^3}{q^3}}(1-c)\frac{81}{2}\frac{S^3}{q^4} \tag{5.37}$$

and:

$$\begin{aligned}\frac{\partial}{\partial q}\{A_g\} &= \frac{\partial}{\partial q}\left\{1 + \frac{1}{K_{1g} M_g(S)}\frac{q}{p'}\right\} = \frac{1}{K_{1g} M_g(S)}\frac{1}{p'}\frac{\partial q}{\partial q} + \frac{1}{K_{1g}}\frac{q}{p'}\frac{\partial}{\partial q}\left\{\frac{1}{M_g(S)}\right\} \\ &= \frac{1}{K_{1g} M_g(S)}\frac{1}{p'}\left\{1 + \frac{(1-c)}{(1+c)-(1-c)\frac{27}{2}\frac{S^3}{q^3}}\left[\frac{81}{2}\frac{S^3}{q^3}\right]\right\}\end{aligned} \tag{5.38}$$

In similar way:

$$\frac{\partial}{\partial q}\left\{B_g\right\}=\frac{1}{K_{2g}M_g(S)}\frac{1}{p'}\left\{1+\frac{(1-c)}{(1+c)-(1-c)\frac{27}{2}\frac{S^3}{q^3}}\left[\frac{81}{2}\frac{S^3}{q^3}\right]\right\} \tag{5.39}$$

Substituting Equations (5.38) and (5.39) into (5.36) it follows:

$$\begin{aligned}\frac{\partial g}{\partial q}&=A_g^{\frac{K_{1g}}{C_g}}B_g^{-\frac{K_{2g}}{C_g}}\left[\frac{1}{C_gM_g(S)}\right]\left\{1+\frac{(1-c)}{(1+c)-(1-c)\frac{27}{2}\frac{S^3}{q^3}}\left[\frac{81}{2}\frac{S^3}{q^3}\right]\right\}\left(A_g^{-1}-B_g^{-1}\right)\\&=A_g^{\frac{K_{1g}}{C_g}}B_g^{-\frac{K_{2g}}{C_g}}\left[\frac{1}{C_gM_g(S)}\right]\left\{1+\frac{(1-c)}{(1+c)-(1-c)}3\right\}\left(A_g^{-1}-B_g^{-1}\right)\end{aligned} \tag{5.40}$$

- Derivative of q with respect to **σ'**:

$$\begin{aligned}\frac{\partial q}{\partial \boldsymbol{\sigma}'}&=\frac{\partial q}{\partial \mathbf{s}}:\frac{\partial \mathbf{s}}{\partial \boldsymbol{\sigma}'}=\frac{\partial}{\partial \mathbf{s}}\left\{\sqrt{\frac{3}{2}}\|\mathbf{s}\|\right\}:\frac{\partial}{\partial \boldsymbol{\sigma}'}\left\{\boldsymbol{\sigma}'-\frac{1}{3}\mathrm{tr}(\boldsymbol{\sigma}')\mathbf{1}\right\}=\sqrt{\frac{3}{2}}\frac{\mathbf{s}}{\|\mathbf{s}\|}:\left(\mathbf{I}-\frac{1}{3}\mathbf{1}\otimes\mathbf{1}\right)\\&=\sqrt{\frac{3}{2}}\frac{\mathbf{s}}{\|\mathbf{s}\|}=\frac{3}{2}\frac{\mathbf{s}}{q}\end{aligned} \tag{5.41}$$

- Derivative of g with respect to S:

$$\frac{\partial g}{\partial S}=\frac{\partial g}{\partial M_g(S)}\frac{\partial M_g(S)}{\partial S} \tag{5.42}$$

with:

$$\begin{aligned}\frac{\partial g}{\partial M_g(S)}&=\frac{K_{1g}}{C_g}A_g^{\frac{K_{1g}}{C_g}-1}\left[\frac{\partial}{\partial M_g(S)}\left\{A_g\right\}\right]B_g^{-\frac{K_{2g}}{C_g}}p'-\frac{K_{2g}}{C_g}A_g^{\frac{K_{1g}}{C_g}}B_g^{-\frac{K_{2g}}{C_g}-1}\left[\frac{\partial}{\partial M_g(S)}\left\{B_g\right\}\right]p'\\&=A_g^{\frac{K_{1g}}{C_g}}B_g^{-\frac{K_{2g}}{C_g}}\frac{q}{C_g}\frac{1}{M_g(S)}\frac{1}{M_g(S)}\left\{-A_g^{-1}+B_g^{-1}\right\}\end{aligned} \tag{5.43}$$

and:

$$\frac{\partial M_g(S)}{\partial S}=\frac{\partial}{\partial q}\left\{\frac{2cM_{cg}}{(1+c)-(1-c)\frac{27}{2}\frac{S^3}{q^3}}\right\}=\frac{M_g(S)}{(1+c)-(1-c)\frac{27}{2}\frac{S^3}{q^3}}(1-c)\frac{81}{2}\frac{S^2}{q^3} \tag{5.44}$$

Substituting Equations (5.43) and (5.44) into (5.42) one obtains:

$$\frac{\partial g}{\partial S} = A_g^{\frac{K_{1g}}{C_g}} B_g^{-\frac{K_{2g}}{C_g}} \frac{1}{C_g M_g(S)} \frac{(1-c)}{(1+c)-(1-c)\frac{27}{2}\frac{S^3}{q^3}} \left[\frac{81}{2}\frac{S^2}{q^2}\right] \left\{-A_g^{-1}+B_g^{-1}\right\}$$
$$\Big| \qquad\qquad (5.45)$$
$$= A_g^{\frac{K_{1g}}{C_g}} B_g^{-\frac{K_{2g}}{C_g}} \frac{1}{C_g M_g(S)} \frac{(1-c)}{(1+c)-(1-c)} \left[\frac{3q}{S}\right] \left\{-A_g^{-1}+B_g^{-1}\right\}$$

- Derivative of S with respect to **σ'**:

$$\frac{\partial S}{\partial \boldsymbol{\sigma}'} = \frac{1}{3}\left[\frac{1}{3}\mathrm{tr}\left(\mathbf{s}^3\right)\right]^{\frac{1}{3}-1} \frac{\partial}{\partial \boldsymbol{\sigma}'}\left\{\frac{1}{3}\mathrm{tr}\left(\mathbf{s}^3\right)\right\} = \frac{1}{9}\frac{1}{S^2}\frac{\partial}{\partial \boldsymbol{\sigma}'}\left\{\mathrm{tr}\left(\mathbf{s}^3\right)\right\} \qquad (5.46)$$

(for detailed computation see Appendix A).

5.4.2 Dependence of Constitutive Parameters on Relative Density

It is very well known fact that granular materials exhibit mechanical behaviour which is both density-dependent (pycnotropy) and pressure-dependent (barotropy). The Nova constitutive model and all the attempts so far with it disregard this dependence and need different set of constitutive parameters for each density and effective confining pressure.

As an alternative of using the state parameter concept, the proposed viscoplastic formulation, as further novelty, is enhanced with the dependence of the constitutive parameters on the relative density. The main scope is to describe with one only set of material parameters the behaviour of a specific type of sand for different densities.

Herein, the transition from dense to loose states and vice versa is modeled by introducing a linear dependence of the constitutive parameters on the relative density, Dr, as has been originally proposed in di Prisco et al. (2002).

Based on the evolution of the volumetric strain, the void ratio and the relative density are updated at each time step (Equation (5.47); (5.48)), allowing the interpolation of the material parameters between loose and dense properties (Equation (5.49)). In particular, a linear interpolation function between the values of the dense (p_{Di}) and the loose (p_{Li}) parameters is chosen.

$$de = -(1+e(t))\cdot d\varepsilon_v, \quad e(t+dt) = e(t) + de \qquad (5.47)$$

$$D_r(t+dt) = \frac{e_{max} - e(t+dt)}{e_{max} - e_{min}} \qquad (5.48)$$

$$p_i = p_{Li} + (p_{Di} - p_{Li})\cdot D_r(t+dt) \qquad (5.49)$$

The constitutive parameters assumed to be linearly dependent on the current value of D_r are the initial shear modulus, G_0, and the hardening parameters, ρ_s ,ξ_s, and r_{sw}.

However, it should be noted that, based on the analyses results, as presented in the following Section 5.5, a non-linear relation is proposed for the dilatancy at failure (ξ_s) and plastic

compressibility (ρ_s). This relation came out after a trial and error procedure and gave the most favorable results that will be shown next.

$$\xi_s = \xi_{sL} + (\xi_{sD} - \xi_{sL})Dr^{5(e_{max}-e_{min})} \tag{5.50}$$

5.4.3 Algorithmic Treatment

For the applications of the theory discussed in the previous sections within the context of the FE method, a suitable computational strategy should be defined to integrate numerically (at the Gauss point level) the evolution equations in time, from a given initial state. In the following a Forward Euler algorithm (Figure 5.15) is adopted for simplicity and therefore the state at current time step (t_{n+1}) depends on the state at the previous time step (t_n).

It is assumed that at time t_n the state of the material ($\boldsymbol{\varepsilon}_n$, $\boldsymbol{\varepsilon}_n^{vp}$, $\boldsymbol{\sigma}'_n$) is known at any quadrature point in the adopted finite element discretization. Then, suppose that an increment in total strain ($\Delta\varepsilon_{n+1}$) is given, which drives the state to time $t_{n+1} = t_n + \Delta t$. The computational problem to be addressed is thus the updating of the state variables at time t_{n+1}, through the integration of the differential-algebraic system, summarized for completeness bellow:

$$\dot{\boldsymbol{\sigma}}' = \mathbf{D}^e : \left(\dot{\boldsymbol{\varepsilon}} - \dot{\boldsymbol{\varepsilon}}^{vp}\right) \tag{5.51}$$

$$\dot{\boldsymbol{\varepsilon}}^{vp} = \gamma \left\langle \Phi(f) \right\rangle \frac{\partial g}{\partial \boldsymbol{\sigma}'} \tag{5.52}$$

$$\dot{p}'_s = \dot{\lambda}\rho_s p'_s \left(\hat{T} + \xi_s \hat{N}\right) - r_{sw} p'_s \dot{S}_w \tag{5.53}$$

with

$$\hat{T} = \mathrm{tr}\left(\frac{\partial g}{\partial \boldsymbol{\sigma}'}\right), \quad \hat{N} = \sqrt{\frac{2}{3}}\left\| \mathrm{dev}\left(\frac{\partial g}{\partial \boldsymbol{\sigma}'}\right)\right\| \tag{5.54}$$

The first step in the algorithm is to calculate the elastically induced trial state by freezing the viscoplastic flow. The trial stress is computed from Equation (5.55). Then, it is tested if the trial state is inside or outside the yield surface, $f_{n+1}^{tr} \le 0$. If it falls within or is on the yield surface the process is elastic and the trial state represents the actual final state of the material.

$$\boldsymbol{\sigma}'^{trial}_{n+1} = \left[\frac{\partial \psi}{\partial \boldsymbol{\varepsilon}^e}\right]_{\boldsymbol{\varepsilon}^e = \boldsymbol{\varepsilon}^{e,trial}_{n+1}} \tag{5.55}$$

If the trial state lies outside the yield locus the process is declared viscoplastic and the inelastic parameter λ is determined through Equation (5.56):

$$\Delta\lambda_{n+1} = \frac{\Delta t}{\eta}\Phi(f)_n \tag{5.56}$$

From the knowledge of $\Delta\lambda_{n+1}$ the viscoplastic strain and the hardening parameter are computed by the explicit integration of Equations (5.52) and (5.53), respectively. Subsequently, the components of the stress tensor can be updated.

$$\boldsymbol{\varepsilon}_{n+1}^{vp} = \boldsymbol{\varepsilon}_{n}^{vp} + \Delta\lambda_{n+1} \left.\frac{\partial g}{\partial \boldsymbol{\sigma}'}\right|_{n} \tag{5.57}$$

Similarly, the hardening parameter is given by:

$$\Delta p_s' = \Delta\lambda_{n+1}\rho_s p_{s,n}' \left(\hat{T} + \xi_s \hat{N}\right) - r_{sw} p_{s,n}' \Delta S_r \tag{5.58}$$

The corresponding numerical algorithm is summarized in Table 5.6, highlighting the essential steps of the numerical implementation.

Table 5.6: Numerical algorithm for the VISCUNsand model.

1. Given strain field ε_n and strain increment $\Delta\varepsilon_{n+1}$

$$\varepsilon_{n+1} = \varepsilon_n + \Delta\varepsilon_{n+1}$$

2. Trial elastic state

$$\boldsymbol{\sigma}'^{trial}_{n+1} = \left[\frac{\partial \psi}{\partial \boldsymbol{\varepsilon}^e}\right]_{\boldsymbol{\varepsilon}^e = \boldsymbol{\varepsilon}^{e,trial}_{n+1}}$$

3. Check viscoplastic flow potential

IF: $f^{tr}_{n+1} \le 0 \rightarrow$ elastic step $\rightarrow$ Set $(\bullet)_{n+1} = (\bullet)^{tr}_{n+1}$ & EXIT

else go to 4

4. Compute $\Delta\lambda_{n+1}$: $\Delta\lambda_{n+1} = \dfrac{\Delta t}{\eta}\Phi(f)_n$

5. Update viscoplastic strain and stress

$$\boldsymbol{\varepsilon}^{vp}_{n+1} = \boldsymbol{\varepsilon}^{vp}_{n} + \Delta\lambda_{n+1} \left.\frac{\partial g}{\partial \boldsymbol{\sigma}'}\right|_{n}$$

$$p'_{s,n+1} = p'_{s,n} + \Delta\lambda_{n+1}\rho_s p'_{s,n} \left(\hat{T} + \xi_s \hat{N}\right) - r_{sw} p'_{s,n} \Delta S_r$$

$$\boldsymbol{\sigma}'_{n+1} = \boldsymbol{\sigma}'_{n} + \mathbf{D}^{el}\left(\Delta\varepsilon_{n+1} - \Delta\lambda_{n+1} \left.\frac{\partial g}{\partial \boldsymbol{\sigma}'}\right|_{n}\right)$$

It is noted that the consistent tangent matrix in explicit viscoplasticity is the elastic (Equation (5.8)) as derived in Equation (5.59). As a final remark, non-locality can be introduced straightforward by simply converting the yield function to a non-local variable, following the procedure described in Section 3.5.

$$C^{vp}_{n+1} = \frac{\partial \boldsymbol{\sigma}'_{n+1}}{\partial \boldsymbol{\varepsilon}^{el,trial}_{n+1}} = \frac{\partial\left[\boldsymbol{\sigma}'_{n} + \mathbf{D}^{el}\left(\Delta\varepsilon_{n+1} - \Delta\lambda_{n+1} \left.\frac{\partial g}{\partial \boldsymbol{\sigma}'}\right|_{n}\right)\right]}{\partial \boldsymbol{\varepsilon}^{el,trial}_{n+1}} = \mathbf{D}^{el} \tag{5.59}$$

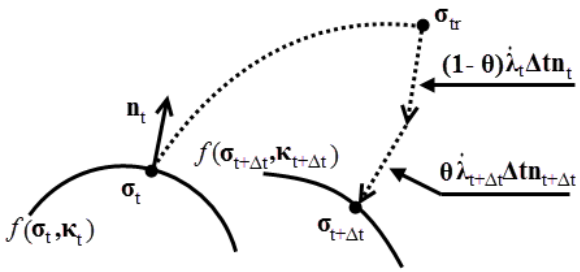

Figure 5.15: Geometric interpretation of the Euler integration scheme (Wang et al. (1997)). Explicit method is obtained for θ=0 and implicit for θ=1, respectively.

5.5 Validation, Calibration and Performance of VISCUNsand Model in Comes-geo F.E. Code

The implementation of the viscoplastic model for unsaturated soils is validated through single-element analyses. A set of oedometer, creep and triaxial tests under different hydraulic conditions is performed to prove the efficiency of the code. Suction controlled triaxial tests, similar to those presented in Section 5.3.1, are given in Appendix B for brevity.

5.5.1 Oedometric Test with Drying-Wetting Paths

The first simulated example is the oedometric test with varying drying and wetting paths, presented in Section 5.3.2 for the elastoplastic model. This test is repeated to prove that also the viscoplastic model can describe complex hydraulic paths as well as the wetting induced collapse phenomenon.

The results are shown in Figures Figure 5.16Figure 5.17 and the viscosity parameters used for the simulation are γ=0.1 s^{-1} and α=1.0. The superposition confirms the correct implementation and the ability of the model to describe the most characteristic features of unsaturated soil behaviour.

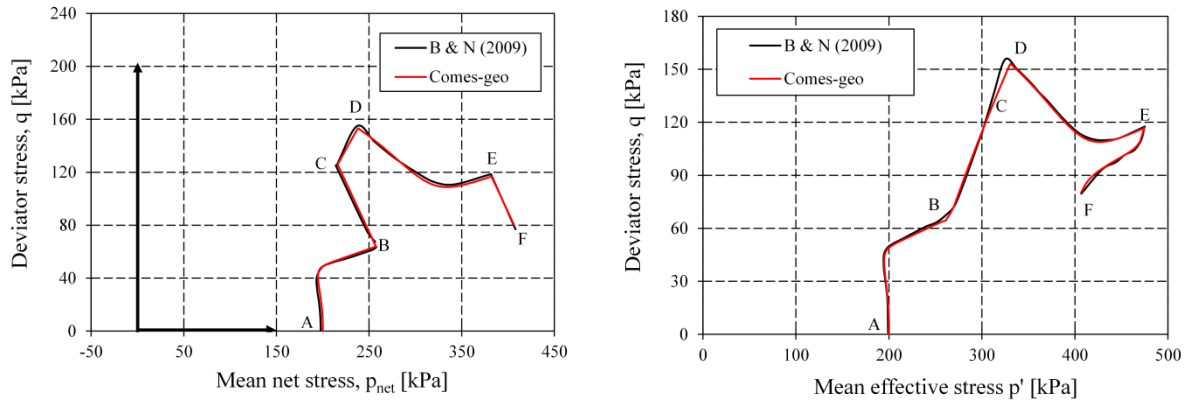

(a) (b)

Figure 5.16: VISCUNsand validation – Results from the oedometer simulation: (a) effective stress path and (b) stress path in the net stress space.

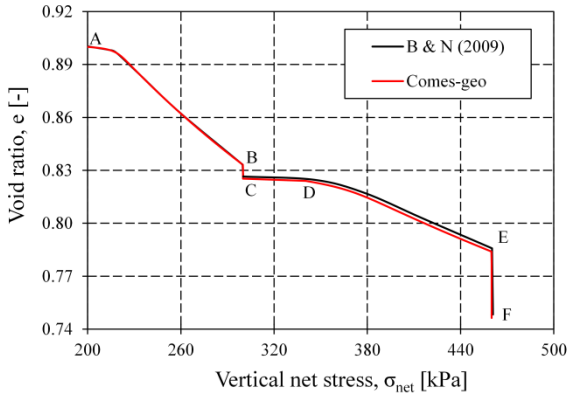

Figure 5.17: VISCUNsand validation – Void ratio with respect to vertical net stress.

5.5.2 Creep Tests on Loose and Dense Hostun Sand

The second simulated example refers to creep tests. Through these tests the time dependency of loose and dense Hostun sand will be observed and reproduced in the framework of elasto-viscoplasticity. The experimental data for the loose Hostun sand were found in the work of di Prisco and Imposimato (1996) while for the dense Hostun sand in the work of Pham Van Bang et al. (2007).

At the same time through these simulations, the material parameters, including viscosity, for both loose and dense Hostun sand are calibrated. The calibrated parameters will be used in the subsequent section to examine the model's behaviour for different densities.

As far as the creep test on loose Hostun sand (D_r = 20 %) is concerned, the material parameters are listed in Table 5.7 and Table 5.8. A non-associated plastic flow rule is used. The drained triaxial load controlled test is carried out by increasing the axial load while keeping constant the radial stress, up to the stress level corresponding to the mobilized friction angle (Figure 5.18a). In Figure 5.18b the axial load time history is illustrated: the time periods between two following load steps are constant, but the load increment values are variable.

Table 5.7: Creep test on loose Hostun sand − List of model parameters.

Elastic parameters	Yield surface parameters	Plastic potential	Hardening parameters	SWCC parameters	Initial state	Initial S_w & void ratio
α=0.0	α_f=0.99	α_g=0.24	r_s=1/0.009	α=0.8	p_0=100 kPa	S_{w0}=1.0
k=0.0046	m_f=1.1	m_g=1.1	ξ_s=0.0	n=1.8	q_0=0 kPa	e_0=0.945
G_0=14MPa	M_{cf}=0.52	M_{cg}=1.28	r_{sw}=5.45	m=1.9	p_{s0}=100 kPa	
p_r=1 kPa	M_{ef}=0.44	M_{eg}=1.0				

Figure 5.19 shows the time-dependent behaviour of the material in both linear and semi-logarithmic scale. The experimental results are denoted with open symbols whereas the results of the numerical analysis are depicted with a red solid line. It is clearly shown that in the time period 200-1000 min where the load is kept constant, the axial strain slowly but continuously increases. It is important to

underline that, this time-dependent behaviour is reproduced both with the linear and the exponential viscous nucleus for the viscosity values presented in Table 5.8.

Table 5.8: Creep test on loose Hostun sand – Calibration of viscous parameters.

Viscous Nucleus	γ [s^{-1}]	a [-]
Linear	$4 \cdot 10^{-9}$	1.0
Exponential	$2 \cdot 10^{-14}$	28.90

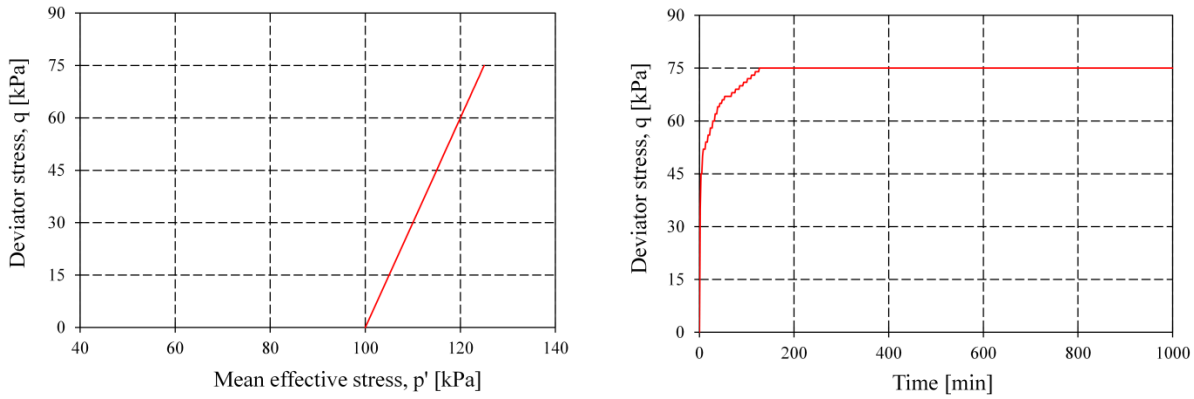

(a) (b)

Figure 5.18: VISCUNsand validation – Results from the creep test on loose Hostun sand: (a) effective stress path and (b) axial load-time history.

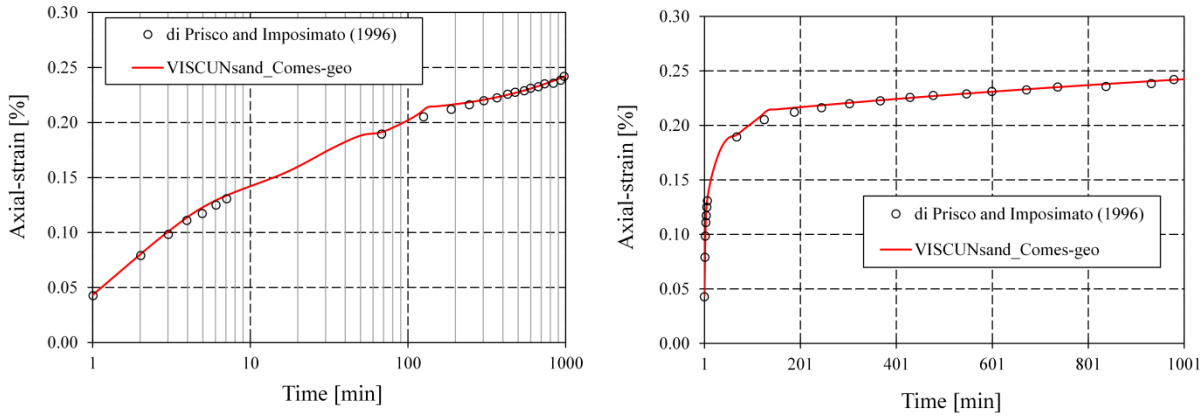

(a) (b)

Figure 5.19: VISCUNsand validation – Results from the creep test on loose Hostun sand: axial strain versus time in a (a) semi-logarithmic and (b) linear scale.

The creep test by Pham Van Bang et al. was performed on air-dried dense Hostun sand (D_r = 81 %). An isotropic consolidation brings the sample to the desired isotropic stress (i.e. 80 kPa) and then a drained triaxial compression path follows. At this path, the experimental procedure included three additional stages: the specimen was loaded at a constant stress rate until a specific point is reached,

then a creep period was imposed and small cycles were applied after the creep, as shown in Figure 5.20.

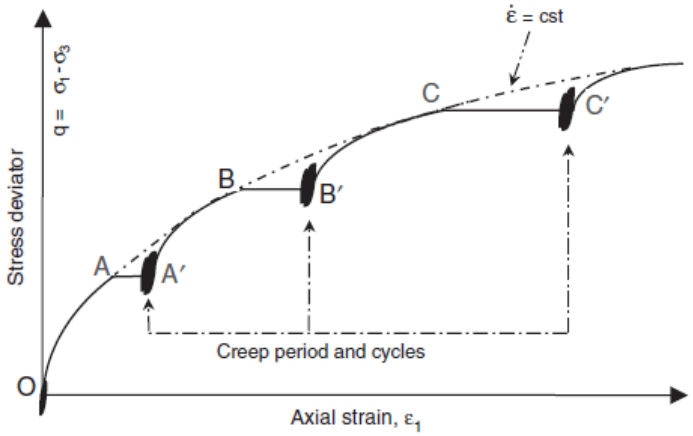

Figure 5.20: VISCUNsand validation – Creep test on dense Hostun sand (Pham Van Bang et al. (2007)).

The model material parameters and the calibrated viscosities for the two viscous nucleus definitions are given in Table 5.9 and Table 5.10 respectively.

Table 5.9: Creep test on dense Hostun sand − List of model parameters.

Elastic parameters	Yield surface parameters	Plastic potential	Hardening parameters	SWCC parameters	Initial state	Initial S_w & void ratio
α=0.0	α_f=0.63	α_g=0.63	r_s=1/0.0005	α=0.8	p_0=80kPa	S_{w0}=1.0
k=0.0046	m_f=1.4	m_g=1.4	ξ_s=0.49	n=1.8	q_0=0 kPa	e_0=0.71
G_0=45MPa	M_{cf}=1.2	M_{cg}=1.28	r_{sw}=0.32	m=1.9	p_{s0}=80 kPa	
p_r=1 kPa	M_{ef}=1.0	M_{eg}=1.0				

Table 5.10: Creep test on dense Hostun sand – Calibration of viscous parameters.

Viscous Nucleus	γ [s^{-1}]	a [-]
Linear	$1 \cdot 10^{-8}$	1.0
Exponential	$2 \cdot 10^{-10}$	28.90

The global stress-strain curve is presented in Figure 5.21a with the location of the four creep periods. The axial strain creep periods obtained after primary loading are plotted in Figure 5.21b both for experimental and numerical observations. The viscoplastic model reproduces in a satisfactory manner the creep periods between the loading stages, however a small deviation is displayed in the global stress-strain behaviour. This discrepancy can be attributed to the different conditions followed

in the simulations compared to the experimental procedure. For the sake of simplicity, in the numerical simulation the performance of small circles after the creep periods was excluded.

Finally, by comparing the creep behaviour of loose and dense Hostun sand, it is observed that the amount of creep strain is more pronounced for the loose sample which is in accordance with the literature. This fact is also highlighted in the values of viscosity parameter (γ increases with increasing density).

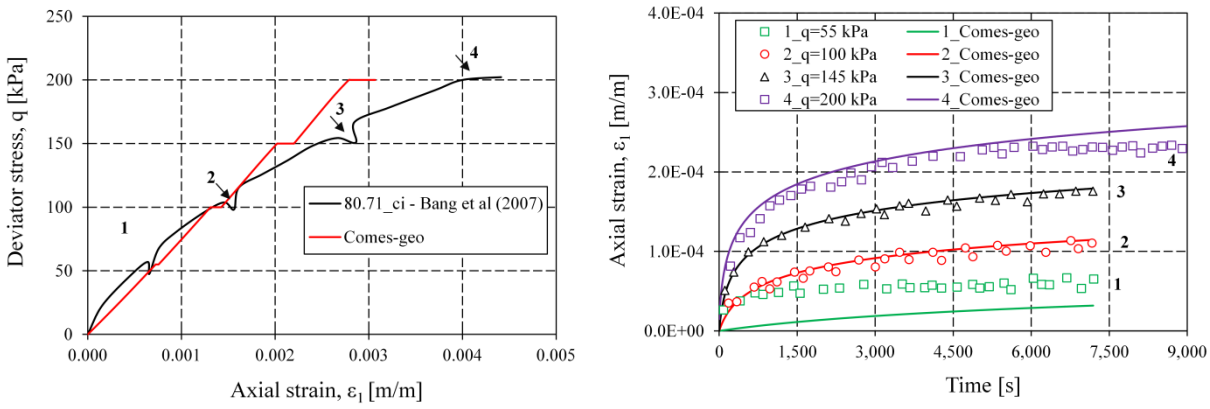

(a) (b)

Figure 5.21: VISCUNsand validation – Results from the creep test on dense Hostun sand: (a) stress-strain curve and (b) time evolution of axial creep strain for primary loading.

5.5.3 Drained and Undrained Triaxial Compression Tests on Loose, Medium and Dense Hostun Sand

In this section it will be discussed the ability of the viscoplastic model to represent the mechanical behaviour of granular soils over a wide range of void ratio. As a reminder to the reader, the VISCUNsand model has been enhanced with density-dependent constitutive parameters. The same dependency has also been applied to the UNsand model however emphasis is here given only to the viscoplastic model.

For calibrating the constitutive parameters and validating the model, standard triaxial tests performed on Hostun sand in different laboratories are used. The data were collected from the work of Gajo and Wood (1999) and Daouadgji et al. (2010) and are presented in Table 5.11 and Table 5.12 respectively.

The main scope is to perform all these tests using only one set of material parameters for the viscoplastic model. Due to the large scatter of the experimental data, the calibration process was performed iteratively in combination with the viscosity values from the creep tests on Hostun sand (presented in the previous section). The complete set of material constants is detailed in Table 5.13 and Table 5.14. The initial conditions in terms of mean stress (p_0), preconsolidation stress (p_{s0}) and void ratio (e_0) depend on each test examined based on Table 5.11 and Table 5.12.

Table 5.11: Characteristics of the triaxial compression tests as in Gajo and Wood (1999).

Test name	Ends	Drainage	p_0 [kPa]	e_0 [-]
hos011	Smooth	Drained	300	0.574
hos027	Smooth	Drained	200	0.578
hosfl10	Smooth	Drained	300	0.800
hosfl11	Smooth	Drained	300	0.897
d4	Smooth	Drained	300	0.945
hosfl14	Smooth	Drained	50	0.838
hflw10	Smooth	Drained	600	0.822
batr02	Rough	Undrained	200	0.940
batr06	Rough	Undrained	200	0.830
alert9	Rough	Undrained	200	0.666

Table 5.12: Characteristics of the triaxial compression tests on loose Hostun sand as in Daouadji et al. (2010).

Test name	Drainage	p_0 [kPa]
CD-1	Drained	100
CD-2	Drained	300
CD-3	Drained	750
ICU-1	Undrained	100
ICU-2	Undrained	300
ICU-3	Undrained	750

Table 5.13: Parameters adopted for the simulations.

Elastic parameters	Yield surface parameters	Plastic potential	SWCC parameters	Initial state	Initial S_w
α=0.0	α_f=0.99	α_g=0.24	α=0.8	q_0=0 kPa	S_{w0}=1.0
k=0.0046	m_f=1.10	m_g=1.10	n=1.8		
p_r=1 kPa	M_{cf}=0.52	M_{cg}=1.28	m=1.9		
	M_{ef}=0.44	M_{eg}=1.0			

Accounting for the interaction between the loading rate and viscosity and their effect on the numerical results, the loading rate was kept constant to delimit the influential parameters. A realistic

loading rate was used. According to prof. J. Desrues (information provided in personal communication) a loading rate 1 to 2 mm/min was applied on specimens with slenderness ratio H/D=1 and H=D=100 mm, depending on the test type. Thus the loading strain rate of the experiments presented in the tables above was 1%/min for the drained and 2 %/min for the undrained tests.

In the following, apart from the comparison of the simulations with the experimental results, it is also discussed the effect of the viscous nucleus definition on the numerical predictions.

Table 5.14: Parameters used for different densities.

Test Name	G_0 [kPa]	B_p [-]	ξ_s [-]	r_{sw} [-]	e_D [-]
TXD-Loose	14000	0.0090	0.00	5.45	0.945
TXD-Medium	17000	0.0045	0.095	0.32	0.800
TXD-Dense	45000	0.0005	0.480	0.32	0.578
TXU-Loose	14000	0.0090	0.00	5.45	0.940
TXU-Medium	17000	0.0045	0.095	0.32	0.830
TXU-Dense	45000	0.0005	0.480	0.32	0.666

5.5.3.1 Linear Viscous Nucleus

In this subsection the comparison between the experimental data and the numerical results is presented for the loose, medium-dense and dense Hostun sand and is discussed in the context of the viscosity value influence. Herein, a linear viscous nucleus is adopted for the description of the material's mechanical response during the time evolution.

Loose Hostun sand

The triaxial compression tests under both drained and undrained conditions for the loose Hostun sand are shown in Figure 5.22. For the drained behaviour the viscous parameter ($\gamma=4\cdot10^{-9}$ s^{-1}), as calibrated in the drained creep test (see Section 5.5.2) was used.

However, it is evident, from Figure 5.22a,b that this value of γ cannot predict the experimental observations. In fact, based on the dilatant behaviour one might say that the response resembles more to a dense sand. This behaviour is weird since the creep and the drained triaxial tests are conducted for exactly the same material, using the same set for the material parameters. Trying to interpret this tendency the accuracy of the calibrated viscous parameters and the loading rate effect were examined.

To ensure the accuracy of the calibrated value, the creep test was repeated varying this time the viscosity value to examine the effect on the numerical results. In Figure 5.23, the variation of the solution of the creep test for different values of the viscosity parameter is presented. For $\gamma=4\cdot10^{-9}$ s^{-1} an almost perfect match with the experimental values is obtained whereas for a small decrease of the

fluidity parameter (from $4 \cdot 10^{-9}$ to $2 \cdot 10^{-9}$) the solution deviates greatly from the expected result. These results confirm that the calibrated value is of the order of 10^{-9} and in particular $\gamma=4 \cdot 10^{-9}$ s^{-1}.

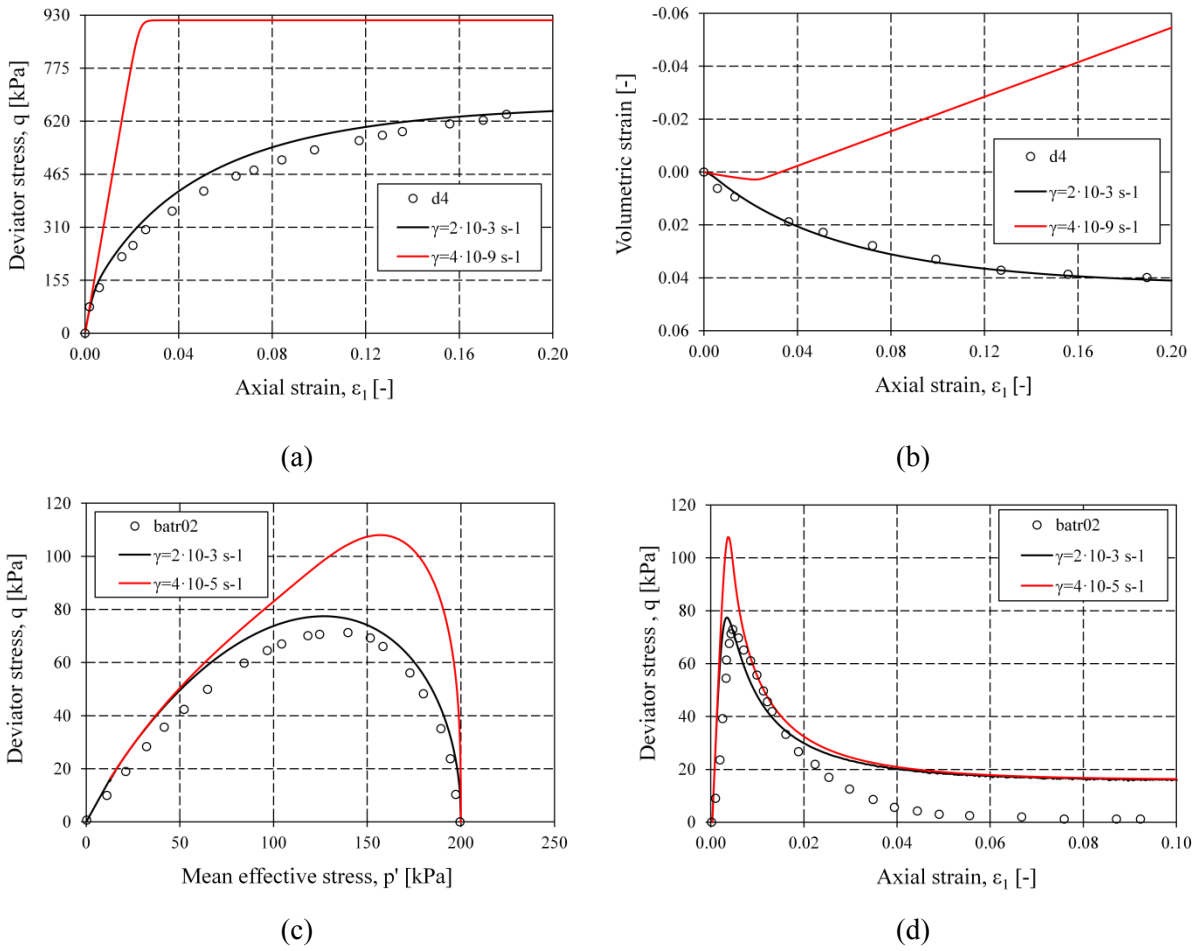

Figure 5.22: VISCUNsand validation – Loose Hostun sand: (a) drained conditions and (b) undrained conditions.

Afterwards, the influence of the loading rate on the numerical predictions was examined. The results are depicted in Figure 5.24 for four different loading rates and applying the calibrated viscosity value $\gamma=4 \cdot 10^{-9}$ s^{-1}. It is evident that for this value of viscosity, the drained triaxial test response is captured only for very small and unrealistic loading rate (10^{-4} mm/min), compared to the real loading velocity of the experiment.

The definition of the viscous nucleus seemed like the only reasonable solution for elucidating this behaviour. Along these lines, the exponential viscous nucleus was introduced and the results are presented in the following subsection.

However, in order to further investigate the influence of the viscous parameter on the consistency of the solution with the experimental results, a parametric analysis is performed for both drained and undrained conditions.

In Figure 5.22, the open symbols denote the experimental data, the red line the numerical results for the calibrated from the creep tests value and the black line denotes the simulation results using a value

of viscosity such that both drained and undrained behaviour is well reproduced. A viscosity parameter $\gamma=2\cdot10^{-3}\ s^{-1}$ shows the best match with the experimental data.

Table 5.15: Re-examined creep test on loose Hostun sand varying viscosity parameter.

Test No	η [s]	γ [s^{-1}]	a
1	$100\cdot10^{6}$	$1\cdot10^{-8}$	1
2	$250\cdot10^{6}$	$4\cdot10^{-9}$	
3	$300\cdot10^{6}$	$3.3\cdot10^{-9}$	
4	$500\cdot10^{6}$	$2\cdot10^{-9}$	

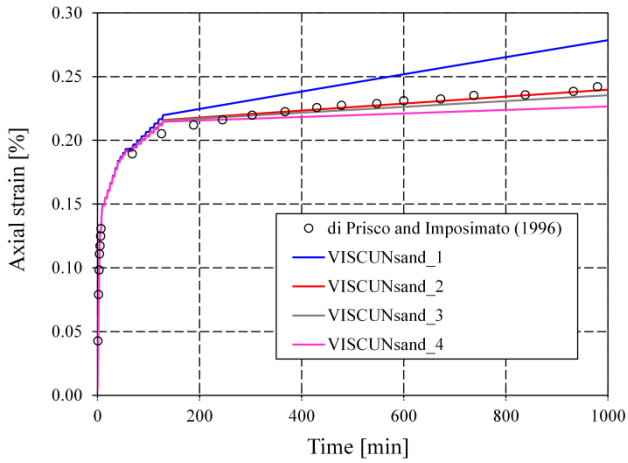

Figure 5.23: VISCUNsand validation – Axial strain evolution for the repeated creep test in loose Hostun sand varying the viscosity parameter.

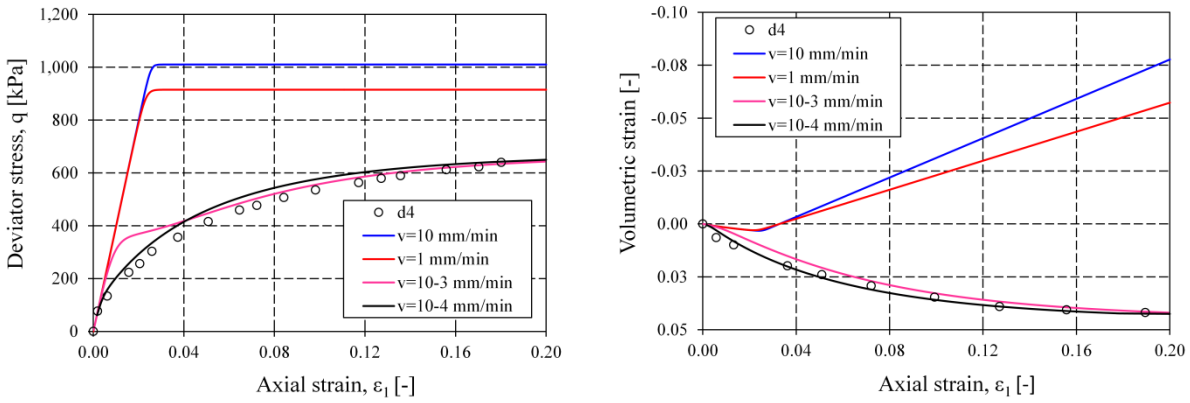

(a) (b)

Figure 5.24: VISCUNsand validation –Comparison of four different loading rates for the simulated drained behaviour of a loose Hostun sand with $\gamma=4\cdot10^{-9}\ s^{-1}$.

Medium-dense Hostun sand

To the author's knowledge, no relevant creep tests on medium-dense Hostun sand were found in the literature and thus no value for viscosity can be initially estimated. Figure 5.25 shows the comparison for both drained and undrained triaxial compression tests on medium dense Hostun sand for two viscosities; one that properly captures the experiments and one that strongly deviates. The value of the viscosity parameter that approaches what was experimentally observed is $\gamma=4\cdot10^{-4}\ s^{-1}$.

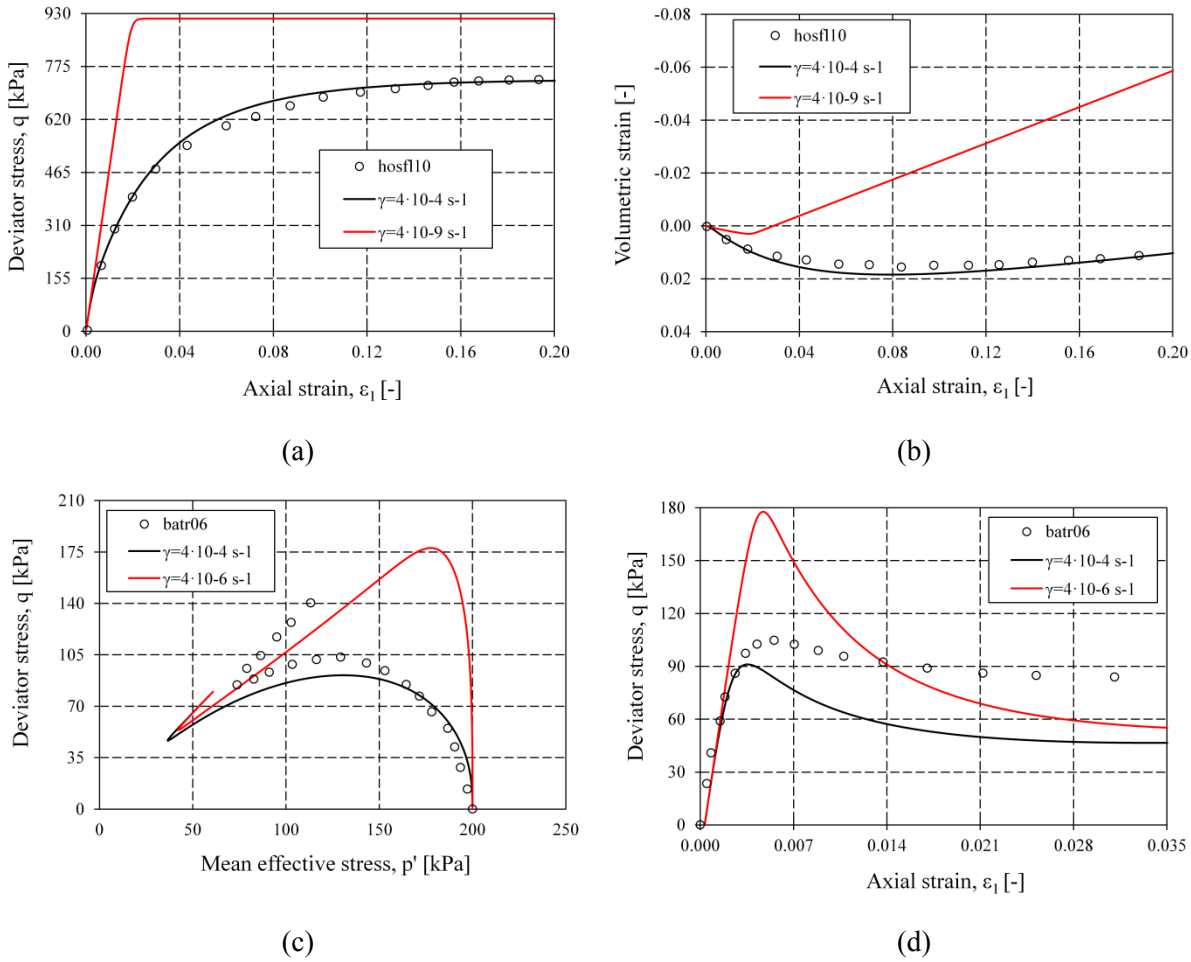

Figure 5.25: VISCUNsand validation – Medium Hostun sand: (a) drained conditions and (b) undrained conditions.

Dense Hostun sand

As in the case of the loose sand, also for the dense Hostun sand, the calibrated viscosity value does not reproduce in a proper manner the experimental data. The scatter however is much smaller than in the case of the loose sand.

Moreover, a value of the viscosity parameter $\gamma=4\cdot10^{-6}\ s^{-1}$ (black solid line in Figure 5.26) gives a better approximation for both drained and undrained conditions.

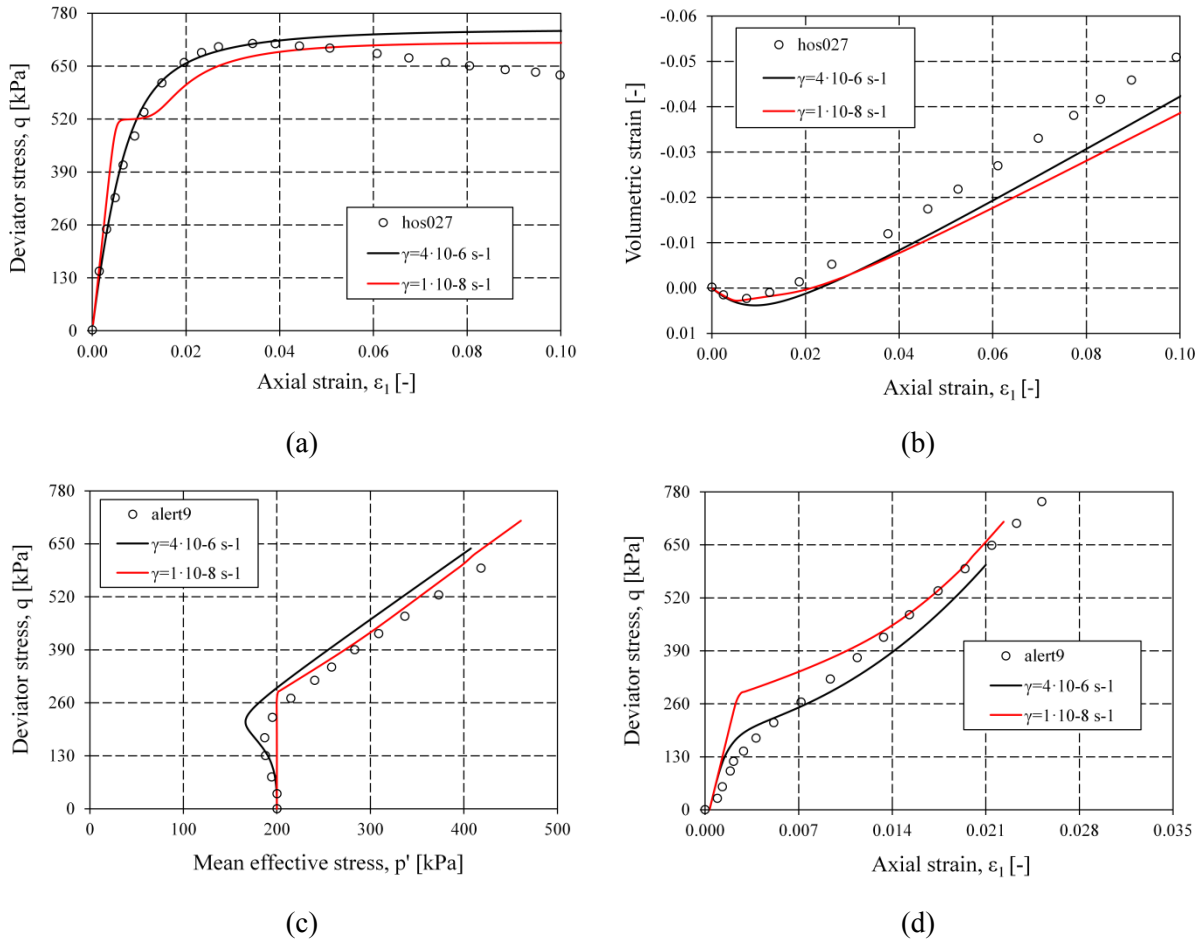

Figure 5.26: VISCUNsand validation – Dense Hostun sand: (a) drained conditions and (b) undrained conditions.

In summary, for each density a viscosity value was iteratively defined to approach the experimental observations. The same viscosities were applied for drained and undrained conditions and their values are as follows:

- Loose Hostun sand: $\gamma=2\cdot10^{-3}\ s^{-1}$
- Medium-dense Hostun sand: $\gamma=4\cdot10^{-4}\ s^{-1}$
- Dense Hostun sand: $\gamma=4\cdot10^{-6}\ s^{-1}$

5.5.3.2 Exponential Viscous Nucleus

Herein, the viscoplastic model is validated by comparison with experimental results obtained from triaxial tests on Hostun sand covering a wide range of density and stress level. An exponential definition for the viscous nucleus is assumed to overcome the obstacle previously discussed regarding the calibration of the viscosity values.

Comparisons of the observed and simulated drained behaviour of Hostun sand are first presented followed by comparisons on the undrained behaviour. In each figure (except if defined otherwise), the open symbols indicate the experimental observations, the dashed black lines the numerical simulations with the model proposed by Gajo and Wood (1999) for a comparison with the viscoplastic

model proposed in this thesis denoted with black solid lines. Moreover, in the figures below the red solid line with the 'with Dr' legend corresponds to the solution of the viscoplastic model applying the suggested Equation (5.50) for non-linear density. To simplify matters, these results came out assuming that the parameters ξ_s and B_p are non-linearly dependent on density whereas the rest of the material parameters vary linearly with density according to Equation (5.49). It is recalled that this expression occurred after a trial and error procedure, performing iteratively all the drained and undrained compression tests. For brevity and for the sake of completeness, an example of comparison between the linear and the non-linear function for the influence of relative density is given in Figure 5.27.

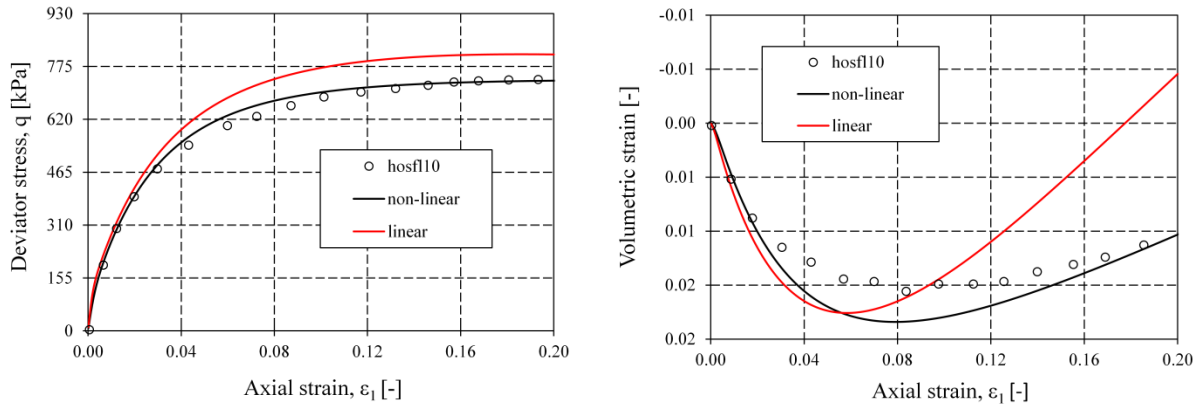

(a) (b)

Figure 5.27: VISCUNsand validation – Exponential viscous nucleus: Indicative comparison between the linear and non-linear function for the effect of D_r.

It should be noted that in the case of the undrained tests no volumetric change (due to isochoric constrain) occurs and therefore no evolution of the sample's density. Thus, no effect for Dr is depicted.

TXD on loose Hostun sand

Figure 5.28 and Figure 5.29 shows the comparison for ordinary drained triaxial compression tests for two samples of loose sand with different initial void ratios but a single confining pressure.

The volumetric strains are very well represented by the model and the maximum strength is perfectly reproduced for the very loose sand but is slightly underestimated for the hosfl11 sample in Figure 5.29a. In the latter, it is evident, that the results are improved in the case of non-linear density-dependence.

Another important aspect here is that the results are obtained using the viscosity value as calibrated from the creep test (Table 5.16), highlighting the crucial role of the viscous nucleus definition in the framework of viscoplasticity.

Table 5.16: Initial density and viscous parameters for the TXD test on loose Hostun sand.

Test name	p_0 [kPa]	e_0 [-]	γ [s^{-1}]	a [-]
d4	300	0.945	$2 \cdot 10^{-14}$	28.90
hosfl11	300	0.897	$2 \cdot 10^{-14}$	28.90

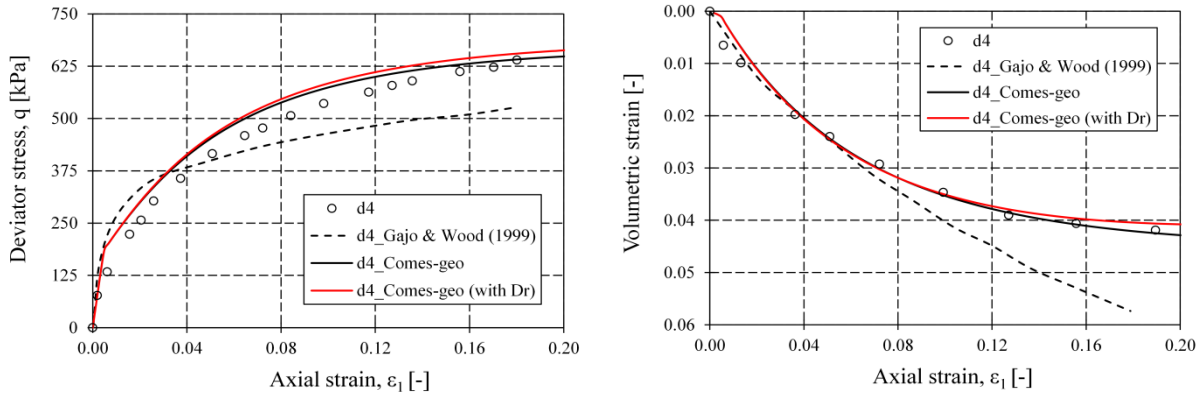

(a) (b)

Figure 5.28: VISCUNsand validation – Exponential viscous nucleus: Drained triaxial compression tests on loose (e_0=0.945) Hostun sand.

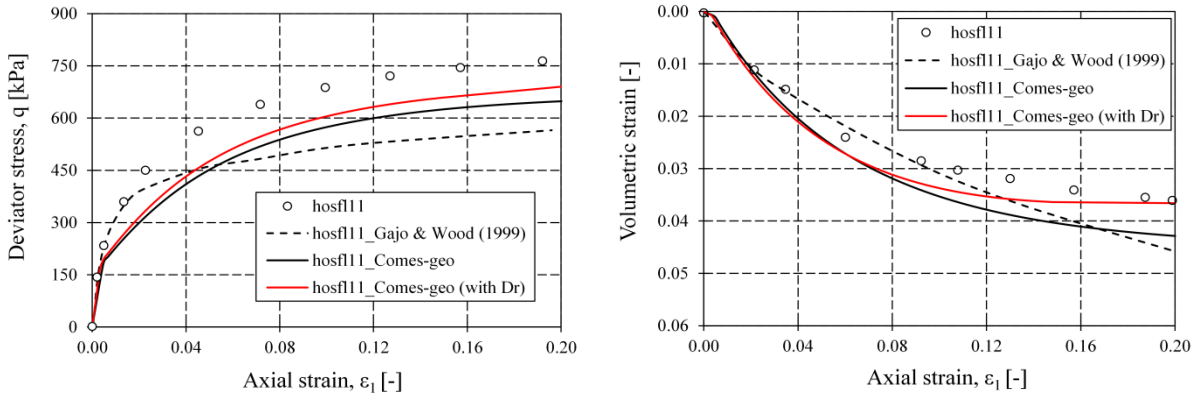

(a) (b)

Figure 5.29: VISCUNsand validation – Exponential viscous nucleus: Drained triaxial compression tests on loose (e_0=0.897) Hostun sand.

Drained tests at different confining pressures on loose samples are shown in Figure 5.30. The three CD tests, namely, CD-1, CD-2 and CD-3, have effective mean pressures of 100, 300 and 750 kPa, respectively. The stress-strain curves of these tests are shown in Figure 5.30a for the same void ratio (e_0=1.0). The full symbols are for the experimental data from Daouadji et al. (see Table 5.12) and with solid lines are the simulated viscoplastic results, applying the calibrated viscosity parameters ($\gamma=2 \cdot 10^{-14}$, a=28.90), and the non-linear relation for the density dependence.

The stress-strain behaviour is well captured for the three confining pressures. The simulated volumetric strain of the loose sample at high confining pressure (CD-3 of Figure 5.30b) slightly

deviates from the experimental however the results are very satisfactory. Finally, it can be seen that the critical state is reached when both the deviator stress and the volumetric strain approach constant.

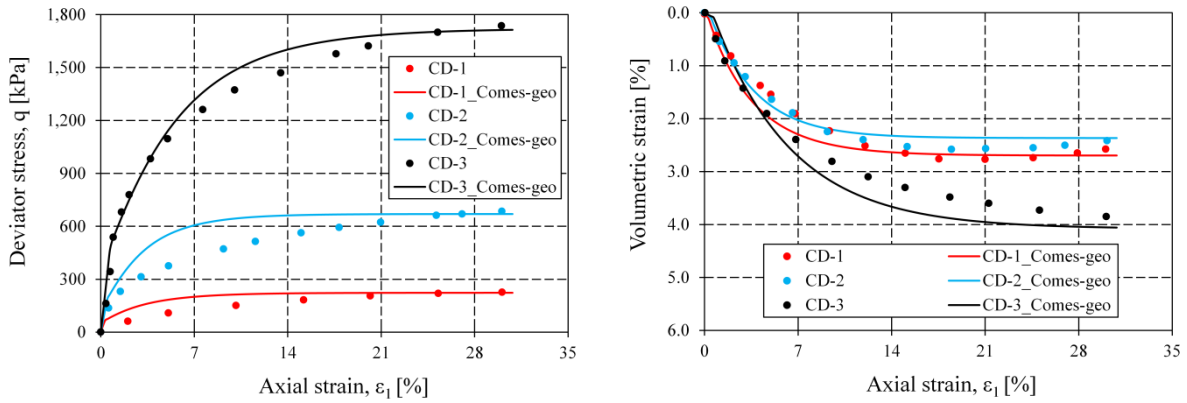

(a) (b)

Figure 5.30: VISCUNsand validation – Exponential viscous nucleus: Effects of the mean stress on drained triaxial compression tests with the same initial loose density.

TXD on medium-dense Hostun sand

The drained behaviour of medium-dense granular material is presented in Figure 5.31 for 300 kPa effective mean pressure. The initial density of the examined material and the viscous parameters applied are given in Table 5.17. The viscosity value used is $\gamma = 2 \cdot 10^{-12}$ s^{-1}.

The results are in good agreement with the experimental and the response is captured well qualitatively, both for the deviatoric stress – strain (Figure 5.31a) and the volumetric strain – axial strain (Figure 5.31b) diagrams. The maximum deviator stress is perfectly matched in Figure 5.31a and also, for increasing axial strain, the dilation of the material is described effectively by the analysis, as evidenced by Figure 5.31b.

Table 5.17: Initial density and viscous parameters for the TXD test on medium Hostun sand.

Test name	p_0 [kPa]	e_0 [-]	γ [s^{-1}]	a [-]
hosfl10	300	0.800	$2 \cdot 10^{-12}$	28.90
hosfl14	50	0.838	$2 \cdot 10^{-12}$	28.90
hflw10	600	0.822	$2 \cdot 10^{-12}$	28.90

The influence of the effective mean stress on drained triaxial compression tests of medium-dense sand is illustrated in Figure 5.32 for two values, 50 kPa and 600 kPa. It is observed that the increase of the mean stress alters the maximum deviator stress and the response is described properly by the examined model. The volumetric strain response is very well approximated for the higher mean stress whereas for the lower confining pressure is much less dilatant than the measured one.

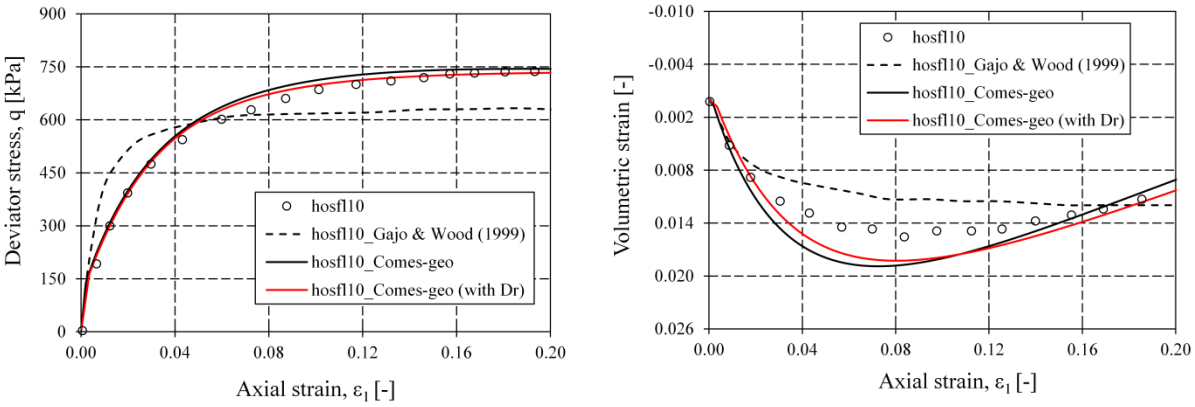

(a) (b)

Figure 5.31: VISCUNsand validation – Exponential viscous nucleus: Drained triaxial compression tests on a medium-dense Hostun sand.

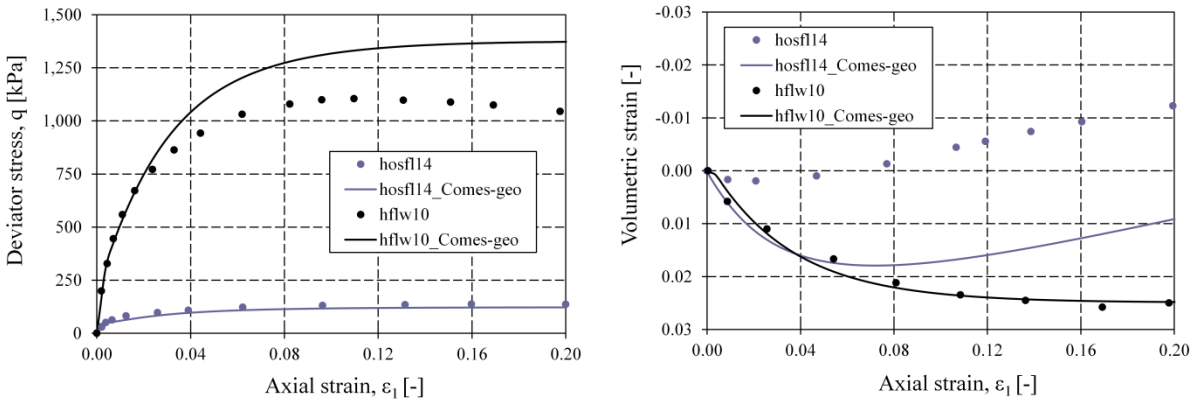

(a) (b)

Figure 5.32: VISCUNsand validation – Exponential viscous nucleus: Effects of the mean stress on drained triaxial compression tests of medium-dense Hostun sand.

TXD on dense Hostun sand

The drained behaviour of dense Hostun sand is tested for two values of effective mean pressure, 200 kPa and 300 kPa. The initial density and viscosity for the examined dense sand are given in Table 5.18. A constant value of viscosity (from calibration of the creep test) is applied in both cases, equal to $2 \cdot 10^{-10}$ s^{-1}.

Table 5.18: Initial density and viscous parameters for the TXD test on dense Hostun sand.

Test name	p_0 [kPa]	e_0 [-]	γ [s^{-1}]	a [-]
hos027	200	0.578	$2 \cdot 10^{-10}$	28.90
hos0l1	300	0.574	$2 \cdot 10^{-10}$	28.90

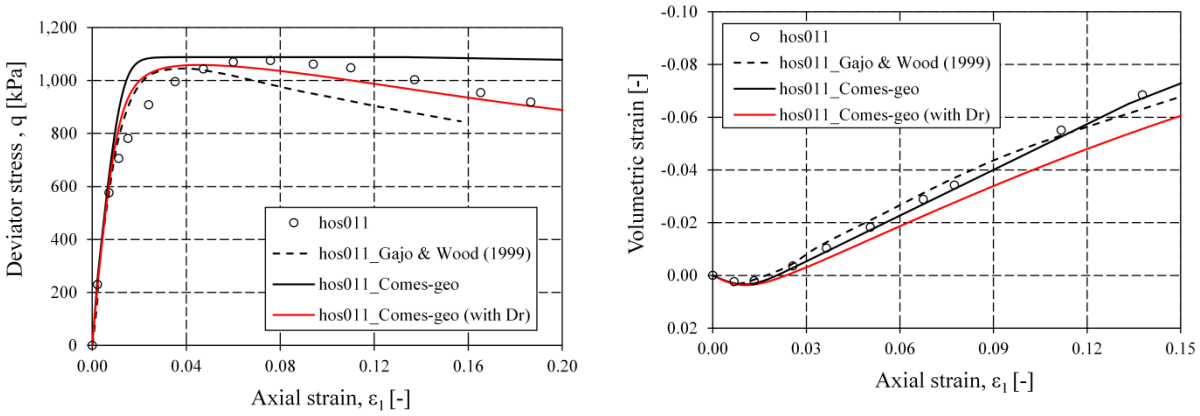

(a) (b)

Figure 5.33: VISCUNsand validation – Exponential viscous nucleus: Drained triaxial compression tests on a dense (e_0=0.574) Hostun sand.

In Figure 5.33 and Figure 5.34 the response of the material for 300 kPa and 200 kPa effective stress accordingly, is presented. It becomes apparent that the effect of relative density is more favorable in the q-ε plane and the behaviour is better approximated, forming also a softening branch.

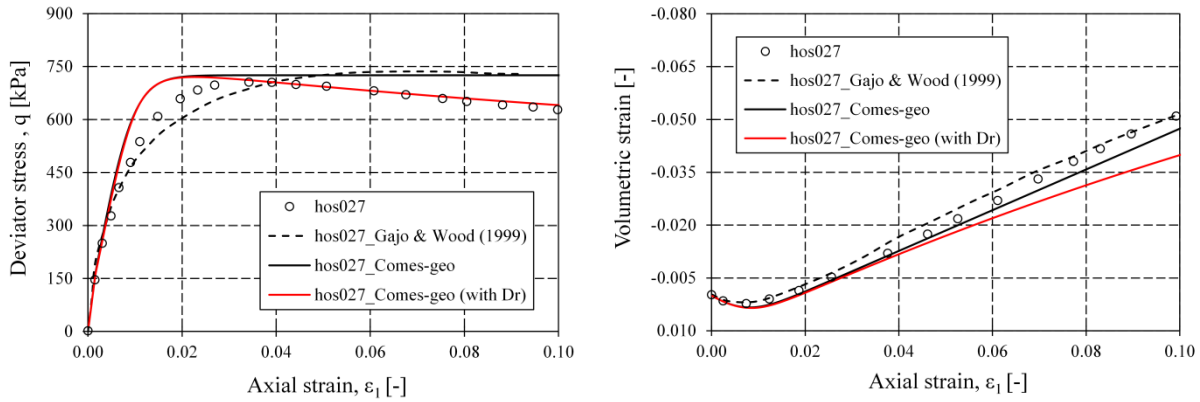

(a) (b)

Figure 5.34: VISCUNsand validation – Exponential viscous nucleus: Drained triaxial compression tests on a dense (e_0=0.578) Hostun sand.

TXU on loose Hostun sand

The undrained behaviour of loose Hostun sand is examined for an effective mean pressure of 100, 200, 300 and 750 kPa.

In Figure 5.35 the undrained response for the loose sand is depicted for the VISCUNsand model, in comparison with experimental results for 200 kPa of confining pressure. The general trends are correctly captured. The peak deviator stress is very well represented however the residual strength is overestimated.

In Figure 5.36 the numerical results indicate appropriate agreement with the experimental and the qualitative response is perfectly described both for the deviator stress – strain and the excess pore pressure – strain diagrams for the three confining pressures. It is noted that Figure 5.36b gives the

evolution of the excess pore pressure normalized by the initial effective mean pressure versus axial strain. As the density of the sample is very low, the material has a tendency to contract. Thus for the chosen three effective mean pressures, the pore pressure always increases.

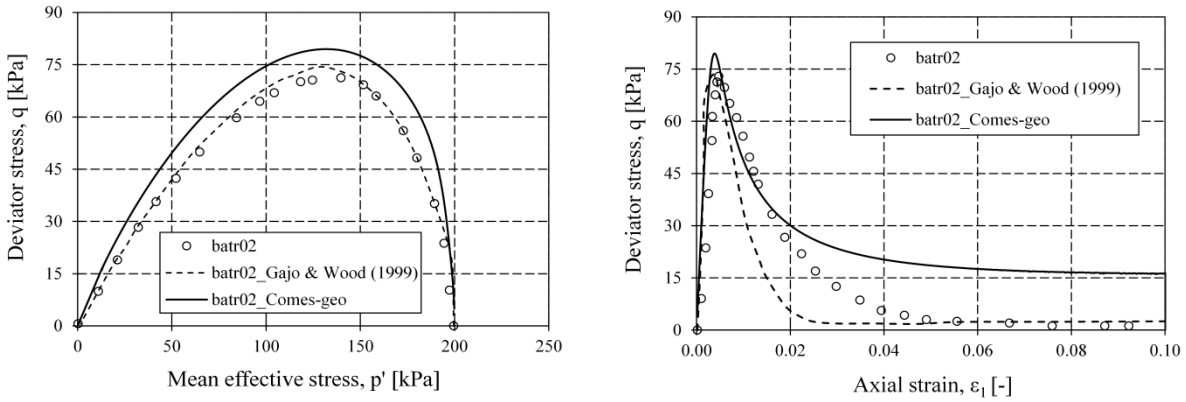

(a) (b)

Figure 5.35: VISCUNsand validation – Exponential viscous nucleus: Undrained triaxial compression tests on loose Hostun sand for p_0=200 kPa.

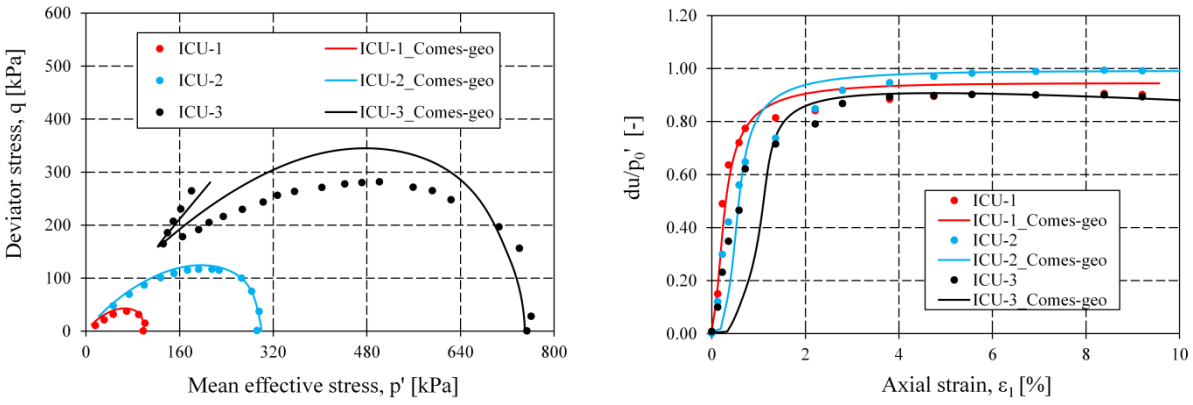

(a) (b)

Figure 5.36: VISCUNsand validation – Exponential viscous nucleus: Undrained triaxial compression tests on loose Hostun sand for p_0=100, 300 and 750 kPa.

However, it is noted that these results occurred for a viscosity value $2 \cdot 10^{-5}$ s^{-1} (Table 5.19) different from the value obtained with the calibration, which was also used to simulate the drained triaxial behaviour for loose sand. As an attempt to interpret this fact, in Figure 5.37 are compared the results using the calibrated viscous parameters from the drained tests (black line) and those fitting better the experimental results (red line). Moreover, in Figure 5.38 the overstress ratio for these two simulations is depicted.

Table 5.19: Initial density and viscous parameters for the TXU test on loose Hostun sand.

Test name	p_0 [kPa]	e_0 [-]	γ [s^{-1}]	a [-]
batr02	200	0.940	$2 \cdot 10^{-5}$	24.90

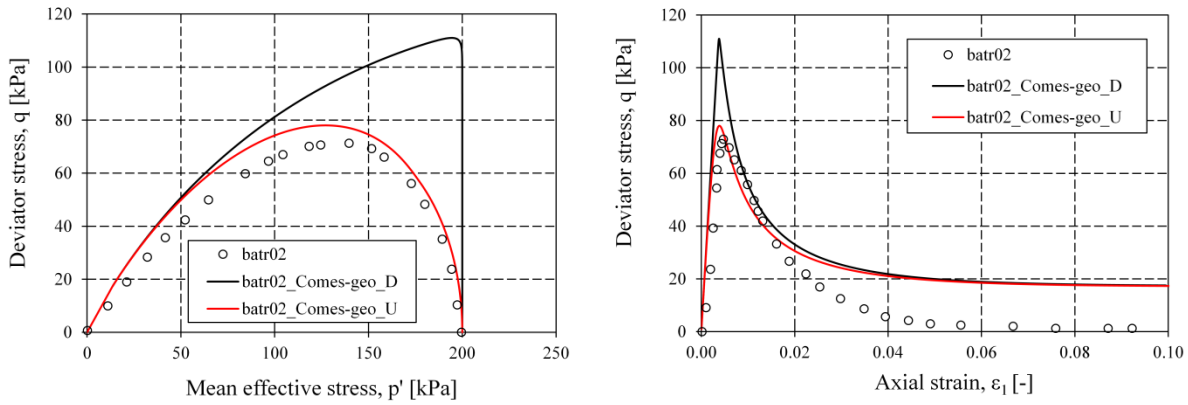

(a) (b)

Figure 5.37: VISCUNsand validation – Exponential viscous nucleus: Comparison with the undrained behaviour of a loose sample and the simulated results using $\gamma=2\cdot10^{-14}$ s^{-1} and a=28.9 (black line) and $\gamma=2\cdot10^{-5}$ s^{-1} and a=24.9 (red line).

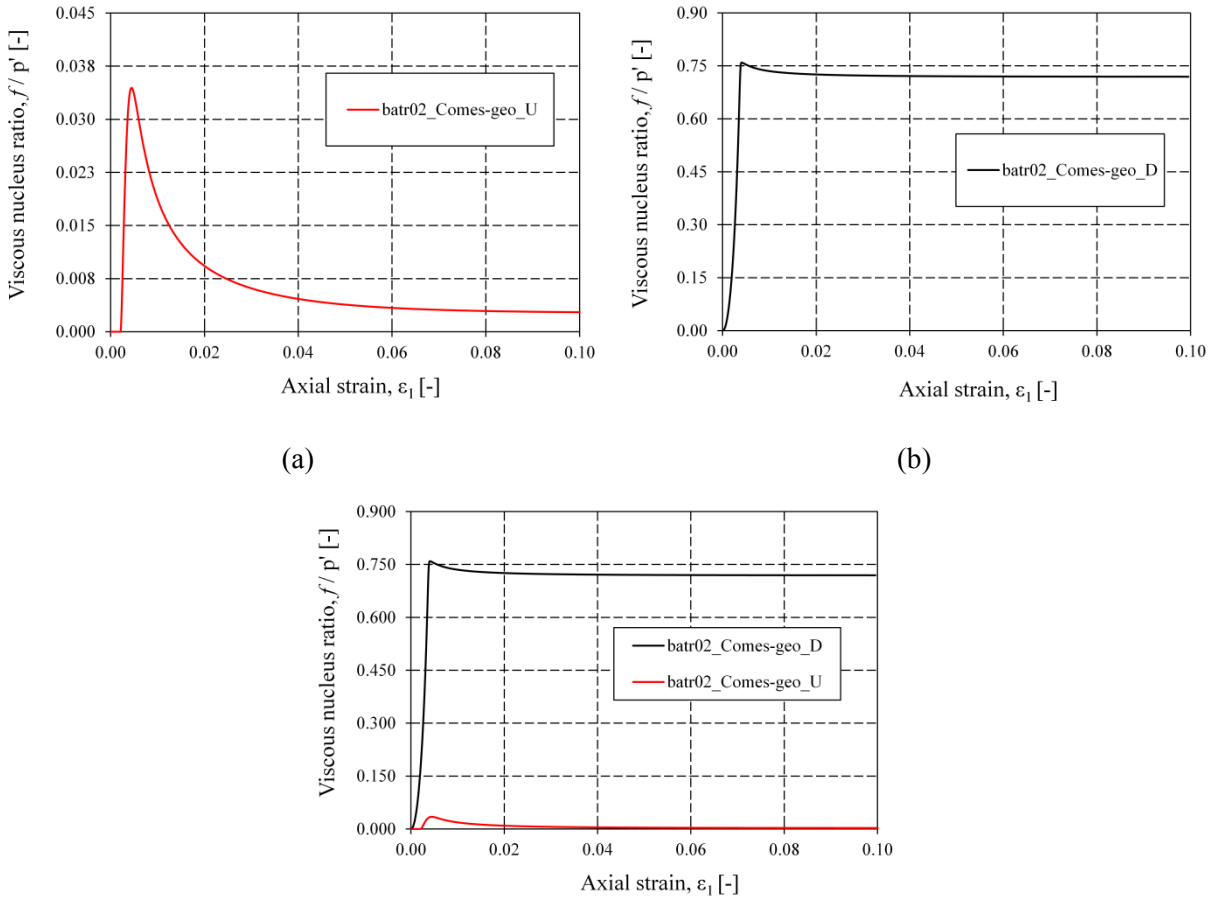

(a) (b)

(c)

Figure 5.38: VISCUNsand validation – Exponential viscous nucleus: Plots of f/p' ratio versus axial strain for (a) γ=2·10-5 s-1 and a=24.9 and (b) γ=2·10-14 s-1 and a=28.9 and (c) comparison of (a) and (b) case.

To better fit the experimental results of the undrained test another set of viscous parameter is required ($\gamma=2\cdot10^{-5}$ s^{-1} and a=24.9) and in that case the values of the viscous nucleus ratio *f*/p' are much

lower than those occurred with the viscous parameters as in drained tests (Figure 5.38). It is also interesting that the set of viscous parameters for the drained triaxial tests ($\gamma=2\cdot10^{-14}$ s^{-1} and a=28.9) leads to a similar overstress ratio in both drained and undrained conditions (Figure 5.38b and Figure 5.39).

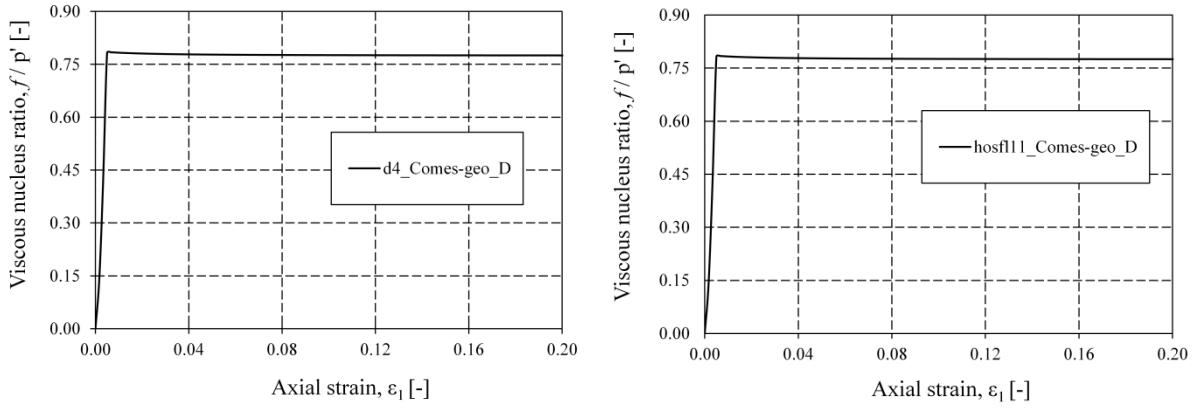

(a) (b)

Figure 5.39: VISCUNsand validation – Exponential viscous nucleus: Plots of *f*/p' ratio versus axial strain with viscous parameters $\gamma=2\cdot10^{-14}$ s^{-1} and a=28.9 for (a) d4 and (b) hosfl11, TXD tests.

The same behaviour is also observed for medium-dense and dense sand, denoting a different effect of viscosity on the yield surface depending on the drainage conditions. This variation shows the great influence of the definition of the viscous nucleus and highlights the need for further investigations.

TXU on medium-dense Hostun sand

A medium-dense sample tested in undrained compression is shown in Figure 5.40. The initial density and the viscosity parameters adopted for the simulation are summarized in Table 5.20. The comparison between model simulations and experimental measurements is almost perfect. Both the simulated stress path and post peak stress-strain behaviour are absolutely consistent with the measurements.

In the same way as in the case of the undrained triaxial compression tests on loose sand, a comparison between the simulated results using two set of viscous parameters, is given in Figure 5.41, leading to the same conclusions as above.

Table 5.20: Initial density and viscous parameters for the TXU test on medium Hostun sand.

Test name	p_0 [kPa]	e_0 [-]	γ [s^{-1}]	a [-]
batr06	200	0.830	$2\cdot10^{-4}$	6.90

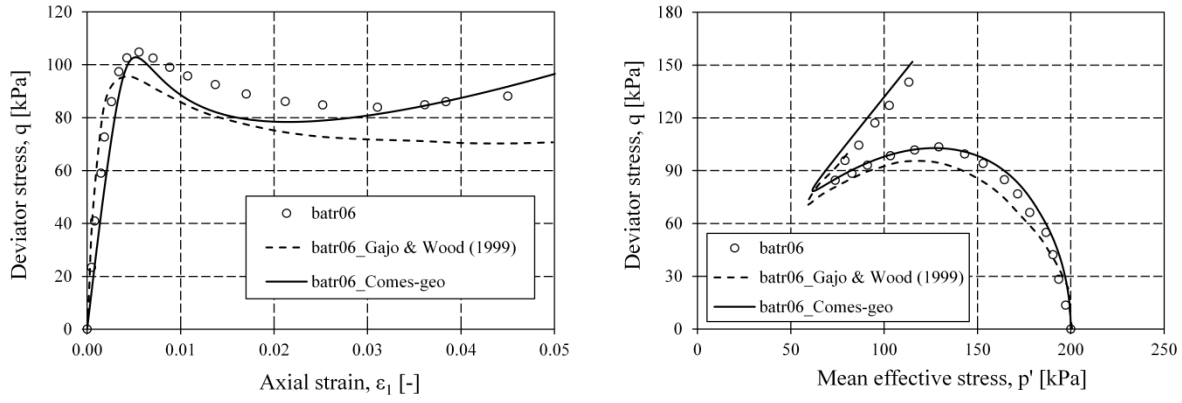

(a) (b)

Figure 5.40: VISCUNsand validation – Exponential viscous nucleus: Undrained triaxial compression tests on medium Hostun sand.

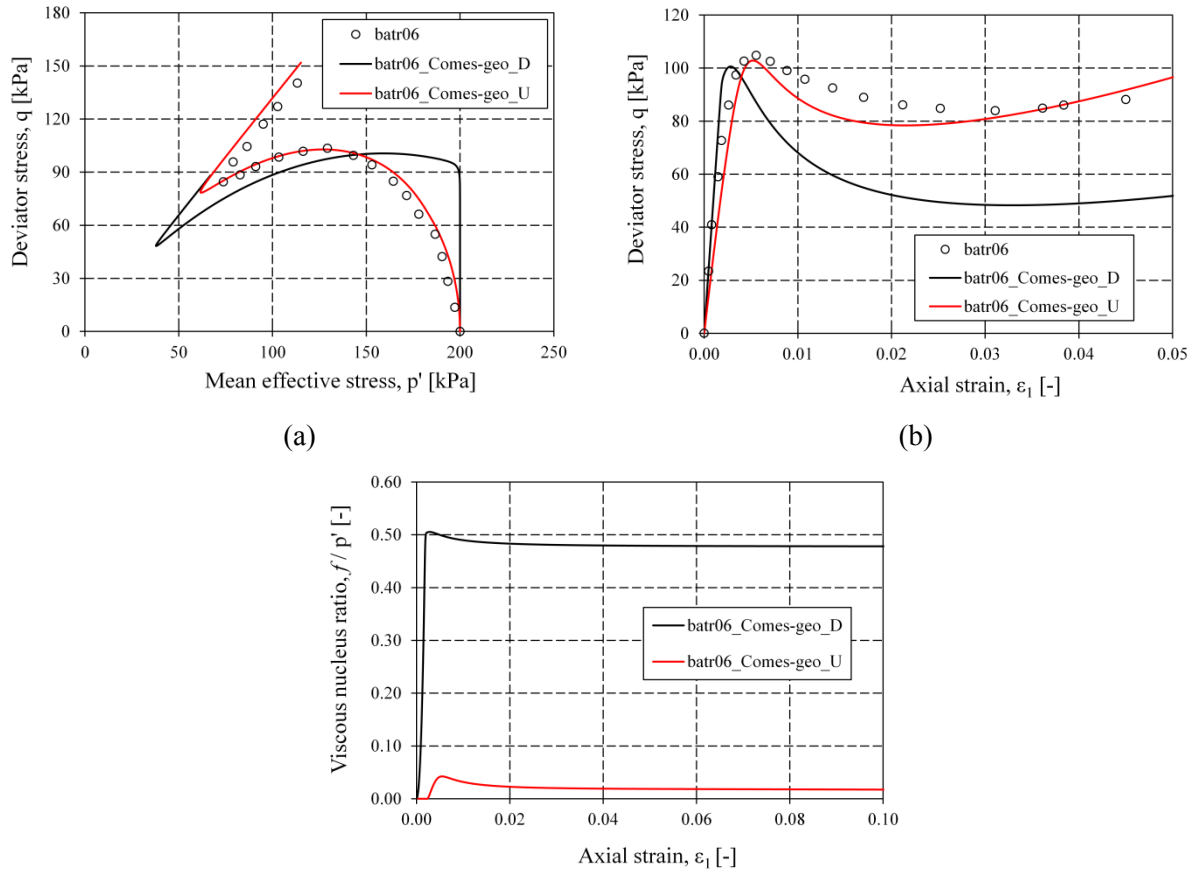

(a) (b)

(c)

Figure 5.41: VISCUNsand validation – Exponential viscous nucleus: (a), (b) Comparison with the undrained behaviour of a medium sample and the simulated results using $\gamma=2\cdot10^{-12}$ s^{-1}, a=28.9 (black line) and $\gamma=2\cdot10^{-4}$ s^{-1}, a=6.9 (red line) and (c) *f*/p' ratio versus axial strain.

TXU on dense Hostun sand

The undrained behaviour of a dense Hostun sand is presented in Figure 5.42 applying the properties listed in Table 5.21. The model is again consistent with the experimental data, capturing very well the characteristics of the undrained behaviour for the specific density.

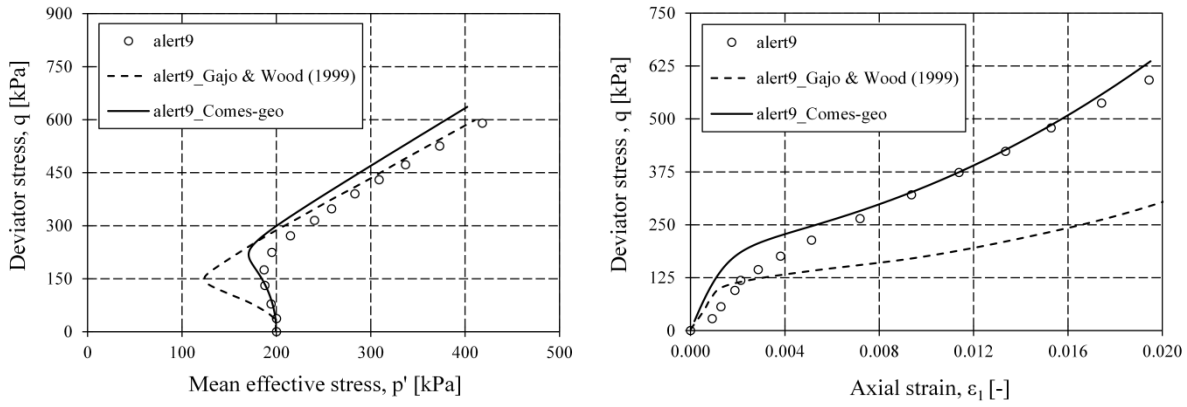

(a) (b)

Figure 5.42: VISCUNsand validation – Exponential viscous nucleus: Undrained triaxial compression tests on dense Hostun sand.

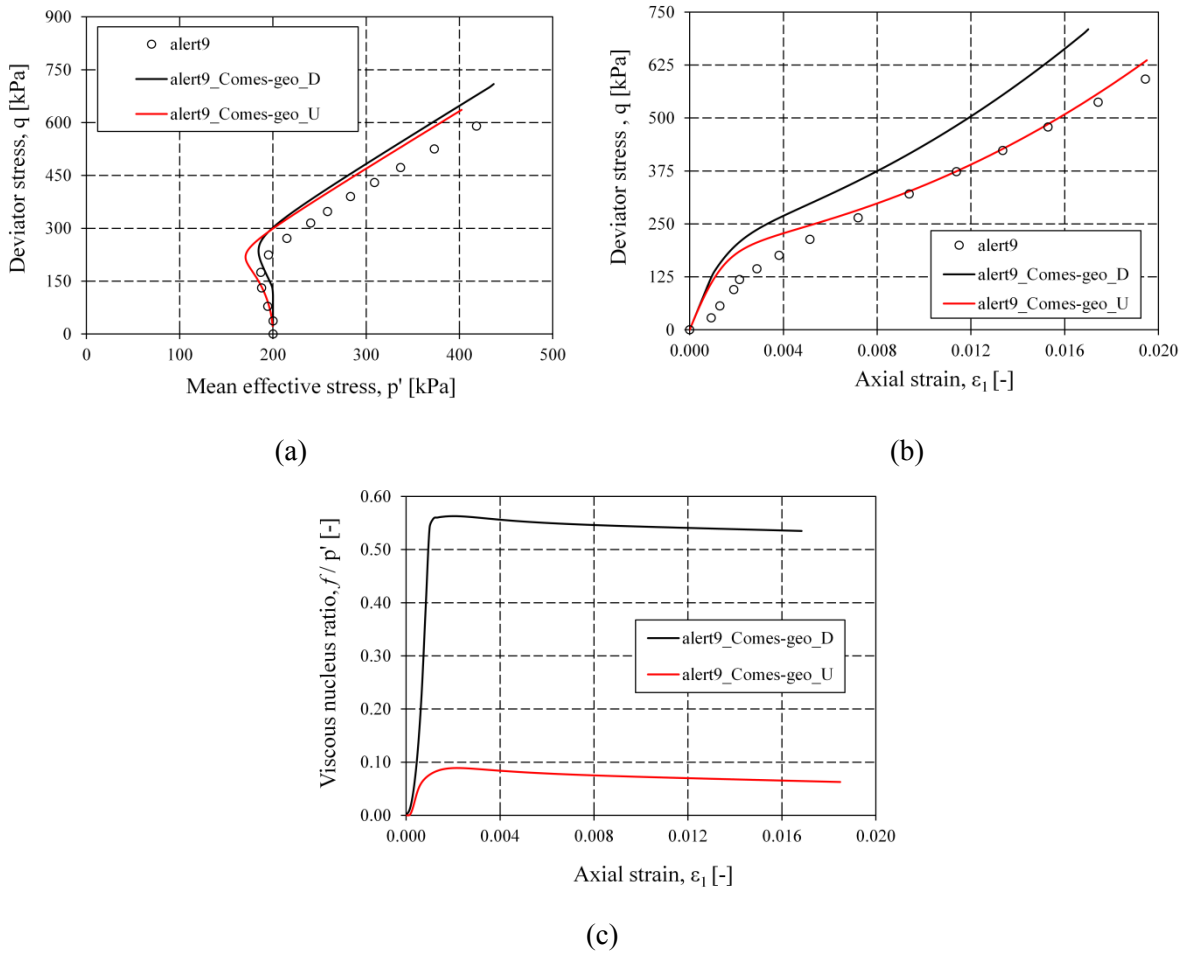

(a) (b)

(c)

Figure 5.43: VISCUNsand validation – Exponential viscous nucleus: (a), (b) Comparison with the undrained behaviour of a dense sample and the simulated results using $\gamma=2\cdot10^{-10}$ s^{-1}, a=28.9 (black line) and $\gamma=4\cdot10^{-4}$ s^{-1}, a=1.0 (red line) and (c) *f*/p' ratio versus axial strain.

Table 5.21: Initial density and viscous parameters for the TXU test on dense Hostun sand.

Test name	p_0 [kPa]	e_0 [-]	γ [s^{-1}]	a [-]
alert9	200	0.666	$4 \cdot 10^{-4}$	1.0

The calibration and the validation of the viscoplastic model, through comparison of the simulations with experimental results, showed the sufficiency to reproduce with a satisfactory accuracy the drained and undrained behaviour of Hostun sand over a wide range of density and confining pressures, using a single set of constitutive parameters except for the viscous parameters.

To obtain the behaviour using the linear viscous nucleus a common value of viscosity is used for both drained and undrained conditions which however is not the one occur from the calibration. On the other hand, when applying an exponential viscous nucleus the calibrated viscosity value is sufficient to reproduce the drained behaviour, whereas for the undrained behaviour a different value is required.

In the following tables the viscosity values are summarized for the linear and exponential viscous nucleus respectively.

Table 5.22: Viscosity parameters varying soil density for linear viscous nucleus.

Test Name	η [s]	γ [s^{-1}]	a
TXD & TXU - Loose	$5 \cdot 10^{2}$	$2 \cdot 10^{-3}$	1.0
TXD & TXU - Medium	$2{,}5 \cdot 10^{2}$	$4 \cdot 10^{-4}$	1.0
TXD & TXU - Dense	$2.5 \cdot 10^{4}$	$4 \cdot 10^{-6}$	1.0

Table 5.23: Viscosity parameters varying soil density for exponential viscous nucleus.

Test Name	η [s]	γ [s^{-1}]	a
TXD - Loose	$5 \cdot 10^{13}$	$2 \cdot 10^{-14}$	28.9
TXD - Medium	$5 \cdot 10^{11}$	$2 \cdot 10^{-12}$	28.9
TXD - Dense	$5 \cdot 10^{9}$	$2 \cdot 10^{-10}$	28.9
TXU - Loose	$5 \cdot 10^{4}$	$2 \cdot 10^{-5}$	24.9
TXU - Medium	$5 \cdot 10^{3}$	$2 \cdot 10^{-4}$	6.9
TXU - Dense	$2{,}5 \cdot 10^{3}$	$4 \cdot 10^{-4}$	1.0

5.5.4 Undrained Plane-Strain Compression Test on Loose Hostun Sand

In this section, to further demonstrate the efficiency of the model, the results of an undrained biaxial test on loose Hostun sand performed by Mokni and Desrues (1998) are predicted with the proposed

model. A confining pressure of 800 kPa was applied and the same set of material parameters was used. The viscosity parameters were taken according to Table 5.23, following the discussion of the previous section.

In Figure 5.44 the comparison between the experimental data and the simulation results is shown in terms of the stress path and effective stress, pore-pressure and effective stress ratio versus axial strain.

Table 5.24: Initial density and viscous parameters for the undrained plane-strain test on loose Hostun sand.

Test name	p_0 [kPa]	e_0 [-]	γ [s^{-1}]	a [-]
SHFND05	800	0.945	$2 \cdot 10^{-5}$	24.9

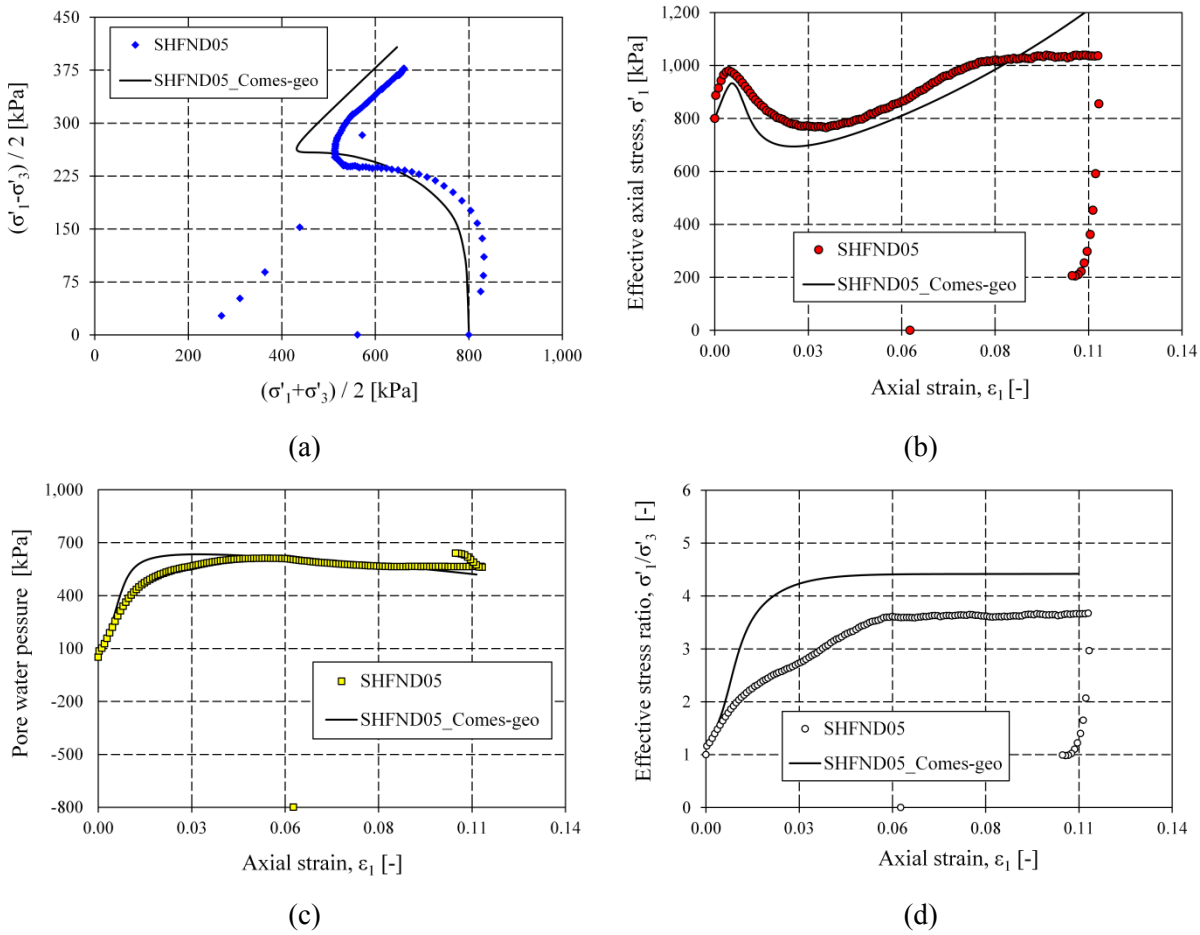

Figure 5.44: VISCUNsand validation – Results for the undrained plane-strain compression test on loose Hostun sand.

The behaviour of the model is satisfactory as the general trends are well captured. However, the model does not experience the sudden reduction of the stress ratio with the axial strain as was experimentally observed. According to Mokni and Desrues this sudden drop corresponds to the onset of localization. This phenomenon is further analyzed and discussed from both theoretical and numerical perspective in the next section.

5.6 On the Simulation of Undrained Shear Banding

Failure of geomaterials specimens tested in the laboratory is often accompanied by the localization of strains in narrow bands. According to experimental observations, distinct shear bands often occur in dense sand specimens under both drained and undrained conditions. In this section one of the experiments on Hostun sand previously presented with single finite element analyses, will be simulated as a boundary value problem with proper discretization. The scope of this example is to demonstrate the performance of the viscoplastic model as well as to illustrate the onset of localization and the evolution of the shear band at post-failure conditions.

The undrained triaxial compression test on a medium-dense Hostun sand is the case study. The main material parameters are summarized in Table 5.13 whereas the initial density and the viscosity parameters adopted for the simulation are listed in Table 5.20. A sketch of the considered boundary value problem is shown in Figure 5.45. The experimental test is conducted by considering the half of the sample due to symmetry. The problem domain is a rectangular specimen 5 cm wide and 10 cm high modeled with 50 eight-node quadrilateral elements. On the top and left sides, the normal stress was kept constant (p_0 = 200 kPa), for the first phase of isotropic compression. The self-weight of the material is not considered and the specimen is assumed to be homogeneous at this stage. On the second phase, on the upper boundary the vertical displacement rate is imposed to be constant, on the right side the normal stress is kept constant (after the isotropic compression), while, on the left boundary horizontal displacements are not allowed.

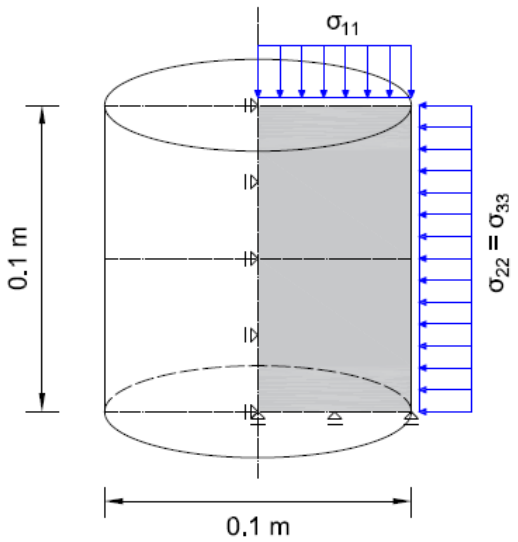

Figure 5.45: Boundary conditions of the triaxial compression test.

Figure 5.46 shows the contour of the equivalent viscoplastic strain at 0.05 of axial strain at the end of the analysis, where the shear bands are fully formed. Two pair of shear bands initiated from the corners of the top and bottom surfaces of the specimen, on the right vertical boundary, and gradually propagated along the diagonal direction of the sample.

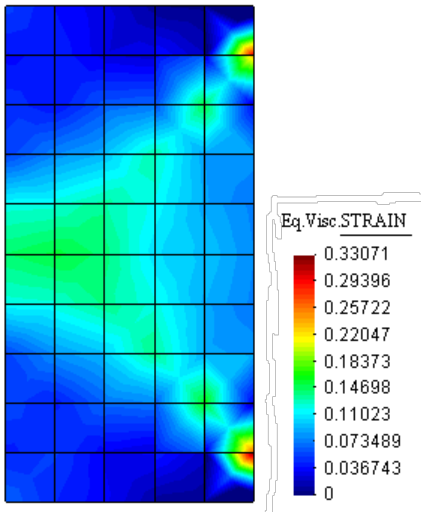

Figure 5.46: Equivalent viscoplastic strain contour.

In more detail in Figure 5.47 the evaluation of the deviatoric stress and equivalent viscoplastic strain with axial strain is plotted for a node inside the shear zone (node 39) with coordinates x = 3 cm y = 7 cm. In the same figure, the comparison of the experimental data (open symbols) with the numerical solution evidence that the behaviour at the post-bifurcation regime is well captured.

The peak of the deviatoric stress for the simulation coincides with the bifurcation point of the experiment and at the same time the equivalent viscoplastic strain begins to develop. This can be regarded as the initiation of the localized failure. Unfortunately, a stability criterion for rate-sensitive materials that could be implemented in a finite element code is still missing in literature, due to the lack of the tangent stiffness operator in Perzyna-type constitutive equations.

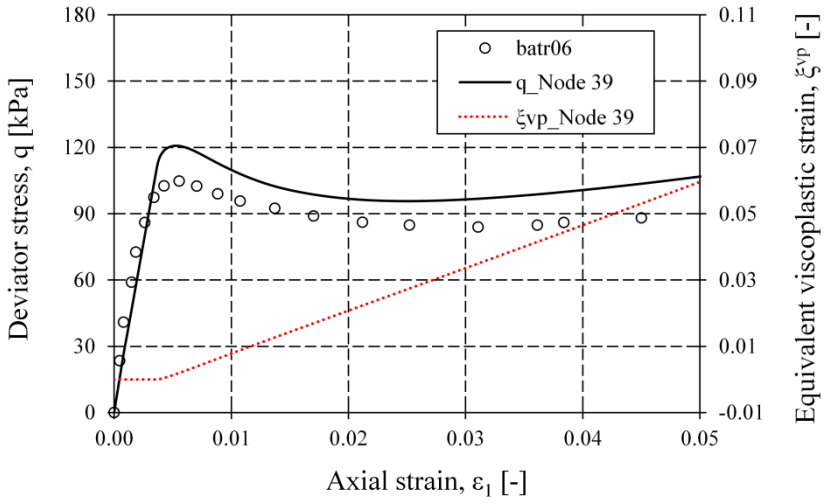

Figure 5.47: Stress-strain response and evolution of equivalent viscoplastic strain with axial strain.

Herein, taking into account that the elasto-viscoplastic response tends to the elastoplastic limit at vanishing rate-sensitiveness (i.e. increasing γ and/or a) and thus with increasing material density and that the elastoplastic stiffness matrix contains information (i.e. hyperelastic tangent and partial

derivatives of the yield function and plastic potential with respect to stress), that are anyway used in the viscoplastic formulation, an attempt is made to plot the determinant of the symmetric part of the stiffness matrix for the viscoplastic model. To this end, the determinant of the symmetric part of the stiffness matrix is reported in a normalized form. The normalization is done using a reference value obtained at a stability point at the beginning of the analysis.

It is recalled that violation of the Hill's criterion at material point level, is associated with possible bifurcations of the stress-strain response and that this criterion is violated for the first time when the determinant of the symmetric part of the stiffness matrix becomes zero (Imposimato and Nova (1998)).

Figure 5.48 shows the stress-strain response and the evolution with strain of the normalized determinant of the symmetric part of the stiffness matrix (det$\mathbf{D}^s$). As can be observed, the normalized determinant vanishes at the same point with the deviatoric peak of the undrained simulation, thus indicating loss of stability of the incremental solution. An also interesting fact is that negative determinants are detected in the localization zones in Figure 5.49.

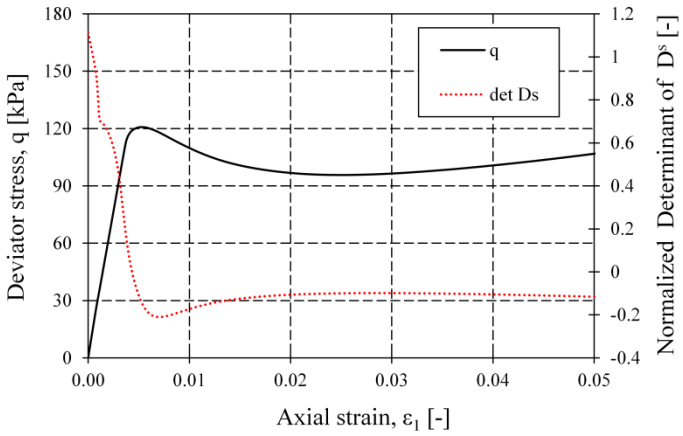

Figure 5.48: Evolution of deviator stress and normalized det$\mathbf{D}^s$ with axial strain.

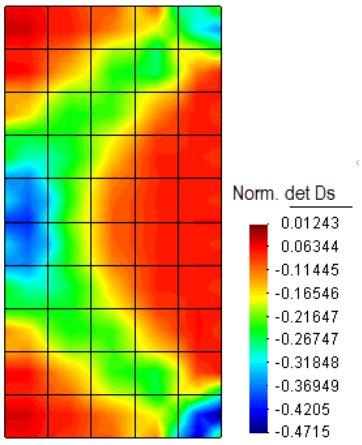

Figure 5.49: Contour of the normalized det$\mathbf{D}^s$.

5.7 Concluding Remarks

This chapter is dedicated to the constitutive modelling of unsaturated soils in the framework of elasto-viscoplasticity. The Nova model, that was recently enhanced to account for hydraulic bonding and debonding effects by Buscarnera and Nova, is adopted and extended to rate-dependent granular material. To model the pycnotropy behaviour of these materials, a dependence of the constitutive parameters on the relative density is incorporated into the viscoplastic formulation.

The elastoplastic model is first implemented and validated in the Comes-geo code through several examples from the literature, that enable the most relevant features of partially saturated soil behaviour to be reproduced.

Afterwards, the viscoplastic model is formulated and implemented in the code. The validation of the viscoplastic model is done with a series of tests on variably saturated conditions as well as standard triaxial and plane-strain tests on sand with varying density. The latter tests are conducted to validate the density-dependence of the model, using only one set of material parameters. An interesting outcome concerned the influence of the definition of the viscous nucleus on the description of the material's mechanical response, suggesting further investigation.

At the end of this chapter a localization failure problem is studied with the viscoplastic model, showing the ability of the model to describe well both the initiation and propagation of this bifurcation mode.

Chapter 6

Implementation of the Constitutive Models for Unsaturated Soil Behaviour in PLAXIS

Chapter 6: Implementation of the Constitutive Models for Unsaturated Soil Behaviour in PLAXIS

6.1 Introduction

In this section the implementation of the elastoplastic (UNsand) and the elasto-viscoplastic (VISCUNsand) constitutive model for unsaturated soils in the commercial FE code PLAXIS - PlaxFlow is presented. This approach within the context of the thesis is aiming at linking academia and industry application.

A set of single element numerical examples is utilized, as also in Sections 5.3 and 5.5 of this thesis, to validate the implementation and examine the effectiveness of the models. Triaxial shear tests at constant suction levels and drained and undrained triaxial compression tests are simulated to illustrate the capabilities of the model within the code. An application inspired by a laboratory experiment aiming to investigate the influence of various groundwater conditions on slope stability, closes this chapter.

6.2 PLAXIS User-Defined Soil Models

In PLAXIS there is the capability to implement user-defined soil models in Fortran-code compiled to dll-files. These constitutive models simulate the soil behaviour at a single material point, i.e. the resulting stress increment due to an applied strain increment. The global behaviour is governed by the Finite Element Method as implemented in PLAXIS.

For a given material point at a certain stress level, there are four necessary operations followed, so as to embody the constitutive model code in the PLAXIS workflow algorithm (PLAXIS, 2012a):

- Initialization of state variables
- Calculation of stresses for the given strain increment
- Creation of elastic material stiffness matrix
- Creation of effective material stiffness matrix.

PLAXIS provides a set of parameters as input to the user-defined subroutine, which are the stresses (Bishop's effective stress), strains, suction and time increments at the previous time step and the state variables of the constitutive model. The routine is expected to return a set of output parameters, the current stresses and state variables.

The flow of the subroutine is governed by an input parameter from PLAXIS main code called IDTask. There are six IDTasks defined and for each, PLAXIS assigns different tasks that the global calculation needs at different stages in the process. The two most important is the IDTask 1, initializing the model and the state variables, and the IDTask 2, calculating the stress increment for

the given strain increment through the applied constitutive model (PLAXIS, 2012a). For IDTask equal to 3 and 6 the material stiffness matrix is defined, as discussed in Section 5.2.4 and 5.4.3 of this thesis.

It should be noted that both the UNsand and VISCUNsand models are implemented, thus a variable called iMod is utilized to define which model is used. The selected option in the user interface activates the corresponding model and dll-file, giving the appropriate value in the iMod variable. For iMod equal to 1 the VISCUNsand model is used whereas for value equal to 2 the UNsand model is activated.

A set of 9 state variables is defined for the implementation of the models: 4 for the plastic strains and one for each of the equivalent plastic strain, the viscoplastic strain, the preconsolidation stress, the degree of saturation increment and the void ratio. These state variables are calculated at each time step and stored for the subsequent step.

The UNsand and VISCUNsand model's subroutine is called for IDTask equal to 2 and the stresses and plastic strains are updated. The same subroutines as developed for the Comes-Geo code are used, with the necessary modifications to adapt to the PLAXIS workflow. A set of indicative numerical examples and tests are presented in the following to illustrate the efficiency of the implementation in PLAXIS - PlaxFlow.

6.3 Numerical Validation and Example

The elastoplastic strain hardening model for soil allowing for hydraulic bonding-debonding effects as presented in Buscarnera and Nova (2009) and the extended viscoplasticic proposed in this thesis, are implemented in PLAXIS - PlaxFlow finite element code. The validation of the implementation is carried out by performing a series of the so-called single element tests. Axisymmetric conditions are assumed and the material is considered to be weightless to have a uniform stress field inside the geometry. The mesh consists of two six node triangular elements with three Gauss integration points to reduce the error due to discretization to a minimum.

6.3.1 Triaxial shear tests at constant suction

The first simulation is focused on the comparison between the predictions of the model used for a saturated material and the results obtained for the same material subjected to a drying path up to 50 kPa. The latter test starts with fully saturated conditions and zero suction, followed by a drying path with suction increase under constant mean net stress, until the desired value i.e. 50 kPa is reached. In the second shearing stage the soil sample is loaded up to failure by applying an increasing vertical net stress while suction and radial net stress remain constant.

Figure 6.1a shows the geometry, the mechanical boundary conditions and the finite element mesh being used for the validation. The hydraulic boundary conditions are shown in Figure 6.1b. The symbol h denotes the total hydraulic head whereas ψ denotes the negative pore water pressure head. A

constant suction profile is generated in accordance to these boundary conditions and its value dependent on ψ value.

The constitutive parameters adopted in this test are given in

Table 6.1 and the soil water characteristic curve (SWCC) is showed in Figure 6.2. The results are compared to those provided by Buscarnera and Nova (2009).

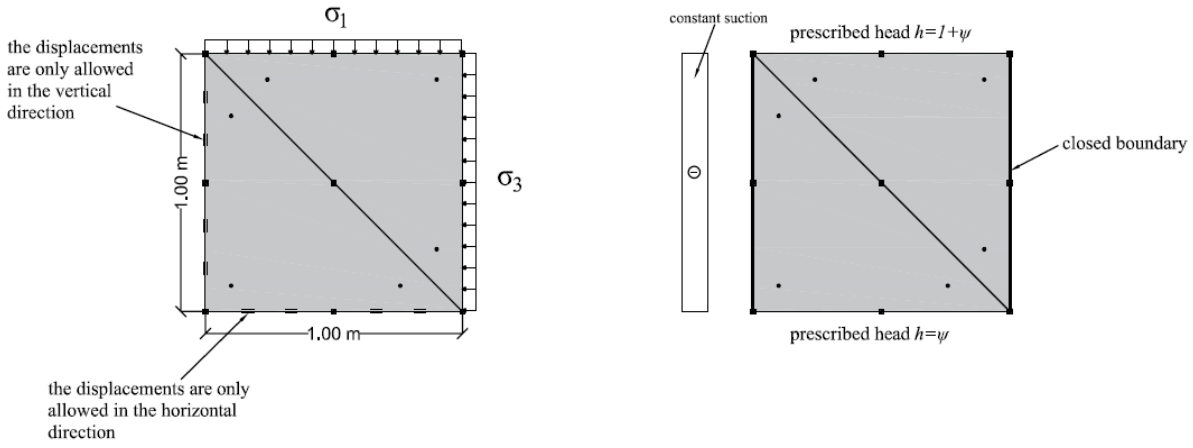

Figure 6.1: Geometry, finite element mesh and boundary conditions as used in the single element tests (a) mechanical boundary conditions (b) hydraulic boundary conditions.

Table 6.1: Parameters adopted for the simulation.

Elastic parameters	Yield surface parameters	Plastic potential parameters	Hardening parameters	Initial state	Initial S_r and void ratio	SWCC parameters
α=0.0	α_f=0.63	α_g=0.63	r_s=1/0.038	p_0=10 kPa	S_{r0}=1.0	S_{res}=0.05
k=0.002	m_f=0.95	m_g=0.95	ξ_s=0.0	q_0=0 kPa	e_0=1.90	S_{sat}=0.98
G_0=32MPa	M_{cf}=0.90	M_{cg}=1.37	r_{sw}=3.86	p_{s0}=10 kPa		g_n=1.29
p_r=10 kPa	M_{ef}=0.70	M_{eg}=1.07				g_a=4.3
						g_l=-0.225

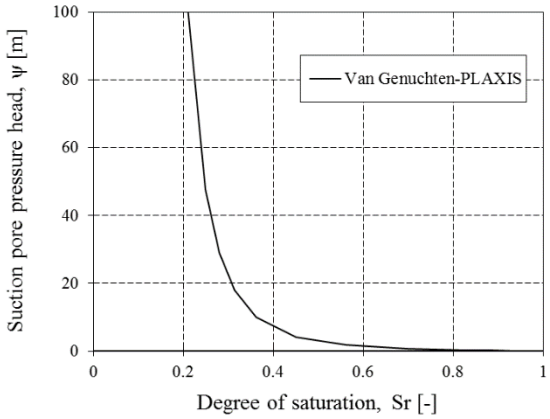

Figure 6.2: SWCC adopted for the analysis.

In Figure 6.3 the stress path of the simulated example in the skeleton and net stress space is presented. The specimen is initially fully saturated and a first stage of drying is applied at constant mean net stress (AB). A triaxial shearing stage follows until the critical state line is reached (BC). The results illustrate the coincidence of the implemented model in PLAXIS with the results by Buscarnera and Nova.

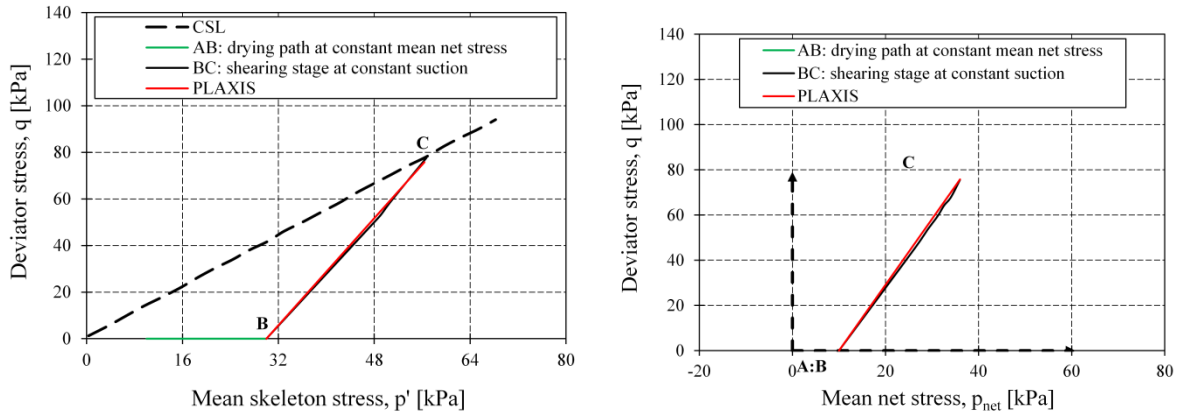

(a) (b)

Figure 6.3: Stress path (a) in the skeleton and (b) net stress space.

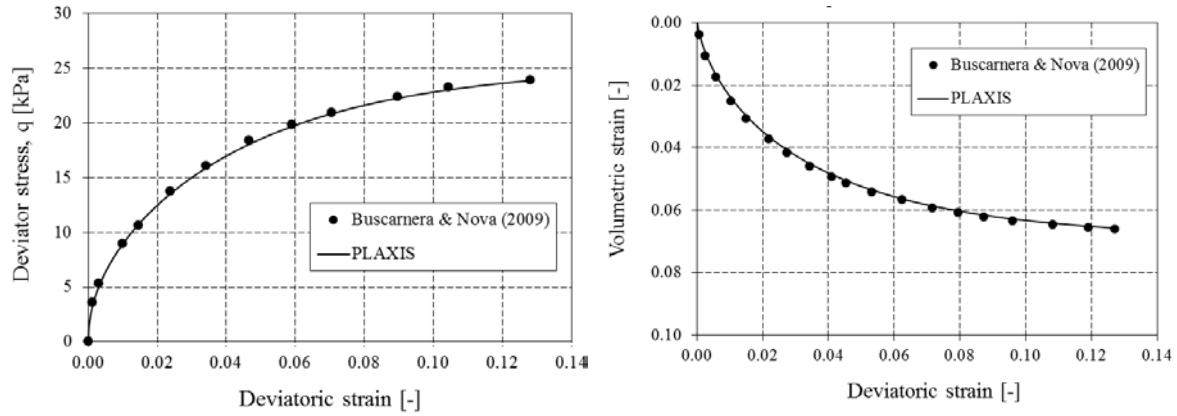

(a) (b)

Figure 6.4: Comparison of tests results on a saturated specimen (suction=0 kPa) in a triaxial test simulation: (a) deviatoric stress versus deviatoric strain and (b) volumetric strain versus deviatoric strain.

As it is evident from Figure 6.4 and Figure 6.5, the stiffness and strength of the soil increases with suction due to the effect of the hydraulic bonding, which occurs by the water menisci. In the same Figures is depicted the very good agreement between the results of the implementation in PLAXIS and the corresponding data from the literature.

In the following Figure 6.6 to Figure 6.7, six simulations are presented for varying suction and net pressure. Three different net confinement pressures and two suction levels are applied (Table 6.2). All tests have been simulated imposing a first drying path at a low net confinement to establish a first suction equilibrium stage. Then a constant suction triaxial stage is imposed under constant radial net

stress. The results indicate coincidence between the simulated example and the data from Buscarnera and Nova.

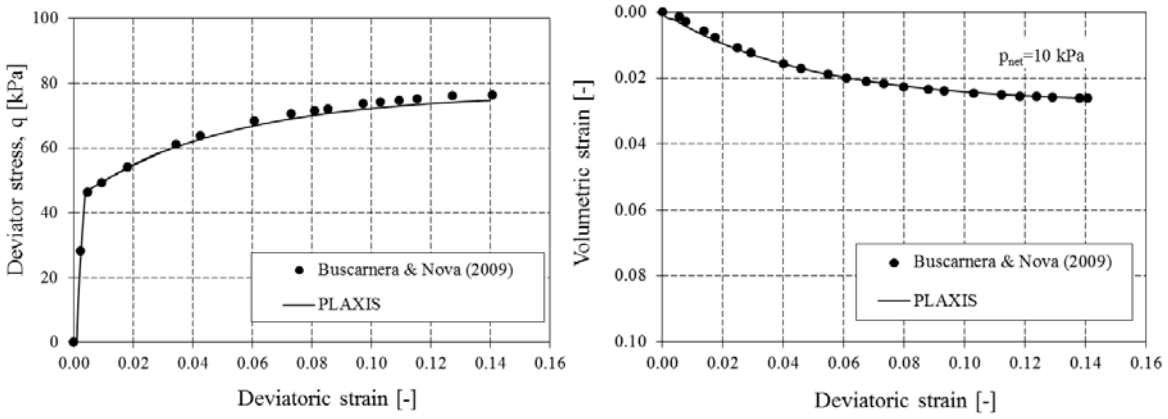

(a) (b)

Figure 6.5: Comparison of tests results on an unsaturated specimen (suction=50 kPa) in a triaxial test simulation: (a) deviatoric stress versus deviatoric strain and (b) volumetric strain versus deviatoric strain.

Table 6.2: Triaxial tests at varying suction and net confinement pressure.

s [kPa]	p_{net} [kPa]
20	10
	30
	50
50	10
	30
	50

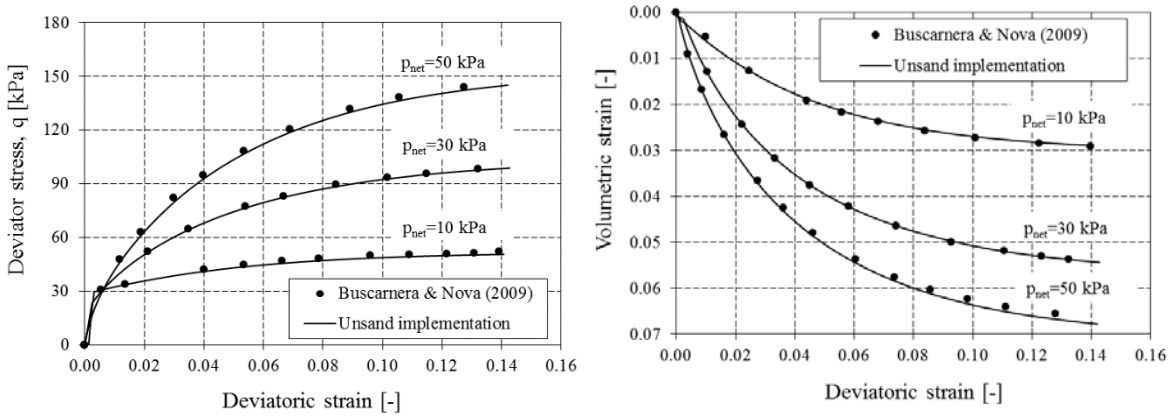

(a) (b)

Figure 6.6: Triaxial tests at suction=20 kPa for varying net confinement pressure: (a) deviatoric stress versus deviatoric strain and (b) volumetric strain versus deviatoric strain.

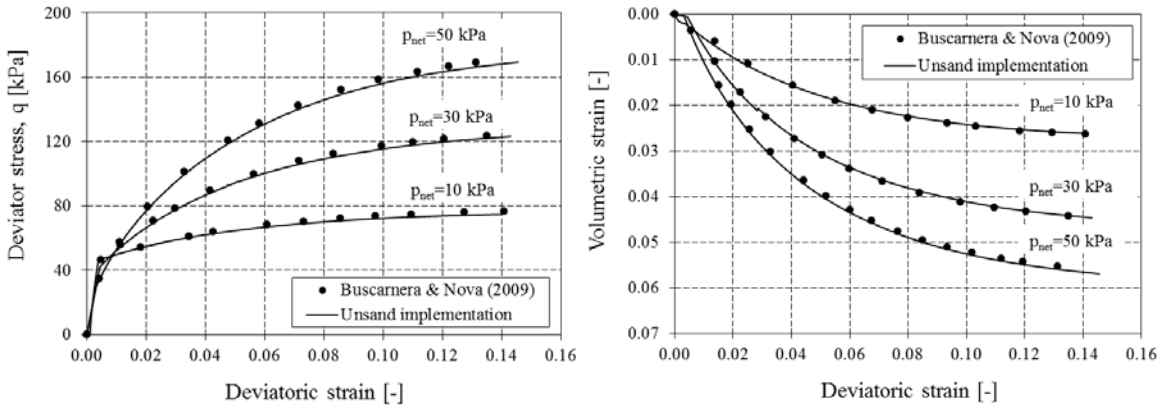

(a) (b)

Figure 6.7: Triaxial tests at suction=50 kPa for varying net confinement pressure: (a) deviatoric stress versus deviatoric strain and (b) volumetric strain versus deviatoric strain.

It should be noted, that these tests have been also simulated with the VISCUNsand model and the outcome was the same as for the UNsand model. Therefore, for the sake of brevity and to avoid repeatability, the results with the VISCUNsand model will not be presented here.

6.3.2 Drained/undrained triaxial compression tests on loose, Hostun sand

Following, drained and undrained loading has been simulated under axisymmetric conditions. The element is considered fully saturated and at first a confining pressure of 300 kPa is applied. Drainage is allowed to simulate the consolidation stage and then shearing is applied in the next stage by increasing the vertical net stress.

The hydraulic boundary conditions define the drainage type during shearing; for the drained loading seepage is allowed from the boundaries whereas for the undrained conditions the boundaries are considered impermeable. The hydraulic boundary conditions for the drained (TXD) and undrained (TXU) loading are shown in Figure 6.9a and Figure 6.9b, respectively.

The material is a loose Hostun sand and is fully saturated prior to the shearing load (subsequently the suction value is zero). The material parameters for the adopted constitutive model are given in Table 6.3 and the soil water characteristic curve is showed in Figure 6.8. In Figure 6.10 a comparison with the results from Mihalache and Buscarnera (2014) is presented.

Perfect matching between the implementation results and those from literature is observed.

Table 6.3. Parameters adopted for the simulation of TXD and TXU tests.

Elastic parameters	Yield surface parameters	Plastic potential parameters	Hardening parameters	Initial state	Initial S_r and void ratio	SWCC parameters
α=0.0	α_f=0.9906	α_g=0.051	r_s=1/0.0074	p_0=300 kPa	S_{r0}=1.0	S_{res}=0.05
k=0.0046	m_f=1.146	m_g=0.98	ξ_s=0.0	q_0=0 kPa	e_0=0.945	S_{sat}=0.98
G_0=14MPa	M_{cf}=0.52	M_{cg}=1.28	r_{sw}=5.45	p_{s0}=300 kPa		g_n=1.29
p_r=1 kPa	M_{ef}=0.442	M_{eg}=1.0				g_a=4.3
						g_l=-0.225

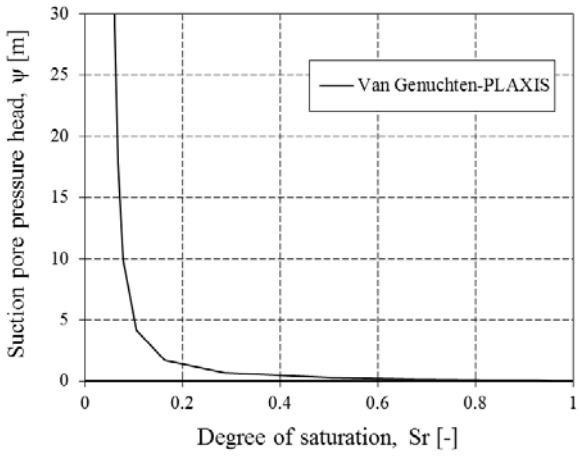

Figure 6.8: SWCC adopted for the TXU and TXD tests.

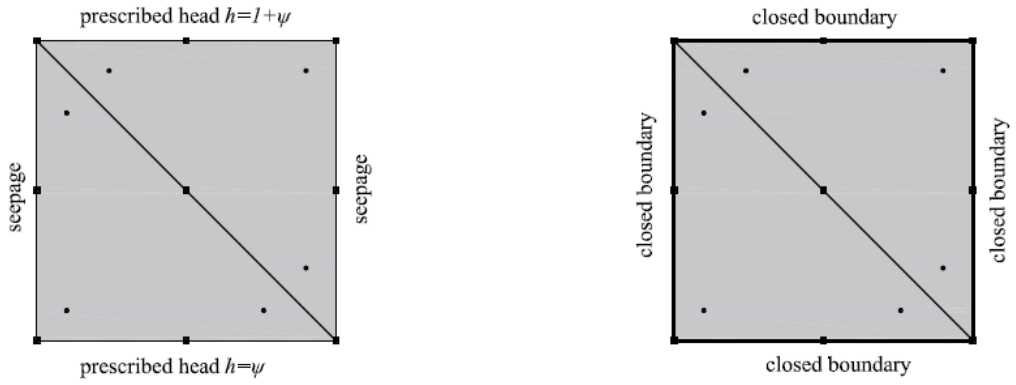

(a) (b)

Figure 6.9: Boundary conditions as used in the single element tests in case of (a) drained conditions and (b) undrained conditions.

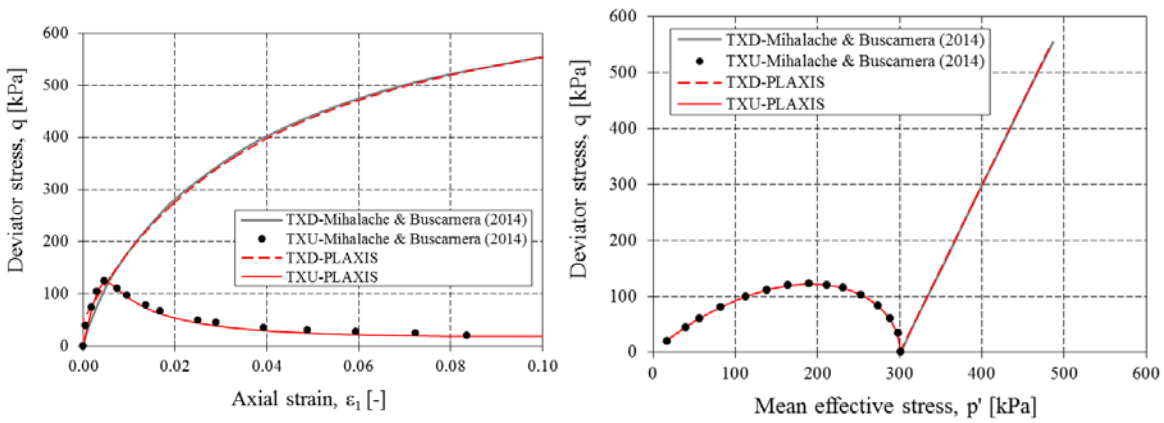

(a) (b)

Figure 6.10: Comparison of the results of drained and undrained triaxial compression tests: (a) effective stress paths and (b) evolution of deviatoric stress with axial strain.

6.3.3 Slope Failure problem

A slope failure problem is examined to illustrate the effectiveness of the viscoplastic model. The geometry of the problem is inspired by a small scale experimental slope of Germer and Braun (2011) as presented in Figure 6.11. The VISCUNsand model is used and the calibrated material parameters for the adopted constitutive model are given in Table 6.4. The soil water characteristic curve is of van Genuchten type, as incorporated in PLAXIS (with PlaxFlow).

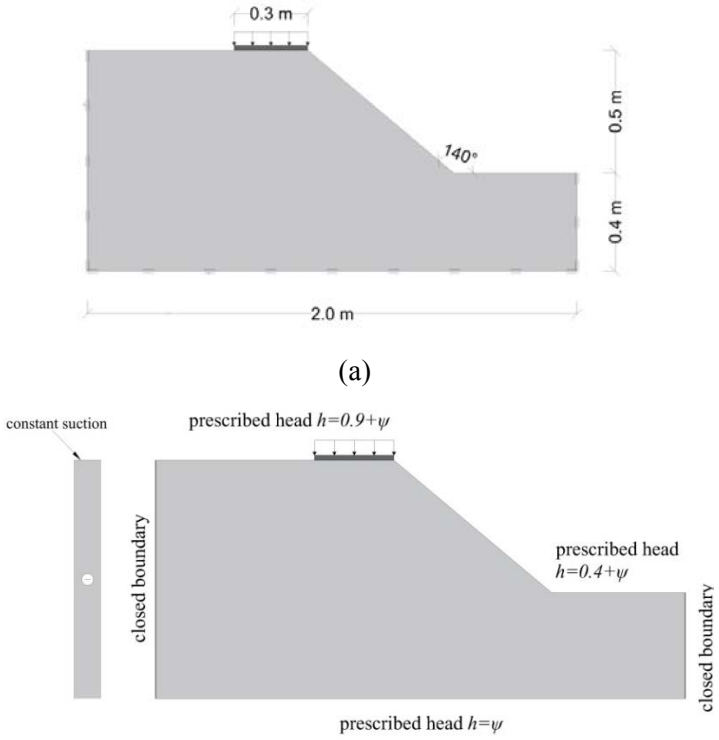

(a)

(b)

Figure 6.11: Geometry and boundary conditions as used in the slope failure problem (a) mechanical boundary conditions (b) hydraulic boundary conditions.

Table 6.4: Parameters adopted for the simulation of the slope failure problem.

Elastic parameters	Yield surface parameters	Plastic potential parameters	Hardening parameters	Initial state	Initial S_r and void ratio	SWCC parameters
α=0.0	α_f=0.99	α_g=0.51	r_s=1/0.007	p_0=10 kPa	S_{r0}=1.0	S_{res}=0.05
k=0.002	m_f=1.14	m_g=0.98	ξ_s=0.0	q_0=0 kPa	e_0=1.90	S_{sat}=0.98
G_0=15MPa	M_{cf}=0.52	M_{cg}=1.28	r_{sw}=5.45	p_{s0}=100 kPa		g_n=1.8
p_r=1 kPa	M_{ef}=0.44	M_{eg}=1.00				g_a=8.0
						g_l=-0.444

In Figure 6.11a, the mechanical boundary conditions are presented. The bottom side of the slope is restrained for vertical and horizontal displacement whereas the vertical sides are restrained for the horizontal displacement. An increasing load is imposed at the top of the slope. The hydraulic boundary conditions are presented in Figure 6.11b. A constant suction is applied by appropriate prescribed head conditions. The vertical boundaries are considered closed to obtain the desired suction level. The mesh consists of six node triangular elements with three Gauss integration points.

6.3.3.1 Effect of viscosity on the failure mechanism

The slope is loaded by increasing the vertical load on the edge. The failure mechanism is examined for three values of viscosity η equal to 20e3, 40e3 and 80e3 s. A constant suction of 20 kPa is applied, resulting in a water degree of saturation of approximately 73%. By the time of the formation of the failure mechanism, the outer edge of the slope moves as one body on the failure zone, as depicted in Figure 6.12. Obviously, the points closer to the imposed load shows greater deformation, as expected, but the failure mode is transmitted along the height of the slope.

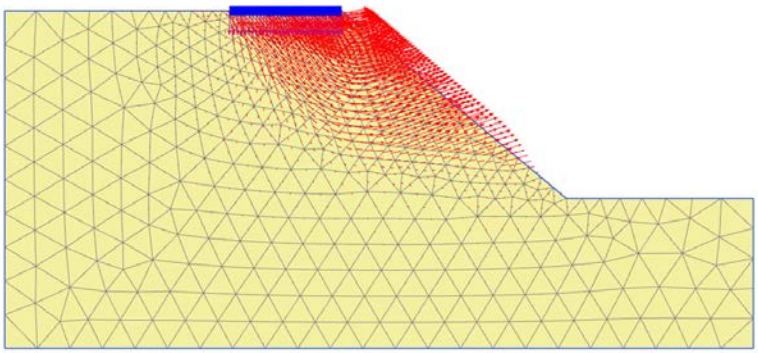

Figure 6.12: Characteristic deformation of the slope mesh for the vertical load (η=20e3 s).

In Figure 6.13 the response of the slope for viscosity η=40e3 s is presented. In Figure 6.13a the total shear strain evolution is concentrated in a slipping zone and in addition a failure zone develops starting by the end of the loading close to the edge of the slope. This response is expected due to the lower mean pressure in this area and the concentrated stress because of the inclined edge. The

equivalent viscoplastic strain of Figure 6.13b follows the same mode of response as the shear strain and it is concentrated in the slipping zone.

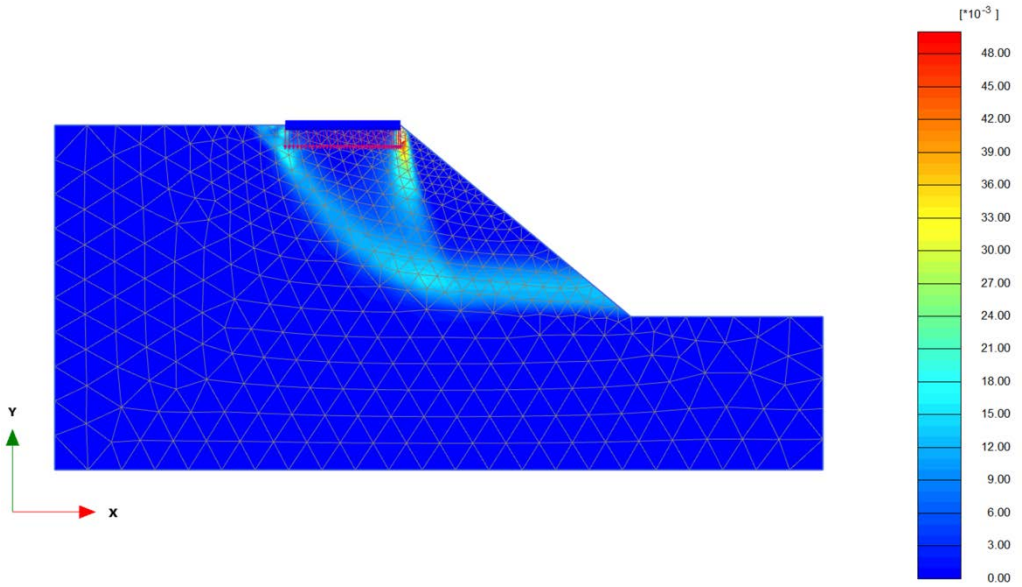

(a)

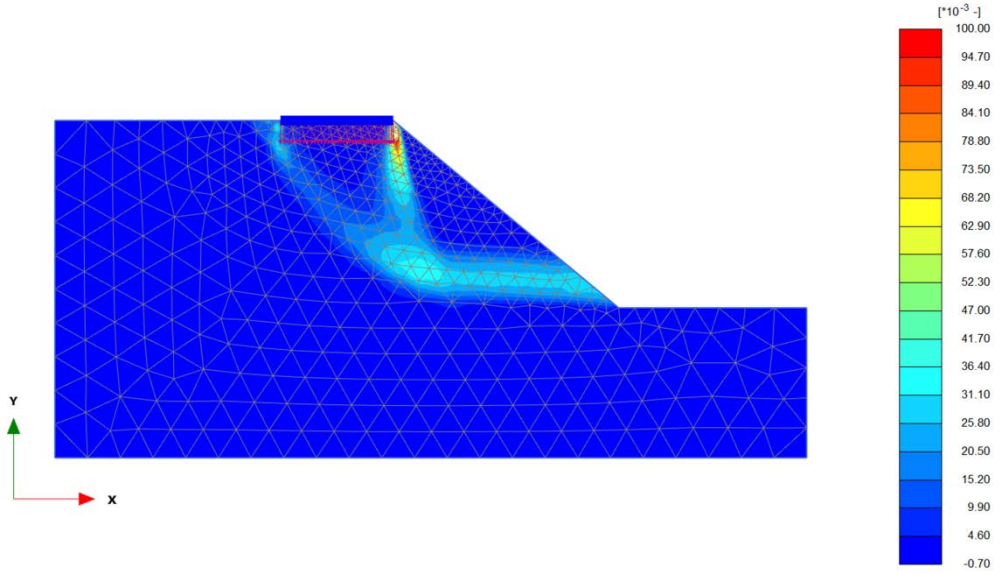

(b)

Figure 6.13: (a) Total shear strain, γ, and (b) equivalent viscoplastic strain for η=40e3 s.

In the following Figure 6.14 the response at the same time interval is presented for the three values of viscosity used. It is evident that for increasing viscosity (Figure 6.14a to Figure 6.14c) at the same time step, the concentration of the shear deformations is delayed. This owes to the effect of viscosity on the yield surface. For a later time step though, the formation of the shear band is complete also for higher viscosity, as occurs by comparing Figure 6.14b with Figure 6.13a. In Figure 6.13a the solution is presented in a later time step, at which the shear band is more properly formed for the same viscosity as in Figure 6.14b.

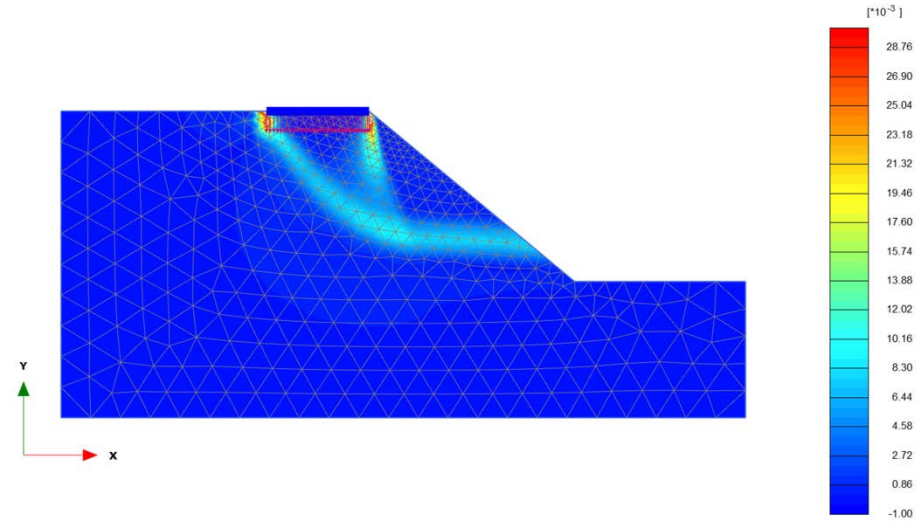

(a)

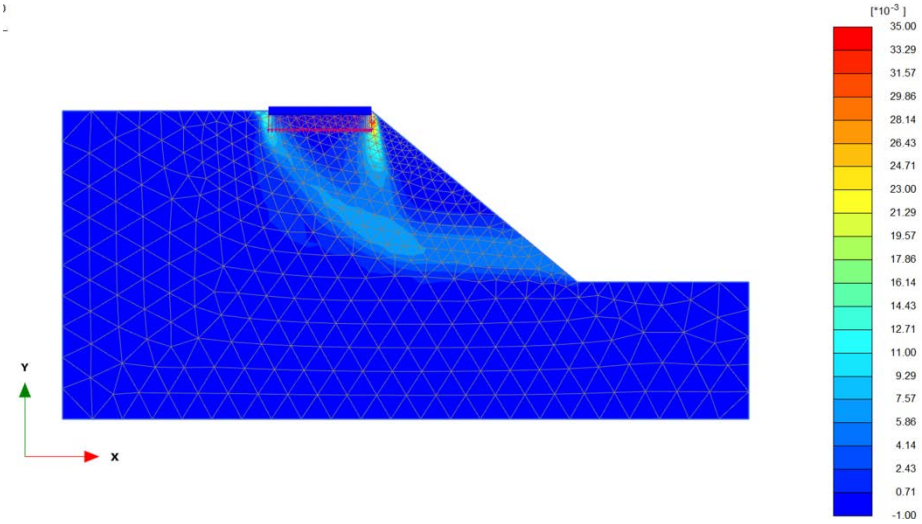

(b)

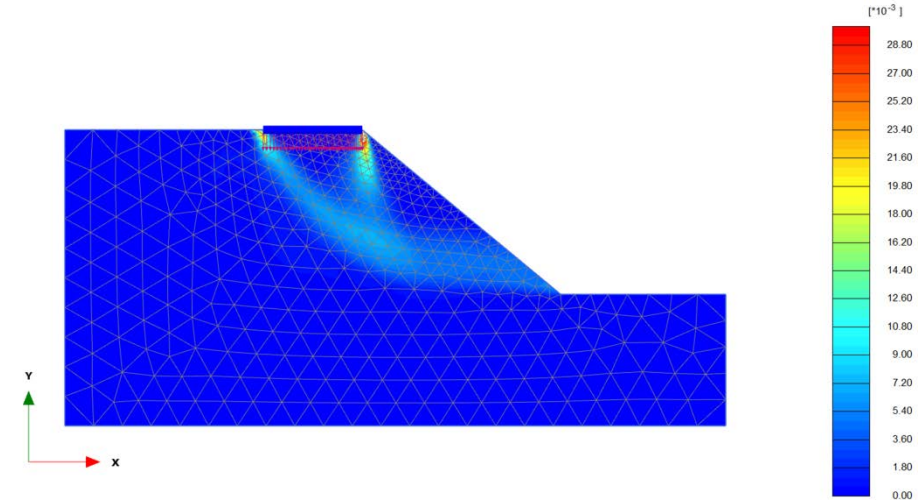

(c)

Figure 6.14: Total shear strain for (a) η=20e3 s, (b) η=40e3 s and (c) η=80e3 s at t=28s.

6.3.3.2 Effect of degree of saturation

The effect of degree of saturation on the response of the slope, from the scope of displacement concentration, is examined. A variation of the degree of saturation and consequently of the capillary pressure with the height of the slope is applied, by modifying the head parameter in PLAXIS. The degree of saturation on the free surface of the slope is considered 100%, simulating a rain event. The mechanical and hydraulic conditions are the same as presented in Figure 6.11 and a maximum capillary pressure of 20 kPa is applied at the bottom of the slope. At the top surface nil capillary occurs due to the material being fully saturated.

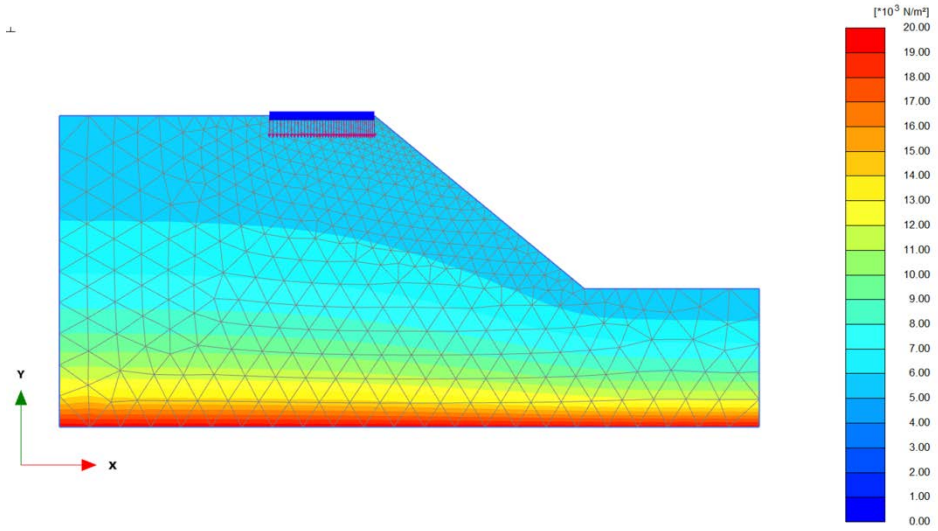

(a)

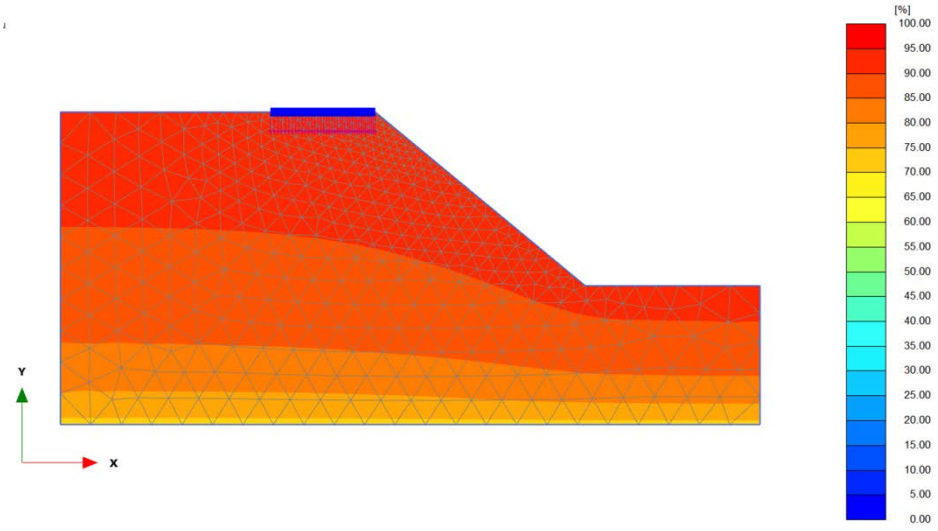

(b)

Figure 6.15: (a) Suction and (b) Degree of Saturation varying with depth.

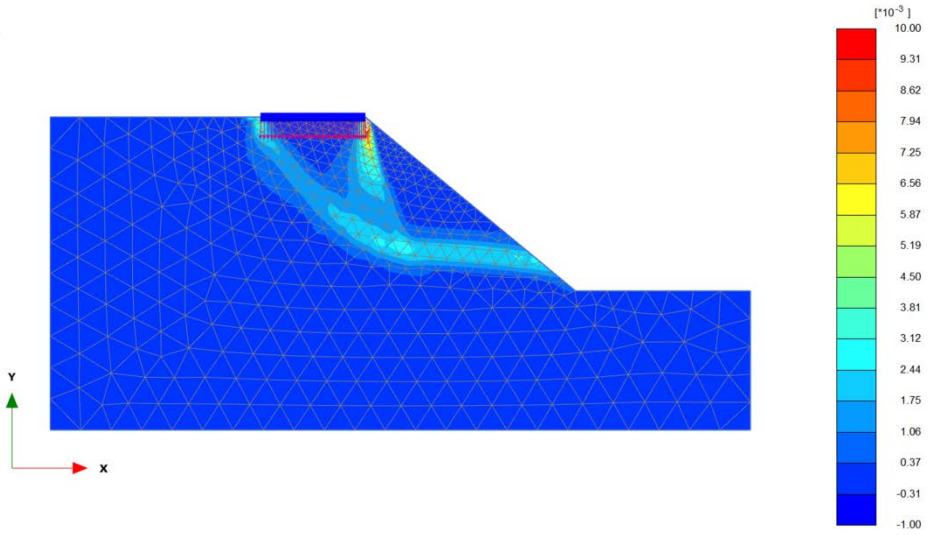

(a)

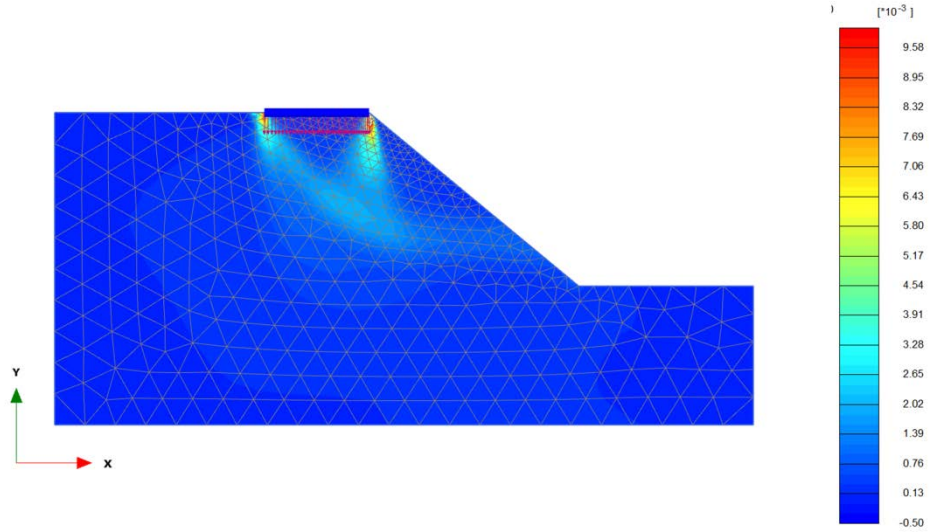

(b)

Figure 6.16: Total shear deformation for (a) varying degree of saturation with depth and (b) constant degree of saturation at the time of the same maximum shear strain value for η=40e3 s.

In Figure 6.16 the response of the slope in terms of total shear strain is presented for viscosity equal to 40e3 s. The influence of the degree of saturation is illustrated by comparing the case of the slope with varying degree of saturation from 73% to 100% with height (Figure 6.16a) and the case of the partially saturated slope with constant suction 20 kPa and degree of saturation 73% throughout the domain (Figure 6.16b). The results are given at the time of the same maximum shear strain. It becomes apparent that the increase of the degree of saturation leads to a more immediate development of shear strain concentration in the failure slipping zone and the expected failure mode appears more pronounced and complete. This is expected due to the hydraulic debonding effect; increasing water content the capillary forces acting between the soils particles decrease and as a consequence the soil loses its strength.

6.4 Concluding Remarks

In this Chapter the implementation of the UNsand and VISCUNsand constitutive models for unsaturated soils in the PLAXIS – PlaxFlow commercial FEM code is discussed. A brief description of the procedure is given and the validation is presented through a set of experimental tests. The validation shows in general a perfect agreement with the data from the literature. The capabilities of the model are illustrated through a small scale slope problem and the effect of viscosity and degree of saturation is discussed. Increase of the viscosity value leads to a delay on the development of the concentration of the deformations in the slipping zone failure mode, whereas the increase of degree of saturation has the opposite effect.

This work was complete in Baugrund Dresden during the last year of the thesis. It is aimed in linking academia with industry and it gives the opportunity to the engineers of practice to use more advanced and sophisticated models for unsaturated soil problems.

Chapter 7

Summary, Conclusions and Future Aspects

Chapter 7: Summary, Conclusions and Future Aspects

7.1 Summary and Conclusions

This dissertation concerns the topic of the numerical modelling of strain localization in variably saturated porous geomaterials. Shear localization is soils is a common failure mechanism e.g. in landslides, originated either by an increase in stress or by a decrease in suction due to water infiltration. In the framework of the standard finite element method, the occurrence of strain localization raises the problem of the objectivity of numerical solution and regularization techniques are necessary to mitigate the mesh dependence effects arising from this bifurcation mode.

In the present work, the localization phenomena in granular materials have been studied adopting regularization techniques taking into account fully coupled hydro-mechanical behaviour and using also developed advanced constitutive models for unsaturated sands. In particular, the novelty of this thesis followed three main directions; an extensive study of local viscoplastic regularization in multiphase porous media with application also in dynamics, the study of non-local viscoplastic regularization in multiphase porous media and the investigation of a new advanced viscoplastic model for unsaturated sands, further enhanced to account for density-dependency. The final result is a finite element tool capable of simulating the initiation and propagation of strain localization on a realistic base.

This research work is summarized in the following fundamental components, all equally critical for an exhaustive understanding of the topic:

- Viscoplasticity and non-local theories have been adopted as regularization techniques to effectively study the localized failure mechanism, assuming the soil as a multiphase porous continuum. Viscoplasticity has been confirmed to be an excellent approach for avoiding mesh-dependency issues, since a material internal length is naturally introduced as a consequence of the rate-sensitiveness. However, this beneficial effect tends to vanish when weakly viscous materials are considered, as for example, in case of dense sands. This difficulty is overcome with the non-local integral approach and the novelty of this formulation stemmed by its application in the context of multiphase porous media (Lazari et al. (2015)). Two types of viscoplastic models have been analytically formulated and implemented in Comes-geo finite element code; the Perzyna and the Duvaut-Lions. The former has been extended with respect to the non-local integral approach. For all the three models the generalized effective stress has been limited by the Drucker-Prager yield criterion with linear isotropic hardening/softening and non-associated flow rule. The non-local method has been formulated in a way convenient for extension to more sophisticated yield criteria.

- Two types of failure problems in soils have been simulated to validate and verify the developed numerical algorithms and procedures; an experimental plane-strain compression test of globally undrained initially water saturated sand and a benchmark slope failure problem. These cases helped in figuring out the merits and drawbacks of each model as well as the influential parameters for the evolution of strain localization. Viscosity, loading velocity, drainage conditions, suction, permeability and internal lengths interaction have been shown to play a significant role on the formation and development of the localization pattern. Mesh insensitive and objective results have been obtained with the width of the shear bands governed by the viscosity parameter and the internal length variable, which can be directly estimated by experimental tests. It is also shown that loading velocity and soil permeability affect the value of viscosity which preserves regularization and that a different viscosity value seems to be needed when drainage conditions change, confirming that the fluid-soil interaction affects the formation and evolution of shear banding. A new finding, that extends the theoretical studies on the topic, is that in quasi-static process, permeability interacts with viscoplasticity activating an internal length when the regularizing influence of rate-dependency is high. The application of the non-local formulation illustrated that the internal length defined in this approach overrides the influence of the viscoplastic internal length for small values of viscosity whereas the opposite trend is observed for high values of viscosity. Moreover, it is shown that the use of non-local approach is pivotal when the soil viscosity is not sufficient for regularizing the numerical solution.
- A new and advanced viscoplastic model for unsaturated soils has been developed. The model constitutes an extension to viscoplasticity of the elastoplastic model for unsaturated soils recently published by Buscarnera and Nova. Moreover, to model the pycnotropy behaviour of granular materials, a dependence of the constitutive parameters on the relative density was further proposed and incorporated into the viscoplastic formulation. Due to the complexity of the model, first the elastoplastic model was implemented in the Comes-geo code and validated through single-element analyses. The validation showed a perfect agreement with the data from the literature.

  Then, the viscoplastic model was formulated and implemented in the code Comes-geo. Its validation was done with experimental tests with variably saturated conditions that enable the most relevant features (i.e. wetting induced collapse) of partially saturated soil behaviour to be reproduced. Then, a series of standard triaxial and plane-strain tests on sand at different densities were conducted to validate the density-dependence of the model using only one set of material parameters. The results showed the capability of the new model to reproduce with a satisfactory accuracy the drained and undrained behaviour of Hostun sand over a wide range of density and confining pressures. An interesting outcome concerned the influence of the definition of the viscous nucleus on the description of the material's

mechanical response, suggested further investigation. On the one hand, using a linear viscous nucleus a common value of viscosity was used for both drained and undrained conditions which however was not the one from the calibration. On the other hand, when applying an exponential viscous nucleus, the calibrated viscosity value was sufficient to reproduce the drained behaviour, whereas for the undrained behaviour a different value was required. As a further step, a localization failure problem was studied with the viscoplastic model, showing the ability of the model to describe well both the initiation and propagation of strain localization.

- Finally, the last contribution of this thesis concerned the implementation and validation of the elastoplastic and the viscoplastic constitutive models for unsaturated soils in the commercial FEM code PLAXIS - PlaxFlow. In the validation process the simulated results were in consistent with the data from the literature. After the validation, the capabilities of the viscoplastic model were illustrated through a small scale slope problem and the effect of viscosity and degree of saturation on slope's stability was discussed. It was shown that an increase of the viscosity value causes a delay on the development of the concentration of the deformations in the slipping failure zone. On the other hand, the increase of degree of saturation leads to the opposite behaviour, because the soil loses its strength due to the hydraulic debonding effect.

In conclusion, theoretical and numerical issues have been addressed in this thesis, with the aim of highlighting some of the factors affecting strain localization phenomena in granular porous material. As has been discussed throughout the dissertation, the description of localization processes is still a major issue in soil mechanics with a particular application to slope stability. In this work shear banding has been studied from the regularization perspective, developed fully coupled hydro-mechanical analyses, based on a physically and well accepted constitutive framework. It has been shown that the choice of the viscosity value is not trivial either when adopted for regularization reasons or for description of the mechanical soil behaviour and a special concern should be taken.

7.2 Future Aspects

The presented findings can serve as a base for future studies and the finite element tool developed is now ready to be applied to study landslides. In particular, further research should be carried on the following topics:

- The formulation of the viscous nucleus should allow for a consistent approximation of the solution and the experimental data, for a wide range of material densities, drainage and loading conditions. The examined viscous nuclei possess the drawback of requiring a different value of viscosity from the calibrated one, depending on the material density and mainly the drainage conditions. Further research should be carried towards the formation of an appropriate viscous nucleus for porous/soil materials.

- A more consistent experimental investigation program should provide appropriate viscosity values for different soil densities.
- In the current approach an explicit integration scheme was adopted for both the elastoplastic and viscoplastic models for unsaturated soils. For future research, an unconditional stable implicit integration scheme could be examined. Moreover, the models could be enhanced to take into account thermal coupling and chemical reaction of the solid and liquid phases.

Bibliography

[1] Alonso, E.E., Gens, A. and Josa, A. (1990). A constitutive model for partially saturated soils. *Géotechnique*, **40**(3): 405–430.

[2] Alshibli, K.A., Bastie, S. and Sture, S. (2003). Strain localization in sand: plane strain versus triaxial compression. *Journal of Geotechnical and Geoenvironmental Engineering*, ASCE, **129** (6): 483–494.

[3] American Society of Heating, Refrigerating and Air-Conditioning Engineers (ASHRAE) Handbook (1993), Fundamentals Volume, ASHRAE, Atlanta.

[4] Ammann, M. (2005). *Parallel Finite Element Simulations of Localization Phenomena in Porous Media*. PhD thesis, Universität Stuttgart, Institut für Mechanic (Bauwesen).

[5] Babuška, I. and Melenk, J.M. (1997). The partition of unit method. *International Journal of Numerical Methods in Engineering*, **40**(4): 727-758.

[6] Bardet, J.P., (1990). A comprehensive review of strain localization in elastoplastic soils. *Computers and Geotechnics*, **10**: 163-188.

[7] Bazănt, Z.P. and Jirásek, M. (2002). Nonlocal Integral Formulations of Plasticity and Damage: Survey of Progress. *Journal of Engineering Mechanics*, **12**8(11): 1119–1149.

[8] Bazănt, Z.P. and Lin, F.B. (1988). Non-local yield limit degradation. *International Journal in Numerical Methods in Engineering*, **8**: 1805-1823.

[9] Bažant, Z.P., Le, J.L., Hoover, C.G., (2010). Nonlocal boundary layer (nbl) model: overcoming boundary condition problems in strength statistics and fracture analysis of quasibrittle materials. *In: 7th International Conference on Fracture Mechanics of Concrete and Concrete Structures (FraMCoS-7)*.

[10] Bažant, Z.P., Lin, F.B. and Pijaudier-Cabot, G. (1987). Yield limit degradation; Nonlocal continuum model with local strain. *Proc. Int. Conf. Computational Plasticity*, Barcelona (eds. Pwen, Histon, Onate), 1757-1780.

[11] Benallal, A., Billardon, R. and Geymonat, G. (1991). Localization phenomena at the boundaries and interfaces of solids. *In Third International Conference on Constitutive Laws for Engineering Materials: Theory and Applications*, Tucson, Arizona, 387-390.

[12] Bigoni, D. (2012). *Nonlinear Solid Mechanics Bifurcation Theory and Material Instability.* Cambridge University Press, ISBN 9781107025417.

[13] Bilotta, E., Cascini L., Foresta, V. and Sorbino, G. (2005). Geotechnical characterisation of pyroclastic soils involved in huge flowslides. *Geotechnical and Geological Engineering*, **23**: 365-402.

[14] Bishop, A.W. (1959). The principle of effective stress. *Tecnisk Ukeblad,* **39**: 859-863.

[15] Bishop, A.W. and Blight, G.E. (1963). Some aspects of effective stress in saturated and partly saturated soils. *Géotechnique*, **13**: 177-197.

[16] Bolzon, G., Schrefler, B.A. and Zienkiewicz, O. (1996). Elastoplastic soil constitutive laws generalized to partially saturated states. *Géotechnique*, **46**(2): 279–289.

[17] Bomberg, M. and Shirtliffe, C.J. (1978). Influence of moisture gradients on heat transfer through porous building materials. Thermal transmission measurements of insulation. ASTM

STP 660, R.P. Tye ed., ASTM, Philadelhia; 211-233.

[18] Borja, R.I. (2004). Cam-Clay plasticity. Part V: A mathematical framework for three-phase deformation and strain localization analyses of partially saturated porous media. *Comput. Methods Appl. Mech. Eng.*, **193**(48–51): 5301–5338.

[19] Borja, R.I. (2006). On the mechanical energy and effective stress in saturated and unsaturated porous continua. *International Journal of Solids and Structures*, **43**(6): 1764–1786.

[20] Borja, R.I., Song, X. and Wu, W. (2013). Critical state plasticity. Part VII: Triggering a shear band in variably saturated porous media. *Comput. Methods Appl. Mech. Eng.*, 261–262, 66–82.

[21] Borja, R.I., Tamagnini, C. and Amorosi, A. (1997). Coupling plasticity and energy-conserving elasticity models for clay. *Journal of Geotechnical and Geoenvironmental Engineering*. **123**(10): 948-957.

[22] Brinkgreve, R.B.J. (1994). *Geomaterial models and numerical analysis of softening*. PhD Thesis, TU Delft.

[23] Brooks, R.H. and Corey, A.T. (1966). Properties of porous media affecting fluid flow. *Journal of Irrigation and Drainage Divisio*n, Proc. of American Society of Civil Engineers, **92**(IR2): 61-68.

[24] Burdine, N.T. (1953). Relative permeability calculations from pore size distribution data. *Journal of Petroleum Technology*, **198**: 71-78.

[25] Buscarnera, G. and Nova, R. (2009). An elastoplastic strainhardening model for soil allowing for hydraulic bonding–debonding effects. *International Journal for Numerical and Analytical Methods in Geomechanics*, **33**(8): 1055–1086.

[26] Buscarnera, G. and Nova, R. (2011). Modelling instabilities in triaxial testing on unsaturated soil specimens. *International Journal for Numerical and Analytical Methods in Geomechanics*, **35**(2): 179–200.

[27] Cao, T.D., Sanavia, L. and Schrefler, B.A. (2015). A thermo-hydro-mechanical model for multiphase geomaterials in dynamics with application to strain localization simulation. *International Journal for Numerical Methods in Engineering*, in print.

[28] Castellanza, R. (2002). *Weathering effects on the mechanical behaviour of bonded geomaterials: An experimental, theoretical and numerical study*. PhD thesis, Politecnico di Milano, Italy.

[29] Ciceri, G. (2014). *Theoretical analysis of failure processes in saturated and unsaturated sands*. Master thesis, Politecnico di Milano, Italy.

[30] Coleman, B.D., and Noll, W. (1963). The thermodynamics of elastic materials with heat conduction and viscosity. *Arch. Ration. Mech. Anal*. **13**: 168-178.

[31] Cui, Y. and Delage, P. (1996). Yielding and plastic behaviour of an unsaturated compacted silt. *Géotechnique*, **46**(2): 291–311.

[32] Cui, Y.J. and Sun, D.A. (2009). Constitutive modelling: from isothermal to non-isothermal behaviour of unsaturated soils. In: Buzzi O, Fityus SG, Sheng D, editors. *Unsaturated soils – theoretical & numerical advances in unsaturated soil mechanics.* CRC Press, 493–506.

[33] Dafalias, Y.F. and Herrmann, I.R. (1986). Bounding surface plasticity II: applicaiotns to isotropic cohesivw soils**.** *JMED, ASCE*, **12**: 1263-1291.

[34] Daouadji, A., Al Gali, H., Darve, F. and Zeghloul, A. (2010). Instability in Granular Materials:

Experimental Evidence of Diffuse Mode of Failure for Loose Sands. *Journal of Engineering Mechanics*, **136**(5): 575-588.

[35] de Boer, R., Ehlers, W., Kowalski, S. and Plishka, J. (1991). Porous media, a survey of different approaches. Forschungsbericht aus dem Fachbereich bauwesen, 54, Universität-Gesamthochschule Essen.

[36] de Borst, R. (1991). Simulation of strain localization: A reappraisal of the Cosserat continuum. *Engineering Computations*, **8**: 317-332.

[37] de Borst, R. and Mühlhaus, H.B. (1992). Gradient-dependent plasticity: Formulation and algorithmic aspects. *International Journal for Numerical Methods in Engineering*, **35**: 521-539.

[38] Della Vecchia, G., Jommi, C. and Romero, E. (2013). A fully coupled elastic–plastic hydromechanical model for compacted soils accounting for clay activity. *International Journal for Numerical and Analytical Methods in Geomechanics*, **37**(5): 503–535.

[39] Desai, C.S. and Zhang, D. (1987). Viscoplastic models for geologic materials with generalized flow rule. *International Journal for Numerical and Analytical Methods in Geomechanics*. **11**: 603–620.

[40] Desrues, J. and Viggiani, G. (2004). Strain localization in sand: an overview of the experimental results obtained in Grenoble using stereophotogrammetry. *International Journal for Numerical and Analytical Methods in Geomechanics*, **28**: 279-321.

[41] Desrues, J., Chambon, R., Mokni, M. and Mazcrolle, F. (1996). Void ratio evolution inside shear bands in triaxial sand specimens studied by computed tomography. *Géotechnique*, **46**(3):529-546.

[42] di Prisco, C. and Imposimato, S. (2003). Nonlocal numerical analyses of strain localization in dense sand. *Mathematical and Computer Modelling*, 37, 497–506.

[43] di Prisco, C. and Imposimato, S. (1996). Time dependent mechanical behaviour of loose sands. *Mechanics of Cohesive-Frictional Materials*, **1**: 45-73.

[44] di Prisco, C. and Imposimato, S. (1997). Experimental analysis and theoretical interpretation of triaxial load controlled loose sand specimen collapses. *Mechanics of Cohesive-Frictional Materials*, **2**: 93–120.

[45] di Prisco, C. and Pastor, M. (2000). Constitutive equations in plasticity. *In Revue française de génie civil*, **4**(5): 109-186.

[46] di Prisco, C., Imposimato, S. and Aifantis, E.C. (2002). A visco-plastic constitutive model for granular soils modified according to non-local and gradient approaches. *International Journal for Numerical and Analytical Methods in Geomechanics*, **26**: 121-138.

[47] Diéz, P., Arroyo, M. and Huerta, A. (2002). Adaptivity based on error estimation for viscoplastic softening materials. *Mechanics of Cohesive-Frictional Materi*als, **5**: 87-112.

[48] Duvaut, G and Lions, L.J. (1972). *Inequalities in Mechanics and Physics*. Springer, Berlin.

[49] Ehlers, W. and Volk, W. (1998). On theoretical and numerical methods in the theory of porous media based on polar and non-polar elasto-plastic solid materials. *International Journal of Solids and Structures*, **35**: 4597-4617.

[50] Ehlers, W., Graf, T. and Ammann, M. (2004). Deformation and localization analysis of partially saturated soil. *Computer Methods in Applied Mechanics and Engineering*, **193**: 2885–2910.

[51] Eringen A.C. (1981). On nonlocal plasticity. *International Journal of Engineering Science*, **19**:

1461-1474.

[52] Eringen A.C. (1983). Theories of nonlocal plasticity. *International Journal of Engineering Science*, **21**: 741-751.

[53] Eringen A.C. and Edelen, D.G.B. (1972). On nonlocal elasticity. *International Journal of Engineering Science*, **10**: 233-248.

[54] Escario, V. and Juca, J.F.T. (1989). Strength and deformation of partly saturated soils. *Proc. 12th Int. Conf. Soil Mech. Found. Eng.*, Rio de Janeiro, **1**: 43-46.

[55] Exadaktylos, G.E. and Vardoulakis, I.G. (2007). *Bifurcations, Instabilities, Degradation in Geomechanics*, Springer, Berlin.

[56] Forsyth, P.A. and Simpson, R.B. (1991). A two-phase, two-component model for natural convection in a porous medium. *International Journal for Numerical Methods in Fluids*, **1**2, 655-682.

[57] Fredlund, D.G. and Xing, A. (1994). Equations for soil-water characteristic curve. *Canadian Geotechnical Journal*, **31**: 521-532.

[58] Fredlund, D.G., Morgenstern, N.R. and Widger, R.S. (1978). The shear strength of unsaturated soils. *Can. Geotech. J.*, **15**(3): 313-321.

[59] Gajo, A. and Wood D.M. (1999), Seven-Trent sand: a kinematic-hardening constitutive model: the q-p formulation. *Géotechnique*, **49** (5), 595-614.

[60] Gawin, D. and Sanavia, L. (2009). A unified approach to numerical modelling of fully and partially saturated porous materials by considering air dissolved in water. *CMES- Computer Modeling in Engineering & Science*, **53**: 255-302.

[61] Gawin, D. and Sanavia, L. (2010). Simulation of cavitation in water saturated porous media considering effects of dissolved air. *Transport Porous Media*, **81**: 141-160.

[62] Gawin, D. and Schrefler, B.A. (1996). Thermo-hydro-mechanical analysis of partially saturated porous materials. *Engineering Computations*, 1**3**(7): 113-143.

[63] Gawin, D., Baggio, P. and Schrefler, B.A. (1995). Coupled heat, water and gas flow in deformable porous media. *International Journal for Numerical Methods in Fluids*, **20**, 969-987.

[64] Gens, A. (1995). Constitutive modelling: Application to compacted soils. Unsaturated Soils, Paris, Balkema, 1179-1200.

[65] Gens, A. (2010). Soil-environmental interactions in geotechnical engineering. *Géotechnique*, **60**: 3–74.

[66] Germer, K. and Braun, J. (2011). Effects of saturation on slope stability:laboratory experiments utilizing external load. *Vadose Zone Journal*, **10**: 477-486.

[67] Giry, C., Dufour, F. and Mazars, J. (2011). Stress-based nonlocal damage model. *International Journal of Solids and Structures*, **48**: 3431–3443.

[68] Gray, W.G. and Hassanizadeh, S.M. (1991). Paradoxes and realities in unsaturated flow theory. *Water Resources Research*, **27**(8): 1847-1854.

[69] Gray, W.G. and Hassanizadeh, S.M. (1991). Unsaturated flow theory including interfacial phenomena. *Water Resources Research*, **37**(8): 1855-1863.

[70] Gray, W.G. and Miller, C.T. (2014). *Introduction to the Thermodynamically Constrained Averaging Theory for porous medium systems*, Springer.

[71] Gray, W.G., Miller, C.T. and Schrefler, B.A. (2013). Averaging theory for description of environmental problems: What have we learned, *Advances in Water Resources*, **51**: 123–138.

[72] Gudehus, G. (1973). Elastoplastische stoffgleichungen für trochkenen sand. Infenieyr-Archiv. **42:** 151-169.

[73] Hassanizadeh, S.M. (1986). Derivation of basic equations of mass transport in porous media, Part 1. Macroscopic balance laws. *Advances in Water Resources*, **9**: 196-206.

[74] Hassanizadeh, S.M. and Gray, W.G. (1979a). General conservation equations for multi-phase system: 1. Averaging technique. *Advances in Water Resources*, **2**: 131-144.

[75] Hassanizadeh, S.M. and Gray, W.G. (1979b). General conservation Equations for multi-phase system: 2. Mass, momenta, energy and entropy equations. *Advances in Water Resources*, **2**: 191-201.

[76] Hassanizadeh, S.M. and Gray, W.G. (1980). General conservation equations for multi-phase systems: 3. Constitutive theory for porous media flow. *Advances in Water Resources*, **3**(1): 25-40.

[77] Hassanizadeh, S.M. and Gray, W.G. (1990). Mechanics and thermodynamics of multiphase flow in porous media including interphase boundaries. *Advances in Water Resources*, **13**(4): 169-186.

[78] Heeres, O., Suiker, A. and de Borst, R. (2002). A comparison between the Perzyna viscoplastic model and the Consistency viscoplastic model. *European Journal of Mechanics A/Solids*, **21**: 1-12.

[79] Hill, R.A. (1958). A general theory of uniqueness and stability in elasto-plastic solids. *Journal of the Mechanics and Physics of Solids*, **6**(3): 236-249.

[80] Hofstetter, G. and Taylor, R.L. (1991). Treatment of the corner region for Drucker-Prager type plasticity. *ZAMM Z angew Math Mech.*, **71**: 589–591.

[81] Imposimato, S. and Nova, R. (1998). An investigation on the uniqueness of the incremental response of elastoplastic models for virgin sand. *Mechanics of Cohesive-Frictional Materials*, **3**: 65-87.

[82] Jardine, R. J., Gens, A., Hight, D.W. and Coop, M.R. .(2004). Developments in understanding soil behaviour. *Advances in Geotechnical engineering*. The Skempton Conference, Thomas Telford, 103-206.

[83] Jiraséc, M. (2002). Objective modeling of strain localization. *Revue française de génie civil*, **6**: 119-1132.

[84] Jirásek, M. and Rolshoven, S. (2003). Comparison of integral-type nonlocal plasticity models for strain-softening materials. *International Journal of Engineering Science*, 41, 1553-1602.

[85] Jommi, C. (2000). *Remarks on the constitutive modelling of unsaturated soils*. Volume 153. eds A. Tarantino and C. Mancuso. Rotterdam: Balkema.

[86] Jommi, C. and Di Prisco, C. (1994). A simple theoretical approach for modelling the mechanical behaviour of unsaturated soils. *In Proceedings of the Conference "Il ruolo dei fluidi nei problemi di Ingegneria geotecnica"*, **1**: 167–188.

[87] Ju, J. (1990). Consistent tangent moduli for a class of viscoplasticity. *Journal of Engineering Mechanics*, **116**: 1764-1779.

[88] Kröner, E. (1967). Elasticity theory of materials with long-range cohesive forces. *Int. J. Solids*

Struct, **3**: 731–742.

[89] Lade, P.V. (1982). Localization effects in triaxial tests on sand. *Proceedings of Conference on Deformation and Failure of Granular Media*, Balkema, Rotterdam, 461–471.

[90] Lagioia, R., Puzrin, A. and Potts, D. (1996). A new versatile expression for yield e plastic potential surfaces. *Computers and Geothecnics*, **19**(3): 171-191.

[91] Lazari M., Sanavia L. and Schrefler, B.A. (2015). Local and non-local elasto-viscoplasticity in strain localization analysis of multiphase geomaterials. *International Journal for Numerical and Analytical Methods in Geomechanics*, **39**: 1570-1592.

[92] Lemaitre, J. and Chaboche, J.L. (1988). *Mécanique des matériaux solides*, Funod, Paris.

[93] Lewis, R.W. and Schrefler, B.A. (1998). *The Finite Element Method in the Static and Dynamic Deformation and Consolidation of Porous Media*. Wiley and Sons: Chichester.

[94] Liingaard, M., Augustesen, A. and Lade, P.V. (2004). Characterization of models for time-dependent behavior of soils. *International Journal of Geomechanics*, **4**(3): 157-177.

[95] Lins, Y. (2009). *Hydro-Mechanical properties of Partially Saturated Sand*. PhD thesis, Bochum University, Germany.

[96] Liu, X. (2003). *Numerical modeling of porous media response under static and dynamic load conditions*. PhD Thesis, TU Delft, the Netherlands.

[97] Loret, B. and Prevost, J.H. (1990). Dynamic strain localization in elasto (visco-) plastic solids, Part 1. General formulation and one-dimensional examples. *Computer Methods in Applied Mechanics and Engineering*, **83**: 247–273.

[98] Lu, X., Bardet, J.P. and Huang, M. (2012). Spectral analysis of nonlocal regularization in two-dimensional finite element models. *International Journal for Numerical and Analytical Methods in Geomechanics*, 36, 219-235.

[99] Luzio, G.D. and Bažant, Z.P. (2005). Spectral analysis of localization in nonlocal and overnonlocal materials with softening plasticity or damage. *International Journal of Solids and Structures*, 42, 6071–6100.

[100] Mihalache, C. and Buscarnera, G. (2014). Mathematical identification of diffuse and localized instabilities in fluid-saturated sands. *International Journal for Numerical and Analytical Methods in Geomechanics*. **38**(2): 111–141.

[101] Mokni, M. and Desrues, J. (1998). Strain localisation measurements in undrained plane-strain biaxial tests on hostun RF sand. *Mechanics of Cohesive-Frictional Materials*, **4**: 419–441.

[102] Moran, M.J. and Shapiro, H.N. (1993). *Fundamentals of Engineering Thermodynamics*. 2nd ed., John Wiley and Sons, New York.

[103] Mualem, Y. (1976). A new model for predicting the hydraulic conductivity of unsaturated porous media. *Water Resources Research*, **12**: 593-622.

[104] Mühlhaus, H.B. (1986). Scherfugenanalyse bei granularem Material im Rahmen der Cosserat-Theorie, *Ingenieur-Archiv*, **56**: 389–399.

[105] Mühlhaus, H.B. and Aifantis, E.C. (1991). A variational principle for gradient plasticity. *International Journal of Solids and Structu*res, **28**: 845–857.

[106] Mühlhaus, H.B. and Vardoulakis, I. (1987). The thickness of shear bands in granular materials. *Géotechnique*, **37**: 271–283.

[107] Needleman, A. (1988). Material rate dependence and mesh sensitivity on localization problems. *Computer Methods in Applied Mechanics and Engineering*, **67**, 69-86.

[108] Nova, R. (2000). Development of elastoplastic strain-hardeing constitutive laws. In *Degradations and Instabilities in Geomaterials*, F. Darve & I.Vardoulakis eds., Springer Verlag, 35-76.

[109] Nova, R., Castellanza, R. And Tamagnini, C. (2003). A constitutive model for bonded geomaterials subject to mechanical and/or chemical degradation. *International Journal for Numerical and Analytical Methods in Geomechanics*, **27**: 705-732.

[110] Nuth, M. and Laloui, L. (2008). Effective stress concept in unsaturated soils: Clarification and validation of a unified framework. *International Journal for Numerical and Analytical Methods in Geomechanics,* **32**: 771-801.

[111] Oka, F., Adachi, T. and Yashima, A. (1994). Instability of an elastoviscoplastic constitutive model for clay and strain localization. *Mechanics of Materials*, **18**: 119–129.

[112] Oka, F., Higo, Y. and Kimoto, S. (2002). Effect of dilatancy on the strain localization of water-saturated elasto-viscoplastic soil. *International Journal of Solids and Structures*, **39**: 3625–3647.

[113] Oka, F., Yashima, A. and Adachi, T. (1995). A strain localization analysis using a viscoplastic softening model for clay. *International Journal of Plasticity*, **11**: 523–545.

[114] Oldecop, L.A. and Alonso, E.E. (2007). Theoretical investigation of the time-dependent behaviour of rockfill. *Géotechnique*, **57**(3): 289–301.

[115] Owen, D.R.J and Hinton, E. (1980). *Finite Elements in Plasticity: Theory and Practice*. Pineridge Press: Swansea, U.K.

[116] Passatotto, M. (2013). *Development of a model for the thermo-hydro-mechanical analysis of multiphase porous media in dynamics*. Ph.D. thesis, Padova University, Italy.

[117] Perzyna, P. (1966). Fundamental problems in viscoplasticity. *Advances in Applied Mechanics*, **9**: 243-377.

[118] Pham Van Bang, D. and Di Benedetto, H., Duttine, A. and Ezaoui, A. (2007). Viscous behaviour of dry sand. *International Journal for Numerical and Analytical Methods in Geomechanics*, **31**: 1631-1658.

[119] Pijaudier-Cabot, G. and Bažant, Z.P. (1987). Nonlocal damage theory. *Journal of Engineering Mechanics*, ASCE, **113**: 1512-1533.

[120] Pisanò, F. (2011). Seismic Performance of Infinite Earth Slopes: Numerical Modelling, Constitutive Issues and Theoretical Considerations, Ph.D. thesis, Politecnico di Milano, Italy.

[121] PLAXIS (2012a), PLAXIS 2D. Material Models Manual.

[122] Regueiro, R.A. and Borja, R.I. (2001). Plane strain finite element analysis of pressure sensitive plasticity with strong discontinuity. *International Journal of Solids and Structures*, **38**: 3647-3672.

[123] Rolshoven, S. and Jirásek, M. (2003). Numerical aspects of nonlocal plasticity with strain softening. *In Bićanić, N., de Borst, R., Mang, H., and Meschke, G., editors, Computational Modelling of Concrete Structures (EURO-C 2003)*, St. Johann im Pongau, Austria, Lesse, The Netherlands, Swets & Zeitlinger B.V., 305-314.

[124] Roscoe, K.H. (1970). The influence of strains in Soil Mechanics. *Géotechnique*, **20**: 129-170.

[125] Rudnicki, J.W. and Rice, J.R. (1975). Conditions for the localization of deformation in pressure-sensitive dilatant materials. *Journal of the Mechanics and Physics of Solids*, **23**: 371-394.

[126] Safai, N.M and Pinder, G.F. (1979). Vertical and horizontal land deformation in a desaturating porous medium, *Advances in Water Resources*, **2**: 19-25.

[127] Sampaio, R. and Williams, W.O. (1979). Thermodynamics of diffusing mixtures, *Journal de Méchanique*, **18**(1): 19-45.

[128] Sanavia, L., François, B., Bortolotto, R., Luison, L. and Laloui, L. (2008). Finite element modelling of thermo-elasto-plastic water saturated porous materials. *Journal of Theoretical and Applied Mechanics*, **38**: 7-24.

[129] Sanavia, L., Pesavento, F. and Schrefler, B.A. (2006). Finite element analysis of non-isothermal multiphase geomaterials with application to strain localization simulation. *Computational Mechanics*, **37**: 331-348.

[130] Schrefler, B.A. (1984). *The Finite Element Method in Soil Consolidation (with applications to Surface Subsidence)*. Ph.D. thesis, University College of Swansea, UK.

[131] Schrefler, B.A. (2002). Mechanics and thermodynamics of saturated/unsaturated porous materials and quantitative solutions. *Applied Mechanics Reviews*, **55**(4): 351-388.

[132] Schrefler, B.A., Sanavia, L. and Majorana, C.E. (1996). A multiphase medium model for localization and post localization simulation in geomaterials, *Mechanics of Cohesive-Frictional Materials*, **1**: 95-114.

[133] Schrefler, B.A., Simoni, L., Xikui, L. and Zienkiewicz, O.C. (1990). Mechanics of partially saturated porous media. *Numerical Methods and Constitutive Modelling in Geomechanics*, C.S. Desai and G. Gioda (eds), Springer-Verlag, Wien, 196-209.

[134] Schrefler, B.A., Zhang, H.W. and Sanavia, L. (2006). Interaction between different internal length scales in fully and partially saturated porous media – The 1-D case. *International Journal for Numerical and Analytical Methods in Geomechanics*, **30**: 45-70.

[135] Schwer, L. (1994). Viscoplastic augmentation of the smooth cap model. *Nuclear Engineering and Design*, **150**: 215-223.

[136] Sheng, D. (2011). Review of the fundamental principles in modelling unsaturated soil behaviour. *Computer and Geotechnics*, **38**: 757-776.

[137] Sheng, D., Sloan, S. and Gens, A. (2004). A constitutive model for unsaturated soils: thermomechanical and computational aspects. *Computational Mechanics*, **33**(6): 453–465.

[138] Simo, J. C., Kennedy, J. G., and Govindjee, S. (1988b). Non-smooth multisurface plasticity and viscoplasticity. Loading/unloading conditions and numerical algorithms. . *International Journal for Numerical Methods in Engineering*, **26**:2 161-2185.

[139] Simo, J.C and Hughes, T.J.R. (1998). *Computational Inelasticity*, Springer, New York.

[140] Simo, J.C. (1989). Strain softening and dissipation: a unification of approaches. *In Mazars, J., Bazant, Z.P. (Eds.), Cracking and Damage, Strain Localization and Size Effects*, Elsevier, London, 440-461.

[141] Simo, J.C. and Taylor, R.L. (1985). Consistent tangent operators for rate independent elasto-plasticity. *Computer Methods Appl. Mech. Engrg*., **48**: 101-118.

[142] Simpson, B. (1973). *Finite elements applied to problems of plane strain deformation in soil*.

PhD theis, University of Cambridge, England.

[143] Sluys, L.J. (1992). *Wave propagation, localization and dispersion in softening solids*, Ph.D. Dissertation, Delft University of Technology, Delft.

[144] Sluys, L.J., de Borst, R. and Mühlhaus, H.B. (1993). Wave propagation, localization and dispersion in a gradient-dependent medium. *International Journal of Solids and Structures*, **30**: 1153–1171.

[145] Strömberg, L. and Ristinmaa, M. (1996). FE-formulation of a nonlocal plasticity theory. *Computer Methods in Applied Mechanics and Engineering*, **136**: 127-144.

[146] Tamagnini, C., Castellanza, R. and Nova, R. (2002). A generalized backward Euler algorithm for the numerical integration of an isotropic hardening elastoplastic model for mechanical and chemical degradation of bonded geomaterials. *International Journal for Numerical Methods in Engineering*, **26**: 963-1001.

[147] Tatsuoka, F., Nakamura, S., Huang, C.C. and Tani, K. (1990). Strength anisotropy and shear band direction in plane strain tests of sand. *Soils and Foundations*, **30**(1): 35-54.

[148] van Genuchten, M.T. (1980). A closed-form equation for predicting the hydraulic conductivity of unsaturated soils. *Soil Science Society of America Journal*, **44**(5): 892-898.

[149] Vardoulakis, I. (1980). Shear band inclination and shear modulus of sand in biaxial tests. *International Journal for Numerical and Analytical Methods in Geomechanics*, **4**: 103-119.

[150] Voyiadjis, G.Z. and Dorgan, R.J. (2001). Gradient formulation in coupled damage-plasticity, *Archives of Mechanics*, **53**(4–5): 565–597.

[151] Wang, W.M. (1997). *Stationary and propagative instabilities in metals – a computational point of view*. Ph.D. Dissertation, Delft University of Technology, Delft.

[152] Wang, W.M., Sluys, L.J. and de Borst, R. (1997). Viscoplasticity for instabilities due to stain softening and strain-rate softening, *International Journal for Numerical Methods in Engineering*, **40**: 3839-3864.

[153] Wheeler, S. and Sivakumar, V. (1995). An elasto-plastic critical state framework for unsaturated soil. *Géotechnique*, **45**(1): 35–53.

[154] Wu, F.H. and Freund, L.B. (1984). Deformation trapping due to thermoplastic instability in one-dimensional wave propagation. *J. Mech. Phys. Solids*, **32**: 119–132.

[155] Zhang, H.W. and Schrefler B.A. (2000). Gradient-dependent plasticity model and dynamic strain localization analysis of saturated and partially saturated porous media: one dimensional model. *European Journal of Mechanics A/Solid*s, **19**(3): 503–524.

[156] Zhang, H.W. and Schrefler B.A. (2004). Particular aspects of internal length scales in strain localization analysis of multiphase porous materials. *Computer Methods in Applied Mechanics and Engineering*, **193**: 2867–2884.

[157] Zhang, H.W., Sanavia, L. and Schrefler, B.A. (1999). An internal length scale in strain localisation of multiphase porous media. *Mechanics of Cohesive Frictional Materials and Structures*, **4**: 443–460.

[158] Zienkiewicz, O.C. and Taylor, R.L. (2000). *The Finite Element Method, vol. 1: The Basis*, Butterworth-Heinemann, Oxford.

[159] Zienkiewicz, O.C. and Taylor, R.L. (2000). *The Finite Element Method, vol. 2: The Solid Mechanics*, Butterworth-Heinemann, Oxford.

[160] Zytynski, M., Randolph, M.K., Nova, R. and Wroth, C.P. (1978). On modelling the unloading-reloading behaviour of soils. *International Journal for Numerical and Analytical Methods in Geomechanics,* **2**: 87-93.

Appendix A

Derivative of S with respect to σ'

The invariant, S, is introduced, defined as (Dafalias and Herrmann (1986)):

$$S = \left\{ \frac{1}{3} \mathrm{tr}\left(\mathbf{s}^3\right) \right\}^{\frac{1}{3}} = \left\{ J_3 \right\}^{\frac{1}{3}}$$

Thus, for the calculation of the derivative of the third invariant of deviator stress, J_3, with respect to the effective stress σ'_{ij}, the following procedure is applied (for simplicity the components of the generalized effective stress will be referred to without using tonal notation):

- Stress 2nd order tensor in 3D:

$$\sigma_{ij} = \begin{pmatrix} \sigma_{11} & \sigma_{12} & \sigma_{13} \\ \sigma_{21} & \sigma_{22} & \sigma_{23} \\ \sigma_{31} & \sigma_{32} & \sigma_{33} \end{pmatrix}$$

- The first invariant is expressed as:

$$I_1 = \sigma_{11} + \sigma_{22} + \sigma_{33}$$

- The second invariant is expressed as:

$$I_2 = \sigma_{11}\sigma_{22} + \sigma_{22}\sigma_{33} + \sigma_{33}\sigma_{11} - \sigma_{12}\sigma_{12} - \sigma_{13}\sigma_{13} - \sigma_{23}\sigma_{23}$$

- The third invariant is expressed as:

$$I_3 = \mathrm{Det}(\sigma_{ij}) = -\sigma_{13}\sigma_{22}\sigma_{31} + \sigma_{12}\sigma_{23}\sigma_{31} + \sigma_{13}\sigma_{21}\sigma_{32} - \sigma_{11}\sigma_{23}\sigma_{32} - \sigma_{12}\sigma_{21}\sigma_{33} + \sigma_{11}\sigma_{22}\sigma_{33}$$

- The first invariant of deviator stress is expressed as:

$$J_1 = 0$$

- The second invariant of deviator stress is expressed as:

$$J_2 = \frac{I_2^2}{3} - I_2$$

- The mean pressure is expressed as:

$$p = (\sigma_{11} + \sigma_{22} + \sigma_{33}) / 3$$

- The Kronecker delta is expressed as:

$$\delta_{ij} = \begin{pmatrix} 1 & 0 & 0 \\ 0 & 1 & 0 \\ 0 & 0 & 1 \end{pmatrix}$$

- The deviator stress tensor is expressed as:

$$s_{ij} = \sigma_{ij} + p\delta_{ij}$$

- The third invariant of deviator stress tensor is expressed as:

$$J_3 = \mathrm{Det}(s_{ij}) = \frac{1}{27}(2\sigma_{11}^3 + 2\sigma_{22}^3 - 18\sigma_{13}\sigma_{22}\sigma_{31} + 27\sigma_{13}\sigma_{21}\sigma_{32} + 9\sigma_{22}\sigma_{23}\sigma_{32} +$$
$$9\sigma_{12}(3\sigma_{23}\sigma_{31} + \sigma_{21}(\sigma_{22} - 2\sigma_{33})) - 3(\sigma_{22}^2 - 3\sigma_{13}\sigma_{31} - 3\sigma_{23}\sigma_{32})\sigma_{33} - 3\sigma_{22}\sigma_{33}^2 + 2\sigma_{33}^3 - 3\sigma_{11}^2(\sigma_{22} + \sigma_{33}) +$$
$$3\sigma_{11}(3\sigma_{12}\sigma_{21} - \sigma_{22}^2 + 3\sigma_{13}\sigma_{31} - 6\sigma_{23}\sigma_{32} + 4\sigma_{22}\sigma_{33} - \sigma_{33}^2))$$

Finally, the derivative of the third deviator stress invariant to σ_{ij} is obtained as:

$$\frac{\partial J_3}{\partial \sigma_{11}} = \frac{2\sigma_{11}^2}{9} + \frac{\sigma_{12}\sigma_{21}}{3} - \frac{2\sigma_{11}\sigma_{22}}{9} - \frac{\sigma_{22}^2}{9} + \frac{\sigma_{13}\sigma_{31}}{3} - \frac{2\sigma_{23}\sigma_{32}}{3} - \frac{2\sigma_{11}\sigma_{33}}{9} + \frac{4\sigma_{22}\sigma_{33}}{9} - \frac{\sigma_{33}^2}{9}$$

$$\frac{\partial J_3}{\partial \sigma_{22}} = -\frac{\sigma_{11}^2}{9} + \frac{\sigma_{12}\sigma_{21}}{3} - \frac{2\sigma_{11}\sigma_{22}}{9} + \frac{2\sigma_{22}^2}{9} - \frac{2\sigma_{13}\sigma_{31}}{3} + \frac{\sigma_{23}\sigma_{32}}{3} + \frac{4\sigma_{11}\sigma_{33}}{9} - \frac{2\sigma_{22}\sigma_{33}}{9} - \frac{\sigma_{33}^2}{9}$$

$$\frac{\partial J_3}{\partial \sigma_{33}} = -\frac{\sigma_{11}^2}{9} - \frac{2\sigma_{12}\sigma_{21}}{3} + \frac{4\sigma_{11}\sigma_{22}}{9} - \frac{\sigma_{22}^2}{9} + \frac{\sigma_{13}\sigma_{31}}{3} + \frac{\sigma_{23}\sigma_{32}}{3} - \frac{2\sigma_{11}\sigma_{33}}{9} - \frac{2\sigma_{22}\sigma_{33}}{9} + \frac{2\sigma_{33}^2}{9}$$

$$\frac{\partial J_3}{\partial \sigma_{12}} = \frac{\sigma_{11}\sigma_{21}}{3} + \frac{\sigma_{21}\sigma_{22}}{3} + \sigma_{23}\sigma_{31} - \frac{2\sigma_{21}\sigma_{33}}{3}$$

$$\frac{\partial J_3}{\partial \sigma_{13}} = \frac{\sigma_{11}\sigma_{31}}{3} - \frac{2\sigma_{22}\sigma_{31}}{3} + \sigma_{21}\sigma_{32} + \frac{\sigma_{31}\sigma_{33}}{3}$$

$$\frac{\partial J_3}{\partial \sigma_{23}} = \sigma_{12}\sigma_{31} - \frac{2\sigma_{11}\sigma_{32}}{3} + \frac{\sigma_{22}\sigma_{32}}{3} + \frac{\sigma_{32}\sigma_{33}}{3}$$

Appendix B

Triaxial tests at varying suction and net confinement pressure with VISCUNsand model.

The triaxial shear tests with different suction levels and net confinement pressures have been investigated with the VISCUNsand model. For brevity, the results were not presented in Section 5.5. However, for the sake of completeness of model's validation at different hydraulic conditions, the simulation results are summarized below.

The material parameters are as in Table 5.2 and the set of the analyses performed are listed in Table 5.3. To be able to compare the viscoplastic results with the elastoplastic, published in Buscarnera and Nova (2009), suitable viscosity parameters were adopted.

It is noted that the elasto-viscoplastic response tends to the elasto-plastic limit at vanishing rate-sensitiveness. Thus, the viscosity parameters used for the simulations are γ=0.1 s^{-1} and α=1.0.

The results illustrate the coincidence of the viscoplastic model with the results by Buscarnera and Nova.

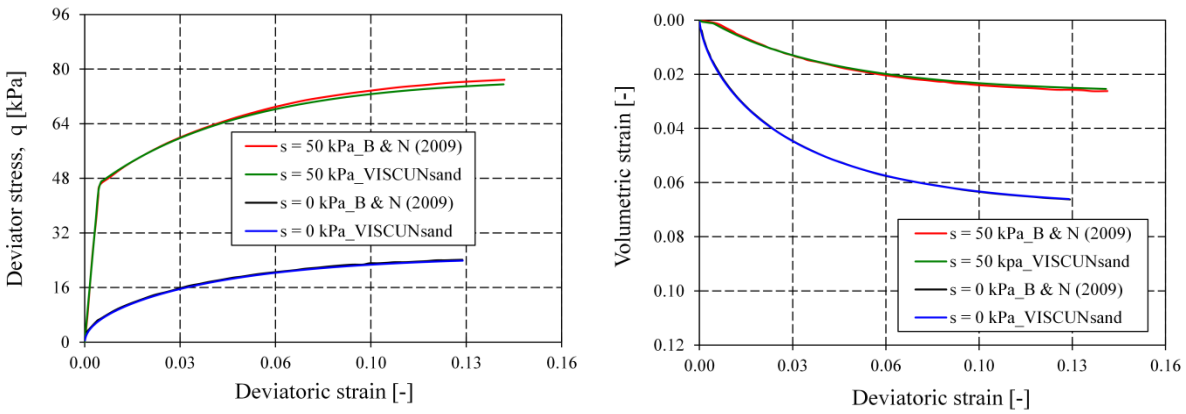

(a) (b)

VISCUNsand validation: Comparison of the results of a triaxial test under saturated (s=0 kPa) and unsaturated (s=50 kPa) conditions: (a) deviatoric stress and (b) volumetric strain versus deviatoric strain.

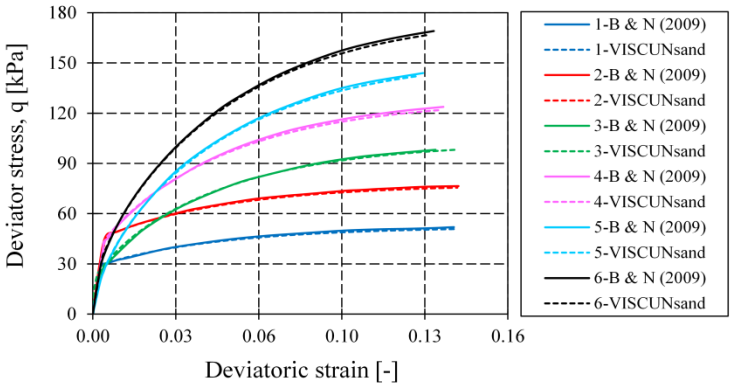

(a)

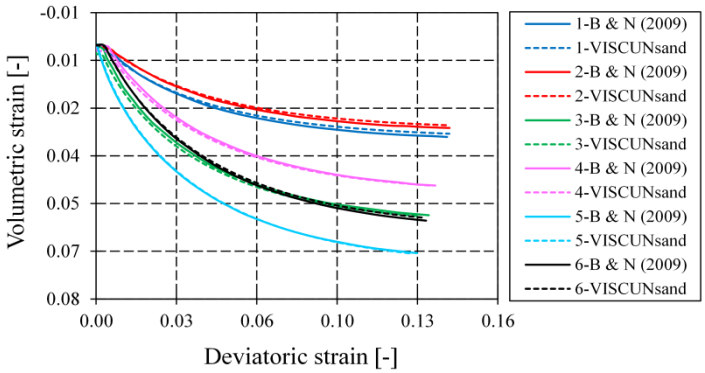

(b)

VISCUNsand validation - Comparison of the results for the six simulations with varying suction and net confinement pressure: (a) deviatoric stress and (b) volumetric strain versus deviatoric strain.

Nomenclature

Conventions

In this thesis direct notation is adopted: Boldface letters will denote vector or 2nd order tensors, boldface capital letters will denote 4th order tensors and lightface (and/or italic) letters will be used for scalar quantities.

- Mathematical notations – Operations:

tr**a**	Trace of **a**
det**a**	Determinant of **a**
dev**a**	Deviatoric part of **a**
$\mathbf{a}^{T}$	Transpose of **a**
$\mathbf{a}^{-1}$	Inverse of **a**
$\|\mathbf{a}\|$	Euclidian norm of **a**; $\|\mathbf{a}\| = \sqrt{\mathbf{a} : \mathbf{a}}$ for second-order tensor, while $\|\mathbf{a}\| = \sqrt{\mathbf{a}^2}$ for vectors
$\mathbf{a} \otimes \mathbf{b}$	Dyadic (or tensor) product of **a** and **b**
a : b	Double dot product (or double contraction) between **a** and **b**, (**a : b**=$a_{ij}b_{ij}$)

- Some important derivative rules for second order tensor **a** are:

$$\frac{\partial \|\mathbf{a}\|}{\partial \mathbf{a}} = \frac{\mathbf{a}}{\|\mathbf{a}\|},$$

$$\frac{\partial (\mathrm{tr}\mathbf{a}^{k})}{\partial \mathbf{a}} = k(\mathbf{a}^{k-1})^{T},$$

$$\frac{\partial (\mathrm{tr}\mathbf{a})}{\partial \mathbf{a}} = \mathbf{1}$$

- Stress 2nd order tensor in 3D:

$$\sigma_{ij} = \begin{pmatrix} \sigma_{11} & \sigma_{12} & \sigma_{13} \\ \sigma_{21} & \sigma_{22} & \sigma_{23} \\ \sigma_{31} & \sigma_{32} & \sigma_{33} \end{pmatrix}$$

and in vector form:

$$\boldsymbol{\sigma} = \begin{pmatrix} \sigma_{11} \\ \sigma_{22} \\ \sigma_{33} \\ \sigma_{12} \\ \sigma_{13} \\ \sigma_{23} \end{pmatrix}$$

$1 \longrightarrow$ vertical (axial, in-plane)

$2 \longrightarrow$ horizontal (axial, out of plane)

$3 \longrightarrow$ horizontal (axial, in-plane)

- Strain 2nd order tensor in 3D:

$$\varepsilon_{ij} = \begin{pmatrix} \varepsilon_{11} & \varepsilon_{12} & \varepsilon_{13} \\ \varepsilon_{21} & \varepsilon_{22} & \varepsilon_{23} \\ \varepsilon_{31} & \varepsilon_{32} & \varepsilon_{33} \end{pmatrix}$$

and in vector form:

$$\boldsymbol{\varepsilon} = \begin{pmatrix} \varepsilon_{11} \\ \varepsilon_{22} \\ \varepsilon_{33} \\ \varepsilon_{12} \\ \varepsilon_{13} \\ \varepsilon_{23} \end{pmatrix}$$

$1 \longrightarrow$ vertical (axial, in-plane)

$2 \longrightarrow$ horizontal (axial, out of plane)

$3 \longrightarrow$ horizontal (axial, in-plane)

Deviatoric part of ε: $\mathbf{e} = \varepsilon - \frac{1}{3}\mathrm{tr}(\varepsilon)\mathbf{1}$

$$e_{ij} = \begin{pmatrix} \varepsilon_{11} - \frac{\varepsilon_v}{3} & \varepsilon_{12} & \varepsilon_{13} \\ \varepsilon_{21} & \varepsilon_{22} - \frac{\varepsilon_v}{3} & \varepsilon_{23} \\ \varepsilon_{31} & \varepsilon_{32} & \varepsilon_{33} - \frac{\varepsilon_v}{3} \end{pmatrix}$$

and the volumetric strain:

$$\varepsilon_v = \varepsilon_{11} + \varepsilon_{22} + \varepsilon_{33}$$

Rewrite deviatoric strains in vector form:

$$\mathbf{e} = \begin{pmatrix} \varepsilon_{11} - \varepsilon_v / 3 \\ \varepsilon_{22} - \varepsilon_v / 3 \\ \varepsilon_{33} - \varepsilon_v / 3 \\ \varepsilon_{12} \\ \varepsilon_{13} \\ \varepsilon_{23} \end{pmatrix}$$

- 2nd order identity tensor (**1**) and dyadic product:

$$\mathbf{1}=\begin{pmatrix}1\\1\\1\\0\\0\\0\end{pmatrix},\quad \mathbf{1}\otimes\mathbf{1}=\begin{pmatrix}1\\1\\1\\0\\0\\0\end{pmatrix}\otimes\begin{pmatrix}1&1&1&0&0&0\end{pmatrix}=\begin{pmatrix}1&1&1&0&0&0\\1&1&1&0&0&0\\1&1&1&0&0&0\\0&0&0&0&0&0\\0&0&0&0&0&0\\0&0&0&0&0&0\end{pmatrix}$$

- 4nd order identity tensor:

$$\mathbf{I}=\begin{pmatrix}1&0&0&0&0&0\\0&1&0&0&0&0\\0&0&1&0&0&0\\0&0&0&1/2&0&0\\0&0&0&0&1/2&0\\0&0&0&0&0&1/2\end{pmatrix}$$

- 4th order deviatoric tensor: $\mathbf{I}_{\mathbf{dev}}=\mathbf{I}-\frac{1}{3}\mathbf{1}\otimes\mathbf{1}$

$$\mathbf{I}_{\mathbf{dev}}=\begin{pmatrix}2/3&-1/3&-1/3&0&0&0\\-1/3&2/3&-1/3&0&0&0\\-1/3&-1/3&2/3&0&0&0\\0&0&0&1/2&0&0\\0&0&0&0&1/2&0\\0&0&0&0&0&1/2\end{pmatrix}$$

Symbols

D_g^{ga} : effective diffusivity tensor of dry air in water vapour [m^2s^{-1}];

D_g^{gw} : effective diffusivity tensor of water vapour in dry air [m^2s^{-1}];

$\boldsymbol{k}$: intrinsic permeability tensor [m^2];

$k^{r\pi}$: relative permeability of π-phase (π = ga, gw);

$\dot{m}_{vap}$: rate of mass due to phase change [$kgm^{-3}\ s^{-1}$]

M_a : molar mass of dry air [$kg^2\ kmol^{-1}$];

M_w : molar mass of water [$kg^2\ kmol^{-1}$];

M_g : molar mass of gas [$kg^2\ kmol^{-1}$];

RH : relative humidity;

p^c : capillary pressure [Pa];

p^g : gas pressure [Pa];

p^w : liquid water pressure [Pa];

p^{ga} : dry air partial pressure [Pa];

p^{gw} : water vapour partial pressure [Pa];

p^{gws} : saturated water vapour partial pressure [Pa];

q : stress like internal variable [Pa];

R : gas constant ($8314.41 Jkmol^{-1}K^{-1}$)

S_w : liquid phase volumetric saturation [-];

S_g : gas phase volumetric saturation [-];

n : total porosity [-];

t : time [s];

T : absolute temperature [K];

T_{cr} : critical temperature of water [K];

u : displacement vector of solid matrix [m]

$\overline{\boldsymbol{v}}^{\pi s}$: relative velocity of π-phase (π = g, w) with respect to solid phase [ms^{-1}];

v_g^{gw} : diffusion velocity of water vapour in dry air [ms^{-1}]

v_g^{ga} : diffusion velocity of dry air in water vapour [ms^{-1}]

C_p^w : specific heat of liquid phase [$Jkg^{-1}K^{-1}$];

C_p^g : specific heat of gas mixture [$Jkg^{-1}K^{-1}$];

C_p^s : specific heat of solid phase [$Jkg^{-1}K^{-1}$];

C_p : effective specific heat of porous medium [$Jkg^{-1}K^{-1}$];

K_w : Bulk modulus of the water [Pa];

K_s : Bulk modulus of the solid [Pa];

K_g : Bulk modulus of the gas [Pa];

$\boldsymbol{g}$: gravity acceleration [m/s^2];

$\left(\rho C_p\right)_{eff}$: effective thermal capacity of porous medium [$JL^{-3}K^{-1}$];

D^s : symmetric part of the stiffness matrix;

p_s : preconsolidation pressure [Pa];

$\hat{k}$: slope of the swelling line in the lnυ-lnp' plane [-];

r_{sw} : hydraulic hardening parameter [-];

p_r : reference pressure [Pa];

B_p : logarithmic volumetric compliance under isotropic loading [-];

G : shear modulus [Pa]

Greek Symbols

a_c : convective heat exchange coefficient [$Wm^{-2}K^{-1}$];

β_s : cubic thermal expansion coefficient of solid [K^{-1}];

β_w : cubic thermal expansion coefficient of water [K^{-1}];

β_{sw} : combine (solid + liquid) cubic thermal expansion coefficient [K^{-1}];

β_c : convective mass exchange coefficient [ms^{-1}];

β_{swg} : combine (solid + liquid + gas) cubic thermal expansion coefficient [K^{-1}];

χ_{eff} : effective thermal conductivity of the porous medium [$Wm^{-1}K^{-1}$];

ΔH_{vap} : enthalpy of vaporization per unit mass [Jkg^{-1}];

Δt : time step [s];

γ : fluidity parameter [s^{-1}]

ε^e : elastic strain tensor [-];

ρ^{gw} : mass concentration of water vapour in gas phase [kgm^{-3}];

ρ^{ga} : mass concentration of dry air in gas phase [kgm^{-3}];

ρ : apparent density of porous medium [kgm^{-3}];

ρ^g : gas phase density[kgm^{-3}];

ρ^w : liquid phase density[kgm^{-3}];

ρ^s : solid phase density[kgm^{-3}];

μ^π : dynamic viscosity of the constituent of π-phase ($\pi = g, w$) [Pa.s];

λ : consistency parameter [-];

σ : Cauchy stress tensor [Pa];

σ' : effective stress tensor [Pa];

σ_o : Stefan-Boltzmann constant [$5.670 \cdot 10^{-8} Wm^{-2}K^{-4}$];

ξ : equivalent visco-plastic strain [-];

ψ_c : water potential [Jkg^{-1}];

η : soil viscosity [s];

ξ_s : dilatancy at failure [-]

Acronyms

CSL	: Critical State Line
SWCC	: Soil Water Characteristic Curve
FEM	: Finite Element Method
REV	: Representative Elementary Volume
HMT	: Hybrid Mixture Theory
VISCUNsand	: Viscoplastic model for Unsaturated soils
UNsand	: Elastoplastic model for Unsaturated soils
TXU	: Triaxial Undrained Compression test
TXD	: Triaxial Drained Compression test
PSU	: Plane-Strain Undrained Compression test
PSD	: Plane-Strain Drained Compression test
TCAT	: Thermodynamically Constrained Averaging Theory

List of Figures

List of Tables